Deformation Behavior of Reservoir Sandstones from the Seismogenic Groningen Gas Field:

An experimental and mechanistic study

Ronald Petrus Johannes Pijnenburg

Utrecht University

No. 194

Members of the dissertation committee:

Prof. dr. Frederick Chester
Agricultural and Mechanical University of Texas, United States of America

Prof. dr. Martyn Drury
Utrecht University, The Netherlands

Dr. Jérôme Fortin
Ecole Normale Supérieure, Paris, France

Prof. dr. Teng-fong Wong
State University of New York at Stony Brook, United States of America
and
The Chinese University of Hong Kong, Hong Kong SAR, China

Prof. dr. Mark Zoback
Stanford University, California, United States of America

The research was carried out at:
The High Pressure and Temperature Laboratory, Faculty of Geoscience, Utrecht University
(now at: Princetonlaan 4, 3584 CB Utrecht, The Netherlands)

Printed by: Proefschriftmaken

Copyright © Ronald Pijnenburg

All rights reserved. No parts of this publication may be reproduced in any form, by print or photo print, microfilm or other means, without written permission by the publisher.

ISBN/EAN: 978-90-6266-552-5

Deformation Behavior of Reservoir Sandstones from the Seismogenic Groningen Gas Field:

An experimental and mechanistic study

Deformatiegedrag van Reservoirzandstenen
uit het Seismogenetische Groningen Gasveld:

Een experimentele en mechanistische studie
(met een samenvatting in het Nederlands)

Proefschrift

ter verkrijging van de graad van doctor aan de Universiteit Utrecht op gezag van de rector magnificus, prof.dr. H.R.B.M. Kummeling, ingevolge het besluit van het college voor promoties in het openbaar te verdedigen op vrijdag 25 oktober
des middags te 2.30 uur

door

Ronald Petrus Johannes Pijnenburg

geboren op 5 augustus 1988
te Nijmegen, Nederland

Promotor**:** **Prof. dr. C.J. Spiers**
Copromotoren: **Dr. S.J.T. Hangx**
Dr. C.J. Peach

This thesis was financed by the Nederlandse Aardolie Maatschappij (NAM),
as part of the larger data acquisition and study programme
on induced seismicity in the Groningen gas field, North-East Netherlands

To see a World in a Grain of Sand

- William Blake

Explanation of the cover image

The image on the front cover of this book is a microscopy image of a Slochteren sandstone from the Groningen gas field in the Netherlands. From left to right, the image covers about half a millimeter of sandstone. The Slochteren sandstone is the gas bearing *reservoir* of the field, where the gas is contained in the *pores* (black in this image), that is: the space between the sand grains. Several sand grains are shown, each covered with rims of clay. In part, the clay occurs within grain-to-grain contacts and therefore contributes to the total strength of the sandstone when it is compressed, as is the case during gas production. The image was obtained by Dr. B.A. Verberne.

Verklaring van de kaftafbeelding

De afbeelding op de voorkant van dit boekje is een microscopieplaatje van een Slochteren zandsteen uit het Groningen gasveld in Nederland. Van links naar rechts bestrijkt dit plaatje zo'n halve millimeter aan zandsteen. Deze zandsteen is het gasdragende *reservoir* gesteente van het veld, waar het gas aanwezig is in de *poriën* (zwart in dit plaatje), d.w.z. de ruimte tussen de zandkorrels. Hier getoond zijn enkele zandkorrels, ieder bedekt met kleiranden. Deze klei komt gedeeltelijk voor in korrel-tot-korrel contacten en draagt daarmee bij aan de totale sterkte van de zandsteen als deze wordt ingedrukt, zoals het geval is tijdens gaswinning. De afbeelding is verkregen door Dr. B.A. Verberne.

Contents

Technical summary

Production of hydrocarbons from sandstone reservoirs commonly leads to subsidence and seismicity, as notably illustrated in recent years by induced earthquakes up to M_L 3.6 in Europe's largest gas field – the relatively densely populated (province wide average: ~200 inhabitants/km^2) Groningen gas field in the North-East Netherlands. Understanding and modelling the effects of hydrocarbon production on surface subsidence and induced seismicity requires constraints on the reversible elastic and irreversible inelastic deformation (compaction) behavior of the reservoir system in response to pore fluid (gas) pressure reduction. However, experimental data on the partitioning of elastic versus inelastic deformation are scarce at *in-situ* (subsurface) conditions of stress, temperature and pore fluid chemistry, and at the small vertical strains ($\varepsilon \leq 1.0\%$) relevant to producing reservoirs, such as the Slochteren sandstone in Groningen. Moreover, the processes potentially accommodating inelastic deformation are largely unidentified and the question of whether any inelastic strains are time- or loading rate-sensitive remains open. In current geomechanical models, applied to investigate induced subsidence and seismicity in the Groningen and other fields, reservoir compaction is usually taken to be (poro)elastic, or is represented by empirical models that include permanent inelastic deformation but with no mechanistic underpinning to support extrapolation to the field case and (post-)production time scales. In recent years, significant induced seismicity and associated building damage and public unrest in the Groningen field has created an urgent need to understand and quantify reservoir deformation/ compaction behavior better, and thus to improve the physical basis for assessing the effects of production strategies on subsidence and seismicity.

In this thesis, I report the results of an experimental study designed to study the deformation behavior shown by Slochteren reservoir sandstone samples recovered from the seismogenic center of the Groningen field. The elastic versus inelastic deformation behavior is studied by performing triaxial compression experiments of hours to one week duration, at *in-situ* conditions of temperature, stress and pore fluid chemistry, as well as at stresses exceeding those directly relevant to the field. In this way, an empirical model is developed describing reservoir behavior in terms of elastic and plastic strain contributions. State-of-the-art microstructural methods are employed to identify the grain-scale mechanisms accommodating inelastic deformation in the samples, and particularly at the small strains ($\varepsilon \leq 1.0\%$) relevant to the Groningen field. The mechanisms identified are incorporated in a novel microphysical model, which is used to underpin the empirical model describing reservoir deformation in the Groningen gas field, and the implications for induced subsidence and seismicity are examined.

More specifically now, **Chapter 1** outlines the motivation and scope of the study, and summarizes current knowledge on induced reservoir compaction, subsidence, and seismicity in the Groningen field and in other fields. Previous experimental work is discussed and key knowledge gaps are identified. This is followed by the definition of the aims of the thesis.

In **Chapter 2,** I aim to quantify the elastic versus time-independent and time-dependent inelastic strains developing in Slochteren sandstone samples during simulated reservoir depletion. Samples with initial porosities (φ_0) of 12.7 to 24.6% covering the porosity range of the field were subjected to conventional axi-symmetric compression experiments. These were conducted at *in-situ* conditions of temperature (100 °C) and pore fluid chemistry (4.4 M NaCl brine), and at stress conditions simulating full reservoir depletion in an assumed poroelastically deforming reservoir, *i.e.* at differential stresses ($Q = \sigma_1 - \sigma_3$) up to 50 MPa, and effective confining pressures (P_c^{eff} = total value minus pore pressure P_p) of 8 or else 15 MPa representing the initial and depleted reservoir stress state, respectively. Successive stages of active loading at a strain rate $\dot{\varepsilon}$ of 10^{-5} s^{-1} and subsequent stress relaxation were employed to study the partitioning between elastic versus time-(in)dependent inelastic deformation. The results showed that inelastic strain developed from the onset of compression in all samples, revealing near-linear strain hardening trends in low porosity samples ($\varphi_0 < 20\%$) and (concave-down) strain hardening at a decreasing rate in high porosity material ($\varphi_0 > 20\%$). Total axial strains of 0.4 to 1.3% were attained, of which 0.1 to 0.8% strain was inelastic (*i.e.* 25 to 55% of the total). Time-dependent deformation was seen during each stress relaxation interval, although creep strain rates decreased rapidly from 10^{-5} s^{-1} to below 10^{-9} s^{-1} in 24 hours, with no further change measureable in stress supported. The exponential stress versus strain rate relations obtained in relaxation intervals point to rate-sensitive, intergranular slip governing the relaxation rate where near-linear hardening behavior is shown ($\varphi_0 < 20\%$), while stress-corrosion, intragranular cracking is implied where concave-down hardening behavior is shown ($\varphi_0 > 20\%$). At the end of each test, the cumulative, time-dependent strain developed during all relaxation stages (one week in total) contributed only 10 to 20% to the total (instantaneous plus time-dependent) inelastic strain accumulated during the experiment. These results imply a porosity- and (to a lesser extent) rate-sensitive yield envelope that expands with increasing inelastic strain from the onset of compression.

To investigate the expanding yield envelope concept further, **Chapter 3** investigates the elastic versus inelastic deformation behavior of the Slochteren sandstone over a much

wider range of stress changes. I performed deviatoric (axial) and hydrostatic load-cycling experiments, again under the above-mentioned *in-situ* conditions of temperature and pore fluid chemistry. The deformation behavior was explored for initial porosity (φ_0) values of 13.4 to 26.4%, P_c^{eff} values up to 320 MPa and differential stresses (Q) up to 135 MPa, chosen to cover and exceed the stresses relevant for reservoir compaction in Groningen. The results show similar mean effective stress ($P = [\sigma_1 + \sigma_2 + \sigma_3]/3 - P_p$) versus total porosity reduction ($\Delta\varphi_t$) behavior to that typically reported for sandstone. During the near-linear portion of $P - \Delta\varphi_t$ behavior, which is often taken to be fully poroelastic, 30 to 50% of the total axial strain and porosity reduction measured was found to be inelastic. This near-linear behavior, and the associated small elastic plus inelastic strains ($\varepsilon \leq 1\%$) were judged to be most relevant to producing reservoirs. Microstructural observations suggest that the inelastic deformation developing within this near-linear portion is largely accommodated by intergranular displacements, with intragranular cracking becoming increasingly important towards higher strains, and particularly where non-linear, dilatant or compactive behavior is shown. At the small strains relevant to depletion in the Groningen field ($\varepsilon \leq 1\%$), the measured inelastic deformation response is isotropic and well-described by an empirical, Cam-clay-type plasticity model. Applying this inelastic deformation model, plus a poroelastic model describing the elastic contribution, to predict the inelastic versus elastic, 1-D (*i.e.* uniaxial) compaction behavior expected to accompany depletion of the Groningen reservoir, shows that again 30 to 50% of the total uniaxial strain accrued is inelastic. This means that a similar proportion of the total mechanical work input into the reservoir during depletion is dissipated and unavailable for seismic release. It is further demonstrated that by accounting for the inelastic contribution to compaction, the measured *in-situ* horizontal stress evolution during pore pressure reduction is much better reproduced (correspondence within 25%), compared to purely poroelastic estimates (correspondence within 25 to 50%). However, to what extent this essentially time-independent model, calibrated to the data obtained in the above laboratory experiments (hours in duration) applies at the much longer, decade time-scales relevant to production of the Groningen field is as yet unclear, as are the deformation mechanisms operating on the laboratory and field time-scales.

Against this background, in **Chapter 4** I aim to identify the mechanisms accommodating inelastic deformation at each portion, or stage of $P - \Delta\varphi_t$ behavior characterized in Chapter 3, and particularly at the small strains relevant to the field ($\varepsilon \leq 1\%$). A sequence of five stress/strain-cycling plus strain-marker-imaging experiments was performed on a single split-cylinder sample ($\varphi_0 = 20.4\%$) of Slochteren sandstone. The tests

were performed under *in-situ* conditions of effective confining pressure (P_c^{eff} = 40 MPa) and temperature (100°C), exploring increasingly larger differential stresses (Q up to 75 MPa) and/or axial strains (up to 4.8%) in consecutive runs. Control tests confirmed no mechanical effects of the split-cylinder approach. At high strains (> 1.4%), the split-cylinder method revealed pervasive intragranular cracking plus intergranular shear displacements within localized, conjugate bands, as seen in previous experiments on material with similar porosity at similar effective stresses. At smaller, reservoir-relevant strains ($\varepsilon \leq 1\%$), inelastic deformation was largely accommodated by slip on and consolidation of μm-thick clay films present within grain boundaries, with a smaller role played by intragranular cracking. Using a simplified sandstone model, I show that at constant effective stresses corresponding to the current state of depletion in the Groningen field (σ_1^{eff} = 57 MPa, σ_3^{eff} = 27 MPa) deformation by clay consolidation plus intergranular slip is rapid (order: mm/s), hence virtually rate-insensitive at the time-scales pertaining to the field.

In **Chapter 5**, intergranular clay deformation and grain failure are incorporated into a simplified microphysical model, aimed at assessing to what extent these processes can account for the inelastic deformation behavior seen in the experiments on Slochteren sandstones reported in Chapter 3. The model assumes a regular pack of quasi-spherical quartz grains with truncated grain contacts, each covered with μm-thick clay films. Comparison of the model with the experimental data of Chapter 3 show broad agreement. At the small strains relevant to producing reservoirs (*i.e.* where $\varepsilon \leq 1\%$), the inelastic deformation can be largely accounted for by consolidation of and slip on intergranular clay films, while the higher strain behavior exceeding that relevant to reservoirs, is well-captured by assumed dilatant intergranular slip and intragranular cracking. Since grain boundary clay film consolidation and slip were found to be time- or rate-insensitive deformation processes at stresses pertaining to the depletion of the Groningen reservoir, reservoir compaction by these mechanisms is also expected to be time or rate-insensitive. The Cam-clay plasticity model is accordingly anticipated to describe the main trends in compaction behavior at the decade time-scales relevant to the field, though compaction strains and lateral stresses may be slightly underestimated due to other, minor (decelerating) creep effects seen in the experiments, which are likely governed by stress-corrosion cracking. To constrain the long-term (decades - centuries) effect of such stress-corrosion cracking, or other slow creep processes (*e.g.* pressure solution) not seen in lab experiments of conventional (hours/days) duration, further work is needed.

Finally, in **Chapter 6**, the main findings are summarized, along with the key implications for induced subsidence and seismicity in the Groningen field. Issues that remain unsolved are identified, and suggestions for future research are made. A major overall conclusion drawn concerns the significant inelastic contribution to the small strains relevant to the Groningen field, and the demonstrated effects of accounting for this inelastic contribution on the *in-situ* stress evolution, estimates of the elastic strain energy available for seismic release, and on the time-(in)dependence of reservoir compaction, subsidence and seismicity. Thus, we show that for a realistic, physics-based assessment of the effects and risks of hydrocarbon production from the Groningen gas field, both the elastic and the inelastic contributions to reservoir compaction need to be accounted for.

Technische samenvatting

Olie- en gaswinning uit zandsteenreservoirs leidt vaak tot bodemdaling en seismiciteit (aardbevingen). Een voorbeeld hiervan zijn de aardbevingen (M_L tot aan 3.6) die zich in de afgelopen jaren in het relatief dichtbevolkte Groningen gasveld (provincie gemiddelde: ~200 inwoners/km^2) in Noordoost Nederland hebben voorgedaan. Het begrijpen en modelleren van de effecten van olie- en gaswinning op bodemdaling en geïnduceerde seismiciteit vereist een kwantitatief begrip van het elastische (omkeerbare) en inelastische (onomkeerbare) deformatie- of compactiegedrag van het reservoirsysteem als gevolg van gasdrukverlaging. Echter, experimentele data betreffende de verdeling tussen elastische en inelastische deformatie zijn schaars, met name op de *in-situ* (onderbodem)condities van spanning, temperatuur en porievloeistofchemie en op de kleine vervormingen ($\varepsilon \leq 1.0\%$) die relevant zijn voor producerende reservoirs, zoals de Slochteren zandsteen in Groningen. Daarnaast zijn de processen die enige inelastische deformatie accommoderen grotendeels ongeïdentificeerd en de vraag of deze tijd- en/of laadsnelheidafhankelijk zijn blijft dan ook onbeantwoord. In huidige geomechanische modellen toegepast om geïnduceerde bodemdaling en seismiciteit te onderzoeken in Groningen en in andere velden wordt reservoircompactie ofwel beschreven als volledig (poro)elastisch, of door empirische modellen die inelastische deformatie weliswaar in acht nemen, maar geen mechanistische onderbouwing hebben die extrapolatie naar de veldschaal en (post-)productie tijdschalen toestaat. De afgelopen jaren heeft significante seismiciteit en daarmee geassocieerde schade aan gebouwen en publieke onrust een dringende behoefte gecreëerd om het reservoir deformatie/compactie gedrag veel beter te begrijpen en te kwantificeren. Op die manier kan de fysische basis om effecten van productiestrategieën op bodemdaling en seismiciteit te beoordelen verbeterd worden.

In dit proefschrift rapporteer ik de resultaten van een experimentele studie ontworpen om het deformatiegedrag te bestuderen van Slochteren reservoirzandsteenmonsters verkregen uit het seismogenetisch centrum van het Groningen gasveld. Het elastische versus inelastische deformatiegedrag is bestudeerd door triaxiale compressie experimenten, uitgevoerd op de tijdschaal van uren tot een week, op *in-situ* condities van temperatuur, spanning en porievloeistofchemie, als ook op spanningen die voorbijgaan aan de waardes direct relevant voor het veld. Op basis hiervan is een empirisch model ontwikkeld dat het reservoirgedrag beschrijft in termen van elastische en inelastische vervormingcontributies. Het nieuwste van het nieuwste aan microstructurele methodes is toegepast om de korrel-schaal mechanismes te identificeren die inelastische deformatie accommoderen in onze monsters, met name op de kleine vervormingen ($\varepsilon \leq 1.0\%$) die relevant zijn voor het Groningen veld. De geïdentificeerde mechanismes zijn vervolgens opgenomen in een nieuw

microfysisch model dat gebruikt wordt ter onderbouwing van het empirische model voor reservoirdeformatie in het Groningen gasveld. De implicaties van deze mechanismes voor geïnduceerde bodemdaling en seismiciteit zijn ook onderzocht.

In **Hoofdstuk 1** wordt de motivatie en omvang van de studie beschreven en huidige kennis over geïnduceerde reservoircompactie, bodemdaling en seismiciteit in het Groningen gasveld en in andere velden wordt samengevat. Daarnaast wordt voormalig experimenteel werk bediscussieerd en worden essentiële gaten in de huidige kennis geïdentificeerd. Dit wordt gevolgd door de definitie van de doelen van dit proefschrift.

In **Hoofdstuk 2** richt ik me op het kwantificeren van de elastische versus tijdsonafhankelijke en tijdsafhankelijke inelastische vervorming dat zich ontwikkeld in Slochteren zandsteenmonsters tijdens gesimuleerde reservoiruitputting. Monsters met initiële porositeit waardes (φ_0) van 12.7 tot 24.6%, vergelijkbaar met de porositeitwaardes gemeten in het veld, zijn onderworpen aan conventionele axi-symmetrische compressie experimenten. Deze zijn uitgevoerd op *in-situ* condities van temperatuur (100 °C) en porievloeistofchemie (4.4 M NaCl oplossing) en op spanningcondities die volledige reservoir uitputting simuleren in een aangenomen poroelastisch deformerend reservoir, d.w.z. op differentiaalspanningen ($Q = \sigma_1 - \sigma_3$) tot aan 50 MPa en effectieve omgevingsdrukwaardes (P_c^{eff} = totale waarde min de porie druk P_p) van 8 of 15 MPa, welke respectievelijk de initiële en uitgeputte staat van reservoirspanning vertegenwoordigen. Opeenvolgende stadia van actief laden op een vervormingsnelheid ($\dot{\varepsilon}$) van 10^{-5} s^{-1} gevolgd door spanningrelaxatie zijn aangewonden om de verdeling tussen elastische versus tijds(on)afhankelijke inelastische deformatie te kwantificeren. De resultaten laten zien dat inelastische vervorming plaatsvindt vanaf het begin van compressie van alle monsters. Dit gedrag onthult nagenoeg lineair vervorming-verstevigend gedrag in laag poreuze monsters ($\varphi_0 < 20\%$) en non-lineair vervorming-verstevigend gedrag in hoog poreus materiaal ($\varphi_0 > 20\%$). Totale axiale vervormingen van 0.4 tot 1.3% werden behaald, waarvan 0.1 tot 0.8% inelastisch waren (d.w.z. 25 tot 55% van het totaal). Tijdsafhankelijke deformatie werd gezien in elk interval van spanningrelaxatie, hoewel tijdsafhankelijke kruipvervormingsnelheden snel afnamen van 10^{-5} s^{-1} tot onder de 10^{-9} s^{-1} in 24 uur, waarna verdere afname van ondersteunde spanning niet meetbaar was. De exponentiele spanning- versus vervormingrelaties die werden verkregen in relaxatie intervallen wijzen er op dat snelheidsgevoelige inter-korrel slip de relaxatiesnelheid controleerde wanneer nagenoeg lineair verstevigingg gedrag werd getoond ($\varphi_0 < 20\%$). Spanning-corrosie intra-korrel scheurvorming is geïmpliceerd waar non-lineair versteviging

gedrag zich voordeed (φ_0 > 20%). De cumulatieve, tijdsafhankelijke vervorming van alle relaxatie intervals samen droeg slechts 10 tot 20% bij aan de totale (directe plus tijdsafhankelijke) inelastische vervorming dat accumuleerde per experiment. Deze resultaten impliceren een porositeit- en (in mindere mate) een laadsnelheidsgevoelige vloeigrenscurve (Engels: *yield envelope*), die expandeert met toenemende inelastische vervorming vanaf het begin van compressie.

Om het concept van een expanderende vloeigrenscurve verder te onderzoeken, gaat **Hoofdstuk 3** in op het elastische versus inelastische deformatiegedrag van de Slochteren zandsteen op een veel breder bereik aan spanningsveranderingen. Ik voerde deviatorische (axiale) en hydrostatische (isotrope), cyclische compressie experimenten uit, wederom op de bovengenoemde *in-situ* condities van temperatuur en porievloeistofchemie. Het deformatiegedrag werd verkend voor initiële porositeitwaardes van 13.4 tot 26.4%, effectieve omgevingsdrukwaardes (P_c^{eff}) tot aan 320 MPa en differentiaalspanningen (Q) tot aan 135 MPa, gekozen om de spanningen relevant voor reservoir compactie in Groningen te omvatten als ook te overstijgen. De resultaten tonen vergelijkbaar gemiddeld effectieve spanning ($P = [\sigma_1 + \sigma_2 + \sigma_3]/3 - P_p$) versus totale porositeitafname ($\Delta\varphi_t$) gedrag als dat vaak gerapporteerd voor zandsteen. Tijdens de nagenoeg lineaire portie van P - $\Delta\varphi_t$ gedrag, welke vaak als poroelastisch genomen wordt, is 30 tot 50% van de gemeten totale axiale vervorming en porositeitafname inelastisch. Dit nagenoeg lineaire gedrag en geassocieerde kleine elastische plus inelastische vervormingen ($\varepsilon \leq 1\%$) wordt beoordeeld als het meest relevant voor producerende reservoirs. Microstructurele observaties suggereren dat de inelastische deformatie binnen dit nagenoeg lineaire interval voor het grootste deel geaccommodeerd wordt door inter-korrel verplaatsingen, terwijl intra-korrel scheurvorming belangrijker wordt op hogere vervormingen en vooral waar non-lineaire uitzetting of compactie getoond is. Voor de kleine vervormingen ($\varepsilon \leq 1\%$) die relevant zijn voor uitputting van het Groningen gasveld is het gemeten inelastische deformatiegedrag isotroop en goed beschreven door een empirisch, Cam-clay-type plasticiteit-(inelasticiteit)model. Toepassing van dit inelastische deformatiemodel, in combinatie met een poroelastisch model, om samen het inelastische versus elastische, 1-D (uniaxiale) compactiegedrag dat verwacht wordt tijdens uitputting van het Groningen reservoir te beschrijven, laat zien dat wederom 30 tot 50% van de totaal opgebouwde uniaxiale vervorming inelastisch is. Dit betekent dat een vergelijkbare portie van de totale invoer van mechanisch werk in het reservoir tijdens uitputting is vervlogen en daarmee niet beschikbaar is voor vrijlating door middel van seismiciteit. Het wordt verder gedemonstreerd dat door het in acht nemen van de inelastische

contributie aan compactie, de gemeten *in-situ*, horizontale spanningevolutie tijdens poriedrukverlaging veel beter gereproduceerd wordt (overeenkomst binnen 25%), vergeleken met de puur poroelastische schattingen (overeenkomst binnen 25 tot 50%). Echter, de mate waarin dit in essentie tijdsonafhankelijke model, gekalibreerd aan de data verkregen in bovengenoemde laboratorium experimenten (tijdsduur: uren) kan worden toegepast op de veel langere decenniatijdsduren die relevant zijn voor productie van het Groningen veld blijft vooralsnog onduidelijk, evenals de deformatie mechanismes die opereren op de laboratorium- en veld tijdschalen.

Tegen deze achtergrond richt ik me in **Hoofdstuk 4** op het identificeren van de mechanismes die inelastische deformatie accommoderen tijdens elke in Hoofdstuk 3 gekarakteriseerde portie (of elk stadium) van P - $\Delta\varphi_t$ gedrag, met name tijdens de kleine vervormingen die relevant zijn voor het Groningen veld ($\varepsilon \leq 1\%$). Vijf cyclische spanning-vervorming experimenten zijn uitgevoerd op een enkel split-cilinder monster (φ_0 = 20.4%) van Slochteren zandsteen, elk gevolgd door het in beeld brengen van het monster oppervlak plus de daarop aangebrachte vervorming markeringen met een elektronenmicroscoop. De testen zijn uitgevoerd op *in-situ* condities van effectieve omgevingsdruk (P_c^{eff} = 40 MPa) en temperatuur (100°C), waarbij we steeds hogere differentiaalspanningen (Q tot aan 75 MPa) en/of axiale vervormingen (tot aan 4.8%) verkennen in opeenvolgende testen. Controletesten bevestigden dat er geen mechanische effecten waren van de split-cilinder aanpak zelf. Op hoge vervormingen (> 1.4%) liet de split-cilinder methode vergaande intra-korrel scheurvorming plus inter-korrel schuifverplaatsingen zien binnen gelokaliseerde, conjugate banden, zoals ook vaak gezien in voormalige experimenten op vergelijkbaar materiaal en op vergelijkbare effectieve spanningen. Op de kleinere, reservoir-relevante vervormingen ($\varepsilon \leq 1\%$) wordt inelastische deformatie grotendeels geaccommodeerd door slip op- en consolidatie van µm-dikke klei randjes die aanwezig zijn op de randen van de korrels en binnen korrelgrenzen, waarbij intra-korrel scheurvorming een kleinere rol speelt. Gebruikmakend van een simpel zandsteenmodel laat ik zien dat op constante effectieve spanningen, corresponderend aan de huidige staat van uitputting van het Groningen veld (σ_1^{eff} = 57 MPa, σ_3^{eff} = 27 MPa), deformatie door kleiconsolidatie plus inter-korrel slip snel is (orde: mm/s) en daarmee in essentie tijdsonafhankelijk op de tijdschalen die betrekking hebben op het veld.

In **Hoofdstuk 5** worden bovengenoemde inter-korrel kleideformatie en scheurvorming in korrels opgenomen in een gesimplificeerd microfysisch model. Dit model

is gericht op het beoordelen tot op welke hoogte deze processen de inelastische deformatie van de experimenten op Slochteren zandsteen gerapporteerd in Hoofdstuk 3 kunnen verklaren. Het model gaat uit van een regelmatige stapeling van quasi-balvormige kwartskorrels met afgesneden korrelcontacten, elke bedekt met µm-dikke kleirandjes. Vergelijking van het model-geïmpliceerde gedrag met de experimentele data van Hoofdstuk 3 laat een algemene overeenkomst zien. Op de kleine vervormingen die relevant zijn voor producerende reservoirs (d.w.z. waar $\varepsilon \leq 1\%$) kan de inelastische deformatie grotendeels verklaard worden door consolidatie van en slip op inter-korrel klei randjes, waar het hogere vervorminggedrag goed gevangen wordt door inter-korrel slip en intra-korrel scheurvorming. Omdat het consolideren van- en slip op kleirandjes als tijds- of snelheidsonafhankelijk bevonden werd op de spanningen die betrekking hebben op uitputting van het Groningen reservoir, wordt reservoir compactie door middel van deze mechanismes ook verwacht om tijds- of snelheidsonafhankelijk te zijn. De verwachting is dan ook dat het Cam-clay plasticiteits model gerapporteerd in Hoofdstuk 3 de voornaamste trends in compactie gedrag kan verklaren op de decenniatijdschalen relevant voor het veld. Echter, compactievervormingen en laterale spanningen worden wellicht licht onderschat als resultaat van andere, kleine en in snelheid afnemende kruipeffecten die gezien zijn in experimenten. Deze worden vermoedelijk veroorzaakt door spanning-corrosie scheurvorming. Meer werk is nodig om de lange termijn (decennia, eeuwen) effecten van spanning-corrosie scheurvorming, of van andere langzame processen (zoals druk-oplossing) die niet gezien zijn in lab experimenten van conventionele duur (uren/dagen) verder in kaart te brengen.

Tot slot worden in **Hoofdstuk 6** de voornaamste bevindingen van dit proefschrift samengevat, samen met hoofd implicaties voor geïnduceerde bodemdaling en seismiciteit in het Groningen gasveld. Kwesties die vooralsnog onopgelost blijven worden geïdentificeerd en suggesties worden gedaan voor toekomstig onderzoek. Een belangrijke overkoepelende conclusie betreft de significante inelastische contributie aan de kleine vervormingen die relevant zijn voor het Groningen veld en de gedemonstreerde effecten van het in acht nemen hiervan op (1) de *in-situ* spanningevolutie, (2) schattingen van de elastische vervormingsenergie dat potentieel seismisch vrijgelaten kan worden en (3) op de tijds(on)afhankelijkheid van reservoircompactie, bodemdaling en seismiciteit. Op die manier wordt getoond dat voor een realistische, fysisch onderbouwde beoordeling van de effecten en risico's van olie- en gaswinning uit het Groningen gasveld zowel de elastische als de inelastische contributies in acht genomen moeten worden.

Chapter 1

Introduction

1.1 Motivation and scope

Globally speaking, hydrocarbons production from sandstone reservoirs can lead to induced surface subsidence and potentially to induced seismicity [*Davies et al.*, 2013; *Pratt and Johnson*, 1926; *Suckale*, 2009]. Where observed, the magnitude of subsidence amounts to centimeters or several tens of centimeters [*Mallman and Zoback*, 2007; *Morton et al.*, 2001; *Van Thienen-Visser and Fokker*, 2017]. Subsidence is typically a surface expression of compaction at the reservoir level, which can drive induced seismicity. The associated magnitudes sometimes reach up to 5 M_L [*Suckale*, 2009], and can be sufficiently large to induce damage to buildings and to cause societal unrest [*Van Eck et al.*, 2006; *Van der Voort and Vanclay*, 2015]. Examples of fields showing subsidence and seismicity include localities in Texas [*Doser et al.*, 1991; *Morton et al.*, 2001; *Sharp and Hill*, 1995] and Louisiana (USA) [*Mallman and Zoback*, 2007], Alberta (Canada) [*Baranova et al.*, 1999], Italy [*Menin et al.*, 2008], Germany [*Dahm et al.*, 2007] and China [*Genmo et al.*, 1995]. In recent years, the vast (30 x 30 km) and densely populated (~200 inhabitants/km^2 in the province of Groningen) Groningen gas field located in the N.E. Netherlands (Figure 1.1) has attracted much attention, especially since the occurrence of a damaging M_L 3.6 earthquake in 2012 [*Dost and Kraaijpoel*, 2013], which led to much unrest amongst the local population. Within this field, the largest amount of subsidence (up to 36 cm, in 2016; *NAM*, 2016) and the largest and most frequently occurring seismic events are measured in the central part of this field (Figure 1.1a). In this area, the reservoir, the Slochteren sandstone, is at its thickest (~200 m) and most porous (18 - 22%, Figure 1.1b).

Subsidence and seismicity in hydrocarbon fields are both caused by compaction of the reservoir due to an increase in the (Terzaghi) effective vertical stress, as the pore pressure is reduced. Such compaction is in part elastic (reversible/recoverable) and may be in part inelastic (permanent). Elastic plus inelastic (*i.e.* total), vertical reservoir strains, whether these are inferred from subsidence data [*Mallman and Zoback*, 2007; *Morton et al.*, 2001; *Van Thienen-Visser and Fokker*, 2017] or measured directly in the reservoir interval [*Cannon and Kole*, 2017], are typically small (0.1 to 1.0%). Still, these strains imply gradients in compaction within the generally faulted, and mechanically heterogeneous reservoir, *i.e.* variations in vertical (compaction) displacement at a given depth level, for instance arising where the reservoir is juxtaposed to a different lithology [Figure 1.2; *Mulders*, 2003; *Zoback*, 2010]. In particular, such compaction gradients may cause shear tractions along pre-existing faults (Figure 1.2), which can ultimately lead to fault rupture [*Buijze et al.*, 2017; *Van Eijs et al.*, 2006; *Liu et al.*, 1992; *Mulders*, 2003]. Upon rupture, the elastic strain energy stored in

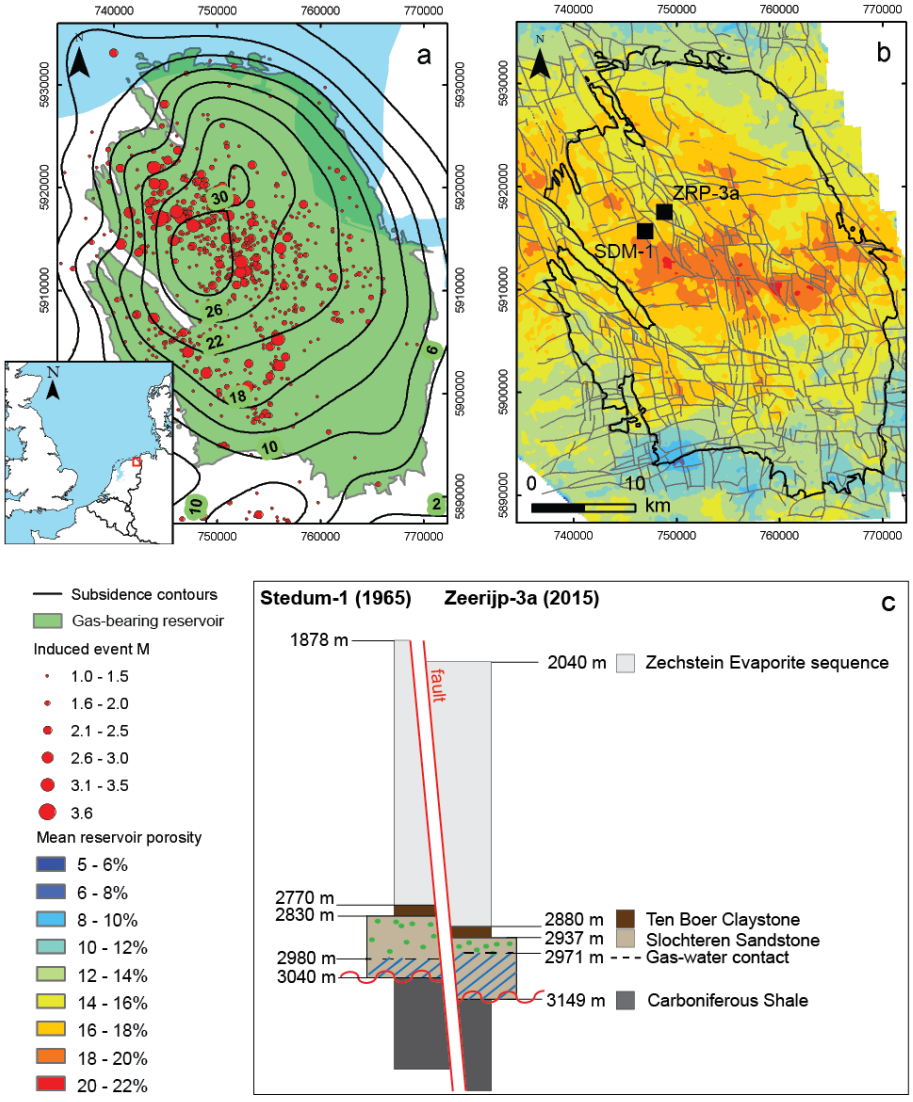

Figure 1.1 a) Map showing the location of the Groningen gas field, the extent of the gas-bearing reservoir at approximately 3000 m depth, contours of the surface subsidence measured in 2013, and induced earthquake magnitudes and locations in the period 1991-2017 (www.knmi.nl – seismic catalogue). **b)** Map showing the mean (vertically averaged) porosity of the Slochteren reservoir sandstone (depth ~3000 m), the main faults (throw typically 50 to 150 m) cutting the top of the reservoir, and the locations of the Stedum (SDM)-1 and Zeerijp (ZRP)-3a wells. The porosity and subsidence data were provided courtesy of the field operator - see NAM [2013]. **c)** Stratigraphy of the Groningen gas field at the SDM-1 and ZRP-3a wells [http://www.nlog.nl/keuzelijst-boringen]. True vertical depths are indicated.

the reservoir and surrounding system is released [*Jaeger et al.*, 2007; *Liu et al.*, 1992; *Zoback*, 2010], giving rise to seismicity and/or associated rupture processes, such as frictional heat release, pore fluid displacements, grain size reduction and fault propagation [*McGarr*, 1999; *Shipton et al.*, 2013]. If the reservoir compaction preceding rupture has been partly inelastic, then the associated mechanical work is dissipated as heat and is therefore unavailable for seismic release [*Cooke and Madden*, 2014]. In addition, the inelastic contribution to reservoir compaction has been shown to affect the evolution of the stresses prevailing in the reservoir and acting on faults [*Chan et al.*, 2004]. Moreover, many inelastic deformation processes exhibit a time- or rate-sensitivity [*e.g. Spiers et al.*, 2004; *Brantut et al.*, 2013], and may therefore control the compaction rate during production [*Hettema et al.*, 2002; *Mallman and Zoback*, 2007; *Pruiksma et al.*, 2015; *De Waal*, 1986], or even accommodate ongoing compaction strains beyond field closure [*NAM*, 2016; *Van Thienen-Visser et al.*, 2015a; *Van Wees et al.*, 2018]. Hence, understanding induced seismicity requires constraints to be placed on the elastic and inelastic deformations occurring in the reservoir sandstone.

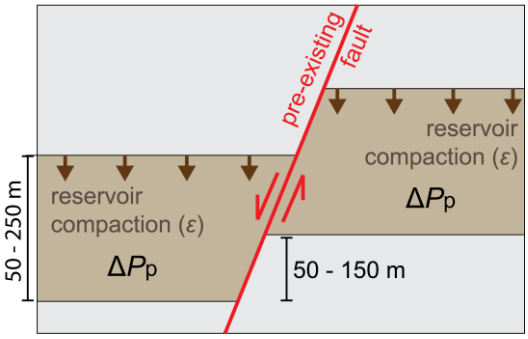

Figure 1.2 Schematic, cross-sectional diagram of a reservoir such as the Slochteren sandstone of the Groningen gas field, illustrating how gradients in reservoir compaction during pore pressure reduction (ΔP_p) along pre-existing faults can lead to shear traction and/or fault displacements along such faults.

A large body of experimental work exists on the time-independent [*Wong and Baud*, 2012 - and references therein] and time-dependent [*Brantut et al.*, 2013, 2014, *Heap et al.*, 2009, 2015] mechanical behavior of sandstones at room temperature (T) and shallow upper crustal pressure (and sometimes T) conditions. In the bulk of these studies, the mechanical behavior seen at the small strains (ε up to ~1%) relevant to producing reservoirs is treated as if elastic [*e.g. Wong et al.*, 1997; *Baud et al.*, 2006; *Brantut et al.*, 2014] and quantified using poroelasticity theory [*Wang*, 2000]. However, several studies demonstrate concomitant inelastic deformation developing even at these small strains [*Bernabe et al.*, 1994; *Hol et al.*,

2018; *Schutjens et al.*, 1995; *Shalev et al.*, 2014; *Wong et al.*, 1992]. Inelasticity is readily investigated at the large compactive strains (ε = 1 to 15%) that correspond to markedly non-linear stress-strain behavior [*Baud et al.*, 2000, 2004, 2006, *Fortin et al.*, 2005, 2006; *Klein et al.*, 2001; *Rutter and Glover*, 2012; *Tembe et al.*, 2007, 2008; *Zhang et al.*, 1990; *Zhu et al.*, 1997]. However, the elastic versus inelastic deformation behavior of sandstone developing at the small-strains (ε < 1%) relevant to producing reservoirs is surprisingly poorly constrained. The corresponding, inelastic contribution is poorly quantified and the underlying mechanisms are generally unclear. As a result, a possible inelastic contribution to reservoir compaction, and any rate-sensitivity thereof is usually omitted in geomechanical models investigating induced seismicity in the Groningen gas field [*Bourne et al.*, 2014; *Dempsey and Suckale*, 2017; *Van Eijs et al.*, 2006; *Lele et al.*, 2016; *Smith et al.*, 2019; *Wassing et al.*, 2016; *Zbinden et al.*, 2017]. If inelastic deformation occurs, these studies may overpredict the elastic energy available for seismicity, misrepresent the *in-situ* stress evolution accompanying production, and, in the case of time-dependent compaction, provide artificially low estimates of the magnitude of subsidence and/or of the time-scale over which seismicity may develop. At present, little physical or mechanistic basis exists to support extrapolation of laboratory data to the conditions and time-scales relevant to the Groningen field [*Spiers et al.*, 2017]. Addressing the issue of induced seismic hazard in Groningen with the rigour required by society, regulator and operator [*De Waal et al.*, 2017] requires a new level of rock physics understanding and quantification.

In this thesis, I report the results of an experimental study designed to quantify the elastic versus inelastic deformation/compaction behavior shown by Slochteren reservoir sandstone samples from the seismogenic center of the Groningen field. This study was funded by the operator of the field (de Nederlandse Aardolie Maatschappij, NAM), as part of its larger data acquisition and study program on induced seismicity in the Groningen gas field, N.E. Netherlands [*NAM*, 2016]. Samples were subjected to triaxial testing, conducted at *in-situ* conditions of temperature and pore fluid chemistry pertaining to the Groningen field, and exploring stresses covering and exceeding those relevant to field production. State-of-the-art microstructural and microscopic strain analysis methods were employed to elucidate the deformation mechanisms operating during our experiments. The mechanical and microscale data obtained were used to test and calibrate existing models for deformation of granular geomaterials, as well as to develop new modelling approaches designed specifically for clarifying the microphysical mechanisms controlling elastic and inelastic compaction of the Slochteren and similar (reservoir) sandstones. The present work contributes both data and physical understanding that is much needed to improve

geomechanical models investigating reservoir compaction, induced subsidence and seismicity in Groningen and in similar fields. In this way, it also contributes to developing a physical basis for assessment of production-induced risks [*NAM*, 2016].

1.2 Background on the Groningen gas field and the Slochteren sandstone

The Groningen gas field covers a vast area of ~30 by 30 km (Figure 1.1) and is largest gas field in Europe and the 7th largest gas field in the world, in terms of initial recoverable gas reserve (2900 billion cubic meter, or 100 trillion cubic feet; *De Jager and Visser*, 2017). It is situated in the NE-Netherlands, on the southern flank of the east – west striking southern Permian basin [*Glennie*, 1972; *Ziegler*, 1990]. The Slochteren reservoir sandstone member, now located at about 3 km depth, is approximately 200 meter thick and constitutes a generally upward-fining succession of conglomerates, fluvial sandstones and cross-bedded aeolian sandstones (Figure 1.1c) [*De Jager and Visser*, 2017]. In the northern part of the field, the sandstone reservoir envelopes the clay-rich Ameland member, which is several tens of meters in thickness [*NAM*, 2013]. The reservoir lies unconformably on organic-rich (coal bearing) Carboniferous shales and is overlain by a 50 m thick claystone, followed by a thick sequence (500 – 1000 m) of Zechstein evaporates [*Amthor and Okkerman*, 1998]. Between the Triassic and the Late Jurassic, regional subsidence resulted in burial and NW-SE trending extensional fracturing of the Permian sediments, and hydrocarbons were expelled from the underlying organic-rich Carboniferous shale and coal intervals into the reservoir [*De Jager et al.*, 1996]. At present, the upper 50 to 150 m of the Slochteren reservoir is gas-bearing and is partly (25 ± 10 % of the pore volume) filled with connate brine [*Waldmann*, 2011]. Since production of the Groningen field began in 1963, the pore fluid pressure has decreased from 35 MPa to a current, uniform 8 MPa, which has caused an upward shift of the gas-water contact by about ten meters, to a current true vertical depth (TVD) of ~2971 m [*NAM*, 2016]. After an initial delay of 5 to 6 years [*Hettema et al.*, 2002], gas extraction has been accompanied by more or less steady subsidence at the surface, reaching up to 36 cm in the center of the field in 2016 [*NAM*, 2016]. Virtually no seismicity was recorded during the first three decades of operation (Figure 1.3). Since the 1990s, an increasing frequency and magnitude of induced seismicity has been recorded (Figure 1.3), culminating in 2012 in the largest event to date, the M_L 3.6 Huizinge earthquake [*Dost and Kraaijpoel*, 2013]. In spite of these adverse effects, production of this field alone has produced revenue of ~ 300 billion Euro to the Dutch government. At present, roughly 25% of the initial gas reserve is still in place [*De Jager and Visser*, 2017].

The Slochteren sandstone is highly porous, with average porosity values ranging

from 18 - 22% in the central, most seismogenic center of the field, where subsidence is also largest, decreasing outward to 12 – 16% at the margins [*NAM*, 2013]. It consists predominantly of quartz (72 – 90 vol%) and feldspar grains (8 – 25 vol%), with lesser amounts of clay (0.5 – 5.5 vol%) [*Waldmann et al.*, 2014; *Waldmann and Gaupp*, 2016]. The average grain size of quartz and feldspars is typically 150 – 250 µm [*Hol et al.*, 2018]. Early diagenetic illite films (1 - 10 µm thick) coat parts of the surfaces of quartz and feldspar grains and frequently occur within grain contacts [*Gaupp et al.*, 1993; *Waldmann*, 2011; *Wilson*, 1992]. As burial progressed, the total initial feldspar content was reduced due to dissolution reactions, leading to precipitation of kaolinite and additional illite in the pores and onto the pore walls [*Waldmann and Gaupp*, 2016].

The Slochteren sandstone samples used in this thesis were obtained from core retrieved by the field operator (Nederlandse Aardolie Maatschappij, NAM) from the Stedum (SDM)-1 well, which was drilled prior to major production in 1965, and from the Zeerijp (ZRP)-3a well, drilled in 2015 (Figure 1.1b). The stratigraphy along these wells is shown in Figure 1.1c. Note the close proximity of the SDM-1 and ZRP-3a wells (within 5 km), and the relative offset of ~150 m of the reservoir plus under/over burden along an intervening fault.

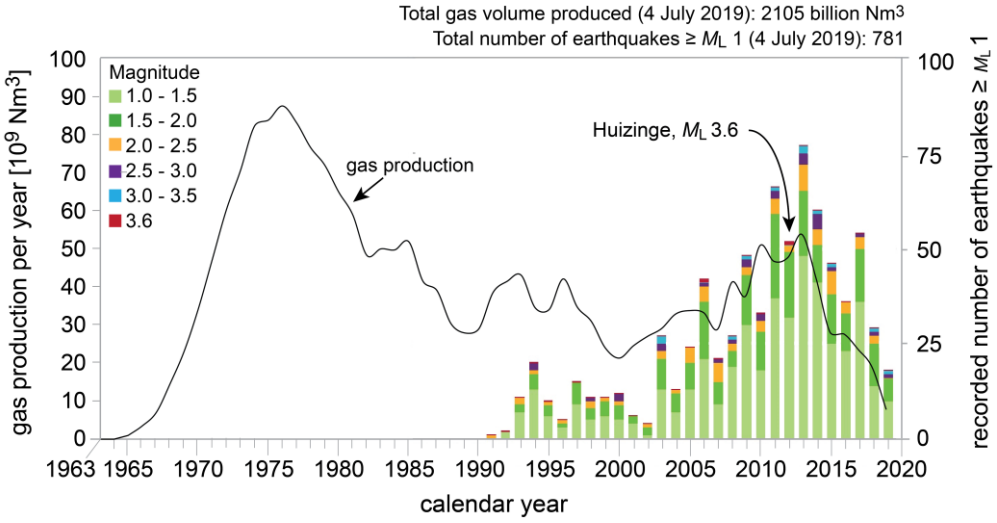

Figure 1.3 Plot showing the annual gas production and the number and magnitude of earthquakes recorded in the Groningen gas field per calendar year, since production started in 1963. Note that during the first three decades of production, virtually no seismicity was recorded. The data presented here were retrieved on 4 July 2019 from: https://www.nam.nl/feiten-en-cijfers/.

1.3 Representation of reservoir compaction in current geomechanical models for induced seismicity in the Groningen gas field

In many geomechanical models currently in use to investigate induced seismicity in the Groningen gas field, the reservoir compaction behavior is generally described using linear, effectively (poro)elastic, and time-independent compaction coefficients, while any inelastic, and potentially time-dependent effects are omitted [*Van den Bogert*, 2015; *Buijze et al.*, 2017; *Dempsey and Suckale*, 2017; *Lele et al.*, 2016; *Wassing et al.*, 2016; *Zbinden et al.*, 2017]. Evidently, if reservoir compaction is in part inelastic, then these models may not fully describe the in-situ behavior, in that they potentially misrepresent the evolution of the stresses acting in the reservoir, in the over-and underlying lithologies, and on faults, and overestimate the strain energy available for seismic release. In the state-of-the-art geomechanical model currently in use by the field operator [*Bourne et al.*, 2014; *NAM*, 2013, 2016], induced seismicity is empirically calibrated to surface subsidence (and hence to reservoir strain), measured since the onset of gas production in 1963. While predictions of future subsidence and seismicity derived from this empirical model do not explicitly include and rely on the elastic versus inelastic nature of reservoir compaction, it is clear that only a minor percentage (0.5% - see: Bourne et al., 2014) of the total strain energy that would have accumulated if all deformation would be poroelastic has been seismically released. This may indicate that a large portion of strain energy has been dissipated by inelastic deformation of the reservoir and on faults, and/or by other dissipative processes related to fault rupture, such as frictional heating, inelastic asperity deformation, wall-rock damage, pore pressure changes and fluid flow, rupture propagation, and grain size reduction (gouge formation) [*Cooke and Madden*, 2014; *McGarr*, 1999]. In addition, a small percentage of remaining stored strain energy may still be released in the future. This highlights a need to improve understanding and quantification of seismic energy storage versus dissipation in the reservoir/fault system, including the contribution to this of elastic versus inelastic reservoir deformation. Furthermore, if rate-sensitive behavior is exhibited in the reservoir, the above models imply conservative estimates of the compaction strains, the amount of subsidence, and induced seismicity, as these effects will then continue to develop progressively, even when production is markedly reduced (such as seen in fields in Louisiana; *Mallman and Zoback*, 2007) or stopped. In the case of the Groningen field, the possibility of delayed, or time-dependent reservoir compaction [*Hettema et al.*, 2002] is investigated using the rate-type isotach compaction model [*De Waal*, 1986; see also: *Van Thienen-Visser et al.*, 2015a], and/or the time-decay model [*Mossop*, 2012]. These models are calibrated to subsidence data measured at the surface since the onset of production and thus provide history-matched estimates of

future subsidence [*Van Thienen-Visser et al.*, 2015a]. However, the physical basis for these models is questionable. There has been much speculation as to whether a significant reduction in production rate applied in 2014 (refer Figure 1.3), has led to a delayed (*i.e.* time-dependent), or rather an immediate (*i.e.* time-independent) response in seismicity or subsidence rate [*Nepveu et al.*, 2016; *Sijacic et al.*, 2017; *Van Thienen-Visser and Breunese*, 2015; *Van Thienen-Visser and Fokker*, 2017; *Van Wees et al.*, 2018], or in the *in-situ* compaction rate [*Cannon and Kole*, 2017]. Moreover, whether any such delayed effects would be caused by time-dependent reservoir (creep) deformation, creep deformation of the overlying evaporites [*Marketos et al.*, 2016], pressure re-equilibration between the reservoir and the low-permeability underburden shales, or by transient fluid flow in the faulted reservoir [*NAM*, 2017; *Postma and Jansen*, 2018; *Zbinden et al.*, 2017], remains similarly unclear. Nonetheless, in an attempt to curb induced seismicity, the Dutch government decided to stop production of the Groningen gas field altogether by 2022 [*Wiebes*, 2019], and to forego further retrieval of the significant gas reserves still in place (~800 billion cubic meter). At present, it is clear that the impact of this, and of other production strategies cannot be fully assessed, as the physical processes governing reservoir compaction and associated seismicity are insufficiently understood [*Spiers et al.*, 2017; *De Waal et al.*, 2015; *Van Wees et al.*, 2018].

1.4 Micro-mechanical behavior of sandstones under upper crustal conditions

Elastic deformation of sandstone is by definition rate-insensitive and it is easily quantified using linear (or non-linear), poroelasticity theory [*Wang*, 2000; *Zoback*, 2010]. By contrast, inelastic deformation, and the governing, grain-scale mechanisms are understood far less well. At the low temperatures (< 150 °C) and decade time-scales relevant for fluid extraction from upper-crustal sandstone reservoirs (< 5 km depth), inelastic processes controlling deformation may develop either within constituent grains through intragranular cracking [*Brantut et al.*, 2013], or at grain-to-grain contacts, via grain boundary asperity crushing, frictional slip [*Menéndez et al.*, 1996], deformation of intergranular clays [*Hawkins and McConnell*, 1992], or intergranular pressure solution [*Spiers et al.*, 2004]. While pressure solution is known to be an important deformation mechanism over time-scales relevant for sandstone diagenesis (> 10,000 years - *Tada and Siever*, [1989]; *Yang*, [2000]), existing rate data [*Chester et al.*, 2004; *Niemeijer et al.*, 2002; *Van Noort et al.*, 2008; *Renard et al.*, 1999] suggest that any contribution of this slow creep process to the compaction of quartz-rich reservoir rock will be small for the decade time-scales and low temperatures that apply to sandstone reservoir systems such as Groningen. In addition, a recent microstructural

investigation of undepleted and depleted reservoir sandstones from the Groningen field showed no detectable evidence that pressure solution, nor intragranular cracking contributed to compaction during more than 50 years of production [*Verberne et al.*, in prep.]. Generally speaking, the extent to which the remaining inelastic processes above can contribute to compaction at a given temperature and time-scale depends on the stresses and strains supported within the grain framework, hence on the porosity (φ).

Experimental studies based on conventional deviatoric and hydrostatic testing generally express the mechanical behavior exhibited by sandstones in terms of mean effective stress ($P = [\sigma_1 + \sigma_2 + \sigma_3]/3 - P_p$, where P_p is pore fluid pressure) versus total porosity reduction ($\Delta\varphi_t$) data [*Wong and Baud*, 2012, and references therein]. Such P - $\Delta\varphi_t$ curves generally show a progression from Stage 1 to Stage 2 and ultimately Stage 3c or 3d behavior, as shown in Figure 1.4 (note the indicated values of $\Delta\varphi_t$ characterizing the end of each stage in this figure). This progression is generally interpreted to reflect an evolution in the relative contribution of the governing grain-scale mechanisms [*e.g. Renard et al.*, 2017]. Here, the initial, compliant behavior seen in Stage 1 is thought to reflect progressive stiffening of the grains and grain framework as the load increases [*Walton*, 1987], combined with semi-recoverable closure of pre-existing damage such as dilated grain boundaries or cracks [*David et al.*, 2012; *Walsh*, 1965]. The near-linear Stage 2 is generally treated to reflect purely poroelastic deformation [*Brantut et al.*, 2014; *Hettema et al.*, 2000; *Wong et al.*, 1997], thereby omitting any inelastic contributions, as previously recognized in several studies [*Bernabe et al.*, 1994; *Schutjens et al.*, 1995; *Wong et al.*, 1992]. During hydrostatic compression, and during deviatoric compression at high confining pressures (P_c > 20 to 40 MPa, depending on φ), Stage 2 gives way to Stage 3c (non-linear compaction), while during deviatoric compression at lower P_c, Stage 1 transitions directly into Stage 3d (dilation). Stage 3c is associated with significant intragranular cracking, which is frequently seen to localize in diffuse (1- 10 mm wide) or discrete (up to 1 mm wide) bands, that are oriented at 45° to 90° to the main compression direction (σ_1) [*Baud et al.*, 2004; *Fortin et al.*, 2005; *Tembe et al.*, 2008]. Stage 3d is associated with the formation of sample-scale shear fractures, which are oriented at 10° to 45° to σ_1 [*Fortin et al.*, 2005]. These fractures are mostly intergranular at low P_c (up to 10 MPa) and high φ (> 20%), while at higher P_c (10 to 40 MPa) and lower φ, they are surrounded by a damage zone where intragranular cracks are abundant [*Dresen and Gueguen*, 2004; *Wu et al.*, 2000].

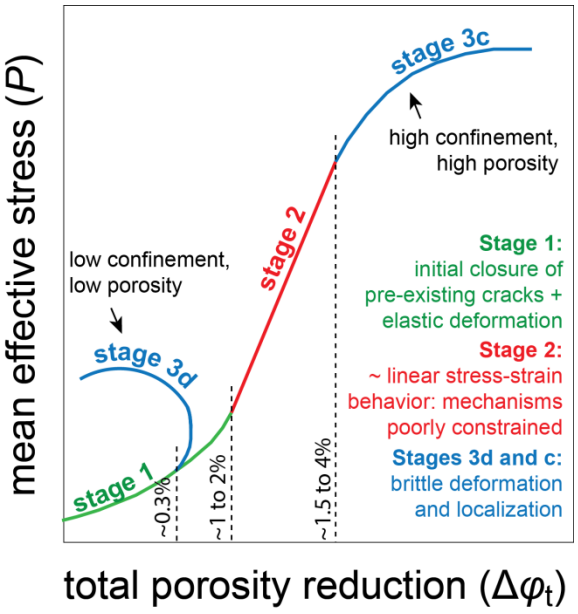

Figure 1.4 Schematic diagram showing the different stages in mean effective stress (P) versus total porosity reduction ($\Delta\varphi_t$) behavior typically seen in mechanical testing of porous sandstones. Note the effects of low porosity and confining pressure and low porosity and high confining pressure on Stage 3 behavior (dilation – suffix "d" versus compaction - "c"). The deformation mechanisms inferred in the literature are shown per stage, as are typical values of $\Delta\varphi_t$ measured at the end of each stage.

1.5 Existing models for inelastic sandstone deformation

Alongside the poro-elastic component, models used to describe the inelastic deformation behavior of sandstone can be grouped into four categories: 1) (Semi-)Empirical plasticity models; 2) Thermodynamically based, breakage mechanics models; 3) Microphysical models; 4) Discrete Element Method (DEM) models. It should be noted that the commonality between all four types of models is that they assume that inelastic deformation is brittle, being associated with intergranular or intragranular cracking, as seen during Stages 3c and 3d. In addition, the possibility of time-dependent deformation is typically not included.

In plasticity models, the stress conditions marking the onset of inelasticity (*i.e.* yield) are described through a yield envelope, which is often taken to be elliptical in shape, when expressed in differential stress ($Q = \sigma_1 - \sigma_3$) versus mean effective stress (P) space [*DiMaggio and Sandler*, 1971; *Muir Wood*, 1991; *Schofield and Wroth*, 1968]. At yield, this envelope expands due to inelastic porosity reduction during continuous deformation,

reflecting strain hardening due to densification. In isotropic materials, the accompanying stress-strain behavior can be directly associated to the shape of the yield envelope [*e.g. Muir Wood*, 1991]. If anisotropic behavior is shown, additional constraints are needed to describe the stress-strain behavior [*Buscarnera and Laverack*, 2014; *Issen and Rudnicki*, 2000; *Rudnicki and Rice*, 1975]. Plasticity models commonly used in geomechanical applications [*e.g. Crawford and Yale*, 2002; *Fredrich and Fossum*, 2002; *Chan et al.*, 2004] include the critical state model [*Schofield and Wroth*, 1968], the cap-model [*DiMaggio and Sandler*, 1971] and the modified Cam-clay model [*Muir Wood*, 1991]. Despite their frequent and convenient use, their capacity to describe sandstone behavior remains, aside from several studies [*Baud et al.*, 2006; *Wong and Baud*, 1999], poorly verified against experiments. If at all applicable, plasticity models require calibration to experimental data, implying that their reliability remains restricted to the experimental conditions explored.

Thermodynamically based, breakage mechanics models consider the stored versus dissipated energy during progressive crushing or brittle failure of the constituent grains [*Einav*, 2007] and/or of the intergranular cement [*Tengattini et al.*, 2014]. The grain size and grain cement volume are taken to be distributed, while the crushed fractions of both (*i.e.* the energy released) at a given applied stress are assumed size-dependent, in line with observations made during experiments [*e.g. Chuhan et al.*, 2002; *Hangx et al.*, 2010; *Brzesowsky et al.*, 2011]. Stored versus released energy are then related to elastic and inelastic strain, respectively, through a thermodynamic approach [*Tengattini et al.*, 2014]. This type of model has been successfully applied to address issues such as compaction band formation and accompanying permeability loss in the subsurface [*Das et al.*, 2014], water retention in undersaturated soils [*Khalili et al.*, 2014; *Zhang and Buscarnera*, 2015], weakening of porous media upon fluid exposure [*Zhang and Buscarnera*, 2018] and the efficiency of industrial mineral grinding [*Zhang et al.*, 2016]. To date though, the underlying processes, hence the applicability of these models, remain unverified for fluid extraction from sandstone reservoirs, particularly since they only address fracturing mechanisms, which may not necessarily be the grain-scale processes controlling low strain reservoir deformation under relevant *in-situ* P_c-T conditions.

Microphysical models typically address the high strain behavior (1 - 15%) associated with pervasive intra- and intergranular cracking [*Kemeny and Cook*, 1991; *Wong and Baud*, 2012]. Such models invoke combined frictional slip plus intergranular or intragranular cracking to describe the dilatant Stage 3d behaviour [*Ashby and Sammis*, 1990; *Baud et al.*, 2014; *Guéguen and Fortin*, 2013] and intragranular cracking to describe the compactive Stage 3c behaviour [*Baud et al.*, 2014; *Sammis and Ashby*, 1986; *Wong et al.*, 1997; *Zhang et*

al., 1990]. In both cases, cracks are thought to emanate from stress-concentrators within the microstructure, such as pre-existing flaws and pores [*Sammis and Ashby*, 1986], or from surface flaws at the periphery of assumed Hertzian contacts [*Brzesowsky et al.*, 2014a; *Wong et al.*, 1997; *Zhang et al.*, 1990], and are assumed to grow according to the Griffith equilibrium condition [*Griffith*, 1921]. These models have several limitations, including: 1) In natural sandstones, grain contacts are often rough, indented, truncated and/or cemented and are therefore not necessarily well-described by a Hertzian contact model; 2) The stress versus inelastic strain behavior is frequently not described; and 3) Strength heterogeneity within the microstructure, resulting from differences in mineralogy [*Hangx et al.*, 2010a], or in the size of grains, grain contacts or grain asperities [*Brzesowsky et al.*, 2011] is generally neglected. The latter point implies discrete threshold stress states marking the onset of inelastic/plastic deformation (*i.e.* a sharp yield criterion), this being preceded at lower stress levels by purely poroelastic behavior [*cf. Guéguen and Fortin*, 2013]. Several studies have already demonstrated that sandstones do not always show such an idealized transition from elastic to inelastic behavior [*Bernabe et al.*, 1994; *Shalev et al.*, 2014; *Wong et al.*, 1992], though the grain-scale mechanisms controlling this behavior are not yet elucidated.

Discrete (or Distinct-) Element Method (DEM) models simulate compression and deformation of an aggregate consisting of discrete particles, or grains [*Antonellini and Pollard*, 1995; *Cheng et al.*, 2003]. Inelastic deformation developing at the grain-scale is frequently considered to arise from intergranular slip or by grain breakage, collectively contributing to global inelastic deformation which may be uniformly distributed or localized [*Marketos and Bolton*, 2009; *Wang et al.*, 2008]. The grains considered are often unbonded and disc-, or spherical shaped, implying Hertzian-like contact properties. However, grain bonding [*Marketos and Bolton*, 2009; *Potyondy et al.*, 1996], other particle shapes [*Fu et al.*, 2017; *Kawamoto et al.*, 2016], and different contact laws more realistic for geo-materials [*Cole and Hopkins*, 2017] have also been considered. DEM models have some advantage over microphysical models, in that they can more easily account for several microstructural features typical for natural sandstone [*e.g. Brzesowsky et al.*, 2011; *Cook et al.*, 2015], such as distributed grain/grain contact sizes and strengths [*Van den Ende et al.*, 2018; *Wang et al.*, 2008], or spatial variations in grain packing. However, simulation of deformation in sands or sandstone with realistic microstructural features remains computationally challenging [*Kawamoto et al.*, 2016]. More importantly, again, it is unclear whether the intergranular and intragranular processes usually considered in the above DEM studies contribute significantly to the small-strain ($\varepsilon \leq 1\%$) reservoir accompanying pore pressure depletion.

Against this background, and in the context of subsidence and induced seismicity in

the Groningen field, it is crucial to verify to what extent the above outlined models describe inelastic deformation of the Slochteren sandstone at the small strains relevant to gas production from the field. If these models are unsatisfactory, a new model needs to be developed, preferably based on the physical processes governing inelastic deformation at strains and P_c-T conditions relevant to this reservoir and other depleting reservoirs. Only then can the compaction behavior be explored for the decade time-scales and boundary conditions that are relevant to the field, but are difficult or impossible to explore in the lab. Ultimately, such a model can then be applied in field-scale models developed to investigate induced seismicity and subsidence in the (post-) production phase.

1.6 Structure and aims of this thesis

From the foregoing it is evident that: 1) The elastic versus inelastic, and possibly time-dependent contributions to the small total strains (0.1 to 1.0%) developing during depletion of reservoir sandstones are poorly constrained. As a result, the elastic energy budget available for seismic release is unquantified; 2) The mechanisms governing inelastic deformation at these small strains are unidentified, and the question of whether these are rate-dependent remains open; 3) The applicability of existing sandstone deformation models to predict reservoir deformation, and hence to assess a main controlling factor for induced seismicity, is yet unclear; and 4) The current lack of a physics-based description of reservoir sandstone compaction behaviour hampers realistic assessment of the impact of current and future production and strategies for reducing production on induced subsidence and seismicity, in the Groningen field and in other, similar fields worldwide.

The research conducted here aims to address these points. To do so, we provide new mechanical data on Slochteren sandstones from the Groningen field, obtained from conventional triaxial experiments and microstructural data, using the latest advances in scanning electron microscopy and image processing/handling. These data are directly relevant to the small-strain, *in-situ* compaction behavior of the reservoir but also cover the behavior seen at higher strains *i.e.* exceeding those seen in the field. We subsequently use the data obtained to test and calibrate existing models for sandstone and to develop a new, microphysical model to underpin the physical mechanisms underlying such models. The results are intended to provide input for understanding and geomechanical modelling of the behaviour of the Slochteren Sandstone reservoir within the context of subsidence and induced seismicity in the Groningen gas field.

The specific aims of this thesis are:

1) To quantify the elastic and time-(in)dependent inelastic strain development, and so to evaluate the stored versus dissipated energy available for seismic release, during simulated depletion of the Slochteren Sandstone reservoir under *in-situ* conditions of stress, temperature and chemistry (pore fluid), relevant for the Groningen gas field;
2) To identify the micro-scale mechanisms accommodating any inelastic strain contribution;
3) To test whether the mechanisms identified quantitatively account for the inelastic deformation behavior seen, and whether they exhibit any rate-sensitivity;
4) To use the mechanical and mechanistic data obtained to test and calibrate existing models for sandstone compaction. In that way we aim to provide quantitative descriptions of elastic plus inelastic deformation of the Slochteren reservoir sandstone, as relevant for depletion of the Groningen gas field under the boundary conditions and at the decade time-scales pertaining to this field.

Chapter 2 is concerned with determining the partitioning between elastic and time-(in)dependent inelastic strain of Slochteren sandstones from the Groningen field under the stress conditions simulating depletion of this field (Aim 1). Chapter 3 extends on this work by investigating the time-independent elastic and inelastic behavior of Slochteren sandstones under a wider range of stress conditions (Aim 1). The data are then applied to test and calibrate an existing plasticity model, and to provide quantitative descriptions of the time-independent elastic versus inelastic deformation behavior (Aim 4). In Chapter 4, we present a series of consecutive triaxial experiments performed on a single splitcylinder sample of Slochteren sandstone. State-of-the-art microstructural methods are employed to identify the grain-scale mechanisms controlling inelastic compaction at the small, reservoir-relevant strains (ε = 0.1 to 1.0%; Aim 2). The rate-sensitivity exhibited by these mechanisms is then analytically explored (Aim 3). The experimental and microstructural observations made in Chapters 2, 3 and 4 are used as a basis to derive a new microphysical model for inelastic deformation of Slochteren sandstone, aiming to test whether the mechanisms identified can account for the deformation behavior seen in our experiments (Aim 3). We thus obtain a mechanistic basis to underpin the empirical model used in Chapter 3. In turn, this allows evaluation of the extent to which this time-independent model can be applied to describe the *in-situ* behavior at the decade time-scales relevant to the (post-)production phase of the Groningen field (Aim 4).

Chapter 2

Deformation behaviour of sandstones from the seismogenic Groningen gas field: Role of inelastic versus elastic mechanisms

Based on: R. P. J. Pijnenburg, B. A. Verberne, S. J. T. Hangx and C. J. Spiers
Journal of Geophysical Research: Solid Earth, 123
DOI: 10.1029/2018JB015673

Abstract

Reduction of pore fluid pressure in sandstone oil, gas or geothermal reservoirs causes elastic and possibly inelastic compaction of the reservoir, which may lead to surface subsidence and induced seismicity. While elastic compaction is well-described using poroelasticity, inelastic and especially time-dependent compaction are poorly constrained, and the underlying microphysical mechanisms are insufficiently understood. To help bridge this gap, we performed conventional triaxial compression experiments on samples recovered from the Slochteren sandstone reservoir in the seismogenic Groningen gas field in the Netherlands. Successive stages of active loading and stress relaxation were employed to study the partitioning between elastic versus time-independent and time-dependent inelastic deformation upon simulated pore pressure depletion. The results showed that inelastic strain developed from the onset of compression in all samples tested, revealing a non-linear strain hardening trend to total axial strains of 0.4 to 1.3%, of which 0.1 to 0.8% were inelastic. Inelastic strains increased with increasing initial porosity (12 – 25%) and decreasing strain rate (10^{-5} s^{-1} to 10^{-9} s^{-1}). Our results imply a porosity and rate-dependent yield envelope that expands with increasing inelastic strain from the onset of compression. Microstructural evidence indicates that inelastic compaction was controlled by a combination of intergranular cracking, intergranular slip, and intra/transgranular cracking with intra/transgranular cracking increasing in importance with increasing porosity. The results imply that during pore pressure reduction in the Groningen field, the assumption of a poroelastic reservoir response leads to underestimation of the change in the effective horizontal stress, and overestimation of the energy available for seismicity.

2.1 Introduction

Fluid extraction from subsurface sandstone reservoirs, in the context of oil, gas and geothermal energy production, frequently results in surface subsidence [*Fialko and Simons*, 2000; *Morton et al.*, 2001; *Pratt and Johnson*, 1926; *Sharp and Hill*, 1995; *Van Wees et al.*, 2014] and sometimes in induced seismicity [*Davies et al.*, 2013; *Van Eijs et al.*, 2006; *Grasso*, 1992; *Segall and Fitzgerald*, 1998; *Suckale*, 2009]. Both effects are caused by the stress changes due to depletion of pore fluid pressure, and the associated reservoir compaction. Depletion-induced subsidence is observed globally in both onshore [*Bardainne et al.*, 2008; *Davies et al.*, 2013; *Fialko and Simons*, 2000] and offshore settings [*Cuisiat et al.*, 2010; *Davies et al.*, 2013; *Santarelli et al.*, 1998] and may cause damage to buildings and infrastructure [*Koster and Ommeren*, 2015; *Mitchell and Green*, 2017; *Van der Voort and Vanclay*, 2015]. The magnitude of subsidence is typically several centimeters to several tens of centimeters. Examples include the Port Neches, Clam Lake and Caplen oil fields in Texas [4 - 63 cm; *Morton et al.*, 2001], the giant Groningen gas field in the Netherlands [*NAM*, 2016], and the Geysers geothermal field, California [40 - 80 cm; *Mossop and Segall*, 1997]. In fields showing tens of cm of subsidence, induced seismicity is often widespread, as seen in the Groningen field, [*Van Eijs et al.*, 2006], the Geysers geothermal field in California [*Eberhart-Phillips and Oppenheimer*, 1984], and the War-Wink gas field in Texas [*Doser et al.*, 1991]. Despite these adverse effects, continued exploitation is likely to remain a necessity if we are to meet energy demand, at least in the coming few decades [*Brouwer et al.*, 2016; *GEA*, 2012; *IEA*, 2016].

Compaction of reservoir formations and associated surface subsidence and seismicity are driven by the increase in effective stress that accompanies fluid extraction [Zoback, 2010]. In sandstones, compaction is for a large part poroelastic [*Wang*, 2000; *Zoback*, 2010]. However, the systematically observed discrepancy between dynamic (elastic) stiffness moduli derived from well-logs, and the 1.2 to 3 times lower static (elastic + inelastic) moduli obtained from triaxial testing, suggests that deformation of reservoir sandstones is in part inelastic [*Yale and Swami*, 2017]. Moreover, some sandstone reservoirs show delayed subsidence after production initiation [*Hettema et al.*, 2002; *Van Thienen-Visser et al.*, 2015a], or ongoing subsidence after production has been reduced [*Mallman and Zoback*, 2007]. This too implies that inelastic, time-dependent deformation processes may play a role. Elastic compaction is relatively easily modeled using poroelasticity theory [*Altmann et al.*, 2010; *Dzung et al.*, 2009; *Geertsma*, 1973]. However, inelastic and especially time-dependent inelastic compaction are not, as the underlying deformation mechanisms are still poorly understood and the associated stress versus strain and strain-rate behaviour is quantified to

only a limited extent [*Bernabe et al.*, 1994; *Brantut et al.*, 2013; *Brzesowsky et al.*, 2014a; *Heap et al.*, 2015; *Shalev et al.*, 2014; *De Waal*, 1986].

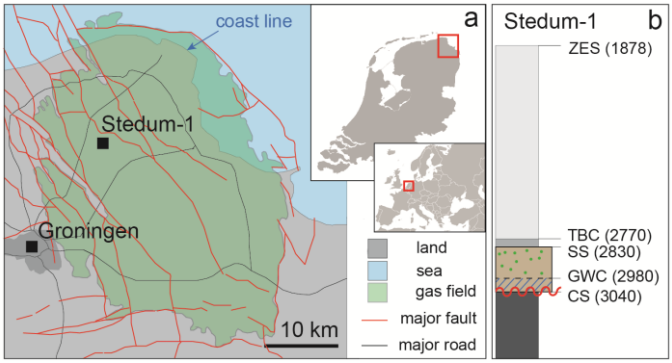

Figure 2.1 a) Location of the Groningen gas field in the NE-Netherlands, and of the Stedum (SDM)-1 well. Major normal faults (*i.e.* vertical throw > 150 m) cutting the Slochteren reservoir at 2830 m true vertical depth (TVD) are indicated in red. Image modified after NAM [2016]. **b)** Stratigraphy of the Groningen gas field at the SDM-1 well [*http://www.nlog.nl/keuzelijst-boringen*]. Depths (TVD, in m) to the top of the intersected units are indicated. The gas is present in the upper part of the reservoir (*i.e.* from 2830 – 2980 m TVD in the SDM-1 well). ZES: Zechstein evaporite sequence; TBC: Ten Boer claystone, SS: Slochteren sandstone; GWC: gas-water contact; CS: Carboniferous shale.

In sandstone reservoirs in the upper crust (< 5 km), inelastic deformation processes include: 1) intergranular (grain boundary) microcracking, 2) intergranular slip [*Bernabe et al.*, 1994; *Menéndez et al.*, 1996; *Shalev et al.*, 2014], 3) intra- and transgranular microcracking [*Baud et al.*, 2000; *Wong and Baud*, 2012], and 4) intergranular pressure solution [*Rutter*, 1983; *Spiers et al.*, 2004]. While pressure solution is known to be an important deformation mechanism over time-scales relevant for sandstone diagenesis (> 10,000 years [*Tada and Siever*, 1989; *Yang*, 2000], existing rate data [*Chester et al.*, 2004; *Dewers and Hajash*, 1995; *Gratier and Guiguet*, 1986; *Niemeijer et al.*, 2002; *Van Noort et al.*, 2008; *Renard et al.*, 1999; *Schutjens*, 1991] suggest that any contribution of this slow creep process to the compaction of quartz-rich reservoir rock will be small over time-scales (decades) and temperatures (T < 150 °C) relevant for upper crustal fluid extraction. Rather, for these conditions, inelastic deformation in sandstone is expected to be accommodated by the above grain-scale, brittle processes [*Baud et al.*, 2000; *Brantut et al.*, 2013; *Guéguen and Fortin*, 2013; *Heap et al.*, 2009, 2015; *Hol et al.*, 2018; *Menéndez et al.*, 1996; *Tengattini et al.*, 2014; *Wong and Baud*, 1999, 2012].

The onset of inelastic deformation by these processes is typically described using a discrete yield criterion, or yield envelope, assumed to be rate-insensitive [*Baud et al.*, 2000, 2004, 2006; *Klein et al.*, 2001; *Rutter and Glover*, 2012; *Skurtveit et al.*, 2013; *Tembe et al.*, 2008; *Wong et al.*, 1997; *Wong and Baud*, 2012; *Zhang et al.*, 1990]. Brittle yield is usually determined at the onset of non-linear stress-strain behaviour, which is associated with shear-coupled dilatancy at low mean effective stresses, and with compaction at high mean effective stresses [*Wong et al.*, 1997; *Wong and Baud*, 2012]. This type of brittle deformation behaviour in sandstones is well-known to be favored by higher initial porosity [*Wong and Baud*, 2012], since higher porosity leads to higher stress concentrations at grain contacts [*Cook et al.*, 2015; *Dobereiner and De Freitas*, 1986].

A range of microphysical models has been formulated to explain the above empirical observations [*Kemeny and Cook*, 1991; *Paterson and Wong*, 2005; *Wong and Baud*, 2012]. At low mean effective stresses, models for inelastic sand or sandstone deformation invoke 1) intergranular (tensile) grain boundary cracking plus subsequent frictional slip along the boundaries of assumed spherical grains [*Guéguen and Fortin*, 2013], or 2) intergranular or intragranular (wing-)cracking plus subsequent frictional slip along the newly formed cracked surfaces [*Ashby and Sammis*, 1990; *Baud et al.*, 2014]. In both cases, crack propagation is described by (Griffith-) equilibrium crack growth. At high mean effective stresses, intra- and transgranular cracking is proposed to be the dominant deformation mechanism, with Mode 1 equilibrium crack extension initiating from flaws at the periphery of assumed Hertzian contacts [*Guéguen and Fortin*, 2013; *Wong et al.*, 1997; *Zhang et al.*, 1990].

However, such models have limitations. First, grain-to-grain contacts in sandstones are often indented and/or cemented [*McBride*, 1989] and are hence non-Hertzian. This significantly increases the resistance to grain-scale cracking [*Bernabe et al.*, 1992; *Sackfield and Hills*, 1986; *Wong and Wu*, 1995]. Second, heterogeneity in the strength of the constituent grains or grain contacts is often neglected. In loose quartz sand, the strength of grains has been shown to be distributed [*Brzesowsky et al.*, 2011], with the weak grains failing in the early stages of deformation [*Brzesowsky et al.*, 2014b; *Karner et al.*, 2003]. Moreover, inelastic deformation developing at the earliest stages of compression has also been demonstrated for cohesive sandstones [*Hol et al.*, 2018; *Shalev et al.*, 2014]. This suggests that, at least for these materials, inelastic strain development plus work-hardening must occur continuously during loading, and that deformation cannot be adequately described by a discrete yield criterion based on the onset of non-linear stress-strain behaviour [*Karner et al.*, 2003, 2005a]. Third, the effects of time-dependent deformation processes,

such as subcritical crack growth, or rate-dependent grain boundary friction have been largely neglected, leaving the rate-dependence of the stress-strain and yield behaviour of sands and sandstones quantified to only a limited extent [*Brantut et al.*, 2013, 2014; *Brzesowsky et al.*, 2014a; *Heap et al.*, 2009, 2015; *Karner et al.*, 2005b; *De Waal*, 1986]. Indeed, in many treatments of pressure depletion during oil, gas or geothermal energy production from sandstone reservoirs, inelastic deformation is neglected completely and reservoir compaction is, in first approximation, assumed to be characterized by a simple, elastic compaction coefficient [*Altmann et al.*, 2010; *Van Eijs et al.*, 2006; *Geertsma*, 1973; *Lele et al.*, 2016; *Mulders*, 2003; *Wassing et al.*, 2016; *Zoback*, 2010].

However, the evolution of the yield envelope with strain and the effects of loading rate on stress-strain and yield behaviour are of key importance in determining the reservoir response to the partitioning between elastic and inelastic strain. This partitioning directly controls the evolution of compaction and hence surface subsidence during production [*Mallman and Zoback*, 2007; *Schutjens et al.*, 1995], and the stresses [*Buijze et al.*, 2017] and elastic energy available to drive induced seismicity as well as associated energy dissipating processes occurring upon fault rupture [*Cooke and Madden*, 2014; *McGarr*, 1999; *Shipton et al.*, 2013]. In recent years, the onset of significant induced seismicity in strongly depleted reservoirs, such as the large Groningen field in the NE-Netherlands [*Grötsch et al.*, 2011], has created an urgent need to understand these effects much better [*e.g. de Waal et al.*, 2017; *Spiers et al.*, 2017].

This paper addresses this need. We studied the deformation behaviour of samples recovered from the reservoir formation at the heart of the vast Groningen gas field, *i.e.* the Slochteren sandstone (Figure 2.1). To investigate the relative contributions of elastic and inelastic deformation, we performed conventional triaxial compression tests, employing successive stages of axial compression and stress relaxation. The experiments were conducted at applied differential stresses up to 50 MPa, in a manner designed to simulate the effective stress changes accompanying pore pressure depletion in a poroelastic reservoir. A poroelastic stress path was chosen in order to test whether Slochteren sandstones showed purely elastic (reversible) stress-strain behaviour under these conditions. Conversely, if inelastic strain would develop, then inelastic deformation should accordingly be expected to occur during field depletion. We used samples with a range of porosities (φ = 12 – 25%) representing those present in the reservoir. Microstructural analysis of undeformed and deformed samples was used to gain insight into the operating inelastic deformation mechanisms and any influence on these of factors such as porosity, grain size and grain size distribution. Our results are directly relevant to understanding elastic versus inelastic strain

and strain energy partitioning in the Slochteren reservoir sandstone, and to understanding the mechanisms controlling depletion-induced reservoir compaction, subsidence, stress evolution and induced seismicity in the Groningen field and in similar gas fields worldwide.

2.2 Geological setting of the Groningen gas field and slochteren reservoir

The Groningen gas field is a ~30 by 30 km field located in the NE-Netherlands (Figure 2.1a) on the southern flank of the east – west striking southern Permian basin [*Glennie*, 1972; *Ziegler*, 1990]. Thick continental sediments were deposited in this basin in the Permian under semi-arid to arid conditions, on top of an eroded, upper Carboniferous shale basement [*Glennie*, 1972 - see Figure 2.1b for the stratigraphy]. The Slochteren reservoir sandstone member, now located at about 3 km depth, is approximately 200 meter thick and constitutes a generally upward-fining succession of conglomerates and fluvial sandstones, overlain by cross-bedded aeolian sandstones, muddy siltstones and ultimately lacustrine mudstones, forming the Ten Boer claystone formation [*Waldmann and Gaupp*, 2016]. A thick sequence (500 – 1000 m) of Zechstein evaporites, characterized by a basal anhydrite/dolomite unit (~40 m) and multiple halite units overlies the Slochteren sandstone [*Amthor and Okkerman*, 1998]. Between the Triassic and the Late Jurassic, regional thermal subsidence resulted in burial and NW-SE trending extensional fracturing of the Permian sediments, and hydrocarbons were expelled from the underlying organic-rich Carboniferous shale and coal intervals into the reservoir [*De Jager et al.*, 1996]. At present, the Slochteren reservoir consists of a gas-bearing interval, and a water-saturated interval, which typically comprise the upper 50 – 150 m, and lower 50 – 150 m, respectively [*NAM*, 2013]. Since production from the field began in 1963, the pore fluid pressure has decreased from 35 MPa to a surprisingly uniform ~ 8 MPa [*NAM*, 2016].

The porosity of the Slochteren sandstone is well constrained from wireline logs and fluid-immersion tests on core plugs, with average values ranging from 18 – 22% in the centre of the reservoir, decreasing laterally to 12 - 16% at the margins [*NAM*, 2016]. The sandstone can be classified as a subarkose to lithic subarkose [*McBride*, 1963], consisting on average of 72 – 90 vol% quartz, 8 – 25 vol% feldspar, 0.5 – 5.5 vol% clay, and 3 – 10 vol% of lithic rock fragments, which include basaltic and sedimentary lithoclasts [*Waldmann et al.*, 2014; *Waldmann and Gaupp*, 2016]. During burial diagenesis, the total initial feldspar content was reduced by dissolution reactions, leading to precipitation of kaolinite and illite in the pores and onto the pore walls [*Waldmann and Gaupp*, 2016].

2.3 Sample material and pore fluid chemistry

Samples used in this study were obtained from core material composed of Slochteren sandstone (2830 – 3040 m true vertical depth [TVD]), taken during drilling of the Stedum (SDM)-1 well (Figure 2.1a) and provided courtesy of the field operator (Nederlandse Aardolie Maatschappij). The SDM-1 well was drilled in 1965, prior to major gas production.

Sets of two to three cylindrical plugs, each 25 mm in diameter and 50 – 55 mm in length were drilled from the SDM-1 core, at specific depth intervals, in an orientation parallel to the core axis and sub-perpendicular to the often slightly inclined bedding (within 10 degrees). The ends of the plugs were ground flat and perpendicular to the sample axis using a polishing wheel, to ensure homogeneous load distribution during testing. The resulting samples were homogeneous to slightly laminated. Samples from above and below the gas-water contact were, respectively, grey and red in colour. All samples tested in the present study are listed in Table 2.1. In naming them, the annotations *g* and *w* indicate that the sample was obtained from core taken from the gas-bearing (*g*) or water-saturated (*w*) intervals of the SDM-1 well. Samples with the same number (*e.g.* Sw07) imply they were taken from the same depth interval, while suffixes *a* to *c* are used to identify deformed samples. The absence of any suffix indicates that the sample was not deformed in a laboratory test. These undeformed samples were used as benchmark samples to identify deformation-induced microstructural changes.

During core storage, the high salinity brine present in the core upon recovery resulted in salt precipitation in the pore space. Prior to each experiment, these precipitates were re-dissolved by vacuum-saturating the sample with de-mineralized water (DMW) to fill it with realistic pore fluid. We determined the corresponding initial porosity (φ_0) using the injected DMW volume, *i.e.* the mass difference between the dry sample (sample + salt precipitates) and the wet sample (sample + salts + DMW), divided by the density of DMW (0.997 g/mL), while taking into account the volume change of the injected fluid upon salt dissolution. The porosity values obtained ranged from 12.7 to 24.6%.

To determine the chemistry of the pore fluid present during our tests, we selected plug-sized fragments from both the gas-bearing and the water-bearing intervals of the SDM-1 core, using the same depth intervals as our test plugs, such that the average porosity of the combined fragments was approximately 20%. The fragments were then crushed, mixed, and sieved to a grainsize < 35 μm, and suspended in a known volume of DMW at room temperature, stirring continuously for three days. After three days, 10 mL samples of filtered fluid were weighed to obtain the density and analyzed using inductively coupled plasma mass spectrometry (ICP-MS).

Table 2.1 List of experiments, conditions and key data. Experiments were performed wet (see Table 2.2 for brine composition), at $T = 100^{\circ}C$ and $P_p = 10$ MPa.

Sample	TVD	φ_0	Q_{max}	$(e_t)_{fin}$	$(e_{el})_{fin}$	$(e_i)_{fin}$	$(\Delta\varphi_t)_{fin}$	$(\Delta\varphi_{el})_{fin}$	$(\Delta\varphi_i)_{fin}$	Q_{max}	E_a	$(e_t)_{fin}$	$(e_{el})_{fin}$	$(e_i)_{fin}$	$(e_i^{inst})_{max}$	$(e_{cr})_{max}$	$(e_i^{\Sigma})_{max}$	$(e_{el}^{\Sigma})_{max}$	$(\Delta\varphi_t)_{fin}$	$(\Delta\varphi_{el})_{fin}$	$(\Delta\varphi_i)_{fin}$	H/S
	[m]	[%]	[MPa]	[%]	[%]	[%]	[%]	[%]	[%]	[MPa]	[GPa]	[%]	[%]	[%]	[%]	[%]	[%]	[%]	[%]	[%]	[%]	
			In-situ conditioning phase (constant P_c^{eff} = 8 MPa)							*Multi-step phase* (constant P_c^{eff} = 15 MPa)												
Sw09b	3036.6	12.7	23.2	0.35	0.25	0.10	-0.29	-0.19	-0.10	50.4	18.4	0.42	0.31	0.11	0	0.10	0.10	0.32	-0.18	-0.17	-0.01	H
Sw11b	3036.8	14.2	22.4	0.43	0.27	0.16	-0.26	-0.16	-0.10	50.0	20.2	0.38	0.31	0.07	0	0.06	0.06	0.32	-0.22	-0.22	-0.00	H
Sw13a	3044.8	17.4	24.0	0.53	0.27	0.26	-0.32	-0.17	-0.15	50.2	17.7	0.55	0.39	0.16	0	0.16	0.16	0.40	-0.42	-0.26	-0.16	H
Sg09b	2894.1	17.7	24.4	0.50	0.37	0.13	-0.17	-0.05	-0.12	49.0	15.4	0.51	0.34	0.17	0	0.16	0.16	0.35	-0.31	-0.14	-0.17	S
Sg10a	2919.0	18.0	21.7	0.73	0.26	0.47	-0.51	-0.13	-0.38	49.6	13.2	0.77	0.44	0.33	0	0.33	0.33	0.43	-0.43	-0.18	-0.25	H
Sw02a	3053.8	19.9	24.2	0.54	0.30	0.24	-0.30	-0.11	-0.19	49.6	19.1	0.46	0.32	0.14	0	0.15	0.15	0.30	-0.31	-0.18	-0.13	H
Sg05a*	2892.6	21.6	-	-	-	-	-	-	-	45.5	9.3	1.16	0.56	0.60	0.06	0.59	0.64	0.51	-	-	-	H
Sg05c	2892.6	21.6	22.1	0.72	0.31	0.41	-0.51	-0.20	-0.31	48.6	9.4	1.30	0.57	0.73	0.16	0.59	0.75	0.53	-0.61	-0.07	-0.54	H
Sw07a	3034.5	24.6	23.8	0.98	0.21	0.77	-0.39	-0.13	-0.26	40.2	7.6	1.27	0.47	0.81	0.12	0.69	0.81	0.49	-0.65	-0.09	-0.56	H

* Experiment that was not conditioned to the pre-depleted *in-situ* stress, and in which no pore volume data were obtained.

Symbols: TVD: the true vertical depth along the SDM-1core from where samples were derived; φ_0 denotes the initial porosity; Q_{max} denotes the maximum differential stress imposed on the sample; $(e_t)_{fin}$ and $(\Delta\varphi_t)_{fin}$ denote the total axial strain and total porosity change, respectively, at the end of each phase; $(e_i)_{fin}$ and $(\Delta\varphi_i)_{fin}$ denote the final inelastic axial strain and porosity change, respectively, at the end of each phase; $(e_{el})_{fin}$ and $(\Delta\varphi_{el})_{fin}$ denote the final elastic axial strain and porosity change at the end of each phase, determined using: $(e_{el})_{fin} = (e_t)_{fin} - (e_i)_{fin}$, and $(\Delta\varphi_{el})_{fin} = (\Delta\varphi_t)_{fin} - (\Delta\varphi_i)_{fin}$ respectively; E_a denotes the apparent Young's modulus, inferred from a linear fit of the linear part of the stress-strain curve; $(e_i^{inst})_{max}$ and $(e_{cr})_{max}$ denote the sum of all instantaneous and creep inelastic axial strains accumulated during all the active loading and relaxation stages, respectively, of the multi-step phase (see section 2.6.2.1); $(e_i^{\Sigma})_{max}$ denotes the maximum cumulative inelastic axial strain, and is given: $(e_i^{\Sigma})_{max} = (e_i^{inst})_{max} + (e_{cr})_{max}$. $(e_{el}^{\Sigma})_{max}$ denotes the maximum cumulative elastic axial strain, calculated using $(e_{el}^{\Sigma})_{max} = (e_t)_{max} - (e_i^{\Sigma})_{max}$. Note that $(e_i^{\Sigma})_{max} \approx (e_i)_{fin}$, and : $(e_{el}^{\Sigma})_{max} \approx (e_{el})_{fin}$; H/S denotes the use of the Heard vessel (H) or the Shuttle vessel (S).

Using the ICP-MS data, the concentrations of the ions in the pore fluids were calculated, assuming intact and fully saturated sample porosities of 20% (Table 2.2). The brine density measured for the water-bearing interval was 1.23 g/mL, and the total salt concentration obtained was 4.2 mol/L. These values are similar to those determined on fluid samples extracted from the water-bearing interval of the Slochteren sandstone interval of the Zeerijp-3a core [*Hol et al.*, 2018], which was drilled in 2015 at a location ~5 km NE of the SDM-1 well (Table 2.2). The brine density measured for the gas-bearing interval (1.12 g/mL) and the corresponding salt concentrations obtained (2.2 mol/L) are approximately half of the values obtained for the water-bearing interval. This difference is attributed to the fact that the porosity of the gas-bearing sandstone of the SDM-1 core was only partly filled (25 ± 10%) with brine [*Waldmann*, 2011]. Pilot experiments performed on Rotliegend sandstone similar to the Slochteren sandstone showed very little effect of the molarity of saline pore fluids on sandstone creep strains and strain rates. Thus, we anticipate that the difference in brine salinity during testing of samples from the gas-bearing versus water-bearing intervals leads to negligible difference in the mechanical behavior.

Table 2.2 Ion concentration and density data for the pore fluids used during testing of samples from the gas-bearing and water saturated intervals of the SDM-1 well. For comparison, data are shown as obtained for the water-saturated interval of the Slochteren sandstone from the Zeerijp (ZRP-)3a well, drilled in 2015, 5 km from the SDM-1 well [see: *Hol et al.*, 2018].

	Ion concentration (mol/L)						*Density [g/mL]*
	Ca^{2+}	Mg^{2+}	K^{+}	Na^{+}	Cl^{-}	S^{2-}	
Experimental pore fluid: gas interval samples	0.0	0.0	0.1	2.1	1.8	0.1	1.12
Experimental pore fluid: water interval samples	0.1	0.0	0.1	4.0	3.6	0.3	1.23
Reservoir pore fluid (water interval ZRP-3a)	1.0	0.1	0.1	3.4	4.9	0.0	1.21

2.4 Experimental methods

In this study, we performed combined incremental axial loading plus stress relaxation experiments. These were conducted under conventional triaxial test conditions, with $\sigma_1 > \sigma_2 = \sigma_3 = P_c$ (fixed confining pressure). The experiments consisted of constant strain-rate deformation steps ($\dot{\varepsilon} \approx 10^{-5}$ s^{-1}), applied to load the samples to successively higher differential stresses, with each step being followed by a period of stress relaxation at

near-constant load-point position [*Rutter and Mainprice*, 1978]. The aim was to investigate the effect of initial porosity on stress-strain and stress versus strain-rate behaviour, with specific attention for the contribution of elastic versus inelastic strain. All experiments were conducted at a temperature of 100°C, representative of the top of the Slochteren reservoir in the SDM-1 well (at 2830 m TVD, see *NAM*, 2013). We imposed effective stress changes simulating full depletion of the Groningen gas reservoir (*i.e.* a pore pressure drop from 35 to 0.1 MPa), assuming poroelastic behaviour.

2.4.1 Experimental apparatus

The experiments were conducted using two conventional triaxial testing machines at the High Pressure and Temperature laboratory at Utrecht University, referred to here as the Heard vessel (described by Peach 1991; Hangx et al. 2010) and the Shuttle vessel (described by Verberne et al. 2013). One incremental axial loading plus stress relaxation test was performed using the Shuttle vessel, while the other tests were conducted using the Heard vessel (Table 2.1). The differences in capabilities and performance between the two machines are minor and exert little or no influence on the measurement of sample properties. Both vessels are constant volume triaxial pressure vessels. Silicon oil is the confining medium. Viton O-rings ensure sealing on all dynamic and static seals. The Heard vessel is externally heated, while the Shuttle vessel is internally heated. In both vessels, heating is controlled to within 0.1°C of a set-point furnace temperature, chosen to produce a sample temperature of 100˚C. Sample temperature is measured using an inconel-sheathed, K-type (chromel/alumel) thermocouple in contact with the jacketed sample. In both cases, confining pressure was applied using a compressed-air driven diaphragm pump and measured using a Jensen pressure transducer (100 MPa full range, resolution of ± 0.02 MPa). Confining pressure and pore pressure are maintained constant throughout the experiment using two independent, servo-controlled volumometers (syringe pumps with full range 8 mL, resolution ± 2 μL) in the case of the Heard vessel, and two independent ISCO 65D syringe pumps (full range 68 mL, resolution ± 2.5 nL), in the case of the Shuttle vessel. In the Heard machine, axial displacement is achieved via a ball-screw, driven by a constant speed motor plus variable-gear box assembly. It is measured using a linear variable differential transformer (LVDT; 100 mm full range; resolution of ± 0.8 μm), located in the drive system outside the pressure vessel. Axial force is measured using a semi-internal load cell, furnished with an internal differential variable reluctance transformer (DVRT; resolution ± 33 N, full range 400 kN). By contrast, the Shuttle vessel is loaded using an Instron (1362) servo-controlled load frame. Displacement is measured using an LVDT (100 mm full range; resolution of ± 0.8

μm), located in the drive system outside the pressure vessel, and axial force is measured using a semi-internal load cell, furnished with an internal DVRT (resolution ± 33 N; full range 100 kN).

2.4.2 Choice of applied stress path

The stress path applied in the incremental loading steps preceding each stress-relaxation interval was chosen to simulate the effective stress changes that we estimate would occur *in-situ* during full depletion of a poroelastically deforming Slochteren reservoir sandstone. Henceforth, we assume that the maximum *in-situ* stress is vertical [following: *NAM*, 2016] and we refer to the vertical stress, and to the maximum and minimum horizontal stresses within the reservoir as the maximum (σ_1), intermediate (σ_2) and minimum principal compressive stress (σ_3), respectively.

Prior to gas extraction, σ_1 at the top of the reservoir was 65 MPa [*Schutjens et al.*, 1995], σ_3 was determined to be 43 MPa [*Breckels and Van Eekelen*, 1982], while the pore pressure (P_p) measured 35 MPa [*NAM*, 2016; *Schutjens et al.*, 1995]. Taking the Biot coefficient (α) to be equal to 1 (incompressible grains), this implies a maximum principal effective stress $\sigma_1^{eff} = \sigma_1 - \alpha P_p$ of 30 MPa, a minimum principal effective stress $\sigma_3^{eff} = \sigma_3 - \alpha P_p$ of 8 MPa and a differential stress (σ_1 - σ_3) of 22 MPa. The pre-depletion stress-state for the present experiments was chosen to match. We note, though, that in particular for low porosity sandstones (12 to 15%), α values may be lower than 1, falling in the range of 0.7 to 0.9 [*Lele et al.*, 2015]. Hence, for low porosities, the above effective stresses represent lowerbound values. We assumed that the vertical overburden stress (σ_1) could be considered constant. Full depletion of the field to a pore pressure of 0.1 MPa then implies an increase in σ_1^{eff} from 30 to ~65 MPa. The concomitant change in σ_3^{eff} can be roughly estimated assuming poroelastic deformation under uniaxial strain conditions [*Wang*, 2000; *Zoback*, 2010], using:

$$\Delta\sigma_3^{eff} = \alpha\Delta P_p \left(\frac{(1-2\nu)}{(1-\nu)} - 1\right) \qquad \text{(Eq. 2.1)}$$

Assuming a Poisson's ratio (ν) of 0.15 ± 0.05 (as estimated for the Slochteren sandstone by *Hettema et al.*, [2000]), σ_3^{eff} is thus estimated to increase during depletion from 8 MPa to ~15 ± 2 MPa, resulting in an increase in the differential stress from 22 to ~ 50 MPa. These changes in (σ_1 - σ_3) and σ_3^{eff} provided the basis for our choice of loading paths.

We tested our samples in two phases. In the first (*in-situ* conditioning) phase, we imposed the *in-situ* stress conditions expected in the Slochteren sandstone reservoir prior to

depletion, *i.e.* (σ_1 - σ_3) = 22 MPa, at an effective confining pressure ($P_c^{eff} = P_c - P_p$) of 8 MPa. In the second (multi-step) phase, stress conditions were imposed that are expected after depletion in an assumed poroelastic reservoir, *i.e.* (σ_1 - σ_3) up to 50 MPa, and P_c^{eff} = 15 MPa. Poroelastic stress changes were chosen in order to test whether Slochteren sandstone behaved poroelastically under these conditions. Alternatively, if inelastic strains would develop, then inelastic deformation would be expected in the reservoir. If this is the case, the chosen values of (σ_1 - σ_3) and σ_3^{eff} would represent upper and lower bounds, respectively.

2.4.3 Experimental procedure

Each sample was sealed between an upper and lower piston, using a fluorinated ethylene propylene (FEP) jacket. This was heat-shrunk and sealed against the sample pistons, using stainless steel metal wire tourniquets tightened onto underlying ethylene propylene diene monomer (EPDM) bands countersunk into the pistons. To reduce friction at the sample-piston interfaces, thin Teflon sheets (50 μm) were included at these locations during the jacketing procedure. These sheets were perforated to facilitate free pore fluid flow through the pistons and into the sample. After sealing, the sample assembly was emplaced in the oil-filled pressure vessel. The sample was then brought to the desired testing temperature (T = 100°C), while maintaining the confining pressure below the effective value to be used during deformation. Meanwhile, the pore fluid system was evacuated for 15 minutes. Finally, the required confining and pore pressures were applied under servo control, so that the target effective pressure was never exceeded, and the apparatus plus sample were left to equilibrate for 6 - 15 hours.

After sample assembly, our samples were emplaced in the oil-filled triaxial vessel and brought to the testing temperature (T = 100°C) and pressure conditions (P_c = 18 MPa and P_p = 10 MPa) used during the *in-situ* conditioning phase. This was achieved by increasing the confining and pore pressures in steps, such that the effective confining pressure never exceeded the value used during testing. Subsequently, the loading piston was advanced at a near-constant (within 1% of the determined value) total axial strain-rate ($\dot{\varepsilon}_t$) of 10^{-5} s^{-1}, until a differential stress of 22 MPa was attained. The piston was then arrested, allowing stress relaxation for 24 to 48 hours, until the differential stress ($\sigma_1 - \sigma_3$) reached a near-constant value *i.e.* until the decrease in the differential stress fell within the noise on the internal axial load sensor (~ 0.1 MPa). Following this stress relaxation stage, the sample was tested for reversible loading/unloading behaviour, by imposing multiple axial loading/unloading stress cycles of ± 2 MPa. The sample was then fully unloaded (*i.e.* [σ_1 - σ_3] was returned to 0 MPa), and the effective confining pressure was increased to 15 MPa.

In the subsequent multi-step phase, we imposed P_c = 25 MPa and P_p = 10 MPa, so that P_c^{eff} = 15 MPa, at T = 100˚C. We then applied multiple, sequential steps of piston advancement, at $\dot{\varepsilon}_t \approx 10^{-5}$ s^{-1}, to obtain differential stresses of 22, 30, 35, 40, 45 and ultimately 50 MPa (where supportable by the sample). Each loading step was terminated by piston arrest, followed by stress relaxation for 24 hours. Upon completion of the final stress relaxation stage, the sample was unloaded axially, and the confining pressure and pore pressure were removed, maintaining the effective pressure below the test value. After cooling to ~80˚C, the sample assembly was removed from the testing machine, and the sample was extracted for microstructural analysis.

2.4.4 Data acquisition and processing

In processing and presenting our data, we adopt the convention that compressive stresses, compressive axial strains and dilation are positive. Throughout each experiment, the internal axial load, sample temperature, confining pressure, pore pressure, pore fluid volume change, and axial displacement signals were logged at a frequency of 10 Hz during piston advancement intervals, or else at 0.2 Hz, during intervals of stress relaxation. A 16-bit DAQPad National Instruments A/D converter was used.

Internal axial load data were processed to yield axial force versus time. The displacement data were accordingly corrected for apparatus distortion and thermal expansion, using calibrations carried out using a steel dummy, at pressure and temperature conditions covering the present experiments. The pore fluid volume change data were corrected for thermal volume changes upon flowing in or out of the heated pressure vessel. The corrected displacement and pore volume data were used to determine the changes in sample length (ΔL) and pore volume (ΔV) versus time. These data were subsequently used to calculate the total axial strain $\varepsilon_t \approx e_t = \Delta L/L_0$ (for the present low strains), and the total porosity change $\Delta\varphi_t = \Delta V/V_0$, where L_0 and V_0 are the initial sample length and volume, respectively. Differential stress ($Q = \sigma_1 - \sigma_3$) and mean effective stress (P) were computed, assuming that the instantaneous cross-sectional area of the sample (A) is equal to $(V_0 - \Delta V)/(L_0 - \Delta L)$. The quantities Q_{max} and P_{max} refer, respectively, to the maximum differential stress and maximum mean effective stress imposed on individual samples. The apparent Young's modulus E_a was determined for each experiment by linear regression of stress-strain data obtained during piston advancement at $(\sigma_1 - \sigma_3)$ = 22 - 30 MPa (error < 1% of determined value). Since strains measured in our experiments were relatively small, the values of E_a determined in this stress window are assumed to be representative for the entire experiment. The quantities $(e_t)_{fin}$ and $(\Delta\varphi_t)_{fin}$, tabulated in Table 2.1, refer respectively to the final total axial strain and

the corresponding total porosity change determined at the end of either the *in-situ* conditioning phase, or the multi-step phase, assuming zero strain and porosity change at the start of each phase. Thus, in determining $(e_t)_{fin}$ and $(\Delta\varphi_t)_{fin}$ at the end of the multi-step phase, we neglected any permanent strains accumulated during the preceding *in-situ* conditioning phase. Since the inelastic strains developed during the *in-situ* conditioning phase were small, this approach resulted in negligible errors in the values determined (<0.4% of the determined value). Similarly, to determine the final inelastic axial strain $(e_i)_{fin}$ and the final inelastic porosity change $(\Delta\varphi_i)_{fin}$ accumulated after either the *in-situ* conditioning phase, or the multi-step phase, we divided the permanent change in sample length and pore volume, determined upon axial unloading after finalizing each phase, by the initial sample length L_0 and volume V_0, respectively. Again, in determining $(e_i)_{fin}$ and $(\Delta\varphi_i)_{fin}$ in the multi-step phase, any permanent strains accumulated during the preceding *in-situ* conditioning phase were neglected. The final elastic axial strain $(e_{el})_{fin}$ and elastic porosity change $(\Delta\varphi_{el})_{fin}$ were obtained by subtraction of $(e_i)_{fin}$ and $(\Delta\varphi_i)_{fin}$ from $(e_t)_{fin}$, and $(\Delta\varphi_t)_{fin}$, respectively.

During stress relaxation, elastic energy, stored in the sample plus apparatus, is in part dissipated through time-dependent inelastic deformation of the sample [*Rutter and Mainprice*, 1978]. The resultant axial creep strain (e_{cr}) is proportional to the amount of stress relaxation ($\Delta[\sigma_1 - \sigma_3]$), via the compliance (*C;* unit [mm/N]) of the sample plus apparatus combined: $e_{cr} = - \Delta(\sigma_1 - \sigma_3)\ C\ A/L_0$. We determined *C* for each experiment, via linear regression of internal axial load and displacement data, uncorrected for apparatus distortion, representing the (near-) linear part of the displacement versus internal axial load curve. This occurred in the range of 7.4 – 10.8 kN (*i.e.* $[\sigma_1 - \sigma_3]$ = 15 to 22 MPa). Using linear regression analysis, the error in determining *C* was found to be < 1% of the determined value. Using the values obtained for *C*, we determined the evolution of e_{cr} for each individual stress relaxation interval, each time taking the initial (reference) value of e_{cr} upon piston arrest to be 0%. The axial creep strain-rate ($\dot{\varepsilon}_{cr}$) at any instant during relaxation was calculated using the fact that it is proportional to the stress relaxation rate, via *C*: $\dot{\varepsilon}_{cr} = - \mathrm{d}(\sigma_1 - \sigma_3)/\mathrm{dt}\ C\ A/L$ [*Rutter and Mainprice*, 1978]. The stress relaxation rate was calculated by least-squares fitting to obtain the slope of the $(\sigma_1 - \sigma_3)$ versus time data-stream, using a variable window-size corresponding to a fixed stress drop, chosen such that the maximum error in creep strain-rate was always less than ± 8%.

In the present work, the term creep refers to time-dependent deformation at any instant in time and at any magnitude of stress, notably during relaxation stages of the experiments. The relaxation data are used to gain insight into the magnitude of strain rate and any the relationship to imposed stress, as a function of initial porosity. We anticipate that the

strain rates measured, at the given stresses and strains, will be comparable at least in order of magnitude terms, to those measured in constant-stress creep tests at similar stresses and strains [*e.g. Heap et al.*, 2009, 2015; *Brantut et al.*, 2014].

2.4.5 Microstructural analyses

Microstructural investigation was performed on undeformed SDM-1 core materials and on deformed SDM-1 plugs recovered after experimentation. The undeformed SDM-1 samples consisted of core material left over after drilling cylindrical plugs for mechanical testing. Thus, each plug tested has an undeformed microstructural counterpart (no *a-c* suffix in name), sampled within 2 cm, which we used as a benchmark for assessing experimentally-induced microstructural changes. Sectioned samples were investigated using a FEI Nova Nanolab 600 scanning electron microscope (SEM), or using a FEI Helios Nanolab G3 SEM. Imaging was done in backscatter electron (BSE) mode, using an acceleration voltage and beam current of 15 kV and 2.2 nA in the Nova Nanolab, and 10 kV and 1.6 to 3.2 nA in the Helios. The BSE detector in the Nova Nanolab consists of an Everhart-Thornley detector, whereas in the Helios a solid state concentric backscatter (CBS) detector was used [*Sakic et al.*, 2011]. In both SEM's, we employed a working distance of 3 to 5 mm. All samples were imaged by compiling tiled photomosaics. For each tile, we employed a horizontal field width of 2.13 mm and a dwell time of 7 μs in the Nova Nanolab, versus 1.18 mm and 3 μs in the Helios. Prior to stitching, image tiles from the Nova Nanolab were subject to background correction using Adobe Photoshop 2014.1.0. Photomosaic stitching was done using ImageJ [*Preibisch et al.*, 2009].

Quantitative microstructural analysis was performed on portions (~ 10 to 50 mm^2 in size) of stitched images. In the case of undeformed samples, grains were manually delineated using ImageJ software to create grain maps. These maps were used to quantitatively investigate textural features, such as grain size, grain size distribution, grain aspect ratio and shape preferred orientation. Grain size analysis was performed by calculating the equivalent circular radius $r = (3A_p/ 2\pi)^{0.5}$, where A_p is the area of a polygon representing a single grain [*Underwood*, 1970]. Grain aspect ratios (*AR*) were calculated by dividing the length of the major axis by that of the minor axis of a best-fit ellipse. Grain orientations were determined from the angle (β), between the major axis of each grain, and the sample horizontal, *i.e.* a line normal to the coring direction, in the case of undeformed samples, and normal to the σ_1 direction, in the case of deformed samples. Clay particles were excluded from the analysis. To estimate the mean crack density in our undeformed and deformed samples, defined here as the total number of cracks normalized to the number of grains analysed, we employed the

linear intercept method [*Underwood*, 1970]. To do this, a square grid of spacing 0.5 mm, measuring 16 mm^2, was superposed onto the BSE photomosaics at a similar location in each sample. Each intersection of a vertical or horizontal gridline with an intragranular or transgranular crack, and with a grain was tallied, resulting in crack density measured parallel ($CD_{\parallel}$**)** and normal ($CD_{\perp}$**)** to the coring direction, or principal compressive stress axis. Crack density data were obtained for all samples except sample Sg05c.

2.5 Results

2.5.1 Mechanical data

A list of the experiments performed, the corresponding test conditions and key-mechanical data is given in in Table 2.1. A list of the key-symbols used in this study is given in Appendix 2.A1.

2.5.1.1 Mechanical behaviour during the in-situ conditioning phase

To illustrate the mechanical behaviour of our samples during the *in-situ* conditioning phase, plots of differential stress and total porosity change versus total axial strain data, and differential stress versus time data are presented in Figure 2.2, for representative samples of low (Sw11b; φ_0 = 14.2%) and high porosity (Sg05c φ_0 = 21.6%) material. All experiments showed concave-up stress-strain behaviour up to a differential stress of about 10 MPa, after which near-linear stress-strain behaviour was observed (Figure 2.2a). During the entire *in-situ* conditioning phase and at all differential stresses, high porosity samples showed more total axial strain (Figure 2.2a) and total porosity change (Figure 2.2b) than low porosity samples. Within the first 16 hours after piston arrest in the *in-situ* conditioning phase, our data show that the differential stress gradually relaxed by 1 to 4 MPa, after which a near-constant value is reached (Figure 2.2c). Typically, more stress relaxation and thus higher creep strains were observed with increasing porosity. The axial creep strain-rate simultaneously decreased gradually from ~10^{-5} s^{-1} to ~10^{-9} s^{-1}, beyond which the decrease in the differential stress fell within the noise on the internal axial load sensor. After stress relaxation, stress-cycling data show that deformation was nominally reversible, *i.e.* at this point, very little or no additional inelastic axial strain was accumulated during consecutive cycles (Figure 2.2a, inset). Upon full axial unloading, low porosity samples (φ_0 < 17.4%) typically showed final inelastic axial strains $(e_i)_{fin}$ of 0.1 to 0.2%, and final inelastic porosity changes $(\Delta\varphi_i)_{fin}$ of approximately -0.1% (see Table 2.1). Intermediate porosity samples (17.4% ≤ φ_0 < 21.6%) yielded $(e_i)_{fin}$ of 0.1% - 0.5%, and $(\Delta\varphi_i)_{fin}$ of -0.1 to -0.4%. High porosity samples ($\varphi_0 \geq$ 21.6%) showed $(e_i)_{fin}$ of 0.4 – 0.8% and $(\Delta\varphi_i)_{fin}$ of -0.2 to -0.3%.

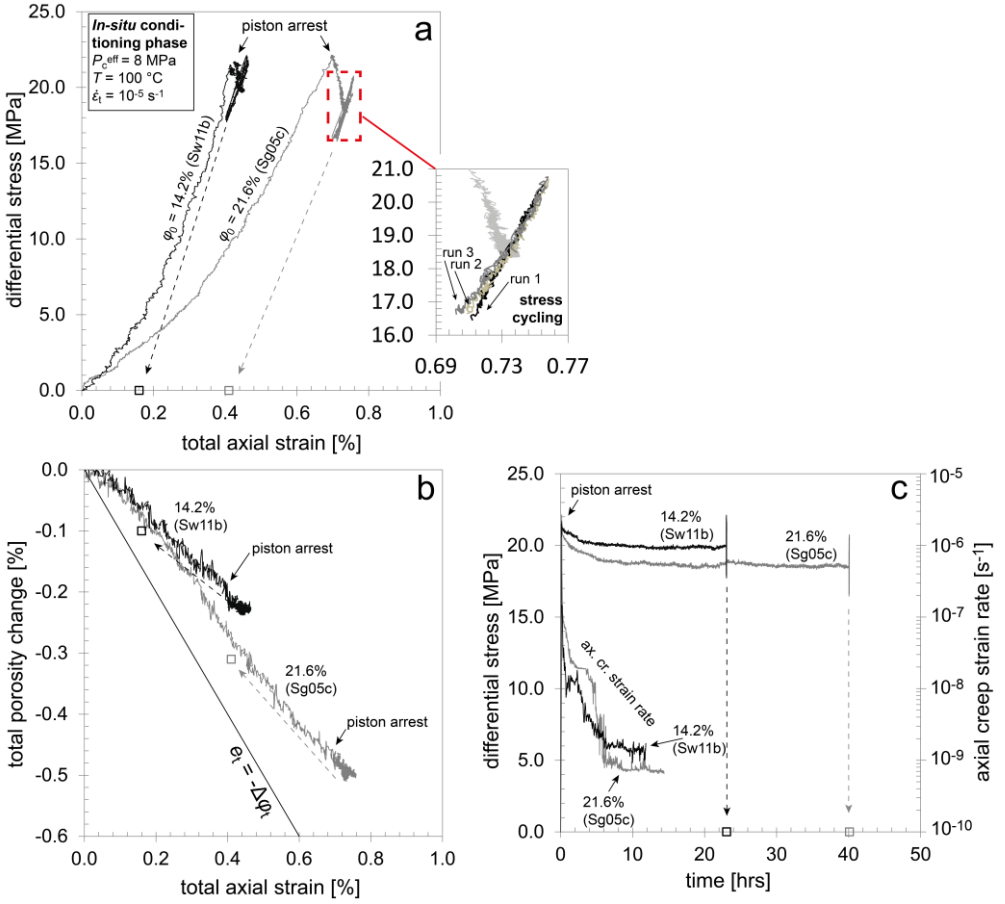

Figure 2.2 Data obtained during the *in-situ* conditioning phase of the present incremental axial loading plus stress relaxation experiments. Representative plots are shown for low and high porosity samples (φ_0 = 14.2%, Sw11b; φ_0 = 21.6%, Sg05c). **a)** Plot showing differential stress versus total axial strain data. During active loading, high porosity samples show more total axial strain than low porosity samples. Inset: after > 24 hours of relaxation, stress cycling through ± 2 MPa demonstrates reproducible, recoverable (*i.e.* elastic) deformation. **b)** Plot showing total porosity change versus total axial strain data. More compaction (-ve) is oberved with increasing initial porosity. **c)** Differential stress versus time data. Upon piston arrest, the differential stress relaxes, and the axial creep strain rate decreases from 10^{-6} s^{-1} to < 10^{-9} s^{-1}. More relaxation is observed with increasing initial porosity. Open square symbols indicate the final inelastic axial strain $(e_i)_{fin}$ and final porosity change $(\Delta\varphi_i)_{fin}$, obtained after axial unloading of the sample (Table 2.1).

2.5.1.2 Mechanical behaviour during the multi-step phase

In this phase, it will be recalled that samples were subjected to multiple differential stress increments up to a maximum total value of 50 MPa, at P_c^{eff} = 15 MPa. Each stress step was followed by 24 hours of stress relaxation (Figure 2.3). During initial active loading up to $(\sigma_1 - \sigma_3) \approx 10$ MPa, all samples showed non-linear, concave-up stress-strain behaviour (Figure 2.3a). Low porosity samples ($\varphi_0 < 17.4\%$) showed relatively stiff, near linear stress-strain behaviour during active loading, up to the maximum differential stress imposed (50 MPa), with the apparent Young's moduli (E_a) ranging from 18.4 to 20.2 GPa. These samples showed compaction throughout active loading (*i.e.* $\Delta\varphi_t < 0$; Figure 2.3b). During each relaxation stage, the differential stress decreased by typically 1 – 2 MPa, while the total axial strain increased slightly (Δe_t = 0.005 to 0.015%) and the total porosity change ($\Delta\varphi_t$) remained approximately constant. After unloading, the final inelastic axial strains ($(e_i)_{fin}$ ~0.1%; Table 2.1), were slightly greater than the final inelastic porosity changes ($(\Delta\varphi_i)_{fin}$ ~0.0%).

Intermediate porosity samples ($17.4\% \leq \varphi_0 < 21.6\%$) showed similar behaviour to the above (Figure 2.3a), but were generally less stiff and their behaviour was less reproducible, with more total axial strain occurring in Sw13a (φ_0 = 17.4%) and Sg10a (φ_0 = 18.0%), than in Sw02a (φ_0 = 19.9%), and Sg09b (φ_0 = 17.7%). During active loading, most stress-strain curves showed near-linear, to just concave-down behaviour at $(\sigma_1 - \sigma_3) > 10$ MPa. Values for E_a ranged from 13.2 to 19.1 GPa. All intermediate porosity samples showed compaction throughout active loading (Figure 2.3b). However, at values of differential stress close to the maximum differential stress imposed, Sg10a showed less compaction with increasing axial strain than was observed at lower differential stresses. During the relaxation stages, the differential stress decreased by 2 - 8 MPa. For each relaxation stage, the increase in total axial strain amounted to 0.01 - 0.07% (Figure 2.3a), while compaction was observed (-0.01 to -0.06%; Figure 2.3b). After unloading, $(e_i)_{fin} \approx -(\Delta\varphi_i)_{fin}$, *i.e.* the final inelastic axial strains and porosity changes were in the range of 0.1 to 0.3%, and -0.1 to -0.3%, respectively (see Figure 2.3b).

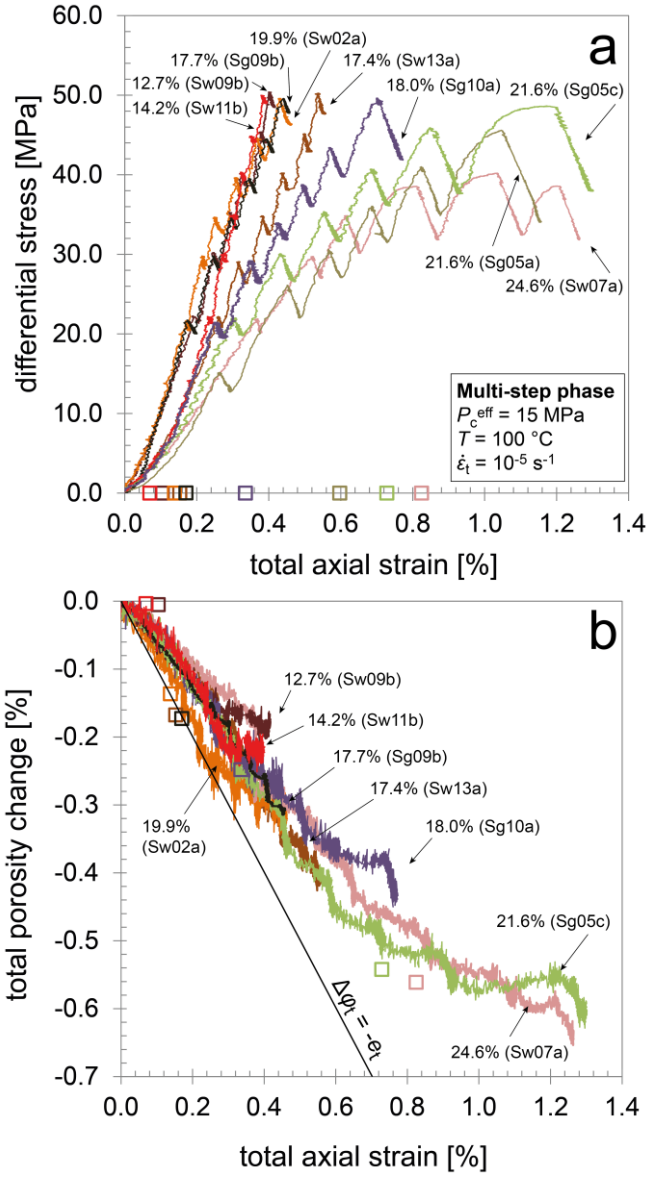

Figure 2.3 a) Differential stress and **b)** total porosity change ($\Delta\varphi_t$) versus total axial strain (e_t) data obtained from the multi-step phase of the incremental axial loading, plus stress relaxation experiments. Initial porosity (φ_0) values are indicated. Samples with high initial porosity show more total axial strain (see a) and compaction ($\Delta\varphi_t < 0$; see b) than samples with low initial porosity. Open square symbols indicate the final inelastic axial strain $(e_i)_{fin}$ and final inelastic porosity change $(\Delta\varphi_i)_{fin}$, determined after unloading (Table 2.1). For Sg05a, the total porosity change was not determined.

High porosity samples ($\varphi_0 \geq 21.6\%$) showed more total axial strain (Figure 2.3a) and total porosity change (Figure 2.3b) than lower porosity samples during individual active loading increments. At $(\sigma_1 - \sigma_3) > 10$ MPa, near-linear, to mildly concave-down stress-strain behaviour was seen during active loading, with E_a ranging from 7.6 to 9.4 GPa. Highly concave-down stress-strain behaviour was observed beyond differential stresses of 44 MPa (Sg05a), 45 MPa (Sg05c) and 38 MPa (Sw07a). Beyond these stresses, samples showed strain hardening at a decreasing rate, towards a peak strength of 40 to 49 MPa at $e_t \approx 1\%$ (Figure 2.3a). The target differential stress of 50 MPa could not be achieved. In these samples, the rate of total porosity change with total axial strain (*i.e.* the slope in Figure 2.3b) decreased with increasing axial strain, becoming even dilatant at the highest axial strains reached (Sg05c). During the relaxation stages, the differential stress decreased from 2 – 12 MPa. The total axial strain accumulated per relaxation stage ranged from 0.02 to 0.10%, while the total porosity change per stage constituted -0.04 to -0.07%. Upon unloading, $(e_i)_{fin} > -(\Delta\varphi_i)_{fin}$, *i.e.* the final inelastic axial strains were in the range of 0.7 to 0.8%, while the final inelastic porosity changes were approximately -0.5%.

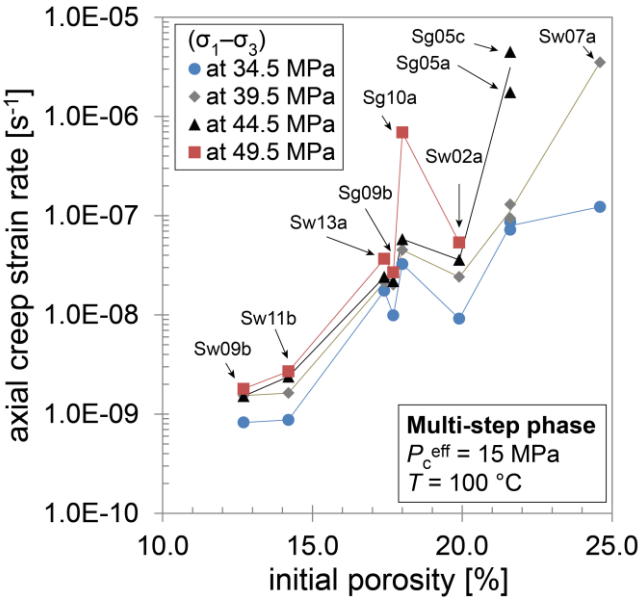

Figure 2.4 Axial creep strain rate versus initial porosity data obtained during stress relaxation at the differential stresses shown, in the multi-step phase of the present experiments. Axial creep strain rates tend to increase with initial porosity and differential stress. Note the increase in sensitivity of creep strain rate to differential stresses at values ≥ 39.5 MPa, and porosities of 18.0% (Sg10a) and those ≥ 21.6% (Sw07a, Sg05a and Sg05c). The total axial strains corresponding to each data point are visible in Figure 2.3a.

For each sample tested in the multi-step phase, the axial creep strain-rate ($\dot{\varepsilon}_{cr}$) during stress relaxation was determined at differential stresses of 34.5, 39.5, 44.5 and 49.5 MPa. The results are plotted against initial porosity (φ_0) in Figure 2.4. Generally, $\dot{\varepsilon}_{cr}$ increased with increasing initial porosity and differential stress. At a constant differential stress of 34.5 MPa, an absolute increase in φ_0 of 5% resulted in an increase of $\dot{\varepsilon}_{cr}$ of about an order of magnitude. At $\varphi_0 \leq 17.7\%$, an increase in ($\sigma_1 - \sigma_3$) of 5 MPa resulted in an increase of $\dot{\varepsilon}_{cr}$ by only a factor of 1.2 – 2. However, the sensitivity of $\dot{\varepsilon}_{cr}$ to ($\sigma_1 - \sigma_3$) increased markedly at higher φ_0 and ($\sigma_1 - \sigma_3$). Indeed, our sample with $\varphi_0 = 18.0\%$, and all samples with $\varphi_0 \geq 21.6\%$ showed an increase in $\dot{\varepsilon}_{cr}$ of more than an order of magnitude after a 5 MPa stress increase at differential stresses ≥ 39.5 MPa (Sw07a), 44.5 MPa (Sg05a and Sg05c), or 49.5 MPa (Sg10a). At these differential stresses, the corresponding total axial strains fell in the range of 0.6 to 0.8% (Figure 2.3a).

2.5.2 Microstructural data

2.5.2.1 Undeformed samples

Examples of BSE micrographs obtained from undeformed Slochteren sandstone with low (φ_0 = 12.7%; Sw09) and high porosity (φ_0 = 24.6%; Sw07), and corresponding grain maps are presented in Figure 2.5. The quantitative textural data obtained for our samples are described in detail in the Appendix 2.A2. In general terms, individual samples showed mean equivalent grain radii of quartz and feldspar grains in the range of 30 to 110 µm (Appendix 2.A2). These grains were sub-rounded, and slightly elongated in shape, with a mean aspect ratio of 1.7. Both quartz and feldspar grains showed indentations at grain-to-grain contacts, suggesting that intergranular pressure solution was active prior to gas production (Figure 2.5). Data on crack densities (mean number of cracks per grain) measured in the undeformed samples are given in Table 2.3. Crack densities measured along gridlines parallel to the coring direction ($CD_{\parallel}$) ranged from 0.03 to 0.14 per grain, while those measured along lines perpendicular to the coring direction ($CD_{\perp}$) fell within a similar range of 0.05 to 0.11 per grain. Within these ranges, a clear trend between the crack density and the initial sample porosity was lacking, although the highest values were observed in one of our high porosity samples Sg05 (φ_0 = 21.6%). The observed similar values of $CD_{\parallel}$ versus $CD_{\perp}$ imply a lack of preferred crack orientation (Table 2.3).

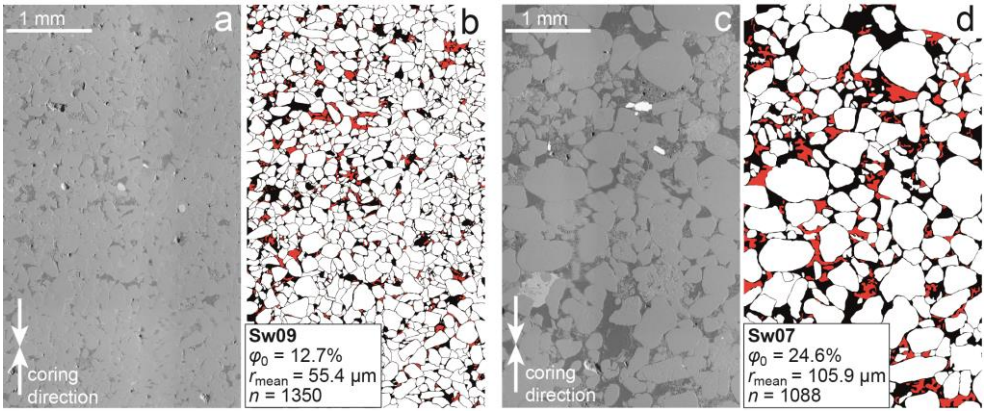

Figure 2.5 BSE micrographs of undeformed Slochteren sandstone. **a)** Micrograph of one of our low porosity samples (φ_0 = 12.7%, Sw09), and **b)** the corresponding grain map used for quantitative analysis of textural features (Appendix 2.A2). Grains and porosity are indicated respectively in white and black, while clay minerals are indicated in red. Values of the mean equivalent grain radius (r_{mean}), and the number of grains analyzed (n) are indicated. **c)** Micrograph of one of our high porosity samples (φ_0 = 24.6%, Sw07), and **d)** the corresponding grain map.

Table 2.3 Intra/transgranular crack density (CD) data of BSE micrographs of undeformed and deformed samples, using the line intercept method in a direction parallel (∥), or perpendicular (⊥) to the coring direction, and/or to σ_1.In each micrograph, ~ 400 grains were analysed. Crack density analysis was not performed on sample Sg05c.

undeformed				*deformed*		
Sample	φ_0	$CD_{\parallel}$	$CD_{\perp}$	Sample	$CD_{\parallel}$	$CD_{\perp}$
	[%]	# per grain	# per grain		# per grain	# per grain
Sw09	12.7	0.08	0.10	Sw09b	0.08	0.11
Sw11	14.2	0.03	0.06	Sw11b	0.03	0.08
Sw13	17.4	0.03	0.05	Sw13a	0.05	0.06
Sg09	17.7	0.09	0.12	Sg09b	0.06	0.11
Sg10	18.0	0.09	0.10	Sg10a	0.17	0.32
Sw02	19.9	0.06	0.07	Sw02a	0.13	0.10
Sg05	21.6	0.14	0.11	Sg05a	0.32	0.63
Sw07	21.6	0.07	0.09	Sw07a	0.28	0.72

2.5.2.2 Deformed samples

Where observed in our samples, brittle deformation localized near (within ~15 mm) the top and bottom of each sample. Therefore, the present microstructural analysis and crack density determination is performed within regions measuring 5 – 15 mm from the top of each sample. For these regions, BSE micrographs of microstructures recovered from deformed samples Sw11b, Sw13a, Sg10a and Sw07a, having porosities of 14.2, 17.4, 18.0 and 24.6% respectively, are shown in Figure 2.6. Crack density data obtained for all deformed samples (except Sg05c) are listed in Table 2.3, where they are compared with the data for the equivalent undeformed material. In all deformed samples studied, intra- and transgranular cracks (indicated by white arrows in Figure 2.6) typically emanated from grain-to-grain contacts. In all low porosity (φ_0 < 17.4%) samples (*e.g.* Sw11b, Figure 2.6a) and all intermediate porosity (17.4% ≤ φ_0 < 21.6%) samples, except Sg10a (*e.g.* Sw13a, Figure 2.6b), mean crack densities were low, and similar to those seen in their undeformed counterparts (Table 2.3). By contrast, intermediate porosity sample Sg10a (Figure 2.6c), and all high porosity samples ($\varphi_0 \geq 21.6\%$; *e.g.* Sw07a; Figure 2.6d) showed a crack density that was 2 to 8 times higher than obtained in their undeformed counterparts. In these samples, most of the observed cracks were orientated sub-parallel to the compression direction, *i.e.* $CD_{\perp} > CD_{\parallel}$ (Table 2.3). In some grains, cracking was pervasive, resulting in triangular crushed zones developing at grain-to-grain contacts (*e.g.* inset, Figure 2.6d). None of our deformed samples showed any evidence for the operation of intergranular pressure solution beyond pressure solution features already present in the starting material (Figure 2.5).

Figure 2.6 (Figure on next page) BSE micrographs of post-deformation microstructures. White arrows indicate intra/transgranular cracks. In **a)** low porosity samples (*e.g.* Sw11b; φ_0 = 14.2%) and **b)** intermediate porosity samples (*e.g.* Sw13a; φ_0 = 17.4%), these are only sporadically observed, except in the case of **c)** intermediate porosity sample Sg10a (φ_0 = 18.0%), which shows abundant intra/transgranular cracks. **d)** Micrograph of high porosity sample Sw07a, showing abundant intra/transgranular cracks. The inset depicts two grains showing pervasive crushing at the grain contact. Where observed, intra/transgraular cracks emanate from grain-to-grain contacts, and tend to be orientated sub-parallel to the main compressive axis (σ_1). Final inelastic axial strains $(e_i)_{fin}$ and final inelastic porosity changes $(\Delta\varphi_i)_{fin}$ developed during the multi-step phase are indicated on the left of the micrographs.

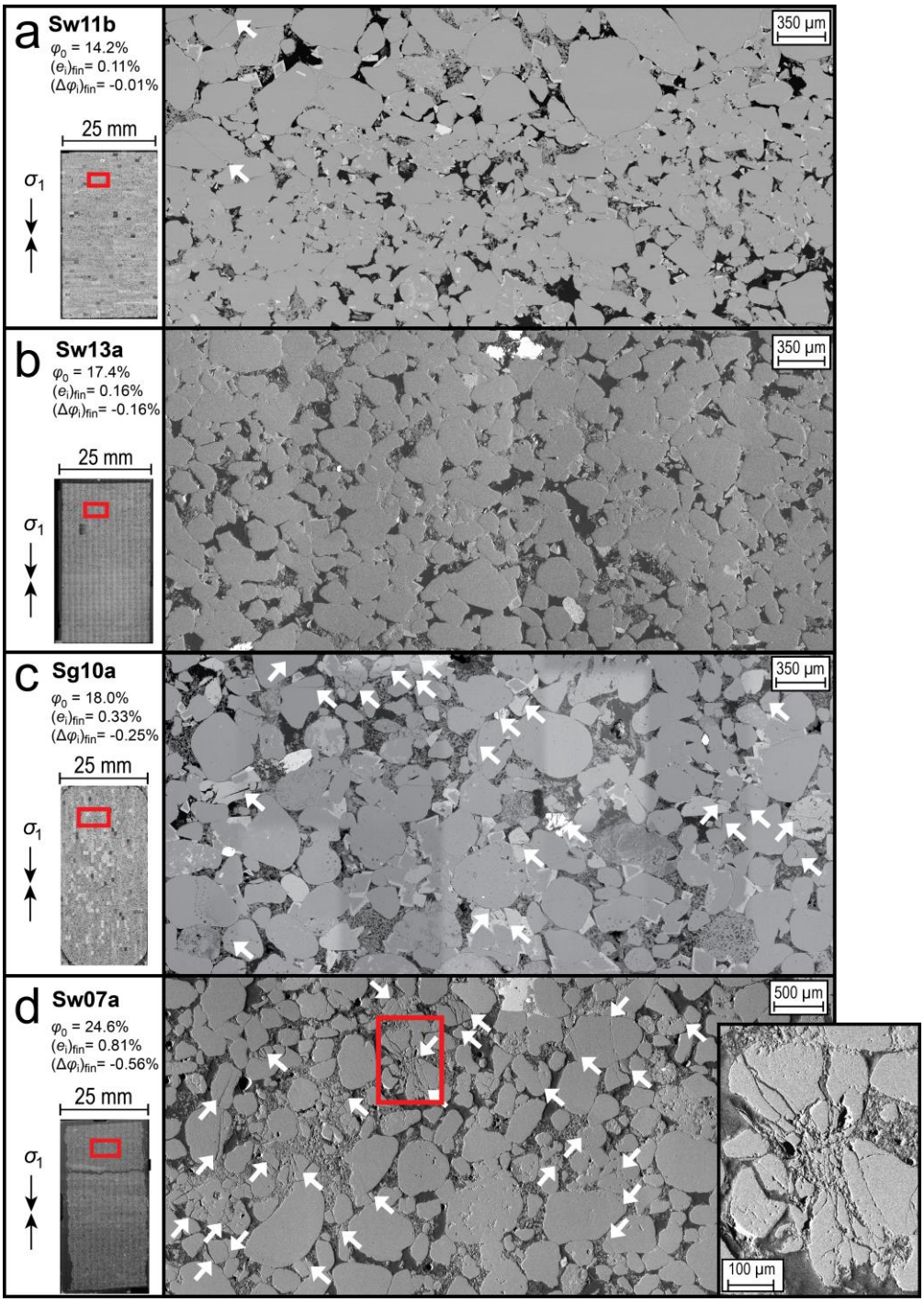

Figure 2.6 (Caption on previous page)

2.6 Discussion

Incremental axial loading plus stress-relaxation experiments on Slochteren sandstone have shown that inelastic deformation played a significant role in all samples, during both the *in-situ* conditioning and the multi-step phases, contributing to 0.1 – 0.8% of inelastic axial strain, versus ~ 0.3 – 0.6% of elastic axial strain, in each phase (Table 2.1). Hence, at the end of each phase, the final inelastic strains were similar in magnitude to the elastic component. During the multi-step phase, a substantial part of this inelastic strain represented time-dependent deformation ($(e_{cr})_{fin} \approx 0.1 – 0.7\%$; Table 2.1), accumulated during the stress relaxation stages (*i.e.* 6 days in total). In particular, samples with high initial porosity ($\varphi_0 \geq 21.6\%$), showed pronounced inelastic deformation (Figure 2.3) and marked acceleration of axial creep strain-rates during relaxation at differential stresses above ~ 41 ± 4 MPa (Figure 2.4). For the initial porosities and stress conditions explored in this study, the total axial strains (0.4 to 1.3%) and total porosity changes (-0.2 to -0.7%) measured were small, and are not expected to result in significant changes in permeability or wave propagation properties. However, given the substantial Groningen reservoir thickness (100 – 200 m), these small strains may lead to significant reservoir compaction of decimeters, and hence potentially to fault reactivation and seismicity [*Bourne et al.*, 2014; *Buijze et al.*, 2017; *Spiers et al.*, 2017]. In addition, the partitioning of inelastic versus elastic strain directly influences the energy budget available within the reservoir interval for seismicity [*Cooke and Madden*, 2014].

In the following, we will first discuss potential causes for the observed inelastic strain development during the *in-situ* conditioning phase of our experiments. We go on to discuss the magnitudes of inelastic versus elastic deformation, at various differential stresses (*cf.* depletion) imposed in the multi-step phase, and any effect on these of initial porosity and strain rate. The microphysical mechanisms controlling inelastic deformation in the multi-step phase and specifically during relaxation stages are discussed, and we evaluate the effects of initial porosity, loading or strain-rate, and progressively increasing strain on yield and yield envelope behaviour. Finally, we apply our results to assess the effects of elastic versus inelastic strain partitioning in the Slochteren sandstone reservoir during production of the Groningen field on the evolution *in-situ* stresses, subsidence and the elastic energy available to drive induced seismicity.

2.6.1 Inelastic strain development during in-situ conditioning

During the *in-situ* conditioning phase of our experiments (Figure 2.2), the final inelastic axial strain developed in our samples ranged from 0.1 to 0.8%, versus 0.2 to 0.4% of elastic axial strain, while the final inelastic porosity change ranged from -0.1 to -0.4%,

versus -0.1 to -0.2% of elastic porosity change (Table 2.1). Initial hysteresis in stress-strain behaviour is well known in a wide range of materials [*e.g. Darling*, 2004; *Guyer*, 2006], and in sandstone is typically attributed to the closure of, and semi-recoverable displacements along pre-existing cracks [*David et al.*, 2012; *Walsh*, 1965]. Such cracks may have been present *in-situ*, or have been introduced upon depressurization during coring [*Holt et al.*, 2000], via core drying during storage [*Santarelli and Dusseault*, 1991], or during sample preparation. Nonetheless, the fully recoverable stress-strain behaviour seen during stress-cycling (Figure 2.2a) at stress conditions simulating the pre-depleted *in-situ* stress state of the Slochteren sandstone, suggests that by imposing these conditions in the *in-situ* conditioning phase, any pre-existing damage causing inelastic strain was largely removed.

2.6.2 Inelastic versus elastic deformation during the multi-step phase

2.6.2.1 Magnitude: effects of porosity and strain rate

To fully characterize the stress versus inelastic and elastic strain behaviour during the multi-step phase, and the effects on these behaviours of initial porosity and strain rate, we must quantify: 1) the time-independent (instantaneous) inelastic axial strain developed during active loading (e_i^{inst}), 2) the time-dependent inelastic axial (creep) strain developed during stress relaxation stages (e_{cr}) and 3) the sum of these, *i.e.* the cumulative inelastic axial strain ($e_i^{\Sigma} = \Sigma e_i^{inst} + \Sigma e_{cr}$). In our analysis, e_i^{inst} was calculated by subtracting the linear (*i.e.* quasi-elastic, see *Bernabe et al.*, [1994]) part of the stress-strain curve, characterized by the apparent Young's modulus (E_a), from the total axial strain achieved in each active loading interval, using $e_i^{inst} = e_t - (\sigma_1 - \sigma_3)/E_a$. Values of E_a ranged from 7 to 20 GPa (Table 2.1), and typically decreased with increasing initial sample porosity [*cf. Chang et al.*, 2006]. Inelastic axial creep strain (e_{cr}) developing during relaxation stages was quantified using the methodology outlined by *Rutter & Mainprice* [1978]. Knowing e_i^{Σ}, the cumulative elastic axial strain (e_{el}^{Σ}) was calculated by subtracting the obtained cumulative inelastic axial strain from the total axial strain. The quantities $(e_i^{inst})_{max}$, $(e_{cr})_{max}$, $(e_i^{\Sigma})_{max}$ and $(e_{el}^{\Sigma})_{max}$, tabulated in Table 2.1, refer respectively to the maximum instantaneous inelastic axial strain and maximum axial creep strain, and the maximum cumulative inelastic and elastic axial strains, determined by summing up all preceding contributions at the end of the multi-step phase of each experiment. This means that $(e_i^{\Sigma})_{max}$ and $(e_{el}^{\Sigma})_{max}$ should be equal to respectively the final inelastic axial strain $(e_i)_{fin}$ and the final elastic axial strain $(e_{el})_{fin}$, which were determined independently from comparison of the piston position before and after the multi-step phase (Table 2.1).

Upon achieving the highest differential stress in any active loading stage, subsequent

relaxation of this differential stress was accompanied by progressively developing creep strains, while the creep strain rate decreased (Figures 2.2a and c; see also: *Rutter and Mainprice*, [1978]). This implies that the magnitude of inelastic strain achieved after imposing a given differential stress must be strain-rate dependent. To investigate this rate-dependence, we employ our relaxation data obtained in the multi-step phase to approximate the expected stress versus inelastic and elastic strain curves, in the case that our samples were continuously compressed (*i.e.* in the absence of relaxation stages) at reference strain rates of $\dot{\varepsilon}_t \sim 10^{-5}$ s^{-1}, or at $\dot{\varepsilon}_t \sim 10^{-9}$ s^{-1}, under the present experimental conditions. To that end, we determined e_{el}^{Σ} and e_i^{Σ} at $\dot{\varepsilon}_{cr} \sim 10^{-5}$ s^{-1} and $\dot{\varepsilon}_{cr} \sim 10^{-9}$ s^{-1}, and plotted these values versus the differential stress attained at the end of each preceding active loading stage (*i.e.* at the onset of relaxation) in Figure 2.7.

Before proceeding with our analysis, we note that the resultant $(\sigma_1 - \sigma_3)$ versus e_{el}^{Σ} curves determined at $\dot{\varepsilon}_{cr} \sim 10^{-5}$ s^{-1} (Figure 2.7a) are lower bounds for the expected elastic behaviour at the reference strain rate of $\dot{\varepsilon}_t \sim 10^{-5}$ s^{-1} (*i.e.* least compliant end-members), since creep deformations developing during the preceding relaxation stages have partly dissipated the accumulated elastic strain. For the expected inelastic behaviour at these reference strain rates, the $(\sigma_1 - \sigma_3)$ versus e_i^{Σ} curves determined at $\dot{\varepsilon}_{cr} \sim 10^{-5}$ s^{-1} (Figure 2.7b) represent upper bounds (*i.e.* most compliant end-members), as they include creep strains that have developed during preceding relaxation stages at creep rates lower than 10^{-5} s^{-1}. By contrast, the curves depicted in Figure 2.7b ($\dot{\varepsilon}_{cr} \sim 10^{-5}$ s^{-1}), are lower bounds for the inelastic behavior expected at the reference strain rate of $\dot{\varepsilon}_t \sim 10^{-9}$ s^{-1}, since e_i^{Σ} increases with decreasing strain rate. An upper bound is given by the differential stresses and strains obtained at $\dot{\varepsilon}_{cr} \sim 10^{-9}$ s^{-1}. Indeed, more realistic inelastic and elastic behaviour in the case of continuous loading at $\dot{\varepsilon}_t \sim 10^{-9}$ s^{-1} is expected to fall in between these upper and lower bounds, such as given by curves describing the $(\sigma_1 - \sigma_3)$ at the end of each active loading stage, versus e_{el}^{Σ} (Figure 2.7c), and e_i^{Σ} (Figure 2.7d), determined at $\dot{\varepsilon}_{cr} \sim 10^{-9}$ s^{-1}.

From Figure 2.7 we observe the following five key points. First, both e_{el}^{Σ} and e_i^{Σ} increased with increasing initial porosity. Second, for both reference strain rates investigated, e_i^{Σ} increased non-linearly with differential stress (Figure 2.7b,d). Specifically, our samples exhibited continuous inelastic strain hardening, at decreasing hardening rates, except in the highest porosity sample (φ_0 = 24.6%, Sw07a), which showed minor inelastic strain softening at $e_i^{\Sigma} > 0.6\%$. Third, for the reference strain rate of ~10^{-9} s^{-1}, inelastic strain was measured at all corresponding differential stresses (*i.e.* $e_i^{\Sigma} > 0$, at all stresses plotted in Figure 2.7d), even during the first relaxation stage at $(\sigma_1 - \sigma_3) \sim 22$ MPa. Fourth, in our low to intermediate porosity samples ($\varphi_0 \leq 19.9\%$), both the cumulative inelastic and elastic strains are virtually

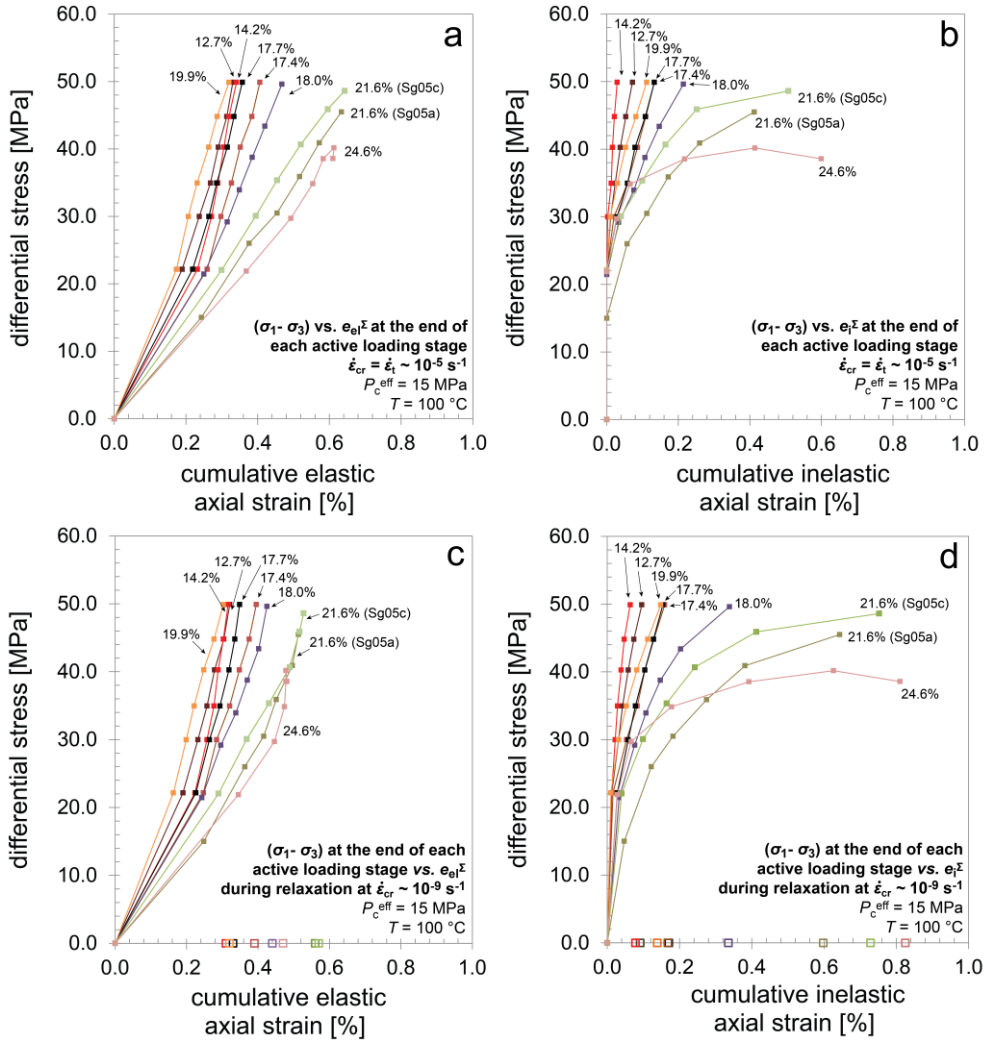

Figure 2.7 a) Plot showing differential stress ($\sigma_1 - \sigma_3$) versus cumulative elastic axial strain (e_{el}^{Σ}) data obtained in the multi-step phase at the end of each active loading stage where $\dot{\varepsilon}_{cr} \approx \dot{\varepsilon}_t \approx 10^{-5}$ s^{-1}. Initial porosities (φ_0) of individual curves are indicated. **b)** Differential stress versus cumulative inelastic axial strain (e_i^{Σ}) data, obtained at $\dot{\varepsilon}_{cr} \sim 10^{-5}$ s^{-1}. These curves show non-linear strain-hardening trends, which are more pronounced with increasing φ_0. **c)** Curves showing the ($\sigma_1 - \sigma_3$) at the end of each active loading stage versus e_{el}^{Σ} data obtained at $\dot{\varepsilon}_{cr} \sim 10^{-9}$ s^{-1}. At this strain rate, and ($\sigma_1 - \sigma_3$) > 30 MPa, high porosity samples show less elastic strain than observed at $\dot{\varepsilon}_{cr} \sim 10^{-5}$ s^{-1}. Final elastic axial strains $(e_{el})_{fin}$ are indicated by open square symbols. **d)** Curves showing ($\sigma_1 - \sigma_3$) at the end of each active loading stage versus e_i^{Σ} obtained during relaxation stages at $\dot{\varepsilon}_{cr} \sim 10^{-9}$ s^{-1}. At these lower reference strain rates, e_i^{Σ} is measured even in the first relaxation stage at ($\sigma_1 - \sigma_3$) ~ 22 MPa. Final inelastic axial strains $(e_i)_{fin}$ are indicated by open square symbols.

independent of the reference strain rate (Figure 2.7). Fifth, in our high porosity samples ($\varphi_0 \geq$ 21.6%), e_i^{Σ} ranged from 0.4 to 0.6%, measured at $\dot{\varepsilon}_{cr} \sim 10^{-5}$ s^{-1} (Figure 2.7b), and increased to 0.6 to 0.8%, measured at $\dot{\varepsilon}_{cr} \sim 10^{-9}$ s^{-1} (Figure 2.7d), while the cumulative elastic strain was 0.6% at $\dot{\varepsilon}_{cr} \sim 10^{-5}$ s^{-1} (Figure 2.7a), and decreased to 0.4 to 0.5%, at $\dot{\varepsilon}_{cr} \sim 10^{-9}$ s^{-1} (Figure 2.7c).

The above-noted sensitivity of the cumulative elastic and inelastic axial strains to initial porosity is similar to the porosity dependence of elastic and inelastic strains observed in previous triaxial tests on Slochteren sandstone [*Hol et al.*, 2015a, 2018; *Schutjens et al.*, 1995], and other types of sandstone [*e.g. Wong et al.*, 1997; *Wong and Baud*, 2012]. Time-, hence rate-dependent inelastic deformation behaviour has been documented previously [*Brantut et al.*, 2013; *Heap et al.*, 2009, 2015], although often at higher differential stresses ($[\sigma_1 - \sigma_3]$ = 50 to 400 MPa) than relevant for upper crustal hydrocarbon (or hydrothermal) fields, such as the Groningen gas field ($[\sigma_1 - \sigma_3] \leq$ 50 MPa). In addition, our data show an apparent rate-dependence of the stress versus cumulative elastic axial strain curves (Figure 2.7a and c). This is due to the fact that during relaxation, elastic strain stored in the sample and apparatus is partly converted into time-dependent deformation [*Rutter and Mainprice*, 1978]. In the case of our high porosity samples, at ($\sigma_1 - \sigma_3$) > 30 MPa, substantial stress relaxation of 5 – 12 MPa was observed in each relaxation stage (Figure 2.3a), leading to the conversion into permanent strain of most, or even all elastic strain accumulated in the foregoing active loading stage (Figure 2.7d). The implications of the time-dependent deformation behavior observed in our experiments are that conventional stress-strain curves obtained in loading at constant strain- or loading rate will depend on the strain- or loading rate imposed, and that the strain represented will always consist of an elastic and inelastic component.

2.6.2.2 Effect of porosity on inelastic deformation mechanisms

As discussed in the introduction, inelastic deformation can be caused by intergranular (grain boundary) cracking, intergranular slip, intra/transgranular cracking, and intergranular pressure solution (IPS). The microstructures of our deformed samples (Figure 2.6) showed no evidence that IPS played a role in our experiments. Indeed, assuming a spherical grain radius of 100 µm, φ_0 = 20%, and conditions similar to those imposed in our experiments (σ_1= 65 MPa, P_p = 35 → 0.1 MPa, and T = 100 ˚C), previous work on the kinetics of IPS in quartz [*Dewers and Hajash*, 1995; *Niemeijer et al.*, 2002; *Van Noort et al.*, 2008; *Schutjens*, 1991] suggests axial creep strain-rates by IPS of approximately 10^{-13} s^{-1} at small reductions of P_p, increasing to 10^{-12} s^{-1} at full depletion of the field. By comparing these strain rates with the

creep rates > 10^{-10} s^{-1} obtained in our experiments (Figure 2.4), we infer that IPS did not play a role in controlling inelastic strain accommodation in our experiments. However, the rates obtained for IPS fall within one order of magnitude from the strain rates derived from the reservoir compaction and surface subsidence data obtained in the Groningen field (10^{-12} s^{-1}) [*NAM*, 2015]. Therefore, and given the uncertainties on the existing rate data for IPS [*e.g. Spiers et al.*, 2004], we cannot completely exclude IPS from playing a role in the field.

However, at least for shorter time-scales, numerous laboratory studies have shown that low-temperature (T < 150˚C) inelastic deformation of sandstone is accommodated by a combination of grain scale cracking, and grain boundary slip [*Baud et al.*, 2000; *Brantut et al.*, 2013; *Heap et al.*, 2009, 2015; *Menéndez et al.*, 1996; *Wong and Baud*, 1999, 2012]. Moreover, previous studies, including stress-cycling data [*Shalev et al.*, 2014], microstructural analyses of lab-deformed samples [*Bernabe et al.*, 1994; *DiGiovanni et al.*, 2007; *Ord et al.*, 1991], acoustic emission data [*David et al.*, 2001; *Menéndez et al.*, 1996], and discrete element modelling [*Estrada et al.*, 2010b, 2010a; *Shen et al.*, 2016] suggest that, for a wide range of sandstones, intergranular cracking plus intergranular slip are the dominant deformation mechanisms accommodating any inelastic strains in the earlier stages of compression, *i.e.* at low stresses. These intergranular processes may initiate at grain contacts that are particularly weak (uncemented, poorly sutured, or clay-coated), and/or favorably oriented with respect to the principal stresses. When grain-contact stresses become sufficiently high, pervasive intra- or transgranular cracking begins to occur. The present experiments on low and intermediate initial porosity samples (φ_0 < 21.6%) showed small inelastic axial strains developing throughout compression (up to 0.1 – 0.3%; Figure 2.7d), whereas the corresponding microstructures showed little or no increase in crack density per grain (Table 2.3). By contrast, in samples with a high initial porosity ($\varphi_0 \geq$ 21.6%), significantly larger inelastic strains of 0.6 to 0.8% were observed at ($\sigma_1 - \sigma_3$) > 30 MPa (Figure 2.7d), while the micrographs of these samples revealed a marked increase in the density of intra/transgranular cracks (Table 2.3). Furthermore, samples showing increased crack densities yielded $CD_{\perp} > CD_{\parallel}$, implying a preferred orientation of cracks parallel to the main compression direction σ_1. Therefore, it is likely that the increase in e_i and $\Delta\varphi_i$ at $\varphi_0 \geq$ 21.6% is related to the observed increased role of intra/transgranular cracking. Thus, we infer that the mechanisms controlling inelastic strain accommodation in the Slochteren sandstone, under the present experimental conditions, involves mainly intergranular cracking plus intergranular slip at low porosity, with an increasingly important role being played by intra/transgranular cracking with increasing initial porosity. However, how intra/transgranular cracking contributes to strain is less clear-cut. Intra/transgranular cracks may contribute to

strain by either 1) pervasive grain contact fragmentation (*e.g.* Figure 2.6d, inset), combined with fragment rearrangement [*Zhang et al.*, 1990], or 2) (partial) loss of the load-bearing capacity of a grain, leading to increased loading of the surrounding grains, which in turn may trigger further grain-scale deformation [*Brzesowsky et al.*, 2014b], in a larger, potentially localizing volume. Resolving how such processes influence strain and strain localization would require quantitative microstructural investigation of pre- and post-test samples, including microstrain analysis and/or particle tracking. We reserve this for future work.

2.6.2.3 Effect of porosity on the rate-dependence

Predictions of induced compaction and seismicity in sandstone reservoirs, in the context of oil, gas or geothermal energy exploitation, require constraints on the amount of both time-independent (instantaneous) and time-dependent compaction [*Hettema et al.*, 2002; *Mallman and Zoback*, 2007; *NAM*, 2016; *Van Thienen-Visser et al.*, 2015a]. In the present experiments (6 days in total), most of the measured inelastic strain developed during the 24 hours relaxation intervals, so is time-dependent (0.1 - 0.7%; see Table 2.1), with relatively little inelastic axial strain accumulating instantaneously, in the brief periods of active loading (0.1 – 0.2%). We note that the importance of time-independent versus time-dependent deformation is defined by the time-scale of observation, and time-dependent deformation observed over the present lab time-scales (days), may therefore be considered to be time-independent over time-scales relevant for reservoir production (decades). However, longer-term creep tests performed on Slochteren sandstone have demonstrated ongoing deformation after a period of several months, yielding very low strain rates of ~10^{-11} s^{-1} [*Hol et al.*, 2015b, 2015a]. To quantify the importance of time-dependent deformation over reservoir production time-scales, a mechanical model is required that is based on the physical processes driving time-dependent deformation in sandstone. It is therefore important to explore what mechanisms controlled time-dependent deformation in our experiments, in order to assess their influence under both lab and field conditions.

During relaxation intervals in the present experiments, the axial creep strain-rate decreased with decreasing differential stress (Figure 2.2c). The dependence of creep strain-rate on differential stress in sandstones is often described using an exponential relation [*Brantut et al.*, 2013, 2014, *Heap et al.*, 2009, 2015; *Rijken*, 2005], of the form:

$$\dot{\varepsilon}_{cr} \propto \exp(B\,[\sigma_1 - \sigma_3]) \qquad \text{(Eq. 2.2)}$$

where B is an empirical constant whose magnitude is often linked to the process, or

processes operating during creep [*Brantut et al.*, 2013, 2014, *Heap et al.*, 2009, 2015]. For instance, in sandstone experiments where creep has been associated with stress-corrosion cracking, *B* is typically in the range of 0.1 – 1.0 [*Brantut et al.*, 2013; *Heap et al.*, 2009, 2015].

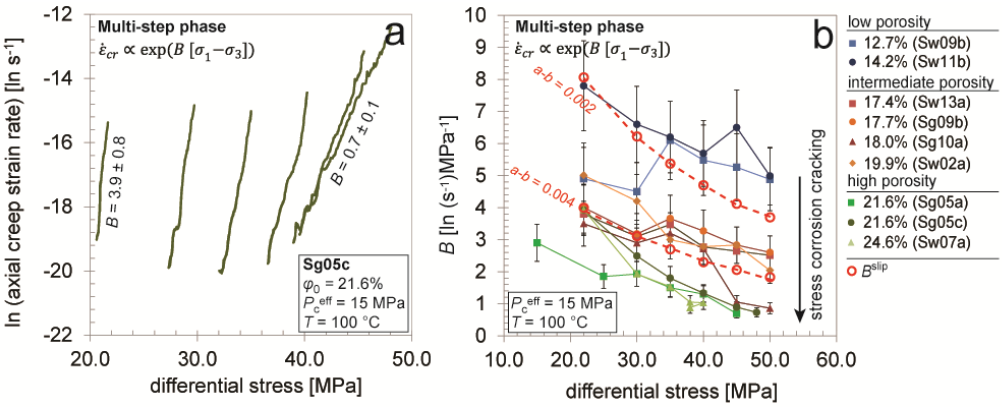

Figure 2.8 a) Plot showing the natural logarithm of our axial creep strain rate data versus differential stress, obtained on sample Sg05c (φ_0 = 21.6%) during stress relaxation stages of the multi-step phase. To describe the stress-sensitivity of the axial creep rates we assume an exponential relation of the form: $\dot{\varepsilon}_{cr} \propto \exp(B\,[\sigma_1 - \sigma_3])$. The stress sensitivity *B*, determined by linear regression of $\ln(\dot{\varepsilon}_{cr})$ versus (σ_1 - σ_3) data, decreases with increasing differential stress. **b)** Plot showing exponent *B* versus differential stress data, obtained for each relaxation stage within the multi-step phases, of all samples. *B* decreases with increasing differential stress and porosity. Error bars resultant from linear regression are indicated. The exponent B^{slip}, describing the rate-dependency of time-dependent intergranular slip was determined using previously described rate-and-state friction parameters ([*a*-*b*] = 0.002 to 0.004) of unconsolidated Slochteren sandstone gouge material [*Hunfeld et al.*, 2017]. Since B^{slip} was similar to *B* values of our low and intermediate porosity samples, we infer that the creep accommodating mechanisms in these samples was predominantly rate-dependent intergranular slip, with an increasing role of stress-corrosion cracking with increasing porosity.

We determined *B* for each stress relaxation interval of the multi-step phase of our incremental axial loading plus stress-relaxation experiments, using linear regression of $ln\,(\dot{\varepsilon}_{cr})$ versus (σ_1 – σ_3) data, as shown for one of our high porosity samples (φ_0 = 21.6 %; Sg05c) in Figure 2.8a. The error obtained in *B* in the linear regression analysis is $\pm$10 - 20% of the determined value. For the complete set of experiments, the value obtained for *B* ranged from 0.7 to 8.4, and, generally, decreased with increasing differential stress and increasing initial porosity (Figure 2.8b). At the highest differential stresses imposed (40 – 50 MPa),

samples with $\varphi_0 \geq 21.6\%$, and sample Sg10a ($\varphi_0 = 18.0\%$) showed B values in the range of 0.7 – 0.9. These values are within the range previously described for creep associated with stress corrosion cracking [*Brantut et al.*, 2013; *Heap et al.*, 2009, 2015]. However, at lower differential stress and porosity, B was higher than typically described for stress corrosion cracking, suggesting that for these samples and conditions, a different mechanism controlled time-dependent deformation. Moreover, from their microstructure, most samples with $\varphi_0 <$ 21.6% (except Sg10a) were inferred to deform predominantly by intergranular cracking and slip, rather than by intra/transgranular cracking (Figure 2.6). Thus, in these samples, mixed intergranular cracking plus frictional slip seems the most likely mechanism controlling creep rates.

This hypothesis will now be analyzed further by examining the expected rate-dependency of frictional intergranular slip [see also: *Karner et al.*, 2005b]. Such a rate-dependency is widely documented in friction experiments performed on loose, granular gouge materials [*e.g. Scholz*, 2002]. It is measured experimentally by imposing direct or rotary shear deformation on a thin layer of gouge material, at constant effective normal stress (σ_n), while measuring the change of the steady state shear stress (τ), and hence of the friction coefficient ($\mu = \tau/\sigma_n$), upon a change in the sliding velocity (v). The resultant rate-dependency of μ is often expressed using the empirical rate-and-state friction (RSF) relation [*Marone*, 1998]:

$$\mu - \mu_0 = a \ln\left(\frac{v}{v_0}\right) + b \ln\left(\frac{v_0 \Omega}{D_c}\right) \qquad \text{(Eq. 2.3)}$$

where μ_0 is a reference friction coefficient, measured at a reference sliding velocity v_0, Ω is a state variable, here taken to be equal to $(d\Omega/dt - 1)(D_c/v)$ [following *Dieterich*, 1972, 1978], D_c is a characteristic sliding distance over which strength evolution takes place, and a and b are constants, reflecting the magnitude of the so-called direct and evolution effect on μ occurring after a stepwise change in sliding velocity. For changes in the steady-state friction resulting from a stepwise change in sliding velocity, this relation yields:

$$a - b = \frac{\mu_{ss} - \mu_0}{\ln\frac{v}{v_0}} \qquad \text{(Eq. 2.4)}$$

[*e.g. Marone*, 1998]. In recent direct-shear experiments performed at our laboratory on gouge material derived from Slochteren sandstone, under similar conditions to those imposed here

(T = 100˚C, effective normal stress σ_n = 40 MPa, pore fluid 4.4M NaCl brine), the steady-state friction coefficient μ was found to be 0.61 at v = 1 µm/s, while (a – b) ranged from 0.002 to 0.004 [*Hunfeld et al.*, 2017]. These values, combined with Equation 2.4 provide a description of the rate-dependence of the steady-state resistance offered by the Slochteren gouge to simulated fault slip.

This rate-dependence of bulk gouge friction can be related to intergranular friction in the gouge experiments and hence to grain boundary friction ($\tilde{\mu}$) in our sandstone experiments, using the microphysical model described by *Niemeijer and Spiers*, [2007] for frictional rate-dependence in granular aggregates (N-S model). Assuming that during relaxation intervals, strain is achieved by frictional sliding along intergranular interfaces that are already broken during the preceding piston advancement intervals, *i.e.* neglecting any effect of intergranular cohesion, then in the N-S model, μ is related to $\tilde{\mu}$ by:

$$\mu = \frac{\sin\Psi + \tilde{\mu}\cos\Psi}{cos\ \Psi - \tilde{\mu}\sin\Psi} \qquad \text{(Eq.2.5)}$$

where Ψ is the dilatancy angle, or the average grain contact angle over which slip occurs. Combining this with Equation 2.4 as shown in Appendix 2.A3, the stress-dependence of the creep strain-rate in the end-member case that creep of our sandstone samples is controlled by intergranular slip is given:

$$\dot{\varepsilon}_{cr}^{slip} \approx \dot{\varepsilon}_{cr,0}^{slip} \exp\left(\frac{1}{a-b}\left(\frac{(\sigma_1-\sigma_3)\sin(2\theta)}{(\sigma_1+\sigma_3)+(\sigma_1-\sigma_3)\cos(2\theta)} - \left(\frac{(\sigma_1-\sigma_3)\sin(2\theta)}{(\sigma_1+\sigma_3)+(\sigma_1-\sigma_3)\cos(2\theta)}\right)_0\right)\right) \qquad \text{(Eq.2.6)}$$

Here $\dot{\varepsilon}_{cr,0}^{slip}$ denotes the initial axial creep strain-rate immediately upon piston arrest and is equal to the axial strain-rate imposed during active loading (~10^{-5} s^{-1}). The angle θ is that between σ_1 and the normal to grain boundaries that are optimally orientated for slip, and is related to grain boundary friction through $2\theta = \tan^{-1}(-1/\tilde{\mu})$. In turn, $\tilde{\mu}$ is determined from the bulk gouge experiments and applying the N-S model to be 0.28, so that θ is equal to 52.8° (Appendix 2.A3). Using this value of θ and values of (a - b) of 0.002 and 0.004 [*Hunfeld et al.*, 2017], we employed Equation 2.6 to calculate $\dot{\varepsilon}_{cr}^{slip}$ for the same range of differential stress as imposed in our experiments (0 – 50 MPa). The stress-sensitivities of $\dot{\varepsilon}_{cr}^{slip}$ (B^{slip}) were then determined from linear regression of plots showing $\ln[\dot{\varepsilon}_{cr}^{slip}]$ versus differential stress (*cf.* Equation 2.2), at ($\sigma_1 - \sigma_3$) = 22, 30, 35 40, 45 and 50 MPa (Figure 2.8b).

From Figure 2.8b it is clear that the dependence of B^{slip} on differential stress obtained is similar to the stress-dependence of experimentally obtained B values. For (a - b) = 0.002, B^{slip} decreased from 8.0 at low differential stress, to 3.7 at high differential stress, while for (a - b) = 0.004, B^{slip} was 4.0 at low differential stress, decreasing towards 1.8 with increasing differential stresses. For each differential stress tested, these values of B^{slip} are roughly similar to the values of B obtained for our low (φ_0 = 12.7 and 14.2%) and intermediate porosity samples (φ_0 = 17.4 and 19.9%). For high porosities, B^{slip} was similar to the experimental B values only at the lowest differential stresses tested (22 MPa). At higher differential stresses, B values were lower than values of B^{slip}, where the lowest values of 0.7 to 1.0, measured at (σ_1 – σ_3) = 38 to 50 MPa fell within the range described for creep associated with stress-corrosion cracking (B = 0.1 – 1.0; *Heap et al.*, 2009, 2015; *Brantut et al.*, 2013]. Moreover, these high porosity samples showed a marked increase in crack density (Table 2.3). Thus, we infer that creep in our low and intermediate porosity samples was predominantly controlled by intergranular slip, while with increasing porosity, the contribution of stress-corrosion cracking within grains increased (*i.e.* intra- and transgranular crack growth and ultimate failure).We explain this inference by noting that for the range of stress conditions explored, grain contact stresses developing during compression of low porosity samples may not be sufficiently high to activate pervasive (intragranular) stress-corrosion cracking. Rather, in these samples, the relatively small creep strains measured (≤ 0.3%) are likely accommodated by intergranular slip, occurring at weakly cemented, weakly sutured, or clay-coated grain contacts, and/or those favorably oriented with respect to the principal stress axes.

2.6.3 Expanding yield envelope: effects of strain and strain-rate on inelastic deformation

Previous studies have characterized the onset of inelastic deformation in sandstone of a given porosity using a discrete yield criterion, assumed to be rate-insensitive [*Baud et al.*, 2004, 2006; *Menéndez et al.*, 1996; *Skurtveit et al.*, 2013; *Tembe et al.*, 2007; *Wong et al.*, 1997; *Wong and Baud*, 2012; *Zhang et al.*, 1990]. Typically, the yield point is determined as the point of departure from linear stress-strain behaviour, which is associated with the start of dilatancy at low mean effective stresses, and the start of enhanced compaction (in a mean effective stress P versus $\Delta\varphi_t$ plot) at high mean effective stresses [*Wong et al.*, 1997]. However, our axial loading plus stress relaxation experiments have demonstrated that inelastic strain develops at all differential stresses imposed, and for all porosities tested (Figure 2.7d). Such inelastic strains developing from the onset of compression have also been demonstrated during hydrostatic testing of Berea and Darley Dale sandstone [*Shalev et*

al., 2014]. Therefore, the above definition of discrete yielding does not adequately describe how inelastic deformation is accommodated in these sandstones. Rather, the continuous accumulation of inelastic strain in our samples, combined with the observed strain-hardening (Figure 2.7b, d) implies a yield envelope which expands continuously with each active loading (at $\dot{\varepsilon}_t \sim 10^{-5}$ s^{-1}) plus stress relaxation step [see also: *Wong et al.*, 1992; *Karner et al.*, 2003, 2005a; *Brzesowsky et al.*, 2014b; *Shalev et al.*, 2014]. Furthermore, the magnitude of inelastic strain was shown to increase with decreasing strain rate and increasing initial porosity (Figure 2.7b, d). Hence, the yield envelope for each sample must be one that expands with increasing inelastic strain, increasing loading or strain-rate and decreasing initial porosity.

To explain the continuous yielding observed throughout our experiments, we note that the bulk strength of a material is determined by its weakest component [*Brzesowsky et al.*, 2011, 2014b; *Diaz et al.*, 2003; *Lawn*, 1993; *Lu et al.*, 2002; *Weibull*, 1951]. In sandstone, the strength determining components are either the grains, or the intergranular grain contacts [*Cook et al.*, 2015; *Saidi et al.*, 2003; *Yin and Dvorkin*, 1994]. The strength of grains increases with grain size [*Borg et al.*, 1960; *Brzesowsky et al.*, 2011, 2014b; *Chuhan et al.*, 2002; *Hangx et al.*, 2010a]. Because of this grain size-dependency, the log-normal grain size distribution observed in our samples (Appendix 2.A2) will inherently result in distributed grain strength. If we assume that the strength of the grain contacts is also distributed, it follows that the weakest grains or grain contacts will fail even in the early, elastically dominated stages of compression, leading to small increments of inelastic strain [*Brzesowsky et al.*, 2014b; *Karner et al.*, 2003]. As the differential stress increases, larger numbers of grains or grain contacts will fail, resulting in an increasingly larger contribution to inelastic strain. This would lead to a non-linear increase of inelastic strain with increasing differential stress, such as observed in our experiments (Figure 2.7b, d).

2.7 Implications

2.7.1 Effect of elastic versus inelastic deformation on reservoir stress changes

Reducing the pore pressure in a reservoir from 35 MPa to 0.1 MPa will lead to an increase of the effective horizontal stress [*Zoback*, 2010]. Specifically, in the case of a poroelastic reservoir compacting under the generally assumed uniaxial strain conditions, and assuming $\nu = 0.15$ and $\alpha = 1$, the effective horizontal stress increases from 8 MPa to ~15 MPa (Equation 2.1). We assumed such a poroelastic stress evolution in choosing the stress path to be applied in our axial loading experiments. However, this study has shown that compaction of Slochteren sandstone is at none of the conditions tested completely

poroelastic (Figure 2.7d), with final inelastic axial strains ranging from 0.1 to 0.8%, versus 0.3 to 0.6% of elastic axial strain (Table 2.1). Moreover, some of our experiments showed inelastic radial expansion, *i.e.* $(e_i)_{fin} > -(\Delta\varphi_i)_{fin}$ (Figure 2.3b). This behaviour is especially evident in our samples with $\varphi_0 \geq 21.6$, that show $(e_i)_{fin}$ in the range of 0.7 – 0.8%, versus $(\Delta\varphi_i)_{fin}$ values of ~ -0.5%.

Under uniaxial strain conditions assumed to be prevalent in the reservoir, the addition of inelastic radial expansion to poroelastic radial expansion will result in an enhanced increase of the effective horizontal stress during depletion. This implies that for our samples with $\varphi_0 \geq 21.6\%$, the experimentally imposed changes in the effective horizontal stress (σ_3^{eff} = 8 to 15 MPa), and differential stress ($[\sigma_1 - \sigma_3]$ = 22 to 50 MPa) underestimate and overestimate, respectively, the changes in σ_3^{eff} and $(\sigma_1 - \sigma_3)$ upon field depletion. The maximum change in the effective horizontal stress that may occur is found by considering the end-member case in which all axial compression is transferred into radial expansion (zero volume change), so that $\Delta\sigma_3^{eff} = \Delta\sigma_1^{eff} = -\Delta P_p$. Assuming an initial (pre-depletion) value for σ_3^{eff} of 8 MPa [*Breckels and Van Eekelen*, 1982], this would imply that upon full depletion of the field (ΔP_p = -35 MPa), the effective horizontal stress would increase from 8 to 43 MPa, at a constant differential stress of 22 MPa. In reality, the horizontal stress evolution is likely to fall in between this maximum value, and that predicted by assuming a purely poroelastic response (Equation 2.1). Interestingly, the effective horizontal stresses measured *in-situ* within the Groningen field at the current pore pressure of 8 MPa yield values that are significantly higher ($\sigma_3^{eff} \approx$ 24 - 31 MPa) than anticipated assuming poroelastic deformation ($\sigma_3^{eff} \approx$ 13 MPa), at least at the few localities determined [*Van Eijs*, 2015]. This appears to confirm an inelastic contribution to production-induced reservoir compaction.

The above further implies that for our high porosity samples ($\varphi_0 \geq 21.6\%$), the poroelastic stress changes imposed, and the strains measured, are unlikely to be representative for the *in-situ* stress evolution and compaction of high porosity regions within the Groningen field. Instead, stress changes developing in these high porosity regions are more likely to follow the yield envelope as it expands with increasing strain. Near faults, such stress changes may influence fault rupture and seismicity, which warrants further analysis of the evolution of the expanding yield envelope with strain and concomitant effects on *in-situ* stress development, and stress evolution along irregular faults. To date, though, any influence of inelastic deformation of the reservoir rock on stress changes and seismicity has been neglected in fault rupture models developed for the Groningen field [*Van den Bogert*, 2015; *Buijze et al.*, 2017; *Van Eijs et al.*, 2006; *Lele et al.*, 2016; *Mulders*, 2003; *Wassing et al.*, 2016]. Future modelling work needs to take these effects into account.

2.7.2 Implications for induced seismicity

In the context of hydrocarbon production from sandstone reservoirs, re-activation of pre-existing faults and associated seismicity may occur when (offset) strata along a fault compact by a different amount, *i.e.* in the case of differential compaction [*Van Eijs et al.*, 2006; *Mulders*, 2003]. Differential compaction may be accommodated by gradual, inelastic fault slip, thus dissipating the developing strain in a virtually aseismic manner. Alternatively, differential compaction may not initially cause fault slip , resulting in elastic and/or inelastic distortion of the surrounding reservoir rock and an increase of the shear stresses acting on the fault [*Jaeger et al.*, 2007; *Scholz*, 2002]. The elastic component of this deformation leads to energy storage, whereas any inelastic deformation dissipates energy. Once these shear stresses exceed the resistance of the fault to slip, rupture will follow, leading to release of the stored elastic strain energy accumulated within the fault and surrounding reservoir system. This release occurs by various processes such as frictional heating, inelastic asperity deformation, wall-rock damage, pore pressure changes and fluid flow, rupture propagation, and grain size reduction (gouge formation) [*Cooke and Madden*, 2014; *Shipton et al.*, 2013], while only a small proportion (5 to 20%) is consumed in generating seismic waves [*McGarr*, 1999]. It follows that discriminating inelastic from elastic reservoir compaction is important for estimating the seismic energy budget. However, as already indicated, most existing seismological models assume a linear poroelastic response of the reservoir to pore pressure depletion [*e.g. Lele et al.*, 2016]. The assumption of poroelastic reservoir deformation is also employed in the fault strain versus seismicity model formulated by *Bourne et al.*, [2014, 2015], although these authors did allow for partitioning between seismic from aseismic strain energy developing within faults.

The mechanical response of the reservoir to depletion is often quantified using a simple compaction coefficient, or an apparent stiffness (S_a), given $S_a = -\Delta P_p/\Delta e_t$. This apparent stiffness is frequently obtained from mechanical plug testing data [*Hettema et al.*, 2000; *Hol et al.*, 2015a; *Schutjens et al.*, 1995], surface subsidence data [*Ketelaar*, 2009; *NAM*, 2015], and/or *in-situ* compaction data [*NAM*, 2015]. Note, though, that since Δe_t denotes the change in the total axial strain, the apparent stiffness includes both elastic and inelastic contributions. Values of S_a obtained from mechanical testing of Slochteren sandstone plugs show a relatively wide range, notably from 3 to 30 GPa [*Hettema et al.*, 2000; *NAM*, 2016]. For comparison with surface subsidence data, we apply the most simple approach to estimate S_a from these data, by assuming that $\Delta e_t = \Delta L/L_0$. Here, ΔL is the amount of surface subsidence and L_0 is the initial reservoir thickness. Inserting values measured at the SDM-1 well for ΔL = 0.35 m, L_0 = 200 m and ΔP_p = -27 MPa [*NAM*, 2016],

we obtain S_a = 15 GPa. *In-situ* compaction measurements, based on the displacement of radio-active markers located along the reservoir intersection of the SDM-1 well show slightly more compliant S_a values, ranging from 9 – 13 GPa [*NAM*, 2015].

To determine the elastic contribution to induced reservoir compaction, and hence the percentage of total strain energy available for seismicity, we now apply our strain-partitioning data (Figure 2.7) to determine both the apparent stiffness S_a as well as the elastic stiffness, given $S_{el} = -\Delta P_p/\Delta e_{el}^{\Sigma}$. Since the stress changes imposed on our samples with $\varphi_0 \geq 21.6\%$ may not be representative for stress changes developing in high porosity regions within the Groningen field (see Section 2.7.1), we exclude these results from the present analysis. Neglecting any influence of the small inelastic radial expansions ($(e_i)_{fin} > -(\Delta\varphi_i)_{fin}$; Figure 2.3b) measured in our lowest porosity samples (φ_0 = 12.7 and 14.2%), we use Equation 2.1, inserting $\alpha = 1$ and $\nu = 0.15$ to calculate the differential stress that occurs upon reducing the pore pressure from 35 MPa to the current 8 MPa, *i.e.* ΔP_p = -27 MPa [*NAM*, 2016]. The result shows an increase from 22 to 44 MPa. For this stress window, Δe_t ranges from 0.11 to 0.33% (Figure 2.3a), so that S_a = 8 to 23 GPa. These values of S_a are in the same range as described in previous work [*NAM*, 2016]. To determine the elastic component of these values of Δe_t, we used our cumulative elastic axial strain data obtained for $\dot{\varepsilon}_t \sim 10^{-9}$ s^{-1} (Figure 2.7c). Hence, for the above stress window, Δe_{el}^{Σ} = 0.08 to 0.15%, and the elastic stiffness S_{el} ranges from 18 to 34 GPa. These values of S_{el} are significantly stiffer than the range described for S_a. Moreover, they show that for Slochteren sandstones with $\varphi_0 < 21.6\%$, deformed at $\dot{\varepsilon}_t \sim 10^{-9}$ s^{-1}, 30 to 55% of the total axial strain accumulated upon simulated pore pressure depletion is dissipated through inelastic deformation, and is therefore unavailable for seismicity. The implication is that at least for these porosities, the assumption of a poroelastic reservoir response to pore pressure reduction leads to an overestimation of the stored energy available in the reservoir rock for driving seismicity by as much as 30 – 55%. These values are likely higher for sandstones with $\varphi_0 \geq 21.6\%$, since previous compression experiments performed on Slochteren sandstone under uniaxial strain conditions have shown an increasing relative contribution of inelastic strain, with increasing initial porosity [*Hol et al.*, 2015a, 2018; *Schutjens et al.*, 1995]. Moreover, our experiments yielded a larger contribution of inelastic deformation with decreasing strain rate (Figure 2.7). Therefore, for strain rates relevant for production of the Groningen gas field (~10^{-12} s^{-1}) [*NAM*, 2015], the relative contribution of inelastic compaction may be larger still. To realistically resolve the magnitude of inelastic and elastic compaction of the Slochteren reservoir for these low strain rates, a full constitutive microphysical model for sandstone deformation is required that describes the relationship between stress and strain, including effects of strain- and loading

rate, initial porosity, progressively developing inelastic strain and concomitant stress changes.

2.8 Conclusions

We performed conventional triaxial compression experiments on Slochteren sandstone samples from the currently producing, seismogenic Groningen gas field. Each experiment was performed under *in-situ* conditions of temperature and chemistry (T = 100°C; 4.4M saline brine, see Table 2.2), and consisted of 1) an *in-situ* conditioning phase, in which samples were equilibrated to the pre-depletion stress state of $\sigma_3^{eff} = P_c^{eff}$ = 8 MPa and ($\sigma_1 - \sigma_3$) = 22 MPa, in order to remove any pre-existing damage induced during core retrieval and storage, and 2) a multi-step phase, in which we employed successive stages of active axial loading and stress relaxation at P_c^{eff} = 15 MPa and ($\sigma_1 - \sigma_3$) up to 50 MPa, to investigate the relative contributions of elastic strain, and time-independent (plastic) and time-dependent (creep) inelastic strain. These stress changes were chosen to simulate pore pressure reduction in the field, assuming a poroelastic response of the reservoir to depletion. A poroelastic stress path was chosen to test whether Slochteren sandstones (φ_0 = 12 – 25%) behaved elastically under these conditions, while any inelastic strain development would demonstrate that inelastic compaction should accordingly be expected in the field. In addition, a quantitative microstructural comparison of undeformed and deformed samples was carried out in order to gain insights into the microphysical mechanisms accommodating inelastic strain.

1) The present incremental axial loading plus stress relaxation experiments showed that for the chosen poroelastic stress changes, inelastic axial strain developed throughout triaxial compression, reaching final values of 0.1 to 0.8%, versus 0.3 to 0.6% of elastic axial strain in the multi-step phase. A substantial part of this inelastic strain constituted time-dependent deformation ((e_{cr})$_{fin}$ = 0.1 – 0.7%; Table 2.1).
2) The shape of each differential stress versus cumulative elastic axial strain curve was near-linear to slightly concave-up, with elastic strains generally increasing with increasing initial porosity and increasing strain rate (Figures 2.7a and c).
3) The shape of individual stress versus cumulative inelastic axial strain curves was non-linear and concave-down, revealing a strain hardening trend at decreasing rates. For a given stress, the magnitude of inelastic strain generally increased with increasing initial porosity and decreasing strain rate (Figures 2.7b and d).
4) Microstructures of deformed samples revealed that the deformation mechanisms operating during the present experiments were a combination of intergranular (grain

boundary) cracking, intergranular slip, and intra/transgranular cracking (Figure 2.6). Crack density data showed that the importance of intra/transgranular cracking increased with increasing porosity (Table 2.3).

5) During stress relaxation stages, the mechanisms accommodating creep strain were inferred to be a combination of rate-dependent intergranular slip, and stress-corrosion cracking leading to time-dependent grain failure (Figure 2.8). The importance of stress-corrosion cracking increased with increasing porosity.
6) The observations of continuous inelastic strain development, strain hardening and a rate- and porosity dependence of the magnitude of inelastic strain (Figures 2.7b and d), suggest that inelastic deformation in Slochteren sandstone is best described by a yield envelope which expands with increasing inelastic strain, increasing strain-rate and decreasing initial porosity.
7) During the multi-step phase, our samples with $\varphi_0 \geq 21.6\%$ revealed marked inelastic horizontal expansion (*i.e.* $e_i > -\Delta\varphi_i$; Figure 2.3b). This implies that at least in high porosity regions within the reservoir, the assumption of poroelastic stress changes accompanying pore pressure depletion underestimated the change in the effective horizontal stress developing under assumed uniaxial strain conditions. *In-situ* stress measurements appear to confirm this observation [*Van Eijs*, 2015], confirming an inelastic contribution to *in-situ* compaction.
8) Application of the data obtained on our samples with $\varphi_0 < 21.6\%$ at axial creep strain rates of $\sim 10^{-9}$ s^{-1}, showed that for the current state of pore pressure depletion ($\Delta P_p = -27$ MPa), 30 to 55% of the total strain energy was dissipated by inelastic deformation, and is therefore unavailable for seismicity, and other energy-dissipating processes associated with fault rupture. This effect is expected to be larger for higher porosities and lower strain rates (*i.e.* $< 10^{-9}$ s^{-1}).
9) For strain-rates relevant for gas production in the Groningen field ($\sim 10^{-12}$ s^{-1}), estimations of inelastic versus elastic strain-partitioning require a full microphysical model, incorporating effects of initial porosity, strain- or loading rate, and progressively developing inelastic strain on yield envelope expansion and hence stress-strain behaviour. Such a microphysical model is currently under development, and may in future work be implemented in larger-scale seismological models.

Acknowledgements

This research was carried out in the context of the research program funded by the Nederlandse Aardolie Maatschappij (NAM). Initiated in late 2014, this program aims to fundamentally improve understanding of production-induced reservoir compaction and seismicity in the seismogenic Groningen gas field. We thank the NAM and Shell Global Solutions for providing samples and data and the NAM for allowance to publish this study. Specifically, the authors like to thank the involved teams at Shell Global Solutions and NAM for numerous useful scientific interactions. Colin Peach is thanked for advice and help both in- and outside of the lab. We thank UU employees Gert Kastelein, Thony van der Gon-Netscher, Floris van Oort, Peter van Krieken and Eimert de Graaff for technical assistance. Finally, we would like to thank Dirk Doornhof, and two anonymous reviewers for constructive comments that helped increase the quality of this paper. The data for this paper are available as Pijnenburg, Ronald; Verberne, Berend; Hangx, Suzanne; Spiers, Christopher (2018): Mechanical and microstructural data used in the article Pijnenburg et al., Deformation behaviour of sandstones from the seismogenic Groningen gas field: Role of inelastic versus elastic mechanisms. GFZ Data Services. http://doi.org/10.5880/fidgeo.2018.005

Appendix 2.A1: List of Key-symbols

e_t	total axial strain ($\Delta L/L_0$)
$\dot{\varepsilon}_t$	total axial strain rate
$\dot{\varepsilon}_{cr}$	axial creep strain rate
$(\sigma_1\text{-}\sigma_3)_{max}$	maximum differential stress imposed
$(e_t)_{fin}$	final total axial strain measured at the end of each phase
$(e_i)_{fin}$	final inelastic axial strain measured at the end of each phase
$(e_{el})_{fin}$	final elastic axial strain at the end of each phase: $(e_t)_{fin}$ - $(e_i)_{fin}$
$(e_i^{inst})_{max}$	sum of all instantaneous axial strains of all active loading stages
$(e_{cr})_{max}$	sum of all axial creep strains of all relaxation stages
$(e_i^{\Sigma})_{max}$	maximum cumulative inelastic axial strain: $(e_i^{inst})_{max}$ + $(e_{cr})_{max}$
$(e_{el}^{\Sigma})_{max}$	maximum cumulative elastic axial strain: $(e_t)_{max}$ - $(e_i^{\Sigma})_{max}$
$\Delta\varphi_t$	total porosity change ($\Delta V_{pore}/V_0$)
$(\Delta\varphi_t)_{fin}$	final total porosity change measured at the end of each phase
$(\Delta\varphi_i)_{fin}$	final inelastic porosity change measured at the end of each phase
$(\Delta\varphi_{el})_{fin}$	final elastic porosity change at the end of each phase: $(\Delta\varphi_t)_{fin}$ - $(\Delta\varphi_i)_{fin}$
E_a	apparent (quasi-elastic) Young's modulus: $\Delta(\sigma_1\text{-}\sigma_3)/\Delta e_t$
S_a	apparent (elastic + inelastic) stiffness: $-\Delta P_p/\Delta e_t$
S_{el}	elastic stiffness: $-\Delta P_p/\Delta e_{el}^{\Sigma}$

Appendix 2.A2

Grain size analysis of the BSE-derived grain maps obtained for undeformed samples (*e.g.* Figure 2.5a-d) showed the equivalent circular grain radius (r) to be log-normally distributed, with r ranging from 1 to 500 µm (Figure 2.A1a), and mean r-values ranging from 30 – 110 µm (Figure 2.A1b). The standard deviation (SD) ranges from 0.6 to 0.9 ln µm (Figure 2.A1b). No clear correlation is visible between the mean grain radius, or standard deviation and initial porosity (Figure 2.A1b). Ellipse-fitting showed that most grains are slightly elongated (*i.e.* $AR > 1$) and the mean aspect ratio (AR_{mean}) is relatively constant for all samples ($AR_{mean} \approx 1.7$; Table 2.3). For all samples, the mean grain orientation (*i.e.* the mean angle β_{mean} between the major axis of each grain and the sample horizontal) is approximately 0 ± 5°, indicating that on average, grain long-axes are oriented sub-perpendicular to the coring direction. The kurtosis of the frequency distribution of β values ranges from -1.2 (a flat distribution, without preferred orientation), to -0.5 (a weakly developed preferred grain orientation).

To determine if there is any grain-size dependence of the grain orientation

distribution, we compiled all the statistical data presented here (n = 7052). In Figure 2.A1c, the grain orientation (β) distribution is shown for a fine (r = 10 - 20 µm) and a coarse (r = 100 - 200 µm) grain radius range. No preferred orientation is observed in the fine grain radius range, yielding a kurtosis of -1.14. However, for the coarse grain radius range, a preferred orientation around $\beta = 0^{\circ}$ is observed, yielding a kurtosis of -0.65. Thus, kurtosis [β] increases with increasing grain size (Figure 2.A1d), implying a tendency of larger grain long-axes to be oriented parallel to the sample horizontal and hence perpendicular to the coring direction. By contrast, *AR* values decrease with increasing grain size (Figure 2.A1d).

Table 2.A1 Quantitative microstructural data obtained from backscattered electron microscopy images of undeformed samples and samples deformed in incremental loading, plus stress relaxation tests. Initial porosities (φ_0) are given for reference. r_{mean} denotes the mean grain radius; SD ln(r) denotes the standard deviation of the natural logarithm of the equivalent grain radius; AR_{mean} denotes the mean of the grain aspect ratio, *i.e.* the long axis of a grain divided by the short axis of the grain; β_{mean} denotes the mean of the grain orientation, given by angle β between the long axis of a grain and the sample horizontal perpendicular to the core axis.

Sample	φ_0	r_{mean}	SD ln(r)	AR_{mean}	β_{mean}
	[%]	[µm]	[ln(µm)]	[-]	[$^{\circ}$]
Sw09	12.7	37.8	0.67	1.79	-3.7
Sw11	14.2	52.8	0.78	1.80	-3.7
Sw13	17.4	93.8	0.69	1.69	1.0
Sg09	17.7	55.4	0.59	1.75	2.5
Sg10	18.0	108.8	0.95	1.75	-0.3
Sw02	19.9	37.4	0.86	1.75	0.7
Sg05	21.6	83.7	0.62	1.78	-4.9
Sw07	21.6	105.9	0.69	1.78	2.5

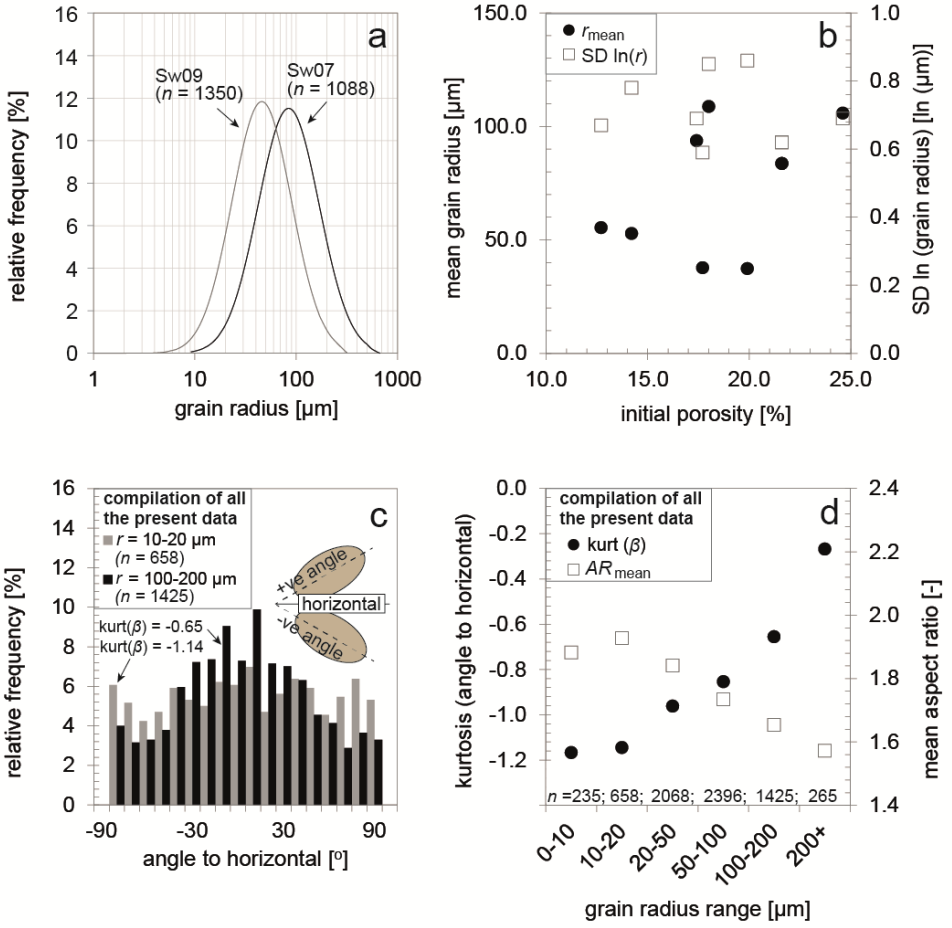

Figure 2.A1: Quantitative microstructural data obtained from BSE derived grain maps (*e.g.* Figure 2.5, main text) of undeformed material **a)** Log-normal fits (R^2 > 0.95) to grain-radius distributions for a low porosity sample (φ_0 = 12.7%; Sw09) and a high porosity sample (φ_0 = 24.6%; Sw07). **b)** Mean grain radius and the standard deviation of the natural logarithm of the grain radius distribution, versus initial porosity plot. No clear trend is visible. **c)** Grain orientation [β] distribution, for grain radius ranges of 10-20 µm and 100-200 µm, obtained from a compilation of all the statistical data presented here (n = 7052). No clear preferred orientation is observed in the finer grain radius range.The larger grain radius range shows a peak around $\beta \approx 0^{\circ}$, indicating a preferred grain orientation parallel to the sample horizontal. **d)** With increasing grain size, kurt [β] increases (*i.e.* the preference of grains to be oriented perpendicular to the coring direction increases), while the mean aspect ratio of grains (AR_{mean}) decreases.

Appendix 2.A3

In the microphysical model for rate-dependent sliding behavior of gouge materials, outlined by *Niemeijer and Spiers* (N-S), [2007] (Figure 2.A2), the friction coefficient μ is dependent on: 1) the average grain contact angle over which slip occurs, referred to as the dilatancy angle (Ψ), 2) the local friction coefficient acting on grain contacts ($\tilde{\mu} = \tilde{\tau} / \tilde{\sigma}_n$, where $\tilde{\tau}$ and $\tilde{\sigma}_n$ are respectively the shear stress and the normal stress, acting on grain contacts) and 3) intergranular cohesion. If we assume that during relaxation intervals strain is achieved by frictional sliding along intergranular interfaces that are already broken during the preceding piston advancement intervals, *i.e.* neglecting any effect of intergranular cohesion, then in the N-S model, μ is related to $\tilde{\mu}$ by:

$$\mu = \frac{\sin\Psi + \tilde{\mu}\cos\Psi}{cos\ \Psi - \tilde{\mu}\sin\Psi} \qquad \text{(Eq. 2.A1)}$$

where Ψ is dependent on the porosity (φ) [*Bouckovalas et al.*, 2003; *Xenaki and Athanasopoulos*, 2003], through:

$$\tan(\Psi) = H(q - 2\varphi)^x. \qquad \text{(Eq. 2.A2)}$$

Here, H, x and q are constants with values of approximately 1, 1, and 0.8, respectively [*Niemeijer and Spiers*, 2007]. In recent direct-shear experiments, performed at our laboratory on gouge material derived from Slochteren sandstone, and under similar conditions as imposed here (T = 100˚C, effective normal stress σ_n = 40 MPa, pore fluid is 4.4M NaCl brine), the friction coefficient μ was found to be 0.61 at v = 1 µm/s [*Hunfeld et al.*, 2017]. Using this value of μ = 0.61 and the reported average post-test gouge porosity of 26% to be representative for the Slochteren sandstone gouge during shear, the microphysical model due to *Niemeijer and Spiers*, [2007] can be used to obtain estimates of dilation angle (Ψ) and grain boundary friction coefficient ($\tilde{\mu}$), characteristic of granular Slochteren sandstone gouge. Applying the *Niemeijer and Spiers*, [2007] model in this way, we obtain Ψ = 15.6˚, and $\tilde{\mu}$ = 0.28, at a grain boundary slip velocity $\tilde{v}$ = $\cos(\Psi)^{-1}$ = 1.04 µm/s.

In a triaxial test on a sandstone such as the Slochteren sandstone (Figure 2.A2), intergranular slip will occur most easily along grain boundaries aligned with their normal at an angle θ to σ_1 [*Jaeger et al.*, 2007], where:

$$\tan 2\theta = -1/\tilde{\mu}. \qquad \text{(Eq. 2.A3)}$$

On this grain boundary plane, the instantaneous grain boundary friction coefficient is related to the instantaneous friction coefficient by $\tilde{\mu}_{\text{inst}} = \tilde{\tau}/\tilde{\sigma}_n = \tau/\sigma_n = \mu_{\text{inst}}$, and to the principal stresses by:

$$\tilde{\mu}_{inst} = \mu_{inst} = \frac{(\sigma_1 - \sigma_3)\sin(2\theta)}{(\sigma_1 + \sigma_3) + (\sigma_1 - \sigma_3)\cos(2\theta)} \qquad \text{(Eq. 2.A4)}$$

The instantaneous sliding velocity (v_θ) and initial sliding velocity ($v_{\theta,0}$) along this plane are related to, respectively, the instantaneous sliding velocity in the direction of σ_1 (v_{ax}), and the initial sliding velocity in the direction of σ_1 ($v_{\text{ax},0}$), using (v_θ) = v_{ax} /sin θ, and $v_{\theta,0}$ = $v_{\text{ax},0}$ /sin θ. If we assume that for a given change in slip velocity, $\Delta\tilde{\mu}_{\text{inst}} \approx \Delta\mu_{\text{ss}}$, then combining these relations, Equation 2.A4, and Equation 2.4 (see main text), we obtain the stress-sensitivity of the sliding velocity in a triaxial configuration, in the direction of σ_1, as:

$$v_{\text{ax}} \approx v_{\text{ax},0} \exp\left(\frac{1}{a-b}\left(\frac{(\sigma_1 - \sigma_3)\sin(2\theta)}{(\sigma_1 + \sigma_3) + (\sigma_1 - \sigma_3)\cos(2\theta)} - \left(\frac{(\sigma_1 - \sigma_3)\sin(2\theta)}{(\sigma_1 + \sigma_3) + (\sigma_1 - \sigma_3)\cos(2\theta)}\right)_0\right)\right) \qquad \text{(Eq.2.A5)}$$

The creep strain-rate for intergranular slip is now obtained by dividing v_{ax}, by the initial sample length (L_0):

$$\dot{\varepsilon}_{\text{cr}}^{\text{slip}} = \frac{v_{\text{ax}}}{L_0} \approx$$

$$\dot{\varepsilon}_{\text{cr},0}^{\text{slip}} \exp\left(\frac{1}{a-b}\left(\frac{(\sigma_1 - \sigma_3)\sin(2\theta)}{(\sigma_1 + \sigma_3) + (\sigma_1 - \sigma_3)\cos(2\theta)} - \left(\frac{(\sigma_1 - \sigma_3)\sin(2\theta)}{(\sigma_1 + \sigma_3) + (\sigma_1 - \sigma_3)\cos(2\theta)}\right)_0\right)\right) \qquad \text{(Eq.2.A6)}$$

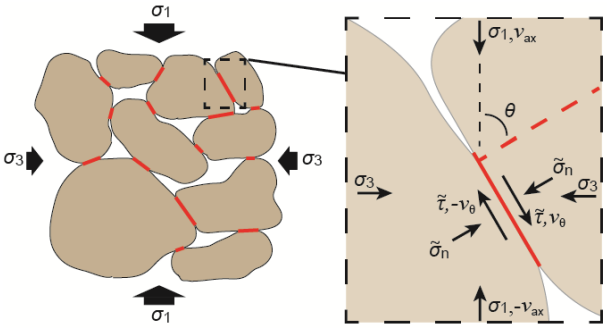

Figure 2.A2 Microphysical model for rate-sensitive intergranular slip in sandstone, modified after *Niemeijer and Spiers* [2007]. The axial sliding velocity (v_{ax}) and principal stresses σ_1 and σ_3 act on grain boundaries described by the plane normal at angle θ to σ_1.The intergranular sliding velocity and the contact normal and shear stress are given by v_θ, $\tilde{\sigma}_n$, and $\tilde{\tau}$, respectively.

Chapter 3

Inelastic deformation of the Slochteren sandstone: Stress-strain relations and implications for induced seismicity in the Groningen gas field

Based on: R.P.J. Pijnenburg, B.A. Verberne, S.J.T. Hangx, C.J. Spiers
Journal of Geophysical Research: Solid Earth, 124
DOI:10.1029/2019JB017366

Abstract

Pore pressure reduction in sandstone reservoirs generally leads to small elastic plus inelastic strains. These small strains (0.1 – 1.0% in total) may lead to surface subsidence and induced seismicity. In current geomechanical models, the inelastic component is usually neglected, though its contribution to stress-strain behavior is poorly constrained. To help bridge this gap, we performed deviatoric and hydrostatic stress-cycling experiments on Slochteren sandstone samples from the seismogenic Groningen gas field in the Netherlands. We explored *in-situ* conditions of temperature (T = 100°C) and pore fluid chemistry, porosities of 13 to 26% and effective confining pressures (≤ 320 MPa) and differential stresses (≤ 135 MPa) covering and exceeding those relevant to producing fields. We show that at all stages of deformation, including those relevant to producing reservoirs, 30 - 50% of the total strain measured is inelastic. Microstructural observations suggest that inelastic deformation is largely accommodated by intergranular displacements at small strains of 0.5 – 1.0%, with intragranular cracking becoming increasingly important towards higher strains. The small inelastic strains relevant for reservoir compaction can be described by an isotropic, Cam-clay plasticity model. Applying this model to the depleting Groningen gas field, we show that the *in-situ* horizontal stress evolution is better represented by taking into account combined elastic and inelastic deformation, than it is by representing the total deformation behavior using poroelasticity (up to 40% difference). Therefore, inclusion of the inelastic contribution to reservoir compaction has a key role to play in future geomechanical modelling of induced subsidence and seismicity.

3.1 Introduction

Pore pressure reduction accompanying the production of oil, gas or geothermal fluids from sandstone reservoirs may lead to surface subsidence and induced seismicity [*Evans et al.*, 2012; *Fialko and Simons*, 2000; *Grünthal*, 2014; *Pratt and Johnson*, 1926; *Van Wees et al.*, 2014]. Both effects are caused by compaction of the reservoir, resulting from the increase in effective stress accompanying pore pressure reduction. Subsidence typically constitutes several tens of centimeters [*Ketelaar*, 2009; *Mallman and Zoback*, 2007; *Morton et al.*, 2001], corresponding to vertical reservoir strains generally < 1% [*Cannon and Kole*, 2017; *Kole*, 2015]. The densely populated Groningen gas field (~200 inhabitants/km^2, province wide) located in the Netherlands (Figure 1.1a of Chapter 1) has attracted much attention in recent years, particularly since the occurrence of a damaging M_w 3.6 earthquake in 2012 [*Dost and Kraaijpoel*, 2013]. In this field, the greatest subsidence (up to 34 cm, in 2013), the largest vertical strains [~ 0.3%; *NAM*, 2015; *Cannon and Kole*, 2017] and the largest and most frequently occurring seismic events (Figure 1.1a of Chapter 1) are all seen in the central part of the field (Figure 1.1a), where the reservoir, the Slochteren sandstone, is thickest (~200 m) and most porous (18 - 22%, Figure 1.1b).

Compaction of sandstone reservoirs may be in part elastic (reversible) and part inelastic (permanent). Quantifying the partitioning between elastic and inelastic contributions is essential for induced seismicity studies, as it directly affects *in-situ* stress changes during pore pressure reduction [*Chan et al.*, 2004; *Pijnenburg et al.*, 2018], as well as the elastic energy available to drive induced seismicity [*Cooke and Madden*, 2014; *Pijnenburg et al.*, 2018; *Shipton et al.*, 2013]. However, while the elastic component is well understood and easily quantified in terms of poroelasticity [*Wang*, 2000], the inelastic contribution has received little attention at reservoir-relevant strains (< 1%). Rather, most previous research on sandstone mechanics [*e.g. Wong et al.*, 1997; *Baud et al.*, 2004; *Tembe et al.*, 2008; *Rutter and Glover*, 2012] has focused on inelastic deformations developing at much larger compressive strains (2 - 15%).

At the low temperature conditions (T < 150°C) and decade time-scales relevant for fluid extraction from the upper crust (< 5 km), inelastic deformation of sandstone is believed to occur mostly through grain-scale, brittle/frictional processes, including intergranular (grain boundary) cracking and slip [*Bernabe et al.*, 1994; *Menéndez et al.*, 1996; *Pijnenburg et al.*, 2018], as well as intragranular and transgranular cracking [*Baud et al.*, 2004; *Brantut et al.*, 2013; *Heap et al.*, 2009, 2015]. In addition, intergranular mass transfer (or pressure solution) may occur, although existing rate data [*Chester et al.*, 2004; *Niemeijer et al.*, 2002; *Van Noort et al.*, 2008; *Renard et al.*, 1999; *Spiers et al.*, 2004] suggest that the contribution

of this slow creep process will be small. The extent to which each of these processes operates at a given temperature and time-scale depends on the stresses imposed and on the stresses transmitted to the constituent grains, hence on the porosity (φ).

Experimental studies based on conventional deviatoric and hydrostatic testing [*Wong and Baud*, 2012, and references therein] generally express the mechanical behavior shown by sandstones in terms of mean effective stress ($P = [\sigma_1 + \sigma_2 + \sigma_3]/3$ – pore pressure P_p) versus total porosity reduction ($\Delta\varphi_t$) data (Figure 3.1). Such P - $\Delta\varphi_t$ curves typically show a transition from initial, non-linear, concave-up behavior (Stage 1), followed by near-linear behavior (Stage 2), which in turn is followed by non-linear behavior, characterized by dilation at low P and φ (Stage 3d – suffix *d* for dilation) and by non-linear compaction at high P and φ (Stage 3c – suffix *c* for compaction). The initial Stages 1 and 2 frequently show similar behaviors in deviatoric and hydrostatic compression [*Baud et al.*, 2000; *Wong et al.*, 1997], suggesting roughly isotropic behavior. During low P, deviatoric compression, deviation from the hydrostatic P - $\Delta\varphi_t$ trend characterizes the onset of dilatancy (*i.e.* Stage 3d – see Figure 3.1) and is in this work marked by the mean effective stress $P_{stage3d}$. The mean effective stress marking the onset of non-linear compaction (Stage 3c) is referred to as $P_{stage3c}$. Hence, in the present study, these terms are preferred over the more commonly used factors *C*' , *C** and *P**, defined in the pioneering work by *Zhang et al.*, [1990] and *Wong et al.*, [1997]. While it was recognized by these authors that inelastic deformation may occur at stresses below *C*', *C** and *P** [see also: *Menéndez et al.*, 1996], these thresholds are often effectively treated as elastic-inelastic yield points, with poroelasticity theory applying at lower stress levels [*e.g. Wong et al.*, 1997; *Wong and Baud*, 2012; *Guéguen and Fortin*, 2013; *Brantut et al.*, 2014]. To avoid the connotation that the onset of dilation or non-linearity corresponds to the onset of inelastic behavior, $P_{stage3d}$ and $P_{stage3c}$ are used instead.

The compliant, concave-up behavior seen in Stage 1 is thought to reflect poroelastic deformation, combined with semi-recoverable closure of pre-existing damage or cracks [*David et al.*, 2012; *Walsh*, 1965]. Stage 1 typically persists up to $\Delta\varphi_t$ values in the range of 0.3% (at low effective confining pressures P_c^{eff} = confining pressure P_c - P_p, and at low φ) to 2.0% (high P_c^{eff}, high φ). The near-linear behavior seen in Stage 2 is in the bulk of the literature treated as if reflecting purely poroelastic deformation [*Baud et al.*, 2000, 2004, 2006; *Brantut et al.*, 2013; *Heap et al.*, 2009, 2015; *Klein et al.*, 2001; *Rutter and Glover*, 2012; *Wong and Baud*, 2012]. However, the most recent experimental studies, including previous work on the Slochteren sandstone [*Hol et al.*, 2015a, 2018; *Pijnenburg et al.*, 2018], have shown that this near-linear behavior in fact reflects combined elastic and inelastic behaviour, where the inelastic part constitutes some 20 to 70% of the total deformation

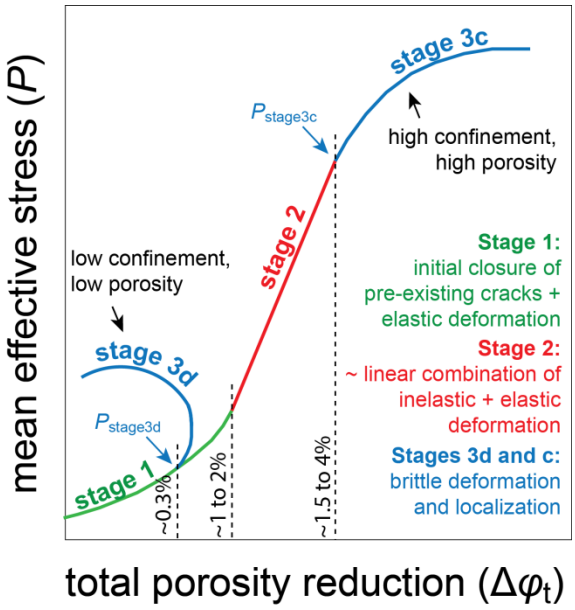

Figure 3.1 Schematic diagram showing the different stages in mean effective stress (P) versus total porosity reduction ($\Delta\varphi_t$) behavior typically seen in mechanical testing of sandstones (see in-text references). Note the effects of low porosity and confining pressure and low porosity and high confining pressure on Stage 3 behavior (dilation – suffix "d" versus compaction - "c"). The deformation mechanisms inferred in the literature are shown per stage, as are typical values of $\Delta\varphi_t$ measured at the end of each stage.

(see also: *Bernabe et al.*, [1994]). At P_c^{eff} > 20 MPa, Stage 2 behavior typically persists up to $\Delta\varphi_t$ values of 1.5 – 4.0%, then giving way to Stage 3c (non-linear compaction). At lower P_c^{eff}, Stage 1 transitions directly into Stage 3d at $\Delta\varphi_t \approx 0.3\%$. In both cases, Stages 3c and d are accompanied by pervasive intragranular cracking and intergranular or inter-particle shear, frequently localizing in shear fractures (Stage 3d), or compaction bands (Stage 3c) [*Baud et al.*, 2004; *Fortin et al.*, 2005; *Tembe et al.*, 2008; *Wu et al.*, 2000].

On the above basis, notably the latest experiments on Slochteren sandstone [*Hol et al.*, 2015a, 2018; *Pijnenburg et al.*, 2018] and earlier tests [*Bernabe et al.*, 1994], it is increasingly clear that inelastic deformation contributes significantly to the compressive deformation of sandstone at the small strains (< 1%) relevant for producing reservoirs. However, most geomechanical models addressing induced subsidence and seismicity ignore any inelastic contribution to the deformation of the reservoir, and describe compaction using a simple compaction coefficient, in effect a poroelastic stiffness or compliance constant [*Bourne et al.*, 2014; *Dempsey and Suckale*, 2017; *Van Eijs et al.*, 2006; *Lele et al.*, 2016;

Mulders, 2003; *Postma and Jansen*, 2018; *Wassing et al.*, 2016; *Zbinden et al.*, 2017]. When an inelastic contribution is included, it is typically described using plasticity theory, originally developed to represent the inelastic deformation behavior of incohesive soils [*Chan et al.*, 2004; *Crawford et al.*, 2011; *Crawford and Yale*, 2002; *Fredrich and Fossum*, 2002; *Han et al.*, 2005]. Common examples of soil mechanics models utilizing plasticity theory include the critical state model [*Schofield and Wroth*, 1968], the cap-model [*DiMaggio and Sandler*, 1971] and the modified Cam-clay model [*Muir Wood*, 1991]. These models are characterized by a yield envelope which is elliptical in differential stress ($Q = \sigma_1 - \sigma_3$) versus mean effective stress (P) space. This yield envelope expands due to inelastic porosity reduction during compressive deformation, reflecting strain hardening due to densification. While strain hardening behavior has been observed in cohesive sandstones in qualitative terms [*Rutter and Glover*, 2012; *Wong et al.*, 1992; *Wong and Baud*, 1999], at least the high strain, compactive Stage 3c behavior (see Figure 3.1) appears to be poorly described by plasticity theory [*Baud et al.*, 2006]. The extent to which plasticity models can describe Stage 1 and 2 behavior at the smaller strains relevant for depleting reservoirs remains unclear and insufficiently tested against experiments. Still, if applicable, plasticity models provide a convenient framework for quantifying the inelastic behavior of sandstone reservoir rocks, not least because they are often already included in the finite element modelling packages used in geomechanics (*e.g.* Abaqus, Ansys, DIANA).

In this paper, we investigate to what extent, if at all, the inelastic deformation behavior shown by the Slochteren sandstone from the Groningen gas field can be described by an isotropic plasticity model. To that end, we systematically quantify the elastic and inelastic deformation behavior characterizing all three stages of deformation commonly seen in sandstones (Figure 3.1), including the small strain behavior relevant for compacting reservoirs. This was done by performing both hydrostatic and deviatoric (differential) stress-cycling experiments, under *in-situ* conditions of temperature (T = 100°C) and pore fluid chemistry, using samples with a range of porosities (φ = 13 to 26%) covering that observed in the field. Quantitative microstructural investigation of undeformed and deformed sample material was used to identify the microphysical mechanisms accommodating inelastic deformation during Stages 1, 2, 3d and 3c. In addition, an isotropic, Cam-clay-type plasticity model was fitted to the mechanical data to assess its applicability to describe and compute the inelastic response of the Slochteren sandstone to pore pressure reduction. Finally, we apply our results to assess the importance of including inelastic deformation in estimating changes in *in-situ* stress, strain and stored elastic strain energy - in the context of investigating induced seismicity in the Groningen gas field and other, similar fields.

3.2 Background on the Slochteren sandstone

The Groningen gas field is a vast ~30 by 30 km field located in the NE-Netherlands (Figure 1.1 of Chapter 1). The ~ 100 to 200 meter thick Slochteren reservoir sandstone member is located at about 3 km depth and constitutes coarse, poorly sorted fluvial sandstones and conglomerates at its base, superseded by cross-bedded, intermediate- to well-sorted aeolian sandstones [*Grötsch et al.*, 2011]. The Slochteren sandstone lies unconformably on organic-rich Carboniferous shales, and is overlain by a 50 m thick claystone, followed by a thick sequence (500 – 1000 m) of Zechstein evaporates [*Amthor and Okkerman*, 1998]. At present, the upper 50 – 150 m of the Slochteren reservoir is gas-bearing and is partly (25 ± 10 vol%) filled with connate brine [*Waldmann*, 2011]. Production from the field started in 1963, which has led to a decrease in pore pressure from 35 MPa to ~ 8 MPa, in 2016 [*NAM*, 2016]. This has resulted in an upward shift of the gas-water contact by about ten meters, to a current true vertical depth (TVD) of ~2971 m. The sandstone is quartz-rich (72 – 90 vol%), with lesser amounts of feldspar (8 – 25 vol%), clay (0.5 – 5.5 vol%) and lithic fragments (3 – 10 vol%), which include basaltic and sedimentary lithoclasts [*Waldmann et al.*, 2014; *Waldmann and Gaupp*, 2016]. The mean size of quartz and feldspar grains typically ranges between 150 to 250 µm [*Pijnenburg et al.*, 2018]. Clay films (1 - 10 µm thick) coat the surfaces of quartz and feldspar grains and many grain contacts [*Gaupp et al.*, 1993; *Waldmann*, 2011; *Waldmann and Gaupp*, 2016; *Wilson*, 1992]. The porosity of the Slochteren sandstone is well constrained from wireline logs and fluid-immersion tests on core plugs [*NAM*, 2013], with average values decreasing from 18 – 22% in the center of the field to 12 - 16% at the margins (Figure 1.1b of Chapter 1).

3.3 Experimental aspects

We performed two types of experiments on Slochteren sandstone plugs from the Groningen gas reservoir: 1) purely hydrostatic stress-cycling tests (hydrostatic experiments) and 2) hydrostatic followed by deviatoric stress-cycling tests (combined hydrostatic plus deviatoric experiments). Both experiment types were aimed at systematically investigating the elastic versus inelastic stress-strain and porosity reduction behavior of the material, as a function of initial porosity. We explored hydrostatic mean effective stresses up to 320 MPa, and differential stresses up to 135 MPa, at a temperature of 100°C, representative for the Groningen field temperature at 3000 m true vertical depth (TVD) [*NAM*, 2013]. A constant pore pressure of either 0.1, or 1 MPa was used. These stress conditions were chosen to cover all stages of $P - \Delta\varphi_t$ behavior commonly seen in sandstones (Figure 3.1; *Wong and Baud*, [2012]), and include the effective confining pressures and differential stresses relevant for

fluid extraction from reservoirs at depths up to 5 km [both typically < 50 MPa; *Schutjens et al.*, [2004]). In addition, a set of reference experiments was performed to investigate microstructural changes specific to each stage of deformation. During hydrostatic stress-cycling runs, we imposed a rate of change of mean effective stress ($\dot{P}$) of 0.1 ± 0.05 MPa/s. During deviatoric stress cycling, a total axial strain rate $\dot{\varepsilon}_t$ of 10^{-5} s^{-1} was used, leading to a similar rate of change of the mean effective stress.

3.3.1 Sample material and pore fluid chemistry

The samples used were obtained from Slochteren sandstone core, retrieved by the field operator (Nederlandse Aardolie Maatschappij, NAM) from the Zeerijp (ZRP)-3a well in 2015. Sets of six adjacent samples were extracted from 10 cm diameter core sections obtained from five different depth intervals characterized by different porosities (Table 3.1), in an orientation perpendicular (within ~ 10°) to the often slightly inclined bedding. Each sample set consisted of four uniformly looking, 25.4 mm diameter cylindrical plugs cored with a length of 55 to 65 mm, one smaller cylindrical plug cored with a diameter of 9.8 mm and a length of 20 mm, and one sample of 'interplug' material with an equivalent diameter of ~ 20 mm, and a length of 55 to 65 mm left over after drilling. The interplug samples (no suffix used in Table 3.1) were left undeformed and were used as a benchmark to determine experimentally induced microstructural changes. The ends of all cylindrical plugs were ground flat and perpendicular to the long sample axis using a polishing wheel and support block.

The four longer plugs were used in our hydrostatic plus deviatoric experiments and are annotated with suffixes '*a-d*' (Table 3.1). These experiments were performed using a highly saline pore fluid with ion concentrations of 3.4 M Na^+, 0.1 M K^+, 1.0 M Ca^{2+}, 0.2 M Mg^{2+}, 0.6 M SO_4^{2-} and 5.7 M Cl^-, similar to those measured in pore fluid sampled from the reservoir [*Hol et al.*, 2018]. All samples were pre-saturated with this pore fluid prior to testing (full saturation). We determined the initial porosity of one 25.4 mm diameter sample from each set, using the difference in mass between the washed and dried sample versus that of the sample saturated with the above brine (density = 1.21 g/mL). The values obtained for the samples selected from each set were 13.4, 19.1, 21.5, 21.9 and 26.4% (Table 3.1). These porosities were assumed to be representative for the other long twin plugs and for the interplug sample, in each set (each core interval with given average porosity). This assumption is justified by previous testing of Slochteren sandstone samples from ZRP-3a core, showing similar physio-mechanical properties of samples from the same core interval [*Hol et al.*, 2018].

Table 3.1 (Caption on next page)

Sample	TVD	φ_0	Test-type	$P_c^{eff}{}_{max}$	Q_{peak}	$P_{stage3d}$	$P_{stage3c}$	$\Delta\varphi_{i,stage3d/c}$	$\Delta\varphi_{t,fin}$	$\Delta\varphi_{i,fin}$	$\bar{\rho}_{cr}$
	[m]	[%]		[MPa]	[MPa]	[MPa]	[MPa]	[%]	[%]	[%]	[mm^{-2}]
	Control experiments: (φ_0 = 19.1%)										
z74a	2968.9	19.1 [X]	T	40.0	79.5		65	0.9	2.70	1.42	*n.d.*
z74b*	2968.9	19.1	T	40.0	82.7		65	*n.d.*	2.67	1.39	*n.d.*
	Low porosity samples: (φ_0 = 13.4 to 13.9%)										
z20	2939.6	13.4	U								5.4
z20a	2939.6	13.4 [X]	T	5.0	49.5	11		0.2	-0.39	-0.13	*n.d.*
z20d	2939.6	13.4	T	20.0	83.7	43		0.5	0.97	0.43	*n.d.*
z20c	2939.6	13.4	T	40.0	113.0	75		0.7	1.64	0.62	33.5
z20b	2939.6	13.4	T	80.0	134.4		117	1.0	3.33	1.28	*n.d.*
z20e**	2939.6	13.9 [X]	R	320	*n.a.*		220	1.3	7.4	3.2	*n.d.*
	Intermediate porosity samples: (φ_0 = 21.4 to 21.5%)										
z24	2960.6	21.5	U								8.4
z24b	2960.6	21.5	T	5.0	29.7	9		0.2	-0.39	0.05	10.0
z24d	2960.6	21.5	T	20.0	53.8	32		0.7	1.63	0.78	14.0
z24c	2960.6	21.5	T	40.0	70.4		60	0.9	3.17	1.58	38.7
z24a**	2960.6	21.5 [X]	T	80.0	*n.d.*		93	1.0	3.82	1.32	23.5
z24e**	2960.6	21.4 [X]	R	160	*n.a.*		130	1.1	5.5	2.1	72.8
	High porosity samples: (φ_0 = 25.6 to 26.4%)										
z84	3014.5	26.4	U								11.5
z84a	3014.5	26.4 [X]	T	5.0	22.1	7		0.2	-0.18	0.12	*n.d.*
z84d	3014.5	26.4	T	20.0	39.1	34		1.0	2.22	1.12	*n.d.*
z84c	3014.5	26.4	T	40.0	43.5		53	1.3	3.45	1.83	25.7
z84b**	3014.5	26.4	T	80.0	*n.d.*		86	1.7	5.70	3.18	*n.d.*
z84e**	3014.5	25.6 [X]	R	160	*n.a.*		125	1.8	5.8	2.5	*n.d.*
	Microstructural reference experiments: (φ_0 = 21.9%)										
z77	2977.0	21.9	U								12.8
z77a*	2977.0	21.9 [X]	T	40.0	*n.a.*		*n.d.*	*n.d.*	2.37	1.24	14.2
z77b*	2977.0	21.9	T	40.0	*n.d.*		*n.d.*	*n.d.*	2.72	1.35	17.7
z77c*	2977.0	21.9	T	40.0	59.1		58	*n.d.*	3.10	1.68	54.3

Table 3.1 List of the samples used and key-mechanical data obtained in the present study. TVD refers to the true vertical depth within the Zeerijp (ZRP)-3a well, from which our samples were recovered. φ_0 denotes the initial porosity (measured value indicated with "X" – values of twin samples assumed to be equal); $(P_c^{eff})_{max}$ denotes the maximum effective confining pressure imposed on each sample; Q_{peak} denotes the differential stress ($\sigma_1 - \sigma_3$) at failure, *i.e.* at the onset of strain-softening behavior. $P_{stage3d}$ and $P_{stage3c}$ indicate the mean effective stress beyond which Stage 3d (non-linear, dilatant – see Figure 3.1) and Stage 3c behavior (non-linear, compactant) was seen, while $\Delta\varphi_{i,stage3d/c}$ refers to the corresponding inelastic porosity reduction. $\Delta\varphi_{t,fin}$ denotes the final total porosity reduction measured before the final unloading stage. $\Delta\varphi_{i,fin}$ denotes the final, inelastic porosity reduction measured at the end of each test after full unloading to the initial P of 5 MPa and Q of 0 MPa. $\bar{\rho}_{cr}$ denotes the mean crack density, defined as the number of cracks per mm^2 obtained in backscattered electron images. U, T and R indicate whether the sample was left undeformed (U), or else was tested in hydrostatic plus deviatoric compression in the triaxial vessel (T) or in purely hydrostatic compression in the Rene vessel (R). * monotonic loading without stress-cycling; ** no strain-softening observed.

Three of the short, 9.8 diameter, 20 mm long cylindrical plugs, taken from the depth intervals with long sample porosities of 13.4, 21.5 and 26.4%, were used for (purely) hydrostatic tests. These samples are identified with the suffix '*e*' (Table 3.1). These were drilled from 20 mm long cylindrical plugs with a diameter of 25.4 mm. These 9.8 mm diameter samples were prepared from these larger plugs by first soaking the latter in DMW to replace the saline brine, followed by drying (48 hours, at T = 50˚C). Subsequently, the plugs were impregnated using Polaroid B72 resin, in order to limit damage induced by drilling. The resin was cured at room temperature for 48 hours, after which the 9.8 mm diameter samples were drilled. After drilling, the resin was removed by soaking the samples in acetone for 6-7 days, refreshing the acetone every day, after which they were dried. Since sample drainage is not possible in the purely hydrostatic experiments (see subsequent section), these tests were performed at 50% pore fluid saturation and the same ion concentration as used in combined hydrostatic plus deviatoric tests. This was achieved by first saturating the short samples in full using 50% diluted brine. The mass difference between dry and saturated sample was used to determine the initial porosity, yielding similar values to those obtained for the long samples from the same depth interval, notably 13.9, 21.4 and 25.6% (Table 3.1). Prior to testing, the diluted pore fluid was allowed to evaporate to 50% saturation, using a mass balance.

3.3.2 Experimental apparatus

The combined hydrostatic plus deviatoric stress-cycling experiments were performed

using an externally heated, constant volume triaxial testing machine (*i.e.* the "Heard" apparatus), described in detail in Section 2.4.1. This triaxial machine is capable of operating at servo-controlled confining pressures up to 100 MPa, while axial (deviatoric) loading up to differential stresses of 800 MPa is achieved through motor-driven advancement of a yoke plus loading piston assembly at constant displacement rate.

Given the confining pressure limitations of the above triaxial apparatus, a second, higher pressure apparatus was employed for the purely hydrostatic stress-cycling tests, to ensure that Stage 3c behavior could be accessed in hydrostatic compression. This apparatus, referred to here as the Rene vessel, consisted of an externally heated, cold seal, 400 MPa pressure vessel made of Rene 41 super alloy, having an inner and outer diameter of 12 and 51 mm and containing a sealed cylindrical sample assembly.

Given the confining pressure limitations of the above triaxial apparatus (maximum P_c = 100 MPa), a second, higher pressure apparatus was employed for the purely hydrostatic stress-cycling tests, to ensure that Stage 3c behavior could be accessed. This consisted of an externally heated, cold seal, 400 MPa pressure vessel made of Rene 41 superalloy, with an inner diameter of 12 mm, and an outer diameter of 51 mm. Water was used as the confining medium, and pressure was applied to the sample using a 400 MPa, manually operated, Nova syringe pump (full stroke: 4.7 mL, accuracy: ±0.2 µL). The confining pressure was measured using an E. Brosa pressure transducer (1000 MPa full range) with a resolution of 0.01 MPa at P_c < 40 MPa, and of 0.1 MPa at P_c > 40 MPa. The temperature of the Rene vessel was measured using an Inconel-sheathed, K-type (chromel/ alumel) thermocouple penetrating 2 mm deep into its outer wall, and regulated using a CAL9900 controller that enabled control to within 0.1˚C of the set-point temperature. Pore fluid access to the sample is not possible using this apparatus. Hydrostatic tests were accordingly performed under undrained conditions, using samples incompletely-saturated with water vapor at the testing temperature and pore pressure, to buffer the pore fluid pressure at a value of $P_p \approx 0.1$ MPa under test conditions, *i.e.* at confining pressures up to 320 MPa and a temperature of 100°C.

3.3.3 Sample assembly and experimental procedure

3.3.3.1 Combined hydrostatic plus deviatoric experiments

These tests employed the samples prepared with a diameter of 25.4 mm. In setting up each run, the sample was removed from its brine-filled container and jacketed between an upper and lower loading blocks using a fluorinated ethylene propylene (FEP) sleeve. To reduce friction at the sample/end-block interface, a double layer consisting of two perforated Teflon sheets (50 μm) was included at each end of the sample. After tourniquet sealing, the

sample assembly was emplaced into the pressure vessel. The confining pressure was increased to 5 MPa. The pore fluid system was evacuated for 15 minutes, followed by application of the required pore pressure (P_p = 1 MPa) and confining pressure (P_c = 6 MPa), resulting in an effective confining pressure ($P_c^{eff} = P_c - P_p$) of 5 MPa. The sample was then brought to the desired testing temperature (T = 100°C), while maintaining P_c^{eff} below the initial effective value of 5 MPa used during the test. The sample and vessel were left to equilibrate to these pressure and temperature conditions for 4 hours.

Upon *P-T* equilibration, samples were either maintained at P_c^{eff} = 5 MPa (the lowest value for subsequent axial stress cycling), or else subjected to hydrostatic stress-cycling, at constant pore pressure, until an effective confining pressure of 20, 40, or 80 MPa was reached (the target value for subsequent axial stress cycling). During hydrostatic stress-cycling, the confining pressure was increased at a constant rate $\dot{P}$ of ~0.1 MPa/s to maximum values that were incremented by 5 MPa in each successive cycle. Each pressurization step was followed by depressurization to the initial P_c^{eff} value of 5 MPa, to determine any inelastic (permanent) pore volume changes. Upon achieving the target confining pressure and P_c^{eff} value for axial stress-cycling (5, 20, 40 or 80 MPa), P_c^{eff} was held constant and axial stress-cycling initiated. To achieve axial stress-cycling, we repeatedly loaded and unloaded the sample up to differential stress (σ_1–σ_3) values that were successively increased by 5 MPa (at P_c^{eff} = 5 MPa), or by 10 MPa (at P_c^{eff} = 20, 40, or 80 MPa). Each uploading step was followed by full piston retraction (*i.e.* [σ_1–σ_3] = 0 MPa), to measure the amount of permanent deformation developed in the foregoing stress-cycle. Loading and unloading was performed by applying a near-constant total axial strain rate ($\dot{\varepsilon}_t$) of ~ 10^{-5} s^{-1}, which for the present samples led to an equivalent $\dot{P}$ of 0.1 ± 0.05 MPa/s (as imposed during hydrostatic cycling). This procedure was repeated until the sample showed strain-softening behavior (*i.e.* failure), strain-neutral behavior, or a combination of decreasing strain-hardening rates and strongly non-linear, enhanced porosity reduction (*i.e.* a clear deviation from (quasi-)linear force versus pore fluid volume change behavior). Subsequently, each sample was axially unloaded (σ_1–σ_3 = 0 MPa), and depressurized to P_c^{eff} = 5 MPa. The sample was maintained at these conditions for several minutes to ensure a constant pore volume signal. Finally, the pore pressure was removed, followed by full reduction of the confining pressure, and the furnace was switched off. After cooling to ~80˚C, the sample assembly was removed from the testing machine.

To assess the effect of cyclic hydrostatic plus deviatoric loading on sample behavior, as opposed to monotonic loading, we performed a set of two control experiments on directly adjacent twin samples taken from the same core section (z74a and b; φ_0 = 19.1%, see Table

3.1). One sample (z74b) was monotonically loaded and unloaded, without hydrostatic or deviatoric stress-cycling, while the other was stress-cycled. The hydrostatic and deviatoric loading/unloading stages of both experiments were performed respectively up to- and at an effective confining pressure P_c^{eff} of 40 MPa, using the same baseline P_c^{eff} of 5 MPa, and the same conditions of P_p, T, $\dot{P}$, $\dot{\varepsilon}_t$ and pore fluid chemistry, as employed in all other experiments.

In addition, a set of three microstructural reference experiments was performed on samples with an initial porosity of φ_0 = 21.9% (Table 3.1), to investigate permanent microstructural changes occurring during loading to the point of strain-softening, *i.e.* failure. In these experiments, we imposed hydrostatic compression to a P_c^{eff} of 40 MPa (sample z77a), followed by deviatoric compression reaching Q values up to 50 MPa (sample z77b), followed by deviatoric compression to failure at Q values > 50 MPa (sample z77c). In each case, loading and unloading were performed monotonically to generate reference microstructures for the same stages of deformation explored in load-cycled samples. All other conditions were identical to the main body of tests.

3.3.3.2 Hydrostatic experiments

For these purely hydrostatic tests, we used the (400 MPa) Rene vessel and samples with a diameter of 9.8 mm. To ensure a constant pore pressure of 0.1 MPa throughout testing under undrained conditions (see Section 3.2), these tests were performed using 50 vol% saturated samples (see Section 3.1). Each sample was jacketed using a FEP sleeve and sealed between stainless steel end-pieces. Sealing was achieved using wire tourniquets tightened onto underlying EPDM rubber rings, countersunk into the end-pieces. The sample was subsequently emplaced in the fluid-filled pressure vessel and pressurized at 3 – 5 MPa. The temperature was then raised to 100˚C over 17 hours, while maintaining the confining pressure roughly constant. Upon temperature equilibration, P_c was raised to 5.1 MPa, while assuming that the pore pressure remained constant at 0.1 MPa due to partial saturation.

The confining pressure was then increased in 5 MPa steps, again assuming constant P_p. This was achieved by stepwise injection of confining fluid, leading to an increase in P_c of 5 MPa within 15 ± 2 seconds, in each step. Following each 5 MPa pressure step, the confining pressure was held constant for 30 seconds to allow manual reading of the instantaneous confining pressure, the injected confining fluid volume, and the temperature. The resultant average rate of change of the confining pressure per step was approximately 0.1 ± 0.02 MPa/s. Hydrostatic compression was continued until an effective confining pressure of 20 MPa was reached. At this stage, P_c was lowered in the same 5 MPa steps to

the initial value of 5.1 MPa, to allow for measurement of any inelastic volume changes. At this pressure, the confining pressure was held constant for 15 minutes, in order to ensure full *P-T* equilibration of the confining fluid volume. No, or negligible change in P_c was observed, implying that the pressurization rate was sufficiently low to allow *P-T* equilibration of the confining fluid during successive loading/unloading cycles.

In subsequent stress-cycles, this procedure was repeated, incrementing the maximum effective confining pressure imposed by 20 MPa in each cycle. The procedure was continued until a clear deviation from near-linear confining pressure versus injected fluid volume behavior was observed. Upon completion of the experiment, the temperature was lowered to $T \sim 80$ ˚C, the residual confining pressure of 5.1 MPa was removed, and the sample was extracted from the vessel.

3.3.4 Data acquisition and processing

We adopt the convention that compressive stress, compressive axial strain, and porosity reduction (i.e. compaction) are positive.

3.3.4.1 Combined hydrostatic plus deviatoric experiments

In these experiments, the internal axial load, confining pressure, pore pressure, pore fluid volume change, sample temperature, and axial displacement signals were logged at 2 Hz, using a 16-bit DAQPad National Instruments A/D converter. After correcting for apparatus distortion and thermal pore fluid volume changes during flow in and out of the vessel [*cf. Pijnenburg et al.*, 2018], these data were processed to yield the differential stress ($Q = \sigma_1 - \sigma_3$), the mean effective stress (P), the total axial strain $\varepsilon_t \approx e_t$ (small change in sample length / the initial sample length) and the total porosity reduction $\Delta\varphi_t$ (change in sample pore volume / divided by the initial sample volume) versus time. The peak strength (Q_{peak}) is defined as the maximum differential stress supported by a given sample before failure (*i.e.* strain-softening behavior) was observed.

The elastic behavior of the samples was quantified using the reversible behavior observed during the unloading stages of the hydrostatic and deviatoric load cycles. The bulk modulus (K) and Young's modulus (E) were determined at target mean effective stresses (P) of 10, 30, 50 and 85 MPa, by linear regression of the first P versus $\Delta\varphi_t$ unloading data and Q versus ε_t unloading data, respectively, both obtained within ± 2.5 MPa of the target P-value. The error in K and E resulting from linear regression analysis in the combined hydrostatic and deviatoric experiments lay within 1% of the determined values.

The inelastic (permanent) change in pore volume accumulated during stress-cycling

was obtained from the difference between the pore volumes measured at the start and end of each loading cycle, whether hydrostatic or deviatoric. The inelastic porosity reduction ($\Delta\varphi_i$) accumulated in successive cycles was determined from the sum of the permanent pore volume changes measured per cycle, divided by the initial (pre-test) sample volume V_0. For the small porosity reductions measured in this study, the use of V_0 as reference state, rather than the incremental sample volume, resulted in relative errors in $\Delta\varphi_i$ of < 5%. The inelastic axial strain was determined for each deviatoric stress-cycle by dividing the permanent change in sample length determined upon axial unloading, referenced to the sample length measured at the first axial loading stage, by the initial sample length L_0.

3.3.4.2 Hydrostatic experiments

In the purely hydrostatic stress-cycling experiments performed in the Rene vessel, the confining pressure, confining fluid volume and vessel temperature data were recorded manually upon each 5 MPa change of the confining pressure. Confining fluid volume data were obtained by recording the number of syringe pump rotations required to introduce a given confining pressure. The accuracy of this measurement was ± 0.2 µL. The resulting volumetric data were corrected for distortion of the pressure vessel, using pre-determined calibrations, and for thermal volume changes of the confining fluid during flow in and out of the heated pressure vessel. The corrected sample volume data (ΔV_s) were subsequently used to calculate total porosity reduction ($\Delta\varphi_t \approx \varepsilon_{v,t} = \Delta V_s/V_0$; accuracy ± 0.03%) versus confining pressure change and time. Thus, for the purpose of presenting and comparing the results in the first instance, we assume that the pore and bulk volume responses are equal. The data later demonstrate that this is a good approximation. For each unloading stage, K was determined at target mean effective stresses of 30, 50 and 85 MPa and in a similar manner to that used in the combined hydrostatic plus deviatoric experiments, but employing a mean effective stress range of ± 15 MPa to compensate for the lower data sampling frequency. The error in K resulting from linear regression analysis of our hydrostatic stress-cycling data was ± 10% of the determined value. The inelastic porosity reduction ($\Delta\varphi_i$) occurring in each stress cycle was determined by dividing the permanent change in sample volume, determined after hydrostatic unloading to the starting effective confining pressure of 5 MPa, by the initial sample volume V_0.

3.3.5 Microstructural analysis

To investigate the distribution of intragranular cracks in the deformed versus undeformed samples, and hence to assess any tendency for localization of brittle deformation,

we performed quantitative microstructural analysis of crack density on all 21.9% porosity samples used in microstructural reference tests (z77a-c), all 21.4 – 21.5% porosity samples used in hydrostatic and hydrostatic plus deviatoric stress-cycling tests (z24a-e), and the 13.4% (z20c) and 26.4% (z84c) porosity samples, tested in the hydrostatic plus deviatoric stress-cycling tests performed at a maximum effective confining pressure of 40 MPa. The undeformed counterparts of these samples were also analyzed. Deformed samples were extracted from the relevant apparatus, the jacket was removed and the brine was replaced by demineralized water (DMW) by soaking the sample in DMW for 6-7 days. After drying, the deformed and undeformed samples were impregnated with Araldite 2020 resin, sectioned, and sputter-coated with a 6 nm layer of Pt/Pd. They were then imaged in full using a FEI Helios Nanolab G3 Focused Ion Beam scanning electron microscope operated in backscatter electron (BSE) mode, using a solid state concentric backscatter detector [*Sakic et al.*, 2011]. We used an acceleration voltage and beam current of 10 kV and 1.6 to 3.2 nA, and employed a working distance of 3 to 5 mm. All samples were imaged by compiling tiled photomosaics. For each tile, we employed a horizontal field width of 1.18 mm and a dwell time of 3 μs. Photomosaic stitching was done using ImageJ [*Preibisch et al.*, 2009]. Stitched images were used to investigate the role played by intragranular cracking in accommodating the inelastic deformation measured in our experiments, focusing on the effects of the imposed state of stress and the initial sample porosity. Thick (~ 1 mm) sections were prepared from undeformed material and a representative selection of our experimentally deformed samples.

The analyses were conducted along an axial profile traversing the full length of each sample studied, using stitched, BSE micrographs. For each sample, we analyzed a 1 mm wide strip, manually outlining each visible crack using ImageJ software. Thus, in each sample a total area of 20 to 65 mm^2 was analyzed (containing ~800 – 3000 grains), depending on the length of the sample investigated. From these data, crack densities, defined as the number of intragranular cracks per mm^2, were obtained as a function of position along the length of each sample. Mean crack densities ($\bar{\rho}_{cr}$), and the standard deviation (SD) of the crack density distribution were also computed.

3.4 Stress-cycling test results

In addition to the basic sample data, Table 3.1 lists the experiments performed, the corresponding experimental conditions, and key items of the mechanical and microstructural data obtained.

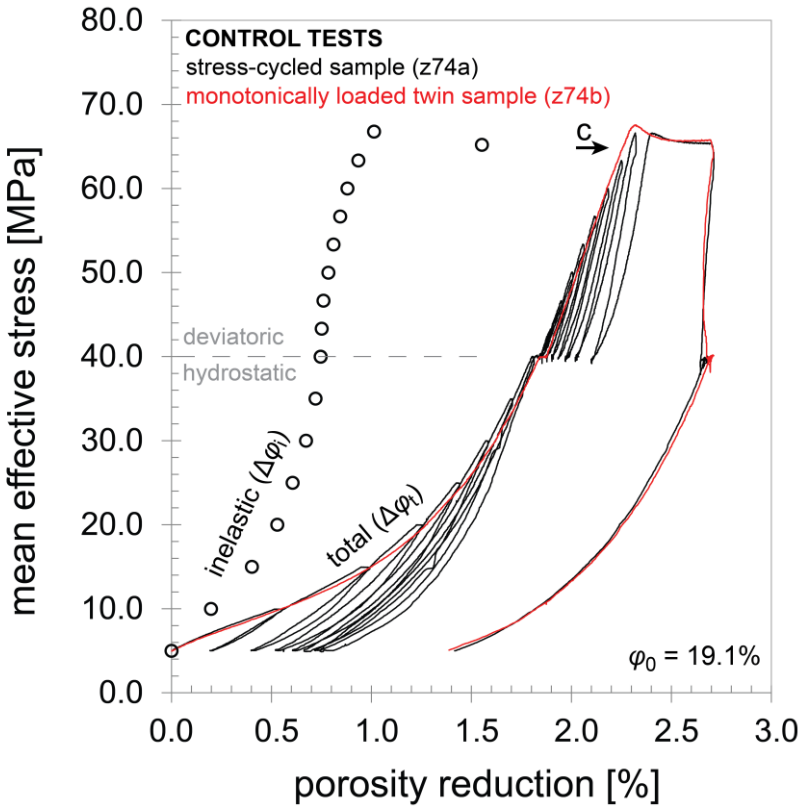

Figure 3.2: Plot showing mean effective stress (P) versus total porosity reduction ($\Delta\varphi_t$) and inelastic porosity reduction data ($\Delta\varphi_i$) obtained for stress-cycled sample z74a, alongside the P - $\Delta\varphi_t$ data obtained during monotonic loading and final unloading of twin sample z74b. In both cases, hydrostatic compression up to P = 40 MPa was followed by axial compression at constant effective confining pressure. The arrow and annotation 'c' indicate the onset of Stage 3c behavior(*cf.* Figure 3.1) in both samples. The stress-cycled sample (z74a) demonstrates inelastic (permanent) compaction throughout compression. Both samples show very similar P - $\Delta\varphi_t$ behavior, implying negligible damaging of samples by stress cycling.

3.4.1 Control experiments: stress-cycling versus monotonic loading behavior

The mean effective stress (P) versus total porosity reduction ($\Delta\varphi_t$) data obtained

during the hydrostatic plus deviatoric stress-cycling experiment performed on sample z74a (φ_0 = 19.1%) are presented in Figure 3.2, alongside the monotonic loading and then unloading data obtained for twin sample z74b. Both samples were subjected to hydrostatic compression up to P_c^{eff} = 40 MPa, followed by deviatoric compression at constant P_c^{eff}. Despite the cyclic versus monotonic loading paths, the P - $\Delta\varphi_t$ behavior shown by both samples is very similar. Both exhibit concave-up P - $\Delta\varphi_t$ behavior up to $P \approx 35$ MPa, followed by near-linear behavior up to $P \approx 65$ MPa. Within the near-linear region, the total hardening rate (*i.e.* the slope $dP/d\Delta\varphi_t$) was 5.8 GPa. At $P > 65$ MPa, this rate decreased towards peak strengths of P = 66.5 MPa (z74a; Q_{peak} = 79.5) and 67.5 MPa (z74b; Q_{peak} = 82.7 MPa) reached at $\Delta\varphi_t \approx 2.3\%$, followed by strain-softening and then strain-neutral behavior, reached at $\Delta\varphi_t \approx 2.5\%$. Upon unloading, the samples again displayed closely similar P - $\Delta\varphi_t$ behavior, yielding near-identical final inelastic porosity reductions ($\Delta\varphi_{i,fin}$ – Table 3.1) of 1.4 ± 0.02% at the reference P value of 5 MPa. Note that the stress-cycled sample z74a showed inelastic porosity reduction after every stress-cycle, as shown by the open circle data points in Figure 3.2. Note also the S-shaped curve defined by these data, with a more or less constant inelastic hardening rate (*i.e.* the slope $dP/d\Delta\varphi_i$) of approximately 14 GPa characterizing the stress interval between $P \approx 35$ MPa and 65 MPa.

3.4.2 Mechanical data for low, intermediate and high porosity sample sets

3.4.2.1 Combined hydrostatic plus deviatoric test data

Figure 3.3 shows the mechanical data obtained during the combined hydrostatic plus deviatoric stress-cycling experiments performed on the low (φ_0 = 13.4%), intermediate (φ_0 = 21.5%) and high porosity (φ_0 = 26.4%) sample sets listed in Table 3.1.

All samples showed typical Stage 1, 2 and 3d or 3c mean effective stress (P) versus total porosity reduction ($\Delta\varphi_t$) behavior of the type often described in the literature (compare Figures 3.3a-c with Figure 3.1). At the lowest effective confining pressure tested (P_c^{eff} = 5 MPa), samples showed a transition from initial, non-linear, concave-up behavior (*cf.* Stage 1, in Figure 3.1) to non-linear, dilatant behavior (Stage 3d), at mean effective stresses ($P_{stage3d}$ – indicated by arrows and annotation *d* in Figures 3.3a-c; see also: Table 3.1) ranging from 7 MPa (high initial porosity) to 11 MPa (low initial porosity). At these low values of P_c^{eff}, near-linear Stage 2 behavior was not seen. All other tests ($P_c^{eff} \geq 20$ MPa) showed Stage 1 behavior up to $P \approx 35$ MPa, followed by near-linear P – $\Delta\varphi_t$ behavior (Stage 2). During this near-linear stage, the total hardening rate (*i.e.* $dP/d\Delta\varphi_t$) decreased with increasing initial porosity, yielding 8.3 ± 0.5 GPa in low porosity sandstones, 5.7 ± 0.4 GPa at intermediate porosities and 4.1 ± 0.5 GPa in high porosity samples. These Stage 2 hardening rates were

similar in both hydrostatic and deviatoric loading, implying isotropic behavior. For all samples tested at P_c^{eff} = 20 MPa, and the low porosity sample tested at P_c^{eff} = 40 MPa, deviation from these near-linear trends was characterized by dilation (Stage 3d). At higher P_c^{eff} and initial porosity, our samples showed non-linear compaction (Stage 3c, marked by $P_{stage3c}$ in Table 3.1). The inelastic porosity reductions ($\Delta\varphi_{i,stage3d/c}$) at these dilatant and compactant deviations from linearity are listed in Table 3.1. Inelastic porosity reduction ($\Delta\varphi_i$; open circles in Figure 3.3) was observed after every hydrostatic and deviatoric stress-cycle, in all experiments. The P - $\Delta\varphi_i$ behavior was qualitatively similar to that shown by $P - \Delta\varphi_t$ data, showing a transition from Stage 1 to Stage 3d behavior at the lowest P_c^{eff} of 5 MPa, and from Stage 1 to Stage 2 and ultimately Stage 3c behavior at higher P_c^{eff} (Figures 3.3a-c). However, for each stage, the observed P - $\Delta\varphi_i$ behavior was stiffer by a factor of 1.5 to 3. During Stage 2, inelastic hardening rates were found to be 27.8 ± 1.2 GPa (low φ_0), 16.7 ± 0.7 GPa (intermediate φ_0) and 9.8 ± 0.5 GPa (high φ_0). These rates were again found to be similar for both hydrostatic and deviatoric stress cycles.

During the deviatoric stages of the combined hydrostatic plus deviatoric experiments, differential stress (Q) versus total axial strain (ε_t) and inelastic axial strain (ε_i) data showed S-shaped behavior, where non-linear Q - ε_t and ε_i behaviors transitioned into near-linear strain hardening trends at Q > 5 to 10 MPa (Fig 4d-f) . These near-linear Q - ε_t and ε_i trends were followed by strain hardening at a decreasing rate, which, in most of our samples, led to a peak strength (Q_{peak}; listed in Table 3.1) followed by strain-softening (*i.e.* failure). However, in the more porous samples ($\varphi_0 \geq 21.5\%$), deviatorically compressed at the highest P_c^{eff} of 80 MPa, the peak strength was not attained and strain hardening continued at decreasing rates to the end of the experiment. Where attained, peak strength values increased with increasing P_c^{eff} and with decreasing φ_0 (Table 3.1). The final inelastic porosity reductions attained in each experiment are listed in Table 3.1.

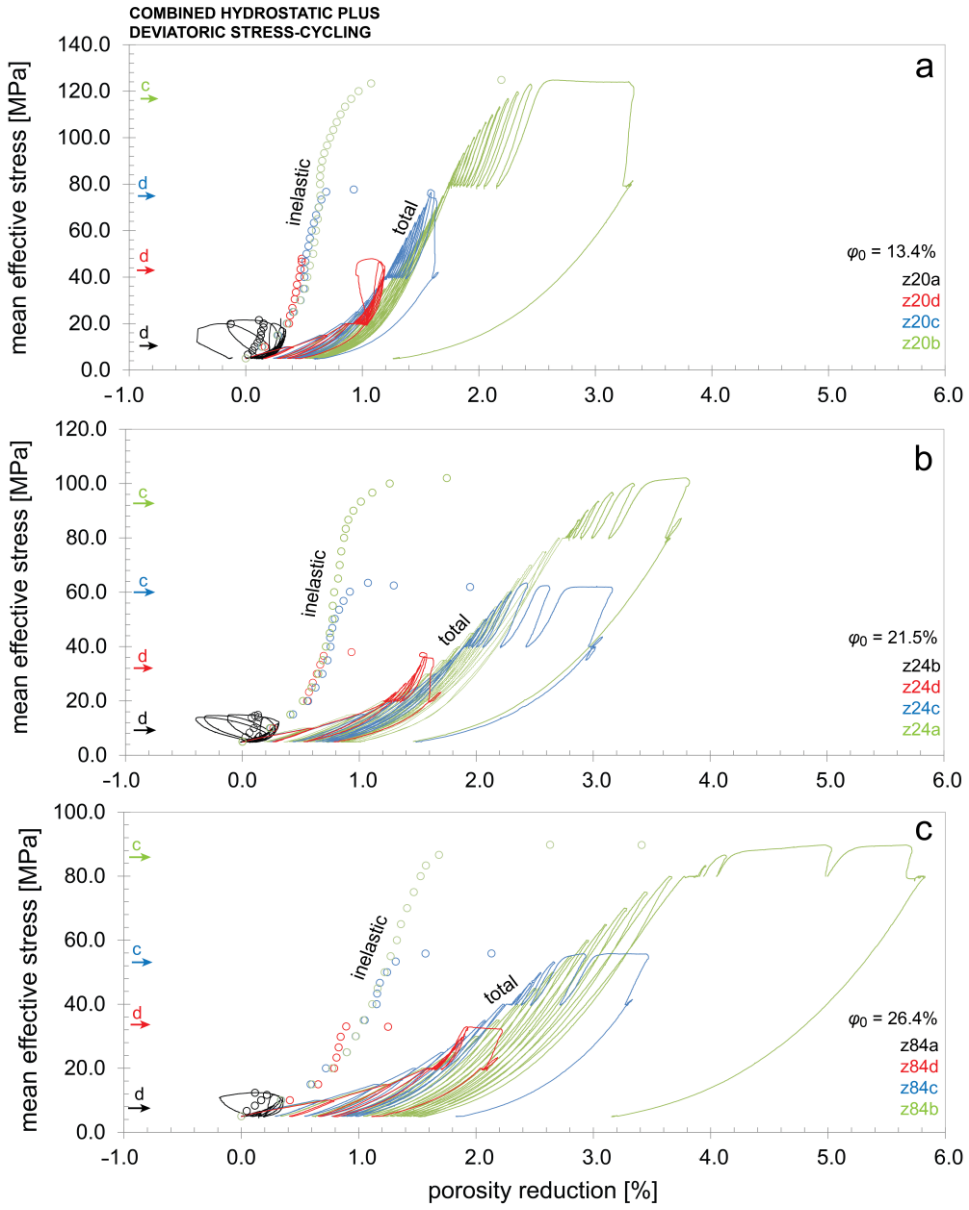

Figure 3.3 Plots showing the mechanical data obtained in our combined hydrostatic plus deviatoric stress-cycling experiments performed in the triaxial vessel on samples with low (φ_0 = of 13.4%; left column), intermediate (φ_0 = 21.5%; middle column) and high initial porosities (φ_0 = 26.4%; right column). Here, hydrostatic stress-cycling up to effective confining pressures (P_c^{eff}) of 5, 20, 40 and 80 MPa was followed by deviatoric stress-cycling at constant P_c^{eff}. **a-c)** Mean effective stress versus total- ($\Delta\varphi_t$; solid curves) and inelastic porosity reduction data ($\Delta\varphi_i$; open circles). (Figure and caption are continued on next page).

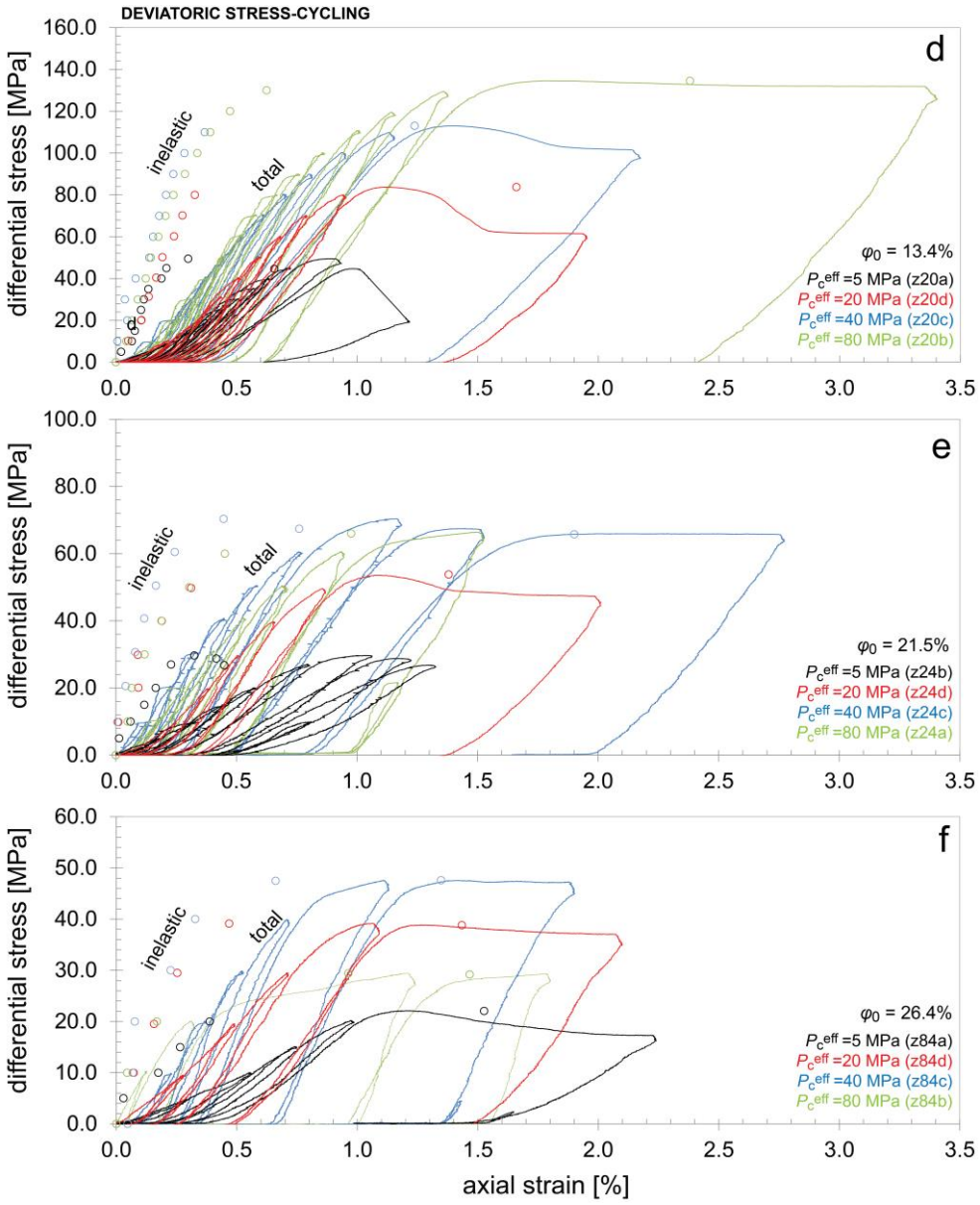

Figure 3.3 (cont.) For all initial porosities explored here, the P - $\Delta\varphi_t$ and P - $\Delta\varphi_i$ data obtained show a typical sequence of initial Stage 1 (non-linear, concave-up), Stage 2 (near-linear), and Stage 3d (non-linear, dilatant) or Stage 3c (non-linear, compactant) behavior (compare with Figure 3.1). Arrows + annotations 'd' and 'c' indicate the onset of Stage 3d or c, respectively (see panels a-c). Inelastic porosity reduction is seen during all stages, including the near linear Stage 2, which is often assumed to reflect poroelasticity. **(d-f)** Plots showing differential stress Q versus total (ε_t; solid curves) and inelastic axial strain (ε_i; open circles) data.

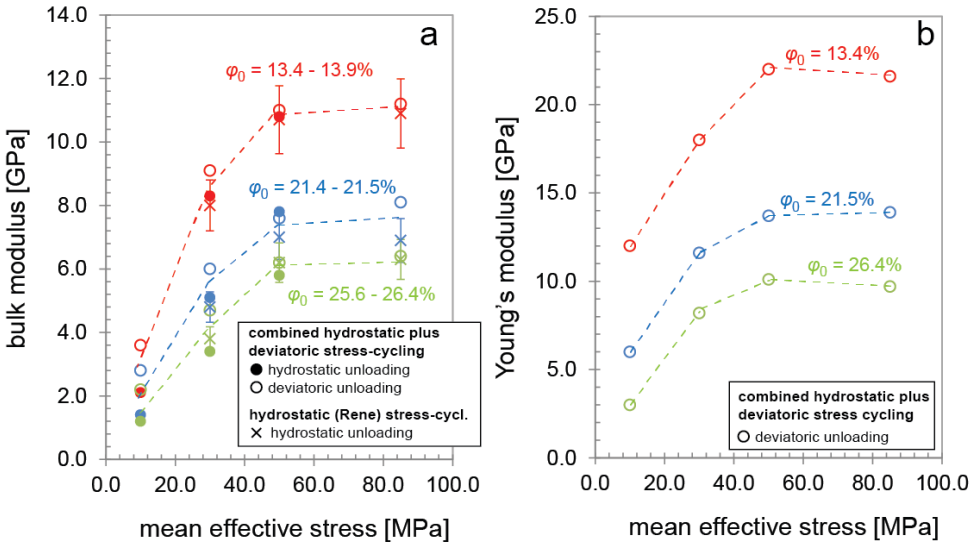

Figure 3.4 Plots showing **a)** bulk modulus (K) and **b)** Young's modulus (E) versus mean effective stress (P) data, obtained using both hydrostatic and deviatoric unloading data of combined hydrostatic plus deviatoric experiments performed in the triaxial vessel on samples with low (φ_0 = of 13.4%), intermediate (φ_0 = of 21.5%) and high initial porosities (φ_0 = of 26.4%). K values are compared to the bulk moduli obtained from the unloading curves of the hydrostatic experiments performed in the Rene vessel (see Figure 3.5), using samples with similar φ_0 of 13.9%, 21.4% and 25.6%. Note that K values obtained using the hydrostatic unloading data obtained in the Triaxial vessel versus those obtained in the Rene vessel are similar within the error in the K values determined using Rene vessel data.

Bulk moduli (K) determined from both hydrostatic and deviatoric unloading data, and the Young's moduli (E) obtained from deviatoric unloading data, are plotted versus the mean effective stresses (P) of 10, 30, 50 and 85 MPa at which K and E were determined, in Figure 3.4. Both K (Figure 3.4a) and E (Figure 3.4b) increase with increasing P and decreasing φ_0, reaching constant values at $P \geq 50$ MPa. At $P \leq 30$ MPa, bulk moduli obtained in deviatoric unloading stages are higher by 1 to 2 GPa than the corresponding hydrostatic values (Figure 3.4a). By contrast, at $P \geq 50$ MPa, deviatoric and hydrostatic K values are similar to within 0.3 GPa.

3.4.2.2 Hydrostatic test data (Rene vessel)

The mean effective stress (P) versus total ($\Delta\varphi_t$) and inelastic porosity reduction ($\Delta\varphi_i$) data obtained in the purely hydrostatic experiments performed in the Rene vessel on our low (φ_0 = 13.9%), intermediate (φ_0 = 21.4%) and high porosity (φ_0 = 25.6%) samples are presented in Figure 3.5. The P versus $\Delta\varphi_t$ and $\Delta\varphi_i$ curves obtained for each sample (*i.e.* each porosity) show S-shaped behavior, again reflecting evolution from Stage 1 to Stage 2 and ultimately Stage 3c behavior (*cf.* Figure 3.1). Non-linear, concave-up Stage 1 behavior was seen up to $P \approx 35$ MPa, followed by a near-linear Stage 2 trend (Figure 3.5). During Stage 2, the total and inelastic hardening rates were roughly similar to those obtained in the Stage 2 intervals of combined hydrostatic plus deviatoric tests, yielding $dP/d\Delta\varphi_t$ values of 7.5 GPa (low φ_0), 5.7 GPa (intermediate φ_0) and 4.1 GPa (high φ_0) while the $dP/d\Delta\varphi_i$ values were 25.4, 17.0 and 11.3 GPa, respectively. In the low porosity sample, this near-linear behavior persisted up to $P \approx 220$ MPa, beyond which hardening rates gradually decreased (Stage 3c) leading to a marked inelastic porosity reduction of 0.6% in the P-interval of 315 to 320 MPa (Figure 3.5a). Higher porosity samples showed non-linear, concave-down compaction (Stage 3c) in the P-intervals of 130 to 150 MPa (φ_0 = 21.4%; Figure 3.5b) and of 125 to 140 MPa (φ_0 = 25.6%; Figure 3.5c), beyond which the samples hardened at increasing rates up to the highest P of 160 imposed. Note that aside from the similar hardening rates shown during Stage 2, the values of $\Delta\varphi_t$ and $\Delta\varphi_i$ determined at given mean effective stress and initial porosity values are similar within ~10% to the values measured during the hydrostatic stages of our combined hydrostatic plus deviatoric experiments (see Figure 3.3a-c), at least up to the highest hydrostatic P of 80 MPa explored in the latter.

Bulk moduli (K) determined from our hydrostatic (Rene vessel) unloading data at P values of 30, 50 and 85 MPa are presented in Figure 3.4a, where they are compared to the hydrostatic bulk moduli obtained in our hydrostatic plus deviatoric experiments. For given P and similar φ_0 values, K values obtained in the purely hydrostatic (Rene) experiments are similar to those obtained in the hydrostatic unloading stages of combined hydrostatic plus deviatoric experiments, within the error of 10% determined for the former (Rene) set of K (Figure 3.4a). Note that the similar P versus $\Delta\varphi_t$, $\Delta\varphi_i$ and K behaviors obtained using the pore volume data of combined hydrostatic plus deviatoric tests versus those determined using the bulk volume data of the hydrostatic (Rene) tests suggests that our initial assumption of roughly equal bulk and pore volume responses (see Section 3.4.2) was a good approximation.

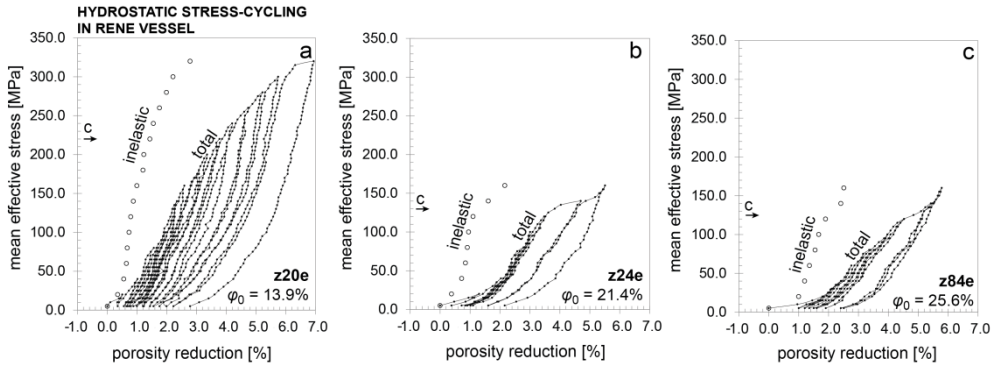

Figure 3.5 Plots showing mean effective stress (P) versus total ($\Delta\varphi_t$) and inelastic porosity reduction ($\Delta\varphi_i$) data obtained in our purely hydrostatic stress-cycling experiments performed in the Rene vessel on samples with **a)** low (φ_0 = 13.9%), **b)** intermediate (φ_0 = of 21.4%) and **c)** high initial porosities (φ_0 = 25.6%). These samples were obtained from the same depth interval as the samples used in the stress-cycling experiments shown in Figure 3.3. P - $\Delta\varphi_t$ and P – $\Delta\varphi_i$ data show typical Stage 1 (non-linear, concave-up), 2 (near-linear) and 3c (non-linear, concave-down) behavior (*cf.* Figure 3.1). Arrows indicate the onset of Stage 3c behavior in each experiment ($P_{stage3c}$; Table 3.1).

3.4.3 Sample-scale observations and microstructural data

3.4.3.1 Sample-scale

Post-test, visual inspection of samples tested in combined hydrostatic plus deviatoric stress-cycling experiments revealed a single shear-fracture in each of the low porosity samples that showed Stage 3d (*i.e.* dilatant) behavior at effective confining pressures P_c^{eff} of 5, 20 and 40 MPa (samples z20a, z20d and z20c, respectively). In these samples, the angle of the fracture plane to the core axis (*i.e.* the main compression direction) increased from 25 to 40 degrees with increasing test P_c^{eff}. The low porosity sample z20b, which showed Stage 3c behavior during deviatoric stress-cycling at P_c^{eff} = 80 MPa (Figure 3.3a) and the intermediate porosity sample z24d, yielding Stage 3d behavior during deviatoric stress-cycling at P_c^{eff} = 20 MPa (Figure 3.3b), revealed multiple, conjugate fractures, located within 20 mm of one sample end. These fractures were orientated at an angle of about 70 ± 10° to the core axis. No macroscopically visible deformation features were observed in any of the remaining experiments, deviatoric or hydrostatic.

3.4.3.2 Microstructure

Mean crack density data obtained as described in Section 3.3.5 from backscatter electron (BSE) images of our deformed samples and of their undeformed counterparts are shown in Table 3.1. Profile lines showing the crack density distribution determined along core axis-parallel sections of backscatter electron (BSE) micrographs of microstructures recovered from all intermediate porosity samples (φ_0 = 21.4 – 21.5%; z24a-e) deformed in combined hydrostatic plus deviatoric experiments (z24a-d) and purely hydrostatic (Rene) experiments (z24e) are shown in Figure 3.6, where they are compared to their undeformed counterpart (z24). In addition, crack density profiles obtained from the low (φ_0 = 13.4%; z20c) and high porosity sample (φ_0 = 26.4%; z84c), recovered after hydrostatic plus deviatoric experiments at P_c^{eff} = 40 MPa are shown. For all deformed samples, the reference mean crack density obtained in the undeformed sample with the same initial porosity is indicated (dashed vertical line).

All deformed samples showed higher mean crack densities than those measured in the undeformed counterparts (Figure 3.6). In intermediate porosity samples (Figure 3.6a-f), mean crack densities increased with increasing $(P_c^{eff})_{max}$, where the lowest and highest values of 8.4 and 72.8 mm^{-2} were measured in, respectively our undeformed sample (Figure 3.6a), and sample z24e, hydrostatically deformed in the Rene vessel (Figure 3.6f). In the undeformed sample, the crack density distribution was roughly uniform along the full length of the sample, yielding values within the range of ± 3.3 mm^{-2} from the mean. By contrast, all deformed samples showed a non-uniform crack density distribution. After deviatoric testing at a P_c^{eff} of 5 MPa, elevated (relative to the undeformed sample) crack densities up to 40 mm^{-2} were seen within a narrow interval spanning 50 to 57 mm measured from the top of the sample (Figure 3.6b). In the other sections of the sample, the crack density remained virtually unchanged. At P_c^{eff} = 20 MPa, the crack density profile line intersected the multiple, conjugate deformation bands seen at the sample-scale, at 46 to 56 mm from the top, where elevated crack densities up to 45 mm^{-2} were measured. Again, crack densities remained virtually unchanged along the rest of the profile line. After deviatoric testing at P_c^{eff} = 40 MPa, intragranular cracking was more wide-spread, and most pervasive along 33 to 58 mm from the top, where crack densities reached up to 90 mm^{-2}. Along the other portions along the profile line, crack densities were lower (typically ~ 30 mm^{-2}; Figure 3.6d). At P_c^{eff} = 80 MPa, high crack densities up to 80 mm^{-2}, were shown at 2, 17, 30 and 60 mm from the top of the sample. In the case of these latter two samples (deviatorically compressed at P_c^{eff} = 40 and 80 MPa), viewing the stitched micrographs at multiple scales, one can see that these high crack densities reflect intersection of the profile line with diffuse bands of high crack density,

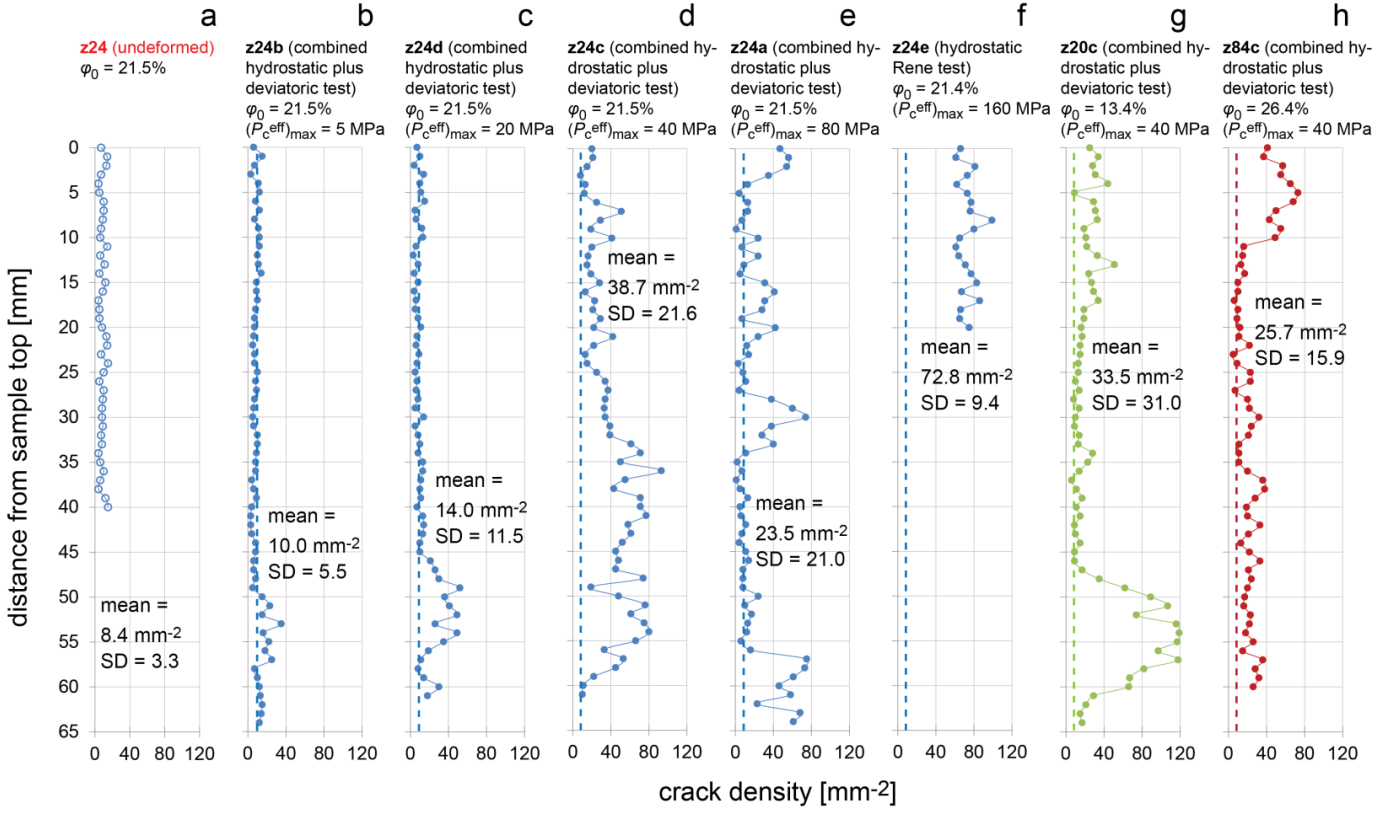

Figure 3.6 (Caption on next page)

Figure 3.6 Plots showing crack densities as a function of sample length, measured along axis-parallel profile lines of stitched, backscattered electron images of a selection of undeformed and deformed samples. We analysed all intermediate porosity samples (φ_0 = 21.4 to 21.5%), whether these were **a)** undeformed, or tested in hydrostatic plus deviatoric compression at a (maximum) effective confining pressure $(P_c^{eff})_{max}$ of **b)** 5 MPa; **c)** 20 MPa; **d)** 40 MPa; or **e)** 80 MPa, or else tested in **f)** purely hydrostatic (Rene) tests, up to a $(P_c^{eff})_{max}$ of 160 MPa. In panels b-e, the undeformed mean crack density is indicated for reference, by the dashed line. We also analysed **g)** a low porosity sample (φ_0 = 13.4%); and **h)** a high porosity sample (φ_0 = 26.4%), tested in hydrostatic plus deviatoric compression at $(P_c^{eff})_{max}$ = 40 MPa, as well as their undeformed counterparts (undeformed mean crack densities indicated in panels g and h by the dashed line).

as exemplified for sampe z24a in Figure 3.9a. These bands are oriented at a high angle to the core axis (70 to 90°), hence to the main compression direction. The hydrostatically deformed sample showed a more uniform crack density along the sample length, yielding a range of ± 15 mm^{-2} around the mean (Figure 3.6f). In the undeformed, low porosity sample, the mean crack density was 7.3 mm^{-2}. In the sample tested in deviatoric experiments at P_c^{eff} = 40 MPa, the profile line intersected the single shear fracture seen at the sample-scale, at 50 to 60 mm from the top. Within this interval, high crack densities up to 119 mm^{-2} were seen (Figure 3.6g). In other locations, any increase in crack density was much smaller (< 40 mm^{-2}). In the undeformed, high porosity sample, the mean crack density was 11.6 mm^{-2}. After deviatoric testing at P_c^{eff} = 40 MPa, crack densities showed significant increases up to 70 mm^{-2} within a discrete band near the top end of the sample (< 11 mm), oriented roughly perpendicular to the core axis. In the other portions of the sample, any increases in crack density were much lower, or absent (Figure 3.6h).

3.5 Microstructural reference test results

3.5.1 Mechanical data

It will be recalled that these experiments consisted of combined hydrostatic plus deviatoric tests performed on samples with an intermediate initial porosity of 21.9% (z77a-c). The experiments consisted of monotonic, hydrostatic and then deviatoric loading and unloading only (no cycling). The mean effective stress versus total porosity reduction data obtained in these tests are presented in Figure 3.7. The data show closely reproducible uploading behavior. All samples showed concave-up P - $\Delta\varphi_t$ behavior up to $P \approx 35$ MPa and $\Delta\varphi_t \approx 2.0\%$. Samples z77b and c showed near-linear behavior beyond this, up to $P \approx 58$ MPa

(Q = 54 MPa), and $\Delta\varphi_t \approx 2.8\%$, at which point z77b was unloaded. Further loading of sample z77c produced a short interval of strain-hardening at decreasing rate (Stage 3c), leading to a broad peak in mean effective stress of P = 59.7 MPa (Q_{peak} = 59.1 MPa), at $\Delta\varphi_t$ = 2.9%, after which minor strain softening occurred (< 1 MPa). After unloading to the reference mean effective stress of 5 MPa, samples z77a, z77b and z77c showed final inelastic porosity reductions ($\Delta\varphi_{i,fin}$) of 1.24%, 1.35% and 1.68%, respectively. Overall, the P - $\Delta\varphi_t$ behavior shown was closely similar to that obtained in the stress-cycled, hydrostatic plus deviatoric experiments performed at the same conditions on sample z24c with similar initial porosity (φ_0 = 21.5%) (Figure 3.3b).

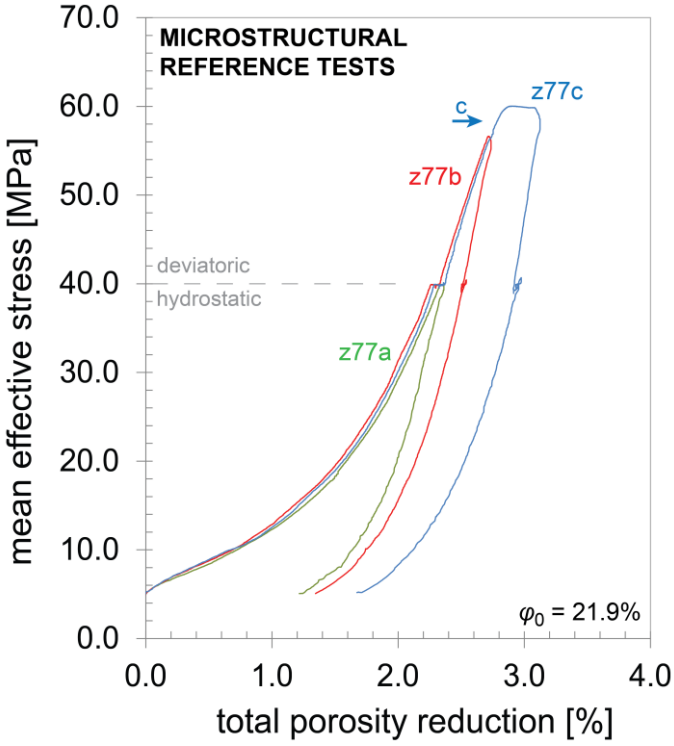

Figure 3.7 Plot showing mean effective stress (P) versus total porosity reduction ($\Delta\varphi_t$) data obtained in our hydrostatic plus deviatoric microstructural reference tests. Samples z77a, z77b and z77c were deformed up to parts of the P - $\Delta\varphi_t$ curve corresponding approximately to the end of Stage 1, Stage 2 and Stage 3c, respectively, as defined in Figure 3.1. These samples were used to investigate the grain-scale mechanisms accommodating inelastic compaction in each of these stages.

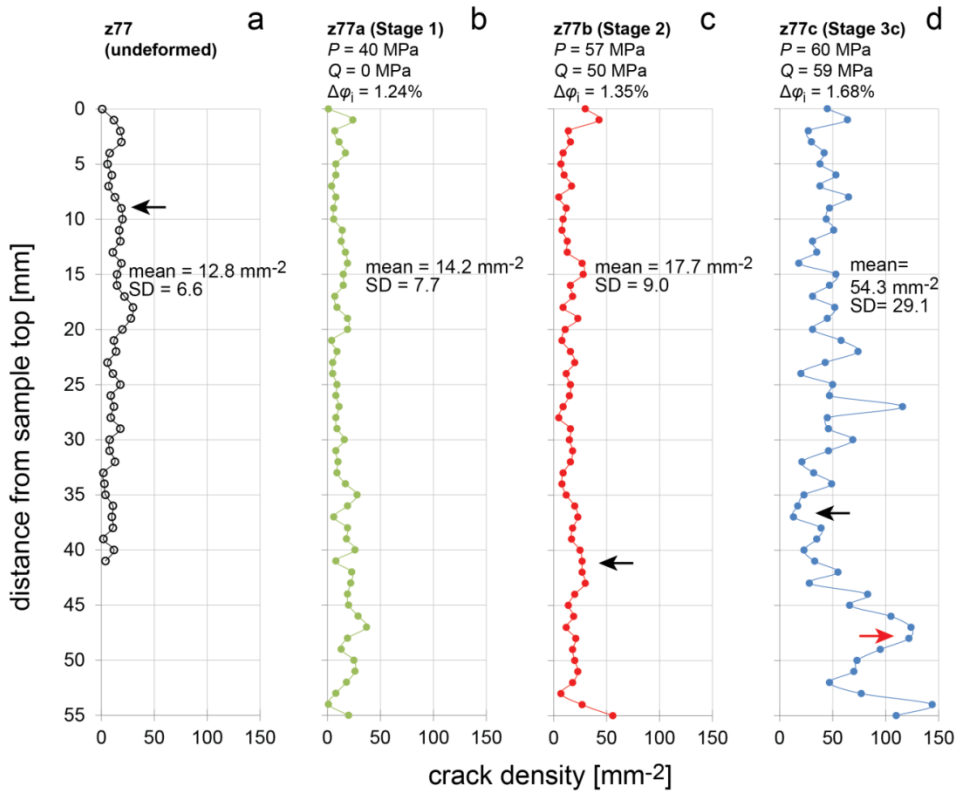

Figure 3.8 Plots showing the intragranular crack density (cracks per mm^2) distribution along the length of each sample (φ_0 = 21.9%) deformed in microstructural reference tests (Figure 3.7), and of their undeformed counterpart. Mean crack densities, the standard deviation of the crack density distribution (SD), and the final inelastic porosity reductions ($\Delta\varphi_{i,fin}$) measured at the end of each test are indicated. Arrows indicate the sample depths of the micrographs shown in Figure 3.10. **a)** Undeformed sample z77, showing a roughly uniform crack density distribution. **b)** Sample z77a, deformed into Stage 1**. c)** Sample z77b, deformed into Stage 2. **d)** Sample z77c, deformed into Stage 3c, and beyond failure. Note the markedly increased, heterogeneously distributed crack densities in this sample**.**

3.5.2 Microstructural data

The intragranular crack densities determined along the plug axis of reference test samples z77a-c (φ_0 = 21.9%) and undeformed counterpart sample z77 are plotted in Figure 3.8. The undeformed sample shows a mean crack density ($\bar{\rho}_{cr}$) of 12.8 mm^{-2} (Figure 3.8a). The distribution of crack densities along the length of the sample is roughly uniform, and is characterized by a standard deviation (SD) of 6.6 mm^{-2} from the mean. In samples z77a,

compressed hydrostatically to P_c^{eff} = 40 MPa, and z77b, which was additionally loaded deviatorically to Q = 50 MPa, the mean crack densities are slightly higher, specifically 14.2 and 17.7 mm^{-2}, respectively (Figures 3.8b and c). In sample z77a, the crack density distribution is still approximately uniform (SD = 7.7 mm^{-2}). In sample z77b, the crack density distribution remains uniform in the bulk of the sample, but higher values are locally seen near the top and bottom of this sample, reaching 50 mm^{-2}. By contrast, Sample z77c, deviatorically compressed at P_c^{eff} = 40 MPa beyond the peak stress (P = 59.7 MPa, Q_{peak} = 59.1 MPa), shows a mean crack density of 55.3 mm^{-2}. Moreover, the crack density distribution is highly heterogeneous (SD = 29.1), locally showing values as high as 70 – 150 mm^{-2}, notably at 27 mm and 44 - 51 mm from the sample top and in the bottom 3 mm of the sample (Figure 3.8c). Viewing the micrographs at multiple scales showed that these high crack densities reflect intersection with 2 – 10 mm wide, diffuse bands of high crack density, which are oriented sub-perpendicular (± 20°) to the main compression direction (*e.g.* Figure 3.9b).

To illustrate the general microstructural character of our microstructural reference test samples, representative BSE micrographs were selected from the locations indicated in Figure 3.8 (arrows), and are presented in Figure 3.10. The undeformed sample (Figure 3.10a) is composed of predominantly quartz grains (~75 vol%), with lesser amounts of feldspar (~20 vol%), and clays (~5 vol%). The latter two are clearly highlighted in an Al element map obtained using electron dispersive X-ray (EDX) spectrometry (Figure 3.10b). Quartz and feldspar grains are typically 100 – 200 µm in size, subrounded, slightly elongated, and frequently oriented with their long axes perpendicular to the sample/core axis (= parallel to sedimentary lamination). Clay films coating the pore walls are often relatively thick (5 – 20 µm), while thinner clay films (1 - 5 µm) are found within grain contacts (Figures 3.10b,d). In both undeformed and deformed samples, intragranular cracks typically emanate from the periphery of grain-to-grain contacts (yellow arrows, in Figure 3.10), or from within grain contacts (white arrows), where they are often found at small grain contact asperities (< 10 µm), or at intergranular pores (Figure 3.10d). In parts of the deformed samples where the intragranular crack density is relatively low (< 30 mm^{-2}; see black arrows, in Figure 3.8), the corresponding microstructure (Figure 3.10c-e) is essentially indistinguishable from that of the undeformed counterpart (Figure 3.10a). By contrast, in the high crack density regions seen in deformed sample z77c (*e.g.* red arrow, Figure 3.8d), intragranular and transgranular cracks are ubiquitous, being associated with pervasive grain crushing in triangular regions at quartz/feldspar grain contacts, and in transgranular zones spanning individual and multiple grains (red arrows, Figure 3.10f).

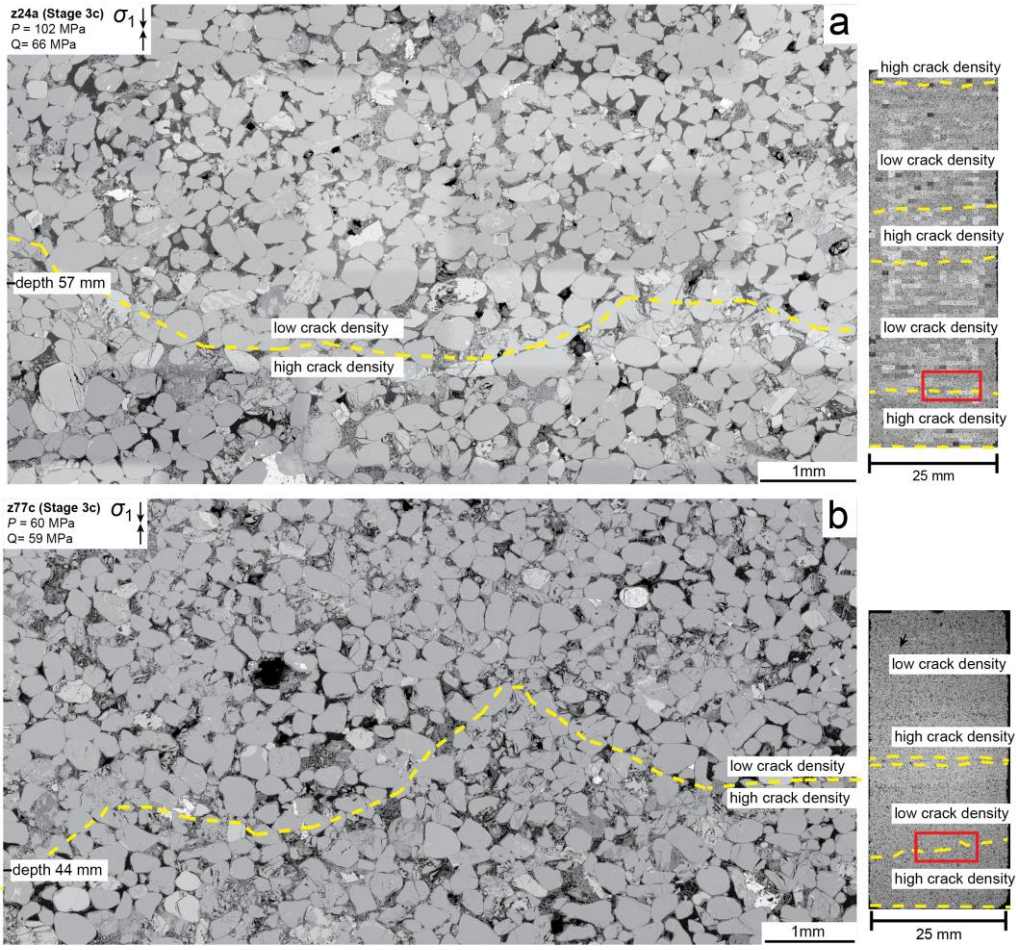

Figure 3.9 Backscatter electron micrographs recovered from **a)** sample z24a (φ_0 = 21.5%; hydrostatic plus deviatoric stress-cycling test), and from **b)** sample z77c (φ_0 = 21.9%; microstructural reference test). Both samples were deformed into the Stage 3c (non-linear compactant behavior) regime. The localized increase in crack densities shown along the profile lines presented in Figures 3.6 and 3.8 often reflect intersection with diffuse, rugged bands of high crack density. These bands were inclined (20 – 40° to σ_1) at low P_c^{eff}, or at a high angle (70 - 90°) to σ_1 at high P_c^{eff}, as exemplified here. The locations of the micrographs shown are indicated by the red box in the sample-scale micrograph on the right hand side.

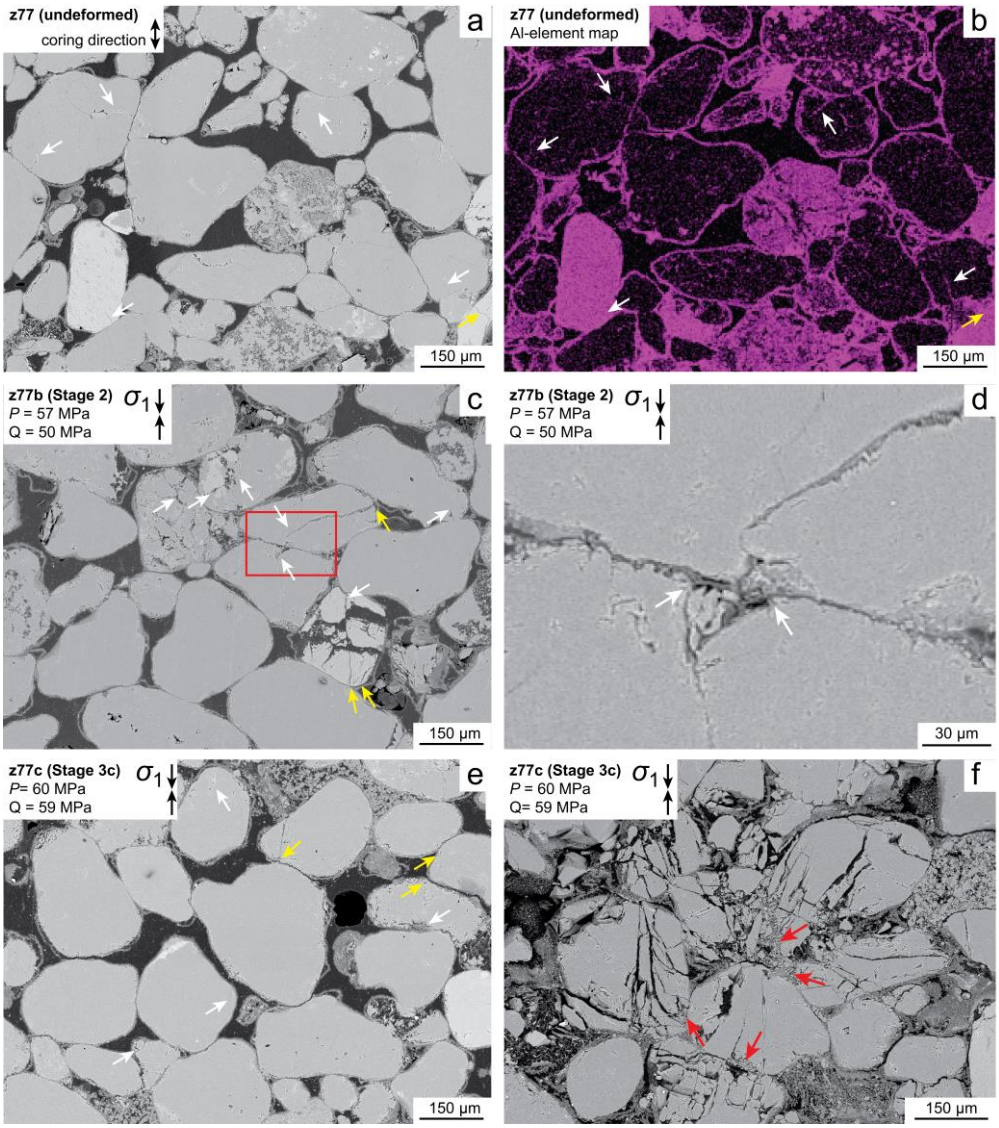

Figure 3.10 Backscatter electron micrographs recovered from samples (φ_0 = 21.9%), deformed in our microstructural reference tests (Figure 3.7), and from their undeformed counterpart. The locations of these micrographs are indicated with arrows in Figure 3.8. White and yellow arrows indicate intragranular cracks emanating, respectively, from within grain contacts, or from the peripheries of grain contacts. **a)** The undeformed sample z77 shows few intragranular cracks. b) Same view as in (a), showing regions of high aluminium content, highlighting feldspar and clay films coating the pore walls and grain-contacts. **c)** Sample z77b, compressed into Stage 2, showing a microstructure similar to that of the undeformed sample. **d)** Close-up from (c), showing a thin

clay film present within a rough grain contact. Intragranular cracks emanate from a pore present within this grain contact. **e)** Micrograph obtained from a low crack density region (black arrow in Figure3.8d) of sample z77c deformed into Stage 3c, showing a very similar microstructure to its undeformed counterpart (a). **f)** Micrograph obtained from a high crack density region (red arrow in Figure 3.8d) of the same sample z77c, showing pervasive grain crushing (red arrows).

3.6 Discussion

The mean effective stress (P) versus total porosity reduction ($\Delta\varphi_t$) and inelastic porosity reduction ($\Delta\varphi_i$) data presented here for Slochteren sandstone show a clear transition from initial, non-linear, concave-up behavior (Stage 1; compare Figures 3.2, 3.3 and 3.5 with Figure 3.1), to subsequent near-linear behavior (Stage 2) and final, non-linear, dilatant (Stage 3d), or compactant behavior (Stage 3c). Both elastic and inelastic deformation contributed significantly to each of these stages, including in the near-linear Stage 2 (Figures 3.2, 3.3 and 3.5), which is often assumed to reflect poroelastic deformation only (see Introduction). During Stage 2, the total hardening rates (*i.e.* $dP/d\Delta\varphi_t$) and inelastic hardening rates (*i.e.* $dP/d\Delta\varphi_i$) were both found similar during deviatoric and hydrostatic uploading, indicating isotropic behavior. Total hardening rates constituted a near-constant 8.3 ± 0.5 GPa in low porosity sandstone (φ_0 = 13.4 – 13.9%), 5.7 ± 0.4 GPa at intermediate porosities (φ_0 = 21.4 – 21.5%), and 4.1 ± 0.5 GPa in high porosity samples (φ_0 = 25.6 – 26.4%). Corresponding inelastic hardening rates (*i.e.* $dP/d\Delta\varphi_i$) were 27.8 ± 1.2 GPa (low φ_0), 16.7 ± 0.7 GPa (intermediate φ_0) and 9.8 ± 0.5 GPa (high φ_0). Thus, during Stage 2, approximately 30 to 50% of the total porosity reduction was inelastic. At higher stresses, *i.e.* in Stages 3d and 3c, a similar inelastic contribution was demonstrated, with final total porosity reductions $(\Delta\varphi_t)_{fin}$ ranging from -0.4% (dilatant; at P_c^{eff} = 5 MPa), to 7.4% (compactive), to which inelastic deformation contributed -0.1 to 3.2% in absolute terms (Table 3.1). Crucially, we demonstrated that the stress-cycling method employed to quantify the reported P - $\Delta\varphi_i$ and Q - ε_i behavior did not impact the overall stress-strain behavior through effects such as damage accumulation (Figure 3.2). Bulk and Young's moduli characterizing the elastic component of deformation were shown to increase with increasing mean effective stress, and with decreasing initial porosity (Figure 3.4). After Stage 1 and 2 deformation, micrographs showed a small increase in intragranular crack density ($\bar{\rho}_{cr}$ = 14.1 and 17.2 mm^{-2}) with respect to the undeformed counterpart samples ($\bar{\rho}_{cr}$ = 12.8 mm^{-2}). By contrast, after Stage 3d or Stage 3c deformation, intragranular crack densities were generally higher ($\bar{\rho}_{cr}$ = 10 to 72 mm^{-2}; Table 3.1).

3.6.1 Elastic behavior of the Slochteren sandstone

The present data on the truly elastic behavior of our samples yielded bulk moduli in the range 1 to 11 GPa and Young's moduli varying from 3 to 22 GPa. Both were found to increase with increasing mean effective stress (P) and with decreasing initial sample porosity (φ_0) (Figure 3.4). Stiffening of elastic moduli with increasing mean effective stress and decreasing initial porosity is well-known in sandstones [*Blöcher et al.*, 2014; *Chang et al.*, 2006; *Fortin et al.*, 2005; *Heap et al.*, 2010; *Ingraham et al.*, 2017]. These effects occur because the (average) grain contact area and (quasi-Hertzian) contact stiffness increases with decreasing initial porosity and with increasing grain contact compression [*Digby*, 1981; *Walton*, 1987].

At low mean effective stresses (≤ 30 MPa), corresponding to Stage 3d behavior in samples deviatorically tested at P_c^{eff} = 5 MPa, and to Stage 1 behavior in all other samples, K-values obtained during (Stage 1) hydrostatic unloading were more compliant than those seen during (Stage 3d) deviatoric unloading at P_c^{eff} = 5 and 20 MPa, suggesting anisotropic elastic behavior. By contrast, at P-values of 50 MPa and 85 MPa, corresponding to the near-linear Stage 2 during both deviatoric and hydrostatic unloading, K was found to be similar in both deviatoric and hydrostatic unloading. This suggests that during Stage 2, the elastic behavior was isotropic. In line with previous work [*David et al.*, 2012; *Walsh*, 1965], we suggest that the anisotropic versus isotropic behaviors were controlled by the elastic closure and opening of intragranular cracks and possibly dilated grain boundaries during loading and unloading, respectively. In part, intragranular cracks are already present in the microstructure (Figure 3.8a). In addition, low confinement (P_c^{eff} = 5 MPa), deviatoric Stage 3d compression was shown to lead to an increase in such cracks (see Section 4.3.2) likely increasing the anisotropy. By contrast, during progressive Stage 1 hydrostatic compression, virtually no new intragranular cracks were formed (Figure 3.8b), while pre-existing cracks are progressively closed and are fully closed at the onset of the near-linear Stage 2.

3.6.2 Inelastic deformation mechanisms in the present experiments

As noted in the introduction, the mechanisms accommodating inelastic deformation of sandstone under low temperature, laboratory conditions (T < 150°C) and relatively rapid strain- or loading rates ($\dot{\varepsilon}_t$ ~ 10^{-5} s^{-1}; $\dot{P}$ ~ 0.1 MPa s^{-1}) have often been reported to include intragranular cracking, intergranular cracking and intergranular shear displacements. In addition, during each of the three deformation stages seen in previous P versus $\Delta\varphi_t$ data for sandstones (Figure 3.1), these inelastic mechanisms are thought to partition differently [*Bernabe et al.*, 1994; *Menéndez et al.*, 1996; *Renard et al.*, 2017; *Wu et al.*, 2000]. In line

with this, our microstructural reference samples z77a-c, deformed to the end of Stages 1 (z77a), 2 (z77b) and 3c (z77c) (Figure 3.7), showed mean intragranular crack densities per unit final inelastic porosity reduction of 11.4, 13.1, and 32.3 mm^{-2}/%, respectively. To investigate the role played by intragranular cracking in accommodating inelastic porosity reduction more specifically for each individual deformation stage, we assume that the initial microstructures of our three deformed reference samples, z77a-c were equivalent prior to testing, and hence to that of the undeformed sample (z77). We further assume that the reproducible P - $\Delta\varphi_t$ behavior seen during testing (Figure 3.7) implies similar microstructural evolution. The role played by intragranular cracking per unit inelastic porosity reduction in each stage can then be quantified from the changes in mean crack density and final inelastic porosity reduction measured in progressing from the undeformed sample, to sample z77a (end Stage 1), to sample z77b (end Stage 2) and sample z77c (end Stage 3c). The resulting stage-specific changes in mean crack density per unit porosity reduction were 1.1, 32.4 and 110.7 mm^{-2}/%, respectively, while the corresponding strain-normalized standard deviations were 6.2, 6.7 and 17.3 mm^{-2}/%, respectively. These results suggest that the role played by intragranular cracking in achieving inelastic porosity reduction is negligible during Stage 1, small during Stage 2, and much larger during Stage 3c [*cf. Menéndez et al.*, 1996; *Wu et al.*, 2000].

As indicated earlier, the initial, compliant and non-linear P - $\Delta\varphi_t$ behavior defining Stage 1 is commonly attributed to the progressive elastic/inelastic closure of pre-existing, intergranular and/or intragranular cracks [*David et al.*, 2012; *Walsh*, 1965], which is consistent with the lack of any increase in crack density seen after Stage 1 deformation only (Figure 3.8b). Beyond Stage 1 and into Stage 2 at P > 35 MPa, near-linear yet partially inelastic (30 – 50%) P - $\Delta\varphi_t$ behavior followed, suggesting a change in both elastic and inelastic deformation mechanisms. Interestingly, this mean effective stress of 35 MPa is similar to the mean effective stresses of 39 MPa, measured in the Slochteren sandstone reservoir in Zeerijp at the time of core extraction [*Van Eijs*, 2015]. This may suggest that inter- and/or intragranular cracks were introduced to our samples as 'core damage' during release of the *in-situ* stresses supported by the sample during core extraction [*Holt et al.*, 2000; *Santarelli and Dusseault*, 1991]. It is anticipated, then, that while exploring mean effective stresses exceeding those prevalent in the reservoir (*i.e.* P > 39 MPa), such initial damage effects are largely removed and the inelastic strains measured from this point onward are newly induced.

During Stage 2, the importance of intragranular cracking per unit inelastic porosity reduction was larger, but still much smaller than that seen during Stage 3c. Therefore, for the

bulk of Stage 2, we speculate that intergranular normal and/or shear displacements likely accommodated most of the inelastic deformation, beyond the 'damage closure' effects of Stage 1. Normal grain boundary displacements could potentially occur by internal grain contact asperity breakage, or through the squeezing and/or dewatering of intergranular clay films (clay films shown in Figure 3.10b,d) at contacts under concentrated normal stress. We note, though, that microstructural evidence for such intergranular normal and shear displacements, or the accommodating mechanism is still lacking and requires further investigation.

Aside from minor increases in intragranular crack density seen at the ends of sample z77b, deformed into Stage 2, no evidence for localization was observed (Figures 3.8b, c). By contrast, all of the microstructurally investigated samples, deformed into the non-linear Stages 3d and 3c of the $P - \Delta\varphi_t$ curve showed a marked increase in intragranular crack density (Figure 3.10f) within localized bands (Figure 3.9). Within these bands, pervasive grain- and grain contact crushing was seen, especially in samples deviatorically tested at $P_c^{eff} \geq 40$ MPa (Figure 3.10f). In addition, all low porosity samples subjected to deviatoric loading into Stages 3d and c, as well as intermediate porosity sample z24d tested in deviatoric compression at $P_c^{eff} = 20$ MPa showed macroscopically visible, localized shear bands. These results are in good agreement with previous experiments on sandstone, which have demonstrated that Stage 3d/c deformation leads to a significant, localized increase in acoustic emissions [*DiGiovanni et al.*, 2007; *Fortin et al.*, 2006], intragranular cracks [*Baud et al.*, 2004; *Tembe et al.*, 2008] and porosity change [*Fortin et al.*, 2005; *Renard et al.*, 2017].

3.6.3 Effects of initial porosity and inelastic porosity reduction on strain-hardening

Here, we analyze the effect of initial porosity and inelastic porosity reduction on the hardening behavior shown by our samples, for the full range of stress conditions explored. The results form the basis needed for assessing to what extent our data can be described by a granular medium plasticity model in which the $P - \Delta\varphi_i$ or $Q - \varepsilon_i$ behavior is solely dependent on initial porosity, and inelastic porosity reduction.

To investigate the sensitivity of the hardening behavior shown by our samples to initial porosity and to inelastic porosity reduction, we contour fixed values of inelastic porosity reduction developed during all stages of strain hardening behavior in differential stress (Q) versus mean effective stress (P) space for each set of samples with similar initial porosity (within 0.8%) [Figure 3.11; *cf. Wong et al.*, 1992; *Karner et al.*, 2005]. Compaction occurring during strain-neutral or strain-softening behavior is not contoured. We assume that

the values of Q, P and $\Delta\varphi_i$ measured after any two consecutive stress-cycles of the same experiment can each be interpolated linearly, to obtain the stress conditions matching fixed 0.1% increments in $\Delta\varphi_i$. For reference, the maximum stress states imposed in individual stress-cycles are indicated in Figure 3.11 with black dots. Peak stress conditions beyond which strain-softening behavior was observed (*i.e.* Q_{peak} in Table 3.1, and the corresponding P) are encircled in red and are used to delineate the stress conditions required for failure in samples with low (φ_0 = 13.4 – 13.9%), intermediate (φ_0 = 21.4 – 21.5%) and high initial porosity (φ_0 = 25.6 – 26.4%).

The red failure lines plotted in Figure 3.11 for samples with low, intermediate and high initial porosities show a positive, slightly downward-curved slope in Q versus P space, with average slopes of about 1.1, 0.8 and 0.6, respectively. These slopes, their porosity-dependence and the dilatant failure modes observed at low P (*i.e.* Stage 3d; Figure 3.3a-c) are qualitatively consistent with typical, Mohr-Coulomb shear behavior [*e.g. Paterson and Wong*, 2005], involving intergranular cracking plus frictional, intergranular slip [*Guéguen and Fortin*, 2013]. The inelastic porosity reduction contours (black lines in Figure 3.11) are orientated at high angles to the red failure lines. From the orientations of these contour lines, and from their spacing, three different types of inelastic deformation behavior can be distinguished, as described below. These correspond to the inelastic porosity reduction values associated with Stage 1 (see Figure 3.1), near-linear Stage 2 and final non-linear Stage 3c behavior (Figures 3.3a-c).

During Stage 1 (P up to 35 MPa), relatively large inelastic porosity reductions were measured in both hydrostatic and deviatoric compression, with $\Delta\varphi_i$ up to 0.6% in low porosity samples (φ_0 = 13.4 – 13.9%), $\Delta\varphi_i$ up to 0.8% for intermediate porosities (φ_0 = 21.4 – 21.5%) and $\Delta\varphi_i$ up to 1.2% in the high porosity sandstones (φ_0 = 25.6 – 26.4%). For these values of $\Delta\varphi_i$, inelastic porosity reduction contours (black lines, Figure 3.11) are closely-spaced and are characterized by steep positive to near-vertical slopes. Hence, at these conditions, inelastic compaction behavior is highly compliant, strongly dependent on the mean effective stress and almost independent of differential stress. This implies that the deformation mechanism inferred to control Stage 1 inelastic deformation, *i.e.* intergranular or inter-particle closure of pre-existing damage, is predominantly controlled by P, not by Q [see also: *Karner et al.*, 2005].

During Stage 2, inelastic porosity reductions ranged from approximately 0.6% to 1.0% (φ_0 = 13.4 – 13.9%; see Table 3.1), 0.8 to 1.1% (φ_0 = 21.4 – 21.5%) and 1.2 to 1.7%, (φ_0 = 25.6 – 26.4%). For these values of $\Delta\varphi_i$, the spacing between inelastic porosity reduction contours is wider. At the onset of Stage 2, the differential stresses delineated by individual

contours show a minor inverse dependence on P. With increasing Q and P, this inverse dependence increases (*i.e.* the slope of contour lines becomes less negative), until the shear failure line, or Stage 3c is reached. This suggests a transition in behavior of the mechanisms suggested to control inelastic compaction during Stage 2 (*i.e.* grain boundary asperity breakage and/or consolidation and shear of intergranular clays, with a smaller role played by intragranular cracking - see previous section) from being initially primarily P-sensitive, to becoming increasingly more sensitive to Q towards the later stages of Stage 2 and into Stage 3c.

Stage 3c hardening behavior was seen at $\Delta\varphi_i$ > 1.0% (low porosity) > 1.1% (intermediate porosity) and > 1.7% (high porosity). Here, all samples, and particularly the intermediate and high porosity ones ($\varphi_0 \geq 21.4\%$) showed Q- and P-sensitive contour lines, where a marked decrease in their spacing implies increased inelastic compaction rates. Such differential stress-, or shear-enhanced compaction behavior is well-known to occur during Stage 3c [*Baud et al.*, 2006; *Curran and Carroll*, 1979; *Tembe et al.*, 2008; *Wong et al.*, 1997]. This behavior is thought to be controlled by intragranular cracking, which is favored upon tangential loading of grain contacts [*Shah and Wong*, 1997]. It appears, then, that compaction during the initial stages of Stage 2 is accommodated by predominantly Q-insensitive, intergranular processes, where the progressive decrease in slope of Stage 2 contour lines (increasing Q-sensitivity) reflects an increasing role played by intragranular cracking, becoming dominant in Stage 3c.

3.6.4 Comparison with plasticity theory

3.6.4.1 Modified Cam-clay yield envelope

We now make use of the data plotted in Figure 3.11 to explore to what extent the present stress versus inelastic strain data can be described using the general plasticity theory for granular media outlined by *Muir Wood*, [1991, Chapter 4]. In principle, this theory provides a description for the stress versus inelastic strain behavior for yield envelopes of any shape in P - Q space. Here, we use the modified Cam-clay yield function, because of its previous use in geomechanical modelling of upper crustal hydrocarbon reservoirs [*Chan et al.*, 2004; *Crawford et al.*, 2011] and in more generic studies of inelastic sandstone deformation [*Schultz and Siddharthan*, 2005; *Skurtveit et al.*, 2013]. In the modified Cam-clay formulation, the stress conditions required for yield are described in differential stress ($Q = [\sigma_1 - \sigma_3]$) versus mean effective stress ($P = [\sigma_1 + 2\sigma_3]/3 - P_p$) space, by the following elliptical function:

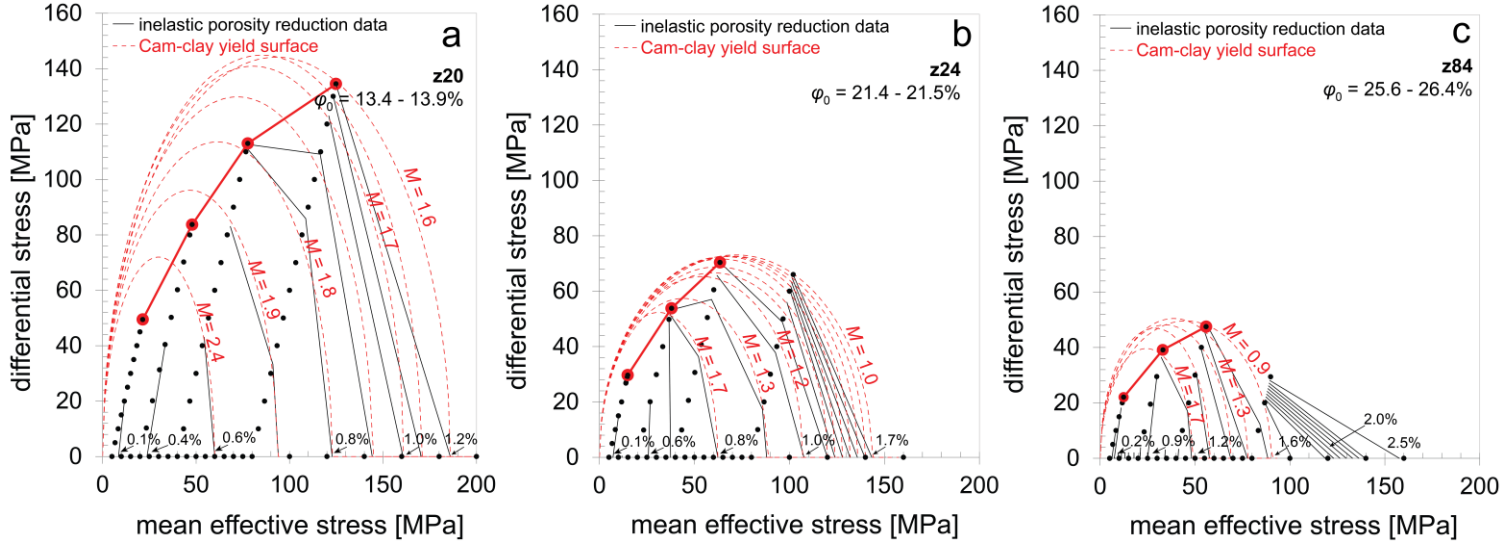

Figure 3.11 Plots showing the differential stress (*Q*) versus mean effective stress (*P*) conditions required for strain-softening (*i.e.* failure - solid red lines) and to induce the indicated values of inelastic porosity reduction (black contour lines), in our samples with **a)** low (φ_0 = of 13.4 – 13.9%), **b)** intermediate (φ_0 = of 21.4 – 21.5%) and **c)** high initial porosities (φ_0 = of 25.6 – 26.4%). Only porosity reductions accompanied by strain hardening (positive slopes of $P - \Delta\varphi_i$ curves in Figures 3.3 and 3.5) are contoured. Black dots represent the maximum stress conditions imposed in each stress-cycle. The differential stresses delineated by inelastic porosity reduction contours show a direct *P*-dependence at low *P*, transitioning into an inverse *P*-dependence at higher *P*. Where an inverse *P*-dependence is observed, these data are compared to modified Cam-clay yield envelopes (dashed red ellipses; see Section 3.6.4.1). However, for the highest inelastic porosity reductions (≥ 1.7%) seen in our high porosity samples, no adequate fit could be achieved. The *M*-factors controlling the shape of the yield envelope generally decrease with increasing inelastic porosity reduction.

$$f(Q, P, \sigma^*) = Q^2 - M^2 P(\sigma^* - P) = 0 \qquad \text{(Eq. 3.1)}$$

Here, σ^* is the hydrostatic mean effective stress required for the onset of inelastic deformation, and M is the slope of the critical state line, along which inelastic axial compression occurs at zero inelastic volume change. The factors σ^* and M control the size and height-over-width ratio (*i.e.* the ellipticity) of the yield envelope, respectively. Most models for inelastic deformation of granular media utilizing plasticity theory, such as the modified Cam-clay model [*Muir Wood*, 1991], the critical state model [*Schofield and Wroth*, 1968] and the cap-model [*DiMaggio and Sandler*, 1971] assume that hardening occurs with inelastic porosity reduction only, with no effect of inelastic axial strain, or shear strain. To test to what extent this assumption applies to our experiments, we directly compare the modified Cam-clay yield surfaces described by Equation 3.1 (*i.e*. the stress conditions required to achieve a given value of compaction), to the inelastic porosity reduction contours outlined in Figure 3.11. In doing so, the σ^* value used to construct a yield surface using Equation 3.1 is given by the mean effective stress required to induce the corresponding value of inelastic porosity reduction during our hydrostatic tests. Since inelastic porosity reduction was observed from the onset of compression (Figures 3.2, 3.3 and 3.5), this means that the initial value of σ^* is equal to the mean effective stress of 5 MPa imposed at the start of each experiment. The shape factor M was varied for each yield envelope, until a best-fit to the corresponding contour line was achieved, based on visual inspection. For each yield envelope fitted in this way, the uncertainty in M was estimated by exploring the M-values for which the yield envelope fitted at least two data points defining the corresponding contour. The uncertainty in M was found to be ± 0.1 (*i.e.* ± 5 - 15%). Note, though, that each of these yield envelopes is typically constrained by only three data points, meaning that additional uncertainty in M will exist due to sample variation. Ideally, more experimental data would be available for samples with the same porosity values, *i.e.* from the same depth intervals used here. In the present study, the number of samples per core interval was limited by the diameter of the core (~ 10 cm). Alternatively, more detailed delineation of inelastic porosity reduction contours could be attempted using the method outlined by *Tembe et al*., [2007], in which the confining pressure and axial stress imposed in a triaxial test are manipulated simultaneously so as to maintain constant pore volume.

Returning to the comparison of our data with the Cam-clay model, for the low inelastic porosity reductions of $\Delta\varphi_i < 0.6\%$ ($\varphi_0 = 13.4 – 13.9\%$), $\Delta\varphi_i < 0.8\%$ ($\varphi_0 = 21.4 – 21.5\%$) and $\Delta\varphi_i < 1.2\%$ ($\varphi_0 = 25.6 – 26.4\%$), corresponding to Stage 1 deformation, the fit between inelastic porosity reduction lines and elliptical Cam-clay yield surface was poor.

However, at greater inelastic porosity reductions of up to 1.2% (φ_0 = 13.4 – 13.9%), 1.7% (φ_0 = 21.4 – 21.5%) and 1.6%, (φ_0 = 25.6 – 26.4%), corresponding to Stage 2 and Stage 3c deformation (Figure 3.3a-c), the stress conditions outlined by inelastic porosity contours were reasonably well-described by the Cam-clay yield surfaces shown in Figure 3.11 (*i.e.* within a difference in *Q* or *P* of 5 MPa). The shape factor *M* used to construct the envelopes shown for samples deformed in Stages 2 and 3c ranged from 2.4 to 0.9, and decreased with increasing inelastic porosity reduction. The highest *M* values were obtained for our samples with the lowest initial porosity during Stage 2 (φ_0 = 13.4 – 13.9%; Figure 3.11a). Similar trends have been seen in previous work on bassanite, showing a decreasing height-over-width ratio of the yield envelope with increasing inelastic compaction [*Bedford et al.*, 2018]. For our high porosity samples (φ_0 = 25.6 – 26.4%), the Stage 3c behavior ($\Delta\varphi_i$ > 1.7%) could not be fitted with elliptical yield envelopes, without having these envelopes cross the envelopes corresponding to the lower inelastic porosity reductions of Stage 2 (Figure 3.11c). Rather, for these highly porous samples and the Stage 3c porosity reductions, a linear end-cap, rather than an elliptical one may be more appropriate, such as proposed by *Guéguen and Fortin*, [2013].

3.6.4.2 Normality condition

The Muir Wood plasticity theory predicts that during yielding of isotropic, granular materials, each increment of inelastic strain develops normal to the yield surface, *i.e.* these materials obey the normality- or associative flow condition [*Muir Wood*, 1991; see also: *Desai and Siriwardane*, 1984]. If the normality condition is not satisfied, more complex, non-associative models are required [*e.g. Rudnicki and Rice*, 1975; *Issen and Rudnicki*, 2000]. Here we test whether the condition holds for the yield surfaces drawn in Figure 3.11. In *P* - *Q* space, the normality condition implies that the ratio between the increments of inelastic volumetric strain ($d\varepsilon_{v,i} = d\varepsilon_i + 2d\varepsilon_{3,i}$), and inelastic shear strain ($d\gamma_i = 2/3[d\varepsilon_i - d\varepsilon_{3,i}]$) developing upon an incremental increase of the mean effective stress (d*P*) and/or differential stress (d*Q*) satisfies the relations [*Muir Wood*, 1991]:

$$\frac{d\varepsilon_{v,i}}{d\gamma_i} = \frac{\delta f/\delta P}{\delta f/\delta Q} = \frac{M^2 - \left(\frac{Q}{P}\right)^2}{2\frac{Q}{P}} \qquad \text{(Eq. 3.2)}$$

Noting that $\varepsilon_{v,i} \approx \Delta\varphi_i$ (see Section 3.4.2), Equation 3.2 can be rewritten as the ratio between the inelastic porosity reduction and the inelastic axial strain:

$$\frac{d\Delta\varphi_i}{d\varepsilon_i} = \frac{3\left(M^2-\left(\frac{Q}{P}\right)^2\right)}{6\frac{Q}{P}+M^2-\left(\frac{Q}{P}\right)^2} \qquad \text{(Eq. 3.3)}$$

Inserting the *M*-values obtained for each yield envelope shown in Figure 3.11 into Equation 3.3, we predicted the $\frac{d\Delta\varphi_i}{d\varepsilon_i}$ versus *P* behavior implied by these envelopes if the normality condition applies. The predicted curves are shown in Figure 3.12, where they are compared to experimental $\frac{\Delta(\Delta\varphi_i)}{\Delta\varepsilon_i}$ versus *P* data, measured during the deviatoric stages of our hydrostatic plus deviatoric experiments at the relevant initial porosity and inelastic porosity reduction values (red and blue symbols). Red and blue symbols indicate that the corresponding data points were obtained within, respectively, the near-linear (Stage 2 - red) and the subsequent non-linear (Stage 3c - blue) portions of the *P* versus $\Delta\varphi_t$ curves shown in Figure 3.3. For reference, we include the $P - \Delta\varphi_i$ data obtained in the purely hydrostatic testing in the Rene vessel (Figure 3.5), by assuming isotropic, inelastic compaction behavior, so that $\Delta\varepsilon_i = \Delta\varepsilon_{2,i} = \Delta\varepsilon_{3,i}$, implying $\Delta(\Delta\varphi_i) \approx 3\Delta\varepsilon_i$. For these samples, $\frac{\Delta(\Delta\varphi_i)}{\Delta\varepsilon_i}$ is accordingly assumed to be equal to 3 (grey symbols).

Figure 3.12 shows that for the same values of mean effective stress, initial porosity, and inelastic porosity reduction, the $\frac{\Delta(\Delta\varphi_i)}{\Delta\varepsilon_i}$ values obtained during deviatoric stress-cycling in Stage 2 (red) are similar to those predicted assuming normality. Hence, during the near-linear, Stage 2 part of the *P* - $\Delta\varphi_t$ curve, the normality condition is satisfied. This, combined with: a) the similar hardening behavior shown during Stage 2 hydrostatic and deviatoric compression (Figure 3.3a-c), and b) the absence of significant localization shown by the intragranular crack density profile measured after Stage 2 deformation (Figure 3.8c), implies that inelastic deformation in Slochteren sandstone behaves isotropically during Stage 2. Furthermore, since the yield envelopes in Figure 3.11 were fitted to inelastic porosity reduction contours (thus ignoring any influence of inelastic axial strain) Stage 2 hardening must be predominantly controlled by inelastic porosity reduction, with a negligible influence of inelastic axial strain.

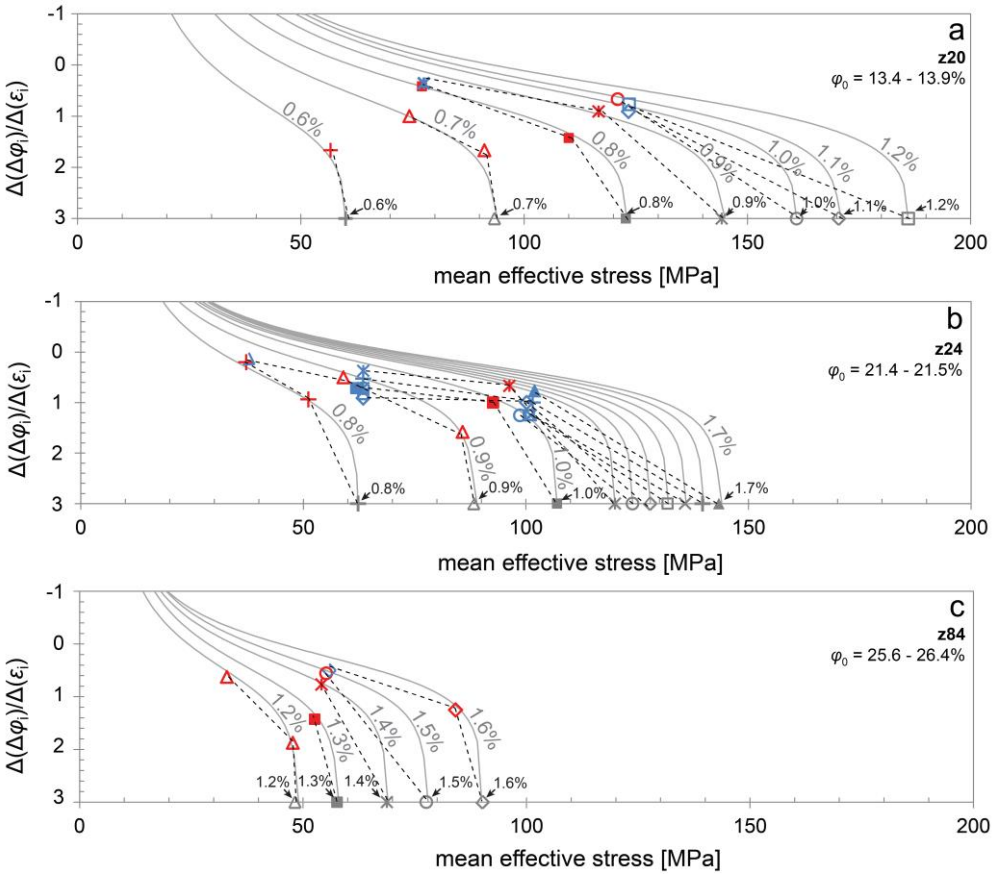

Figure 3.12 Plots showing the ratio of changes in inelastic porosity reduction and inelastic axial strain $\Delta(\Delta\varphi_i)/(\Delta\varepsilon_i)$ versus mean effective stress data (P), obtained for the contoured values of inelastic porosity reduction measured in samples with **a)** low (φ_0 = of 13.4 – 13.9%), **b)** intermediate (φ_0 = of 21.4 – 21.5%) and **c)** high initial porosities (φ_0 = of 25.6 – 26.4%). Only the data that were adequately fitted to Cam-clay yield surfaces in Figure 3.11 are shown. Red and blue symbols indicate data obtained during deviatoric stress-cycling from the near-linear (Stage 2) and non-linear, compactant (Stage 3c) parts of the present P - $\Delta\varphi_t$ curves (Figure 3.3). The P – $\Delta\varphi_i$ data obtained in our hydrostatic experiments, in which ε_i was not measured, are included here for reference (grey symbols) by assuming isotropic inelastic compaction, *i.e.* $\Delta(\Delta\varphi_i)/(\Delta\varepsilon_i) = 3$. Dashed tie-lines connect data corresponding to the fixed values of inelastic porosity reduction indicated in black. These data are compared to the behavior implied by the modified Cam-clay yield envelopes constructed for these values of inelastic porosity reduction shown in Figure 3.11, assuming that the normality condition applies (grey curves). If the normality condition applies, then the grey curves and the $\Delta(\Delta\varphi_i)/(\Delta\varepsilon_i)$ versus P data obtained for the same value of $\Delta\varphi_i$ overlap, which is the case for Stage 2 data (red) only.

By contrast, the $\frac{\Delta(\Delta\varphi_i)}{\Delta\varepsilon_i}$ values obtained during Stage 3c deviatoric stress-cycling (blue points), are higher than those predicted assuming normality at the corresponding values of P, φ_0 and $\Delta\varphi_i$. Hence, for each increase in inelastic axial strain, more inelastic porosity reduction was seen than expected for an isotropic material [*cf. Baud et al.*, 2006]. This is in agreement with the different inelastic hardening trends shown during deviatoric versus hydrostatic compression (Figure 3.3a-c), and with our microstructural evidence for strongly localized deformation in Stage 3c (Figures 3.6, 3.8d, 3.9 and 3.10e,f). This confirms the inference by previous authors that localized, inelastic deformation of sandstone leads to inelastic strains that cannot be directly related to the yield envelope via the normality condition [*Baud et al.*, 2006; *Issen and Rudnicki*, 2000; *Rudnicki and Rice*, 1975].

In summary, the presently used plasticity model, involving a modified Cam-clay yield envelope and porosity-controlled hardening behavior adequately describes the inelastic deformation behavior occurring during the near-linear, Stage 2 part of the $P - \Delta\varphi_t$ curve, while the high-strain Stage 3c behavior is poorly described by this model.

3.7 Implications for the Groningen gas field

3.7.1 Mechanical behavior under in-situ conditions

To assess the impact of current, and future production strategies in producing fields, such as the Groningen gas field on subsidence and induced seismicity, geomechanical models require an accurate description of the elastic versus inelastic deformation behavior, relevant for the small strains accompanying pore pressure reduction [*Spiers et al.*, 2017; *De Waal et al.*, 2015]. In sandstone reservoirs, the vertical strains, whether these are measured *in-situ* [*Cannon and Kole*, 2017; *Kole*, 2015] or are inferred from surface subsidence data [*Bourne et al.*, 2014; *Mallman and Zoback*, 2007; *Morton et al.*, 2006], typically fall in the range of 0.1 to 1.0%. If we assume that any pre-existing cracks present in the sandstone test samples are already closed in the reservoir, then the compliant, Stage 1 inelastic porosity reductions seen in our experiments are not expected to occur in the reservoir. The present deviatoric test data showed that during Stage 2, the changes in total axial strain ranged up to 1.0% (φ_0 = 13.4 – 13.9%), 0.7% (φ_0 = 21.4 – 21.5%), and 0.7% (φ_0 = 25.6 – 26.4%), while the corresponding changes in total porosity reduction ranged up to 1.1%, 1.3% and 1.9%, respectively. The small vertical strains seen in sandstone reservoirs, notably that in Groningen (up to ~0.3%; *NAM*, [2016]; *Cannon and Kole*, [2017]), fall well within these ranges for the total axial strain, suggesting that *in-situ* compaction largely reflects Stage 2 deformation behavior. During Stage 2, inelastic porosity reductions were generally small (0.4

to 0.6%), but still constitute 30 to 50% of the total porosity reduction measured in this Stage (Figure 3.3). In many geomechanical modelling studies [*Bourne et al.*, 2014; *Dempsey and Suckale*, 2017; *Lele et al.*, 2016; *Postma and Jansen*, 2018; *Wassing et al.*, 2016; *Zbinden et al.*, 2017], these inelastic strains are ignored, while the stress versus total strain behavior is quantified using be assumed elastic constants. We emphasize that while this assumption of poroelastic behavior in the near-linear Stage 2 may originate from the small absolute inelastic strains developing here, the relative inelastic contribution to the total deformation behavior (30 -50%) is significant and should therefore be considered alongside the elastic behavior.

In the following, we demonstrate the effect of taking into account inelastic deformation during Stage 2, on *in-situ* stress changes, and on the partitioning of elastic strain energy available for release during fault rupture [*McGarr*, 1999; *Shipton et al.*, 2013]. To do so, we apply our data to the case of the seismogenic Groningen gas field in the Netherlands. We first estimate the *in-situ* stress changes that would occur during pore pressure reduction when treating the total deformation of the reservoir as if purely poroelastic, as is often done in geomechanical studies (see Introduction). This (pseudo)-elastic base-case is then compared to the behavior expected in the more realistic case where the reservoir compacts through combined elastic plus inelastic deformation, described by the Stage 2 behavior of our samples.

3.7.2 Stress-strain relations applying during pore pressure reduction

3.7.2.1 Poroelastic relations

We take the Biot coefficient to be equal to 1 (*i.e.* similar elastic pore and bulk volume response- as shown in Figure 3.4), and assume that the total vertical (overburden) stress remains constant during pore pressure reduction. The incremental increase in effective vertical stress during pore pressure reduction can then be written as $d\sigma_1^{\text{eff}} = -dP_p$, where pore pressure reduction is negative. The increments in vertical elastic strain ($d\varepsilon_{el,1}$) and horizontal elastic strain ($d\varepsilon_{el,3}$) developing upon incremental changes in pore pressure and/or effective horizontal stress ($d\sigma_3^{\text{eff}}$) are then given by poroelasticity theory [*Paterson and Wong*, 2005; *Wang*, 2000] as:

$$d\varepsilon_{el,1} = \left(\frac{2}{9K} + \frac{2}{6G}\right) d\sigma_3^{eff} - \left(\frac{1}{9K} + \frac{2}{6G}\right) dP_p \qquad \text{(Eq. 3.4a)}$$

and:

$$d\varepsilon_{el,3} = \left(\frac{2}{9K} + \frac{1}{6G}\right) d\sigma_3^{eff} - \left(\frac{1}{9K} - \frac{1}{6G}\right) dP_p \quad \text{(Eq. 3.4b)}$$

where G is the shear modulus, relating to the bulk modulus (K) and the Young's modulus (E) through $G = 3KE/(9K - E)$. The change in the effective horizontal stress that would occur if reservoir deformation is fully elastic is given as [*Zoback*, 2010]:

$$\Delta\sigma_3^{eff} = \alpha\Delta P_p \left(\frac{(1-2\nu)}{(1-\nu)} - 1\right) \quad \text{(Eq. 3.5)}$$

where ν is the Poisson's ratio, which can be obtained through $\nu = 0.5 - E/(6K)$.

3.7.2.2 Plasticity model describing Stage 2 behavior

We have shown that the inelastic strains developing during the Stage 2 part of the P - $\Delta\varphi_t$ curves can be described using plasticity theory combined with the the modified Cam-clay yield surface. Inserting the modified Cam-clay yield function (Equation 3.1) into the general inelastic flow rules outlined by Muir Wood [1991, pp.107], as shown in the Appendix, we obtain the following expressions for the increments in inelastic vertical strain ($d\varepsilon_{i,1}$) and inelastic horizontal strain ($d\varepsilon_{i,3}$) developing during incremental reductions in pore pressure and/or increases in effective horizontal stress, at any current state of differential stress (Q), and mean effective stress (P):

$$d\varepsilon_{i,1} = \frac{d\Delta\varphi_i}{d\sigma^*}\left(\left(\frac{2Q}{3PM^2} - \frac{4Q^2}{M^4P^2-(QM)^2} + \frac{2}{9}\left(1 - \left(\frac{Q}{PM}\right)^2\right)\right) d\sigma_3^{eff} - \left(\frac{4Q}{3PM^2} + \frac{4Q^2}{M^4P^2-(QM)^2} + \frac{1}{9}\left(1 - \left(\frac{Q}{PM}\right)^2\right)\right) dP_p\right) \quad \text{(Eq. 3.6a)}$$

and:

$$d\varepsilon_{i,3} = -\frac{d\Delta\varphi_i}{d\sigma^*}\left(\left(\frac{4Q}{3PM^2} - \frac{2Q^2}{M^4P^2-(QM)^2} - \frac{2}{9}\left(1 - \left(\frac{Q}{PM}\right)^2\right)\right) d\sigma_3^{eff} + \left(\frac{Q}{3PM^2} - \frac{2Q^2}{M^4P^2-(QM)^2} + \frac{1}{9}\left(1 - \left(\frac{Q}{PM}\right)^2\right)\right) dP_p\right) \quad \text{(Eq. 3.6b)}$$

Here, $\frac{d\Delta\varphi_i}{d\sigma^*}$ is a factor expressing the hardening rate due to inelastic porosity reduction. Under uniaxial strain boundary conditions expected to be prevalent in the reservoir, the total horizontal strain, which is the sum of its elastic and inelastic components, must be equal to zero, so that $d\varepsilon_{tot,3} = d\varepsilon_{el,3} + d\varepsilon_{i,3} = 0$. Using this relation and Equations 3.4b and 3.6b, we obtain the change in effective horizontal stress developing as the pore pressure is reduced under uniaxial strain boundary conditions:

$$d\sigma_3^{eff} = -dP_p \frac{\left(\frac{d\Delta\varphi_i}{d\sigma^*}\left(\frac{Q}{3PM^2} - \frac{2Q^2}{M^4P^2-(QM)^2} + \frac{1}{9}\left(1-\left(\frac{Q}{PM}\right)^2\right)\right) + \frac{1}{9K} - \frac{1}{6G}\right)}{\left(\frac{d\Delta\varphi_i}{d\sigma^*}\left(\frac{4Q}{3PM^2} - \frac{2Q^2}{M^4P^2-(QM)^2} - \frac{2}{9}\left(1-\left(\frac{Q}{PM}\right)^2\right)\right) - \frac{2}{9K} - \frac{1}{6G}\right)} \quad \text{(Eq. 3.7)}$$

3.7.3 Application to the Groningen gas field

We now apply the above equations to the case of the Groningen field. We assume an initial vertical effective stress of 30 MPa [*Hettema et al.*, 2000] and an initial horizontal effective stress of 8 MPa, as was estimated for the Groningen field by *Breckels and van Eekelen* [1982], meaning that the initial values of P and Q are 15.3 and 22.0 MPa, respectively. During field production, the pore pressure dropped from an initial 35 MPa to the current 8 MPa [*NAM*, 2016], while full depletion would mean a further drop to 0.1 MPa.

We first explore the effective horizontal stress changes that would occur for the elastic base-case scenario.The apparent bulk modului (K_a) are equivalent to the total hardening rates (*i.e.* $dP/d\Delta\varphi_t$) described for Stage 2 in our hydrostatic plus deviatoric tests (see Section 3.4.2.1) and listed in Table 3.2. Apparent Young's moduli are obtained using the uploading $Q - \varepsilon_t$ data (Figure 3.3d-f) measured within the same $P - \Delta\varphi_t$ interval used in determining K_a. Using K_a and E_a, we calculate the corresponding apparent shear moduli (G_a) and the apparent Poisson's ratios (ν_a – Table 3.2), by using the poroelastic relations between K, E, G and ν outlined in Section 3.7.2.1. Inserting the resultant values of ν_a into Equation 3.5, σ_3^{eff} is shown to increase linearly with decreasing pore pressure to final values of 18, 19, and 20 MPa at a final P_p of 0.1 MPa, in low, intermediate and high porosity sandstone, respectively. Hence, in the elastic base-case scenario, the *in-situ* effective stress evolution shown by sandstones with a wide range of porosities (13 – 26%) is expected to be similar within 1 MPa. Moreover, comparing these predicted σ_3^{eff} versus P_p data to *in-situ* σ_3^{eff} versus P_p data [*Van Eijs*, 2015] measured in the more porous parts of the field (mean $\varphi >$ 18%), it is evident from Figure 3.13a that the change in σ_3^{eff} expected for an elastically

deforming reservoir grossly underestimates the measured values by 5 to 12 MPa, *i.e.* by 30 to 60% of the increase in σ_3^{eff}.

Table 3.2 Input parameters used to construct the plots shown in Figure 3.13. φ_0 denotes the initial porosity. E_a, K_a, G_a and ν_a denote the apparent Young's, bulk and shear moduli, and the apparent Poisson's ratio, which are obtained from uploading P – versus total porosity reduction, and from Q versus total axial strain data. E, K, G and ν denote the truly elastic Young's- bulk- and shear moduli and the Poisson's ratio, respectively, and are obtained from unloading data. The $d\Delta\varphi_i/d\sigma^*$ term is the inelastic porosity reduction developing per unit increase of hydrostatic mean effective stress.

φ_0	E_a	K_a	G_a	ν_a	E	K	G	ν	$d\Delta\varphi_i/d\sigma^*$
[%]	[GPa]	[GPa]	[GPa]		[GPa]	[GPa]	[GPa]		[%/GPa]
13.4	13.8	8.3	5.6	0.22	22.0	11.0	9.4	0.17	3.6
21.5	8.6	5.7	3.4	0.25	13.7	7.8	5.7	0.21	6.0
26.4	5.7	4.1	2.2	0.27	10.1	6.2	4.1	0.23	10.3

We now consider the more realistic case where pore pressure reduction leads to combined elastic plus inelastic Stage 2 deformation of the reservoir sandstone. To represent the elastic strain and stress changes developing *in-situ*, we use values of the (true elastic) bulk modulus (K) and Young's modulus (E) obtained from our unloading data at P = 50 MPa, P_c^{eff} = 40 MPa, and Q = 30 MPa. The K and E values obtained, and the corresponding calculated values of G and ν are listed in Table 3.2. Values of M were obtained at the same stress conditions, *i.e.* from the lowest inelastic porosity reduction contours to which Cam-clay yield envelopes were fitted (Figure 3.11). For simplicity, M is assumed to remain constant during deformation, which is a reasonable approximation provided inelastic porosity reductions are small (< 0.3%). The inelastic hardening factors $\frac{d\Delta\varphi_i}{d\sigma*}$ are equal to the inverse of the inelastic hardening rates ($dP/d\Delta\varphi_i$ – similar values in Stage 2 deviatoric and hydrostatic compression) given in Section 3.4.2.1 and are listed in Table 3.2. Inserting these values of K, G, M and $\frac{d\Delta\varphi_i}{d\sigma*}$ into Equation 3.7, we calculate the effective horizontal stress increments ($d\sigma_3^{eff}$) developing during successive pore pressure reduction increments (dP_p) of -0.1 MPa, recomputing the new σ_3^{eff}, Q and P after each increment. For the stress changes obtained, the corresponding increments of elastic ($d\varepsilon_{el,1}$) and inelastic vertical strain

increments ($d\varepsilon_{i,1}$), are calculated using Equations 3.4a and 3.6a, respectively. The cumulative elastic vertical strain ($\varepsilon_{el,1}$) and cumulative inelastic vertical strain ($\varepsilon_{i,1}$) are each the sum of their preceding increments, while the total, uniaxial vertical strain is given as the sum of these cumulative elastic and inelastic components ($\varepsilon_{el,1} + \varepsilon_{i,1}$). The resulting predicted σ_3^{eff} - P_p behaviors and total and elastic strain versus P_p curves are shown in Figures 3.13b and c, respectively.

In Figure 3.13b, the shaded fields around the solid lines show the error in σ_3^{eff} due to the error in M of ± 0.1. The horizontal effective stress increases non-linearly with decreasing pore pressure. For low porosities, the evolution of σ_3^{eff} with decreasing pore pressure is similar to the behavior seen in the elastic base-case (Figure 3.13a). By contrast, for higher porosities, markedly higher effective horizontal stresses are seen, where at full depletion, σ_3^{eff} = 24.0 ± 1.2 MPa (φ_0 = 21.4 - 21.5%) and 26.0 ± 1.5 MPa (φ_0 = 25.6 – 26.4%). These values are much closer (within 1 - 5 MPa) to the *in-situ* data measured at the same pore pressure in the high porosity (φ > 20%) regions of the reservoir, than obtained assuming purely elastic behavior (compare Figures 3.13a and b). Note that the present experimental data used to fit the above plasticity model were obtained at strain- and loading rates ($\dot{\varepsilon}_t \sim 10^{-5}$ s^{-1}; $\dot{P} \sim 0.1$ MPa s^{-1}) that are significantly faster than the strain-rates of ~10^{-12} s^{-1} inferred in the reservoir over decades of production [*Cannon and Kole*, 2017]. In previous experiments on Slochteren sandstone, strain rates down to 10^{-10} s^{-1} were explored over the time-scale of a week [*Pijnenburg et al.*, 2018], or down to 10^{-11} s^{-1} over several months [*Hol et al.*, 2015a], during which the inelastic contribution to the total axial strain measured increased by 10 to 20%. Therefore, at the strain rates of 10^{-12} s^{-1} inferred for the Groningen gas field [*Cannon and Kole*, 2017], and for other fields [*Mallman and Zoback*, 2007; *Morton et al.*, 2001], inelastic deformation may play an even larger role than represented in Figure 3.13 for Groningen, causing a larger increase in σ_3^{eff} with decreasing P_p (grey arrows in Figure 3.13b). We therefore suggest that the *in-situ* stress evolution in Groningen and other hydrocarbon fields is best represented by taking into account not only the elastic and inelastic contributions to deformation, but also any rate-sensitivity of the latter [*cf. Pijnenburg et al.*, 2018]. The implications of accounting for inelasticity for (seismic) fault rupture in the Groningen field are discussed in more detail in Section 6.2.1.4.

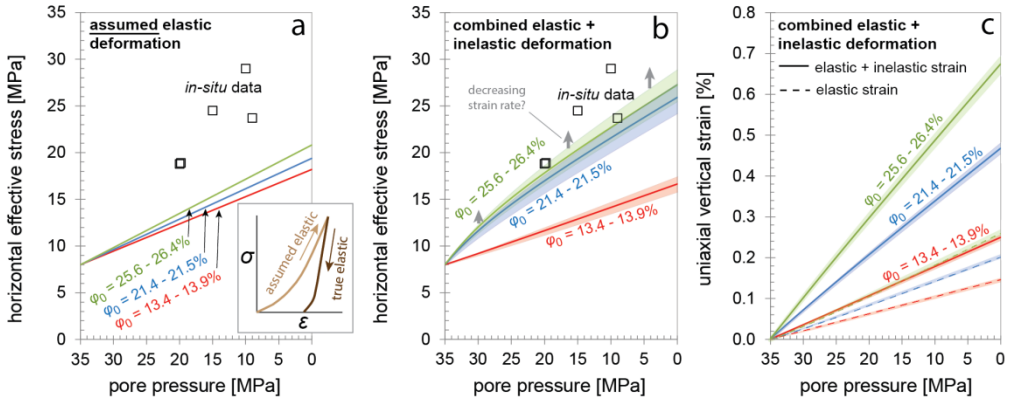

Figure 3.13 Plots showing the effect of the inelastic contribution to compaction of Slochteren sandstone with initial porosities (φ_0) of 13.4 – 26.4%, on predicted effective horizontal stress (σ_3^{eff}) changes and elastic versus inelastic strain partitioning during pore pressure (P_p) reduction under uniaxial strain conditions. **a)** Evolution of σ_3^{eff} with decreasing P_p, obtained by taking Stage 2 uploading data as if fully poroelastic (see inset). Thus obtained stress evolutions significantly misrepresent the values measured in the field (open square symbols; *van Eijs*, [2015]). **b)** σ_3^{eff} versus P_p behaviors obtained by taking into account both the true elastic contribution (see inset [a]) and the inelastic contribution to the total deformation behavior. Shaded areas indicate the error due to the error on M of ± 0.1. Thus predicted σ_3^{eff} - P_p curves are much more sensitive to φ_0 than assumed poroelastic curves (a), while higher porosity sandstones much better represent the measured *in-situ* data. At fixed P_p, σ_3^{eff} is expected to be higher still with decreasing strain rate (grey arrows). **c)** Total and elastic uniaxial vertical strain versus P_p data, predicted for combined elastic plus inelastic deformation.

At full depletion, the total, uniaxial vertical strains obtained for low, intermediate and high porosity sandstones are, respectively 0.23 ± 0.05%, 0.45 ± 0.1% and 0.66 ± 0.1%, to which elastic deformation contributes 0.15 ± 0.02%, 0.22 ± 0.05% and 0.28 ± 0.05%, respectively (Figure 3.13c). Hence, based on these data, 30 to 50% of the total strain energy accumulating during pore pressure reduction is inelastic, hence dissipated [*cf. Hol et al.*, 2018; *Pijnenburg et al.*, 2018]. This is then unavailable for release during fault rupture through seismicity and associated processes, such as frictional heating, fault asperity breakage, wall-rock damage, pore pressure changes and fluid flow [*Cooke and Madden*, 2014; *McGarr*, 1999; *Shipton et al.*, 2013]. Finally, we note that the marked, porosity-sensitive behavior shown by the horizontal stress evolution and by elastic and inelastic deformation imply that different compaction behavior and associated stress changes can be expected in a field like the Groningen field, where different parts of the reservoir are characterized by markedly different mean porosities (Figure 1.1b, of Chapter 1). We

accordingly believe that incorporating inelastic deformation into geomechanical modelling of fields such as Groningen will have significant impact on model outcomes on compaction, subsidence, stress evolution, fault reactivation and induced seismicity.

3.8 Conclusions

In this study, we quantified the elastic and inelastic contributions to the total deformation behavior of Slochteren sandstones from the currently producing, seismogenic Groningen gas field in the Netherlands (Figure 1.1 – of Chapter 1). This was done by performing hydrostatic and deviatoric stress-cycling experiments under conditions of temperature (T = 100°C) and pore fluid chemistry (~4 M saline brine) relevant for the top of the Slochteren reservoir. A wide range of stress changes was employed to include the stress conditions relevant for fluid extraction from reservoirs at depths up to 5 km, and to cover the Stage 1, Stage 2 and Stage 3d or Stage 3c $P - \Delta\varphi_t$ behavior (*cf.* Figure 3.1), in all our samples. Thus, we explored hydrostatic mean effective stresses up to P = 320 MPa, differential stresses up to Q = 135 MPa, pore pressure of 0.1 or 1.0 MPa, and initial sample porosities (φ_0) of 13.4 to 26.4%, covering the porosity range in the field. An axial strain rate of 10^{-5} s^{-1} and a loading rate of ~0.1 MPa s^{-1} were used. We concluded the following points:

1) Stress-cycling did not affect the overall mechanical behavior of our samples (Figure 3.2).
2) Mean effective stress versus total (elastic + inelastic) porosity reduction data obtained in the present combined hydrostatic plus deviatoric stress-cycling tests (Figure 3.3), and in hydrostatic (Rene) stress-cycling tests (Figure 3.5) show typical Stage 1, 2 and 3d or 3c behavior as often described in the literature (*cf.* Figure 3.1).
3) Inelastic deformation contributes to 30 to 50% of the total porosity reduction at each stage, including the near-linear Stage 2, which has been often assumed to be fully poroelastic. The inelastic contribution was larger in higher porosity samples.
4) The elastic bulk moduli (K) and Young's moduli (E) both showed a monotonic increase with increasing P and φ_0 (Figure 3.4). At $P \leq 30$ MPa, K values obtained during deviatoric unloading were larger by 1 - 2 GPa than the values obtained during hydrostatic unloading, implying anisotropic behavior at these low stresses. At P = 50 - 85 MPa, K values showed more isotropic behavior.
5) Quantitative microstructural investigation showed that the role played by intragranular cracking in accommodating the inelastic deformations measured in reference samples deformed up to Stage 1, Stage 2 and Stage 3c (Figure 3.7) was negligible, small, and large, respectively (Figure 3.8), as implied by the obtained, stage-specific changes in

mean crack density per unit porosity reduction of 1.1, 32.4 and 110.7 mm^{-2}/%, respectively.

6) Therefore, the small, inelastic strains developing during Stage 2, expected to be relevant for sandstone reservoirs undergoing pore pressure reduction are thought to be largely accommodated by intergranular displacements developing normal and parallel to grain contacts that are weakly sutured, and/or clay-filled (*e.g.* Figure 3.10b,d), with a smaller role played by intragranular cracking. Intragranular cracking was found to be more significant during non-linear, Stage 3d (dilatant) and Stage 3c (non-linear compactant) $P - \Delta\varphi_t$ behavior (Figures 3.6, 3.8d, 3.9 and 3.10f).
7) Stage 2 inelastic behavior was demonstrated to be well-described by a plasticity model that utilizes the modified Cam-clay yield function (Figure 3.11), while obeying the normality condition (Figure 3.12), thus implying isotropic behavior. This was not the case for the inelastic strains developing during Stages 3d and 3c.
8) We applied this plasticity model in combination with poroelasticity theory to the case of the Groningen gas field (Figure 3.13). It was shown that the *in-situ* effective horizontal stress versus pore pressure data measured in the reservoir were far better represented by this combined elastic plus inelastic model (up to 40% difference), than they were by assuming that the total behavior could be described using poroelasticity. This was particularly apparent in the higher porosity materials ($\varphi_0 \geq 21.4\%$). The implications of this for (seismic) fault rupture in the Groningen field are discussed in more detail in Section 6.2.1.4.
9) Under modelled, uniaxial strain boundary conditions, again 30 to 50% of the total vertical strain was found to be inelastic (*i.e.* dissipated) and is therefore unavailable for release through seismicity, and associated fault rupture processes. This effect is larger in higher porosity sandstones, and is expected to be larger still with decreasing strain rate.
10) Our results indicate that markedly different stress-evolutions may be expected across a field characterized by non-uniform porosity, such as the Groningen field (Figure 1.1b – of Chapter 1). Therefore, taking into account the inelastic contribution to the total deformation of reservoir sandstone has a key role to play in future geomechanical modelling of induced seismicity and subsidence.

Acknowledgements

This research was carried out in the context of the research program funded by the Nederlandse Aardolie Maatschappij (NAM). This program aims to fundamentally improve understanding of production-induced reservoir compaction and seismicity in the seismogenic Groningen gas field. We thank the teams at NAM and Shell Global Solutions for providing samples and data and NAM for allowance to publish this study. Specifically, the authors like to thank Dirk Doornhof, Rob van Eijs (both NAM) and two anonymous reviewers for their help in improving the quality of the manuscript. Colin Peach is thanked for advice and help both in- and outside of the lab. We thank UU employees Gert Kastelein, Thony van der Gon-Netscher and Floris van Oort for technical assistance and Maartje Hamers for acquiring several of the micrographs used in this study. The data used in this paper are available as: Pijnenburg, Ronald; Verberne, Berend; Hangx, Suzanne; Spiers, Christopher (2019): Mechanical and microstructural data used in: "Inelastic deformation of the Slochteren sandstone: Stress-strain relations and implications for induced seismicity in the Groningen gas field". GFZ Data Services. http://doi.org/10.5880/fidgeo.2019.013

Appendix

In the general plastic stress-strain relations outlined by *Muir Wood*, [1991, *pp*. 106-107], the increments of inelastic volumetric strain ($d\varepsilon_{i,v} = d\varepsilon_{i,1} + 2d\varepsilon_{i,3}$) and inelastic shear strain ($d\gamma_i = 2/3[d\varepsilon_{i,1} - d\varepsilon_{i,3}]$) upon incremental excursions in mean effective stress ($dP = [d\sigma_1^{eff} + 2d\sigma_3^{eff}]$) and/or differential stress ($dQ = d\sigma_1^{eff} - d\sigma_3^{eff}$) from a known current mean effective stress (P) and differential stress (Q) are given:

$$d\varepsilon_{i,v} = \frac{-1}{\left(\frac{\delta f}{\delta \sigma^*}\left[\frac{d\sigma^*}{d\varepsilon_{i,v}}\frac{\delta f}{\delta P} + \frac{d\sigma^*}{d\gamma_i}\frac{\delta f}{\delta Q}\right]\right)}\left(\left(\frac{\delta f}{\delta P}\right)^2 dP + \frac{\delta f}{\delta Q}\frac{\delta f}{\delta P}dQ\right) \quad \text{(Eq. 3.A1a)}$$

and:

$$d\gamma_i = \frac{-1}{\left(\frac{\delta f}{\delta \sigma^*}\left[\frac{d\sigma^*}{d\varepsilon_{i,v}}\frac{\delta f}{\delta P} + \frac{d\sigma^*}{d\gamma_i}\frac{\delta f}{\delta Q}\right]\right)}\left(\frac{\delta f}{\delta Q}\frac{\delta f}{\delta P}dP + \left(\frac{\delta f}{\delta Q}\right)^2 dQ\right) \quad \text{(Eq. 3.A1b)}$$

where $\frac{\delta f}{\delta P}$, $\frac{\delta f}{\delta Q}$, and $\frac{\delta f}{\delta \sigma^*}$ are partial derivatives of a given yield function. The ratios $\frac{d\sigma^*}{d\varepsilon_{i,v}}$, and $\frac{d\sigma^*}{d\gamma_i}$ denote the slopes of the hardening relations between σ^* and $\varepsilon_{i,v}$ and γ_i, respectively. We use the modified Cam-clay yield function [*Muir Wood*, 1991]:

$$f(Q, P, \sigma^*) = Q^2 - M^2 P(\sigma^* - P) = 0 \quad \text{(Eq. 3.A2)}$$

The partial derivatives of Eq. A2 are:

$$\frac{\delta f}{\delta P} = M^2(2P - \sigma^*) \quad \text{(Eq. 3.A3a)}$$

$$\frac{\delta f}{\delta Q} = 2Q \quad \text{(Eq. 3.A3b)}$$

and:

$$\frac{\delta f}{\delta \sigma^*} = -M^2 P \qquad \text{(Eq. 3.A3c)}$$

Ignoring any hardening due to inelastic shear strain ($\frac{d\sigma^*}{d\gamma_i} = 0$), and inserting the above partial derivatives in Equation 3.A1a and b, we obtain:

$$\mathrm{d}\varepsilon_{i,v} = \frac{(M^2(2P-\sigma^*))^2 dP + 2QM^2(2P-\sigma^*)dQ}{M^2 P\, M^2(2P-\sigma^*)\frac{d\sigma^*}{\mathrm{d}\varepsilon_{i,v}}} \qquad \text{(Eq. 3.A4a)}$$

and:

$$d\gamma_i = \frac{2QM^2(2P-\sigma^*)dP + 4Q^2 dQ}{M^2 P\, M^2(2P-\sigma^*)\frac{d\sigma^*}{\mathrm{d}\varepsilon_{i,v}}} \qquad \text{(Eq. 3.A4b)}$$

Noting that $(2P - \sigma^*) = P - Q^2/(PM^2)$ (Equation 3.A2), these relations can be written as:

$$\mathrm{d}\varepsilon_{i,v} = \frac{\mathrm{d}\varepsilon_{i,v}}{d\sigma^*}\left(\left(1-\left(\frac{Q}{PM}\right)^2\right)dP + \frac{2Q}{PM^2}\,dQ\right) \qquad \text{(Eq. 3.A5a)}$$

and:

$$d\gamma_i = \frac{\mathrm{d}\varepsilon_{i,v}}{d\sigma^*}\left(\frac{2Q}{PM^2}dP + \frac{4Q^2}{M^4P^2-(QM)^2}dQ\right) \qquad \text{(Eq. 3.A5b)}$$

The inelastic vertical strain increment $\mathrm{d}\varepsilon_{i,1} = \mathrm{d}\gamma_i + \mathrm{d}\varepsilon_{i,v}/3$. Using Equations 3.A5a and b, and writing dP and dQ in terms of the principal effective stress increments ($\mathrm{d}\sigma_1^{\mathrm{eff}}$ and $\mathrm{d}\sigma_3^{\mathrm{eff}}$) we obtain:

$$\mathrm{d}\varepsilon_{i,1} = \frac{\mathrm{d}\varepsilon_{i,v}}{d\sigma^*}\left(\frac{2Q}{3PM^2}d\sigma_1^{eff} + \frac{4Q}{3PM^2}d\sigma_3^{eff} + \frac{4Q^2}{M^4P^2-(QM)^2}d\sigma_1^{eff} - \frac{4Q^2}{M^4P^2-(QM)^2}d\sigma_3^{eff} + \frac{1}{9}\left(1-\left(\frac{Q}{PM}\right)^2\right)d\sigma_1^{eff} + \frac{2}{9}\left(1-\left(\frac{Q}{PM}\right)^2\right)d\sigma_3^{eff} + \frac{2Q}{3PM^2}d\sigma_1^{eff} - \frac{2Q}{3PM^2}d\sigma_3^{eff}\right) \quad \text{(Eq. 3.A6)}$$

For a Biot coefficient of 1, a constant total vertical stress and taking pore pressure reduction as negative, then $\mathrm{d}\sigma_1^{\mathrm{eff}} = -\mathrm{d}P_\mathrm{p}$. Using this relation, and rearranging Equation 3.A6, gives:

$$d\varepsilon_{i,1} = \frac{d\Delta\varphi_i}{d\sigma^*}\left(\left(\frac{2Q}{3PM^2} - \frac{4Q^2}{M^4P^2-(QM)^2} + \frac{2}{9}\left(1-\left(\frac{Q}{PM}\right)^2\right)\right)d\sigma_3^{eff} - \left(\frac{4Q}{3PM^2} + \frac{4Q^2}{M^4P^2-(QM)^2} + \frac{1}{9}\left(1-\left(\frac{Q}{PM}\right)^2\right)\right)dP_p\right) \quad \text{(Eq. 3.A7)}$$

Similarly, the inelastic horizontal strain increment $\mathrm{d}\varepsilon_{\mathrm{i},3} = \mathrm{d}\varepsilon_{\mathrm{i,v}}/3 - \mathrm{d}\gamma_\mathrm{i}/2$. Inserting Equations 3.A5a and b, and noting that $\mathrm{d}\sigma_1^{\mathrm{eff}} = \mathrm{d}P_\mathrm{p}$, gives:

$$d\varepsilon_{i,3} = -\frac{d\Delta\varphi_i}{d\sigma^*}\left(\left(\frac{4Q}{3PM^2} - \frac{2Q^2}{M^4P^2-(QM)^2} - \frac{2}{9}\left(1-\left(\frac{Q}{PM}\right)^2\right)\right)d\sigma_3^{eff} + \left(\frac{Q}{3PM^2} - \frac{2Q^2}{M^4P^2-(QM)^2} + \frac{1}{9}\left(1-\left(\frac{Q}{PM}\right)^2\right)\right)dP_p\right) \quad \text{(Eq. 3.A8)}$$

Chapter 4

Intergranular clay films control inelastic deformation in the Groningen gas reservoir: Evidence from split-cylinder deformation tests

Based on: R.P.J. Pijnenburg, B.A. Verberne, S.J.T. Hangx, C.J. Spiers
Submitted to: Journal of Geophysical Research: Solid Earth

Abstract

Production of oil and gas from sandstone reservoirs leads to small elastic and inelastic strains in the reservoir, which may induce surface subsidence and seismicity. While the elastic component is easily described, the inelastic component, and any rate-sensitivity thereof remain poorly understood in the relevant small strain range (≤ 1.0%). To address this knowledge gap, we performed a sequence of five stress/strain-cycling plus strain-marker-imaging experiments on a single split-cylinder sample (porosity 20.4%) of Slochteren sandstone from the seismogenic Groningen gas field. The tests were performed under *in-situ* conditions of effective confining pressure (40 MPa) and temperature (100°C), exploring increasingly large differential stresses (up to 75 MPa) and/or axial strains (up to 4.8%) in consecutive runs. At the small strains relevant to producing reservoirs (≤ 1.0%), inelastic deformation was observed to be accommodated at least in part by normal and shear displacements occurring within clay-filled grain contacts. High axial strains (> 1.4%) led to pervasive intragranular cracking plus intergranular shear displacements within localized, conjugate bands. Using a simplified sandstone model, we show that the magnitude of inelastic deformation produced in our experiments at small strains (≤ 1.0%) and effective stresses relevant to the Groningen reservoir can indeed be roughly accounted for by clay film deformation. On this basis, inelastic compaction of the Groningen reservoir is expected to be largely governed by clay film deformation. Compaction by this mechanism is shown to be rate-insensitive on production time-scales, and is anticipated to halt when gas production stops, though slow, time-dependent creep by other processes cannot be eliminated. Similar, clay-bearing sandstone reservoirs are widespread globally. Our results may therefore be of direct relevance to many hydrocarbon fields worldwide.

4.1 Introduction

Extraction of oil and gas from sandstone reservoirs frequently leads to surface subsidence and induced seismicity [*Davies et al.*, 2013; *Suckale*, 2009]. Both effects are caused by the development of small vertical compaction strains (ε_1 < 1%) in the reservoir as the effective stress increases during reduction of the pore pressure, typically by several tens of MPa [*Mallman and Zoback*, 2007; *Morton et al.*, 2001]. Reservoir compaction is generally assumed to be poroelastic [*Bourne et al.*, 2014; *Dempsey and Suckale*, 2017; *Zbinden et al.*, 2017], hence reversible, rate-insensitive, linear and easily quantified [*Wang*, 2000]. However, both field data [*Santarelli et al.*, 1998] and experimental studies have shown that, even at the small reservoirs strains pertaining to hydrocarbon production, a significant part of the deformation behavior of sandstone reservoirs is inelastic [30- 70% - see: *Bernabe et al.*, 1994; *Schutjens et al.*, 1995; *Yale and Swami*, 2017; *Hol et al.*, 2018; *Pijnenburg et al.*, 2018]. This inelastic contribution is understood far less well, the mechanisms controlling it remain unidentified [*Hol et al.*, 2018; *Pijnenburg et al.*, 2018, 2019] and the question of whether these are rate-sensitive remains open [*NAM*, 2016; *Spiers et al.*, 2017; *Van Thienen-Visser et al.*, 2015b; *De Waal et al.*, 2015; *Van Wees et al.*, 2018]. If rate-sensitive, such mechanism could potentially cause ongoing compaction, subsidence and possibly seismicity even after production has been strongly reduced or stopped [*Mallman and Zoback*, 2007; *Nepveu et al.*, 2016]. This is of particular interest in the case of the densely populated and seismogenic Groningen gas field in the Netherlands – Europe's largest field. Here, it was recently decided to stop production by 2022 in an attempt to curb future induced subsidence and seismicity [*Wiebes*, 2019]. However, without a better understanding of the mechanisms governing inelastic reservoir compaction and their potential rate-dependence, the effects of such a change in production strategy are difficult to forecast [*NAM*, 2016; *De Waal et al.*, 2015; *Van Wees et al.*, 2018].

At the low temperatures (T < 150 °C) and time-scales (decades) relevant for fluid extraction from upper-crustal sandstone reservoirs (< 5 km), inelastic deformation may occur either through intragranular cracking [*Brantut et al.*, 2013] or else at grain-to-grain contacts via grain boundary asperity crushing, frictional slip [*Menéndez et al.*, 1996], deformation of intergranular clays [*Hawkins and McConnell*, 1992], or pressure solution (stress-driven mass transfer) [*Spiers et al.*, 2004].

Triaxial deformation experiments on sandstones at typical lab strain rates $\dot{\varepsilon}$ of 10^{-6} to10^{-4} s^{-1} and T < 150 °C, generally show three successive stages in mean effective stress (P) versus total porosity reduction ($\Delta\varphi_t$) behavior (Figure 4.1; *cf. Wong and Baud*, [2012]; *Pijnenburg et al.*, [2019]). During Stage 1, seen at total axial strains ε_1 up to 0.1 to 0.7% and

$\Delta\varphi_t$ up to 0.3 to 2.0%, the P - $\Delta\varphi_t$ behavior is compactive, non-linear, and concave-up, and is thought to reflect the semi-recoverable closure of pre-existing cracks [*David et al.*, 2012; *Walsh*, 1965] or grain boundaries [*Tutuncu et al.*, 1998]. During Stage 2, which typically persists to ε_1 of 0.5 to 1.5%, near-linear, compactive P - $\Delta\varphi_t$ behavior is seen. Although this is widely treated as reflecting linear poroelastic deformation [*Wong and Baud*, 2012, and references therein], some authors have recognized that it involves both elastic and inelastic processes [*e.g. Wong et al.*, 1992; *Bernabe et al.*, 1994]. Beyond Stage 2, high porosity sandstones tested at high confinement (typically ≥ 30 MPa; *Wong and Baud*, [2012]), show concave-down strain hardening P - $\Delta\varphi_t$ behavior, characterizing Stage 3c. Here, the suffix '*c*' denotes compaction, as opposed to suffix '*d*', denoting the dilatant behavior frequently seen at lower confinement and porosity (see Figure 4.1). Stage 3c is often envisaged to reflect pervasive intragranular cracking plus intergranular shearing, frequently localizing within diffuse volumes of the sample, or in discrete compaction bands [*Baud et al.*, 2004; *Fortin et al.*, 2005; *Heap et al.*, 2015; *Tembe et al.*, 2008].

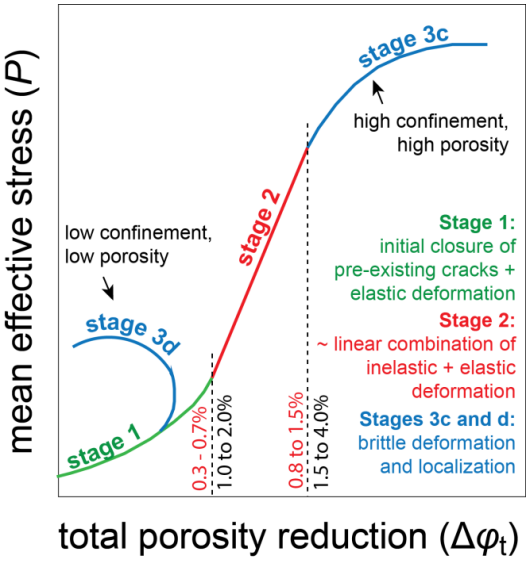

Figure 4.1 Schematic diagram showing the different stages in mean effective stress (P) versus total porosity reduction ($\Delta\varphi_t$) behavior typically seen in mechanical tests on sandstones. Note the effects of confining pressure and porosity on Stage 3 behavior (dilation – suffix "d" versus compaction - "c"). Typical values of total axial strain (red) and total porosity reduction (black), measured at the end of each stage are indicated.

A vast body of work exists on the inelastic, micromechanical behavior of sandstone at high axial strains (1.5 to 15%), focusing on Stage 3c/d behavior [*Baud et al.*, 2004; *Fortin et al.*, 2005; *Klein et al.*, 2001; *Tembe et al.*, 2008; *Wong et al.*, 1997; *Zhang et al.*, 1990]. However, subsidence data [*e.g. Mallman and Zoback*, 2007] and *in-situ* strain measurement data [*Cannon and Kole*, 2017] from gas and oil fields imply that it is the behavior seen at smaller strains (0.1 to 1.0%) that is the most relevant for producing reservoirs. This small-strain behavior has received relatively little attention. Experiments that have explored small reservoir-relevant strains show only sparse intragranular cracks, suggesting that inelastic deformation is predominantly intergranular [*Bernabe et al.*, 1994; *Menéndez et al.*, 1996; *DiGiovanni et al.*, 2007; *Pijnenburg et al.*, 2018; 2019]. In sandstones with a typical grain size of 100 – 300 μm, the grain-to-grain displacements needed to achieve such small-strain deformation would be less than 1 to 3 μm, making microstructural observations of the controlling mechanisms very challenging. Current, state-of-the-art, digital rock imaging methods such as 4-D X-ray tomography [*e.g. Ji et al.*, 2015; *Renard et al.*, 2017] cannot provide the resolution needed to observe these (sub-)micrometer displacements (resolution typically 5 - 20 μm). To elucidate the processes controlling these small, inelastic strains, incremental imaging of deforming sandstone with sub-micrometer resolution is required.

In this study, we investigate the microphysical processes controlling inelastic deformation of Slochteren sandstone from the Groningen gas field, during each of the three main stages of deformation represented in Figure 4.1, *i.e.* Stage 1, 2 and 3c. We adopt an approach similar to that used by *Spiers*, [1979] and *Quintanilla-Terminel et al.*, [2017]. A single split-cylinder sample, consisting of two equidimensional, half-cylinders of Slochteren sandstone (initial porosity = 20.4%; see: Figure 4.2a) was compressed in successive deviatoric stress-cycling experiments, performed at a confining pressure of 41 MPa, a pore pressure of 1 MPa and at 100°C, representing the temperature at the top of the Groningen reservoir [*NAM*, 2013]. In each experiment, we explored successively larger axial stresses (P up to 65 MPa; differential stress Q up to 75 MPa) and/or axial strains (up to 4.8%), covering deformation Stages 1, 2 and 3c. After each experiment, we used high resolution electron microscopy to analyse the permanent deformation recorded on the face of the half cylinders, using Particle Image Velocimetry (PIV) and a strain-marker mesh. We also investigated the microstructural changes seen on the imaged face. Particular attention was paid to identifying the grain-scale deformation mechanisms responsible for small inelastic strains relevant for reservoir depletion.

4.2 Background information on the Slochteren sandstone and the samples used

The 200 meter thick Slochteren sandstone forms the vast reservoir unit that constitutes the Groningen gas field. Located at 3 km depth, it lies unconformably on top of Carboniferous shales, siltstones and coals. It is overlain by a 50 thick claystone, followed by a thick (~ 1000 m) caprock sequence of Zechstein evaporites [*Amthor and Okkerman*, 1998]. The Slochteren sandstone is characterized by vertically averaged porosities ranging from 12 to 22% [*NAM*, 2013]. It is aeolian and fluviatile in origin [*Glennie et al.*, 1978]. Production from the field started in 1963, and has led to a decrease in pore pressure from 35 MPa to ~ 8 MPa in 2016 [*NAM*, 2016] and a corresponding increase in vertical effective stress from 30 to 57 MPa. At present, the upper 50 – 150 m of the Slochteren reservoir is gas-bearing and partly (25 ± 10 vol%) filled with connate brine [*Waldmann*, 2011]. The lower reaches are brine-saturated. The temperature at the top of the reservoir is 100°C [*NAM*, 2013]. The main body of the Slochteren sandstone consists predominantly of quartz (72 – 90 vol%) and feldspar grains (8 – 25 vol%), with smaller amounts of clay (0.5 – 5.5 vol%) [*Waldmann et al.*, 2014; *Waldmann and Gaupp*, 2016]. The detrital grain size is on average 150 – 250 µm [*Hol et al.*, 2018]. Early diagenetic illite films (1 - 7 µm thick) coat much of the surface of the quartz and feldspar grains and frequently occur within grain contacts [*Gaupp et al.*, 1993; *Waldmann*, 2011; *Wilson*, 1992]. Later burial diagenesis dissolved some of the initially present feldspars and precipitated kaolinite and more illite in the pores and onto the pore walls [*Waldmann and Gaupp*, 2016].

The Slochteren sandstone samples used in this study were obtained from core retrieved by the field operator (Nederlandse Aardolie Maatschappij, NAM) from the Zeerijp (ZRP)-3a well in 2015. Upon retrieval, the core was plastic-wrapped and sealed in aluminium barrels to avoid drying out and salt precipitation, which could damage the grain framework. The location of the ZRP-3a well and the local stratigraphy have been presented earlier by *Pijnenburg et al.* [2019]

4.3 Experimental methods

We performed a sequence of five consecutive triaxial stress-cycling experiments on a single split-cylinder sample (Figure 4.2a) of Slochteren sandstone, obtained from the core described above. Before mechanical testing, we ion-milled a strain marker grid into the polished face of one of the split-cylinder halves and imaged this face in full at high resolution (0.54 µm), using an FEI Helios Nanolab G3 Focused Ion Beam Scanning Electron Microscope (FIB-SEM). This was done to provide a means of tracking experimentally induced, inelastic strain field evolution and concomitant microstructural changes.

Experiment 1 involved hydrostatic loading only, up to an effective confining pressure (confining pressure minus pore pressure) up to 40 MPa, while in consecutive Experiments 2 to 5 the sample was subjected to subsequent deviatoric loading. The maximum differential stress-conditions ($Q = \sigma_1 - \sigma_3$) explored in each consecutive Experiment 1 to 5 are listed in Table 4.1. In consecutive Experiments 1, 2, 3 and 5, we explored increasingly large differential stresses (Q up to 75 MPa) and/or axial strains (up to 4.8%), chosen to systematically investigate the mechanisms governing the three main stages of P - $\Delta\varphi_t$ behavior shown in Figure 4.1. In Experiment 4, lower stresses and strains were explored than in the foregoing Experiment 3, with the aim of investigating the effect of loading history on the micromechanical behavior. After each experiment, the increasingly deformed sample was removed from the deformation machine and the grid-marked face was re-imaged to record any permanent changes in the microstructure. In addition, we performed two control experiments, one on a second split-cylinder sample and the other on an intact cylindrical plug to test for possible effects of the split-cylinder configuration on the mechanical behavior measured at the sample scale. In all our tests, we used demineralized water as pore fluid, a pore pressure (P_p) of 1 MPa, an axial strain rate of 10^{-5} s^{-1}, and a temperature of 100°C.

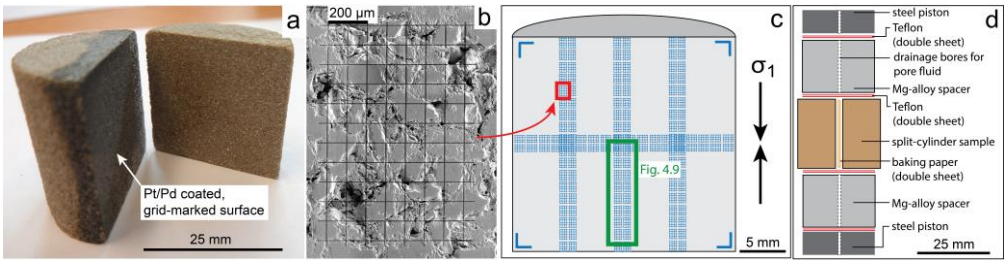

Figure 4.2 Split-cylinder Sample Z1. **a)** Two sample halves with strain marker grids applied to one face; **b)** Secondary electron image of a single strain marker grid; **c)** Illustration of the face of the grid-marked half sample, showing the strain marker array, L-shaped reference corners, and the area used for the grain-scale strain and Electron Dispersive X-ray spectroscopy analyses (green box). **d)** Illustration of the sample-assembly used during mechanical testing. Note the Mg-alloy filler blocks and Teflon sheets emplaced to reduce shear traction at the sample-piston interface.

Table 4.1 Key-mechanical, and microstructural data obtained in this study. All experiments were performed at a temperature of 100°C, a pore pressure of 1 MPa and an effective confining pressure up to 40 MPa. L_0 denotes the initial (pre-test) sample length. $(Q)_{max}$ denotes the maximum differential stress imposed in each experiment on Z1 or in the control experiments on Z2 and Z3. $\Delta\varphi_{t,max}$ and $\varepsilon_{t,max}$ denote, respectively, the maximum values of total porosity reduction and total axial strain (measured during deviatoric compression) explored in each experiment. $\Delta\varphi_i$ is the inelastic porosity reduction measured at the reference effective confining pressure (P_c^{eff}) of 5 MPa. ε_i denotes the inelastic axial strain that developed during deviatoric stress cycles and is obtained at Q = 0 MPa and P_c^{eff} = 40 MPa. $\Delta\varepsilon_i$ denotes the increment in inelastic axial strain, relative to that measured in the foregoing stress-cycling experiment. ε_i^{cal} is the inelastic axial strain measured by caliper after each test. $\bar{\varepsilon}_{11}^{mm}$, $\bar{\varepsilon}_{22}^{mm}$, and $\bar{\omega}_{12}^{mm}$ correspond to the mm-scale, mean inelastic vertical strain, mean inelastic horizontal strain and mean inelastic body rotation, respectively, determined from micrographs covering the face of split-cylinder Z1, obtained after each experiment. $\bar{\varepsilon}_{11}^{grain}$ and $\bar{\varepsilon}_{22}^{grain}$ denote the grains-scale mean inelastic vertical and horizontal strains obtained on Z1 within the area indicated in Figure 4.2c. For control experiments, no microstructures were analyzed.

		mechanical data						*calliper*	*microstructural data*				
	L_0	$(Q)_{max}$	$\Delta\varphi_{t,max}$	$\Delta\varphi_i$	$\varepsilon_{t,max}$	ε_i	$\Delta\varepsilon_i$	ε_i^{cal}	$\bar{\varepsilon}_{11}^{mm}$	$\bar{\varepsilon}_{22}^{mm}$	$\bar{\omega}_{12}^{mm}$	$\bar{\varepsilon}_{11}^{grain}$	$\bar{\varepsilon}_{22}^{grain}$
	[mm]	[MPa]	[%]	[%]	[%]	[%]	[%]	± 0.1 [%]	[%]	[%]	[°]	[%]	[%]
Sequential experiments of hydrostatic and deviatoric stress-cycling plus imaging of split-cylinder Sample Z1													
Exp 1	23.75	0	2.5	1.1	*n.a.*	*n.a.*	*n.a.*	0.0	0.0	0.1	0.0	-0.1	0.1
Exp 2	23.75	50.0	3.2	1.6	1.1	0.4	0.4	0.4	0.4	0.1	0.0	0.4	0.2
Exp 3	23.65	74.8	3.4	1.9	2.2	1.0	0.6	0.6	0.6	-0.1	0.0	0.6	-0.1
Exp 4	23.50	50.0	3.9	1.9	1.6	0.6	-0.4	0.0	0.1	0.1	0.0	*n.d.*	*n.d.*
Exp 5	23.50	66.0	4.4	2.9	4.8	3.5	2.5	2.7	2.3	-1.1	0.0	*n.d.*	*n.d.*
Control experiments													
Z2	24.5	72.9	4.0	2.5	5.0	3.8		3.2	*n.d.*	*n.d.*	*n.d.*	*n.d.*	*n.d.*
Z3	50.0	73.5	3.4	1.9	4.1	3.1		2.8	*n.d.*	*n.d.*	*n.d.*	*n.d.*	*n.d.*

4.3.1 Sample preparation

Two cylindrical plugs, measuring 25.4 mm in diameter, and ~ 70 mm in length, were drilled from immediately adjacent locations in the chosen core section (true vertical depth: 3065 meter), in an orientation parallel to the core axis and sub-perpendicular (within 10 degrees) to the slightly inclined bedding. The reservoir brine present in the pore space was diluted with demineralized water (DMW), by soaking the samples in DMW for 6 - 7 days, refreshing the DMW every day until the brine was essentially replaced. Subsequently, the

samples were dried for 48 hours at T = 50˚C. After drying, one of the two plugs was cut perpendicular to the core axis, using a diamond saw, to obtain two shorter plugs of approximately equal length. The ends of all three plugs were ground flat and perpendicular to the sample axis to ensure a homogeneous load distribution during testing. The final length of the two short plugs (Z1 and Z2) was 24 ± 0.5 mm and that of the longer plug (Z3) was 50.0 mm (Table 4.1). The 50-mm sample (Z3) was then vacuum-saturated with DMW. The difference in mass between the dry and saturated sample was used to calculate the initial sample porosity (φ_0), yielding a value of 20.4%. We assumed that this value was also representative for the two shorter samples, Z1 and Z2.

The 50-mm sample Z3 was stored wet, *i.e.* submerged in DMW, until mechanical testing commended. By contrast, the ~24 mm long plugs Z1 and Z2 were used to prepare split-cylinder samples (Figure 4.2a). Prior to cutting and polishing, these samples were vacuum-impregnated with Polaroid B72 resin to reduce any damage induced by handling. Curing was achieved at room temperature over 48 hours. Each was then sectioned axially using a 0.4 mm thick diamond wafering saw, to obtain two half cylinders of equal radius (within 0.3 mm). The faces of the half cylinders were polished flat using a rotary polishing table and a 1 µm diamond suspension. The resin was then removed by soaking the samples in acetone for 6 days, refreshing the acetone every day. The samples were subsequently removed from the acetone and then oven-dried at T = 50 °C. Sample Z1 (two halves) was used for microstructural investigation, whereas sample Z2 (two halves) was used to conduct the aforementioned control experiment (see Table 4.1). The surface of one half of split-cylinder Sample Z1 was sputter-coated with a 20 nm thick layer of Pt/Pd (Figure 4.2a). To detect grain-scale deformations, a rectilinear array of strain marker grids was milled into the surface of one half of split-cylinder Sample Z1 (Figure 4.2a-c), using the ion mill installed in the Helios FIB-SEM. The detailed procedure adopted during milling is outlined in Section 4.4.1.

4.3.2 Sample assembly

Split-cylinder samples Z1 and Z2 were assembled dry, while cylindrical sample Z3 was installed wet (*cf.* Section 4.3.1). The split-cylinder samples were assembled with three sheets of baking paper between the two sample halves, to separate and protect their surfaces during testing. To reduce mechanical contrast and hence shear traction at the sample-piston interfaces during axial compression [*Olsson and Holcomb*, 2000], we located each sample (Z1, Z2 and Z3) between two cylindrical Mg-alloy (AZ-31) spacers with similar elastic properties, within a factor of two, to the sandstone. The AZ-31 alloy has Young's modulus E

= 32 GPa, and Poisson's ratio v = 0.35, while the sandstone has E = 10 to 20 GPa and $v \approx 0.2$ [*Pijnenburg et al.*, 2019]. The spacers were 15 mm in length and 25 mm in diameter and axially bored to allow free pore fluid access to the sample (Figure 4.2d). To ensure fully elastic response of the spacers during testing, all spacers were pre-compressed to a differential stress of 105 MPa, at the same temperature (T = 100°C) and similar confining pressure (P_c = 40 MPa) as those used in the experiments. To reduce shear traction further, a double layer of perforated Teflon sheet (50 μm) was included at both ends of the sample (Figure 4.2d). The sample plus alloy spacer assembly was then jacketed using a fluorinated ethylene propylene (FEP) sleeve, which was tourniquet-sealed against the top and bottom steel loading blocks with additional, perforated Teflon sheets inserted at the alloy-steel interfaces (Figure 4.2d).

4.3.3 Experimental procedure

4.3.3.1 General procedure applied to all samples

After sealing, each sample assembly was emplaced into an externally heated, conventional triaxial deformation apparatus employing silicone oil as confining medium (for details see: *Peach*, [1991]; *Pijnenburg et al.*, [2018]). The confining pressure was increased to 5 MPa. The pore fluid system was evacuated for 30 minutes, followed by vacuum saturation of the dry split-cylinder samples Z1 and Z2, or injection of DMW onto the surface of the pre-saturated cylindrical sample Z3. We subsequently applied the pore pressure (P_p = 1 MPa) and then increased the confining pressure (P_c = 6 MPa), resulting in an effective confining pressure ($P_c^{eff} = P_c - P_p$) of 5 MPa. The sample was then brought to the desired testing temperature (T = 100°C), while maintaining P_c^{eff} at or just below 5 MPa. The system was subsequently left to equilibrate for 4 hours, and mechanical testing then commenced.

4.3.3.2 Z1-specific aspects

Sample Z1 was subjected to five consecutive experiments, the first involving hydrostatic loading only and the remainder involving subsequent axial shortening. The maximum stresses and axial strains explored in each experiment are listed in Table 4.1.

Each experiment was preceded by the above sample assembly and initial experimental procedure. Each experiment was ended by reducing the pore pressure and then the confining pressure to ambient values, cooling (to T ~ 80 °C), removal of the sample from the vessel and disassembly for microstructural analysis. In Experiment 1, the sample was subjected to a single hydrostatic stress cycle. The confining pressure was gradually increased from 6 to 41 MPa, while maintaining a constant pore pressure of 1 MPa, so that P_c^{eff}

increased from 5 to 40 MPa. We employed a pressurization rate of ± 0.1 MPa/s, chosen such that the rate of change of the mean effective stress ($\dot{P}$) was similar to that used during subsequent deviatoric stress-cycling. Upon reaching P_c^{eff} = 40 MPa, the sample was depressurized to the initial value of 5 MPa to measure any inelastic (permanent) pore volume change at this reference pressure. At this point, Experiment 1 was ended as described above and the sample was removed from the vessel. In all subsequent experiments (2 through 5), the sample was first subjected to the hydrostatic stress-cycle as described above. Following this initial cycle, the P_c^{eff} was returned to 40 MPa, again as outlined above, at which point Sample Z1 was subjected to deviatoric stress cycling. During deviatoric cycling, the piston was first advanced, and then retracted at constant rate ($\dot{\varepsilon}_t$ of ~ 10^{-5} s^{-1}), leading to a gradual increase or decrease in differential stress Q. In Experiment 2, the sample was subjected to a single deviatoric stress cycle, during which a maximum Q value of 50 MPa was reached. The sample was then axially unloaded (Q = 0 MPa) decompressed to P_c^{eff} = 5 MPa, after which the experiment was ended. In Experiment 3, the initial hydrostatic cycle was followed by the same deviatoric cycle as employed in Experiment 2. The sample was then subjected to a second deviatoric stress-cycle at P_c^{eff} = 40 MPa, reaching a maximum Q value of 75 MPa. This was again followed by axial unloading, decompression to P_c^{eff} = 5 MPa, and ending of the experiment. In Experiment 4, we repeated the procedure followed in Experiment 2. In Experiment 5, the same procedure was adopted as that followed in Experiment 3, although here, the maximum differential stress achieved in the second deviatoric cycle was 65 MPa.

After removal of Sample Z1 from the vessel following each experiment, the jacket was carefully taken off, the two split-cylinder halves were taken apart and the sheets of baking paper were removed from the sample faces. Disassembling the sample led to no visual damage of the sample, aside from local removal of the Pt/Pd coating covering the split-cylinder face. Both sample halves were left to dry for 48 hours at T = 50 °C. After drying, the permanent change in sample length (ΔL^{cal}), referenced to the length of the sample before the experiment (L_0 – see Table 4.1) was measured using a calliper (resolution 50 µm - error in ΔL^{cal} of ± 0.1%). The marked sample was then re-imaged, after which the above procedure was repeated for the next stress-cycling experiment. In total, Sample Z1 was deformed 5 times, and imaged 6 times.

4.3.3.3 Procedure for control experiments Z2 and Z3

In the control experiments performed on samples Z2 and Z3, we followed the same procedure as outlined for Z1, but without intermittent removal of the sample from the vessel. Both samples were first subjected to a hydrostatic cycle over the range $5 \leq P_c^{eff} \leq 40$ MPa.

The samples were then reloading to P_c^{eff} = 40 MPa and subsequently subjected to deviatoric stress-cycling. During this deviatoric portion, we imposed three consecutive stress-cycling steps, leading to increases of Q up to 50 MPa, 75 MPa and ~ 72 MPa, respectively. After the final step, the sample was depressurized to P_c^{eff} = 5 MPa and inelastic pore volume changes were measured at this reference pressure. Finally, first the pore pressure, and then the confining pressure was removed, the temperature was reduced and the sample was removed from the deformation apparatus.

4.3.4 Mechanical data acquisition and processing

During testing, the internal axial load, confining pressure, pore pressure, pore fluid volume change, sample temperature, and axial displacement were logged at 2 Hz, using a 16-bit DAQPad National Instruments A/D converter. Internal axial load data were processed to yield axial load versus time. The displacement data were accordingly corrected for apparatus distortion and thermal expansion, using calibrations carried out using a steel dummy plus the pre-compressed Mg-alloy spacers, at representative pressure and temperature conditions. The pore fluid volume change data were corrected for thermal volume changes upon flowing in or out of the heated pressure vessel. The corrected displacement and pore volume data were used to determine the changes in sample length (ΔL), and pore volume (ΔV) versus time. These data were subsequently used to calculate the total axial strain $\varepsilon_t \approx e_t = \Delta L/L_0$ (for the present low strains), and the total porosity reduction $\Delta\varphi_t = \Delta V/V_0$, where L_0 and V_0 are the initial sample length and volume, respectively, measured before each experiment. Differential stress (Q) and mean effective stress (P) were computed, assuming that the instantaneous cross-sectional area of the sample was equal to $(V_0 - \Delta V)/(L_0 - \Delta L)$. In Table 4.1, $(Q)_{max}$ refers to the maximum differential stress imposed in each experiment. The quantities $\Delta\varphi_{t,max}$ and $\varepsilon_{t,max}$ are the maximum values of total porosity reduction and total axial strain explored in each experiment, respectively. We adopt the convention that compressive strains and porosity reduction (compaction) are positive. The inelastic porosity reduction ($\Delta\varphi_i$) was obtained by dividing the inelastic (permanent) change in pore volume determined at the reference mean effective stress of 5 MPa by the initial sample volume V_0. The inelastic axial strain (ε_i) was determined after each deviatoric stress-cycling sequence (*i.e*. before final hydrostatic unloading), by dividing the permanent reduction in sample length determined upon deviatoric unloading, referenced to the sample length measured at the first deviatoric loading step, by the initial sample length L_0. Relative errors in all the above quantities are < 0.04% [*Pijnenburg et al.*, 2018]

4.4 Microstructural/ microchemical methods and data processing: Sample Z1

Here, we describe the detailed methods and data processing procedures applied specifically to the gridded surface of split-cylinder Sample Z1.

4.4.1 Grid milling and sample imaging

As indicated earlier, we milled a rectilinear array of marker grids into the face of one half of splityclinder Sample Z1 (see Figures 4.2a-c), using the ion mill installed in the Helios FIB-SEM. Milling was achieved employing an acceleration voltage of 30 kV, a beam current of 64 nA, a working distance of 25-30 mm and a horizontal field width of 1.41 mm. These parameters were chosen to obtain grid lines ~1 μm deep and wide (calibrated for pure SiO_2). Each strain-marker grid measured 700 μm wide and 1100 μm long (see Figure 4.2b), and consisted of 8 by 12 gridlines with a 100 μm spacing (cf. grain diameter ~200 μm). The arrangement of grids employed is shown in Figure 4.2c. In addition, four L-shaped reference marks were milled at the corners of the gridded sample surface (~ 1 mm from the surface edges), for relocation and image alignment during processing.

The entire sample face was then imaged in Secondary Electron (SE) mode, using an Everhart-Thornley detector [*Everhart and Thornley*, 1960]. Per full sample scan, a mosaic consisting of over 1500 rectangular SE micrograph tiles was constructed, maintaining a vertical and horizontal overlap of 10% between adjacent tiles. Each mosaic tile was obtained at a resolution of 0.54 μm per pixel, using an acceleration voltage of either 2 kV (before mechanical testing and after Experiments 1 and 2) or 1 kV (after experiments 3-5) and a beam current of 0.1 nA. We used a working distance of 4.5 mm (undeformed sample) or 4.0 mm (after each experiment), a horizontal field width of 828 μm and a dwell time of 3 μs. This imaging procedure was performed on the undeformed Z1 sample and repeated after each experiment, *i.e.* after removal of Sample Z1 from the deformation apparatus. After imaging, the sample was removed from the FIB-SEM chamber and prepared for mechanical testing.

4.4.2 Image handling

Secondary electron (SE) mosaic image tiles were stitched together using ImageJ [*Preibisch et al.*, 2009]. Stitched SE image mosaics were rotated to align the bottom two L-shaped reference corners and subsequently cropped to a rectangle bounded by the bottom-left and top-right reference corners. To account for distortion effects due to sample tilting, charging and differences in working distance and acceleration voltages used in the various imaging sessions (see the previous Section 4.4.1), the resolution of the cropped

mosaics was corrected in the manner outlined in Appendix 4.A1. After correction, all mosaics were scaled to a uniform 0.54 µm/pixel. After pre-processing, the mosaics were approximately 42000 by 40000 pixels in size and covered ~92% of the surface of the grid-marked Z1 cylinder half. The mosaic micrographs were subsequently processed to yield the inelastic deformation developing between deformation experiments on two scales: 1) The mm-scale (~1 mm^2) across the full imaged face. In this case, the strain field was quantified using grid-independent, Particle Image Velocimetry (PIV) analysis; 2) The grain-scale (~0.04 mm^2), using the ion-milled strain marker grid to map incremental deformations.

4.4.2.1 Millimeter-scale displacement gradient determination

The incremental, mm-scale displacement field obtained after each sequential experiment was obtained using the Particle Image Velocimetry (PIV) plugin installed in ImageJ [*Tseng et al.*, 2012]. PIV is a widely applied digital image correlation technique [*e.g. White et al.*, 2003; *Stamhuis*, 2006; *Tseng et al.*, 2012], which calculates the displacement of a region, within an image, relative to its previous position. We applied this technique to the whole-sample mosaics obtained before and after each experiment on Sample Z1, in order to map deformation at the mm-scale. To limit PIV computing time, we reduced the width and height resolution of the image mosaics by a factor of four to approximately 2 µm/pixel. For each set of mosaics obtained before and after each experiment, the incremental, internal displacement vectors (s) with vertical and horizontal components s_1 and s_2, respectively, were calculated using a square interrogation window size of 512 x 512 pixels (~1 mm^2) and a search window of 1024 x 1024 pixels. These displacements (s) were determined relative to the bottom-left corner of each mosaic, at regular intervals (w) of 256 pixels (= 552 µm) in both the horizontal and vertical directions. This implies that neighbouring interrogation windows overlapped by 50%, meaning that the displacements obtained were averaged over an area that was four times the interrogation window area. Taking contraction to be positive, the change in displacement (Δs) developing in each 256 by 256 pixel window was obtained by subtracting the displacement measured in this window (s^{ref}) from the displacements measured in the top- (s^T) and right- neighbouring windows (s^R). Thus, for each window, we obtain the displacement increment components reflecting the increments in vertical contraction ($\Delta s_1{}^T = s_1{}^T - s_1{}^{ref}$), horizontal contraction ($\Delta s_1{}^R = s_1{}^R - s_1{}^{ref}$), top-lateral shear displacement ($\Delta s_2{}^T = s_2{}^T - s_2{}^{ref}$), and side-lateral shear displacement ($\Delta s_2{}^R = s_2{}^R - s_2{}^{ref}$). By dividing these displacement increment components by the vector spacing w, we obtain the inelastic displacement gradient tensor (J_{ij}) of each window, notably through:

$$J_{ij} = \begin{pmatrix} J_{11} & J_{12} \\ J_{21} & J_{22} \end{pmatrix} \approx \begin{pmatrix} \frac{{s_1}^{\mathrm{T}} - {s_1}^{\mathrm{ref}}}{w} & \frac{{s_1}^{\mathrm{R}} - {s_1}^{\mathrm{ref}}}{w} \\ \frac{{s_2}^{\mathrm{T}} - {s_2}^{\mathrm{ref}}}{w} & \frac{{s_2}^{\mathrm{R}} - {s_2}^{\mathrm{ref}}}{w} \end{pmatrix} = \begin{pmatrix} \frac{\Delta {s_1}^{\mathrm{T}}}{w} & \frac{\Delta {s_1}^{\mathrm{R}}}{w} \\ \frac{\Delta {s_2}^{\mathrm{T}}}{w} & \frac{\Delta {s_2}^{\mathrm{R}}}{w} \end{pmatrix} \quad \text{(Eq. 4.1)}$$

This can be split into a symmetric part, describing the inelastic, mm-scale strain (ε_{ij}^{mm}) and an anti-symmetric part, specifying the inelastic, mm-scale, rigid body rotation tensor (ω_{ij}^{mm}):

$$J_{ij} = \varepsilon_{ij}^{mm} + \omega_{ij}^{mm} = \frac{1}{2}\begin{pmatrix} 2J_{11} & J_{12}+J_{21} \\ J_{21}+J_{12} & 2J_{22} \end{pmatrix} + \frac{1}{2}\begin{pmatrix} 0 & J_{12}-J_{21} \\ J_{21}-J_{12} & 0 \end{pmatrix} \quad \text{(Eq. 4.2)}$$

where $\omega_{12}^{mm} = -\ \omega_{21}^{mm} \approx \alpha$, the rotation angle in radians. Applying Equations 4.1 and 4.2 to our displacement data we obtained a field of ε_{11}^{mm}, ε_{22}^{mm} and ω_{12}^{mm} data describing the incremental, inelastic deformation recorded on the split-cylinder face after each stress-cycling experiment. The values obtained were linearly interpolated to create contour plots showing the inelastic principal strains and rotation across the entire sample. In addition, after each experiment, the obtained values of ε_{11}^{mm}, ε_{22}^{mm} and ω_{12}^{mm} were averaged to yield their corresponding means $\bar{\varepsilon}_{11}^{mm}$, $\bar{\varepsilon}_{22}^{mm}$ and $\bar{\omega}_{12}^{mm}$, respectively, which are listed in Table 4.1.

Note that the above methodology means that the top-most row and the right-most column of 256 x 256 pixel windows were omitted from the PIV analysis. The error resultant from the PIV analysis is estimated following the method outlined by *Wieneke* [2015] and as described in Appendix 4.A2. The horizontal ($\mathrm{Err_h}^{\mathrm{PIV}}$) and vertical components ($\mathrm{Err_v}^{\mathrm{PIV}}$) of error were both found to be less than ± 0.14 pixels for each interrogation window, implying (for the 256 pixel vector spacing) an acceptable error of ± 0.06% in the mm-scale strains obtained and of ± 0.03° in the mm-scale body rotations. Note, though, that strains and rotations lower than these values cannot be resolved.

4.4.2.2 Grain-scale strain determination

PIV was found to be inadequate to quantify grain-scale (~0.04 mm^2) displacements, as its accuracy was strongly reduced in regions where the Pt/Pd surface coating was damaged, or where grains had broken after a given deformation experiment. Instead, to analyse these smaller-scale deformations, we used the distortion of the ion-milled strain marker grid in the location indicated in Figure 4.2c. For this analysis, we used the stitched images at full resolution (0.54 µm/pixel), obtained before Experiment 1 and after Experiments 1, 2 and 3. These images were selected because each of the corresponding experiments explored one of the three main Stages of $P - \Delta\varphi_t$ behavior seen during sandstone compression (Figure 4.1).

The images obtained after the subsequent experiments 4 and 5 were not analysed.

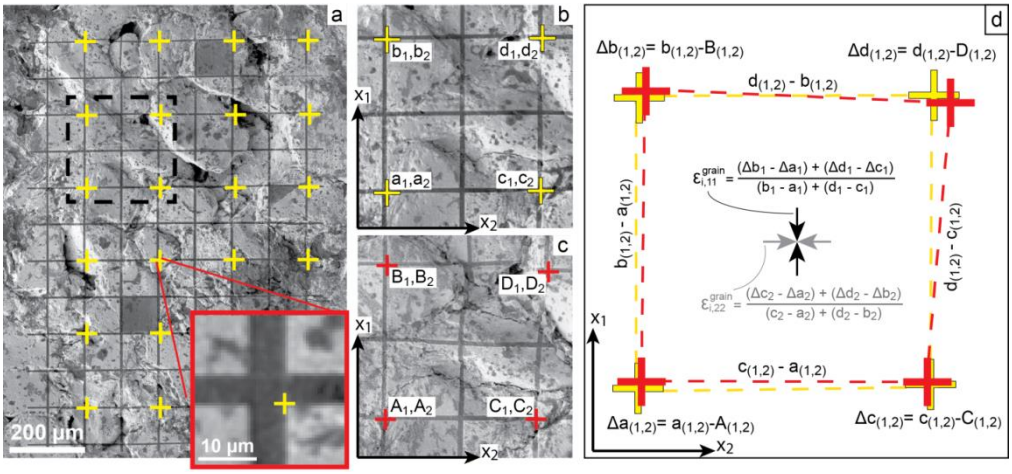

Figure 4.3 Illustration of the approach adopted to obtain grain-scale inelastic strains. **a)** For the strain markers grids enveloped by the green box in Figure 4.2c, the coordinates of the bottom-right corner of ion-milled line crossings were determined before and after stress-cycling Experiments 1, 2 and 3. Grain-scale strains were analysed for each near-square region cornered by four initial reference points. The positions of the bottom-right corners of grid line-crossings (see inset) are measured **b)** before the experiment (here denoted: a,b,c,d) and **c)** after the experiment (A,B,C,D). **d)** The displacements of these points were used to calculate the grain-scale, principal, inelastic strains. In total, 288 grain-scale areas were analysed in this way.

To quantify the incremental, grain-scale, inelastic stain, we measured the position of the bottom-right corner of every 2 x 2 group of strain marker cells (Figure 4.3a) before and after each experiment. The accuracy of measurement of the reference point coordinates is estimated to be ± 1 pixel, since at the scale of the pixels, the boundaries of strain marker lines are often diffuse (see inset Figure 4.3a). The corners of each near-square 2 x 2 cell within the micrographs obtained prior to any given experiment are designated: $a_{(1,2)}$, $b_{(1,2)}$, $c_{(1,2)}$ and $d_{(1,2)}$ (Figure 4.3b), where, the indices 1 and 2 indicate the coordinates in the axis-parallel and axis-perpendicular directions, respectively. After deformation, these points are denoted $A_{(1,2)}$, $B_{(1,2)}$, $C_{(1,2)}$ and $D_{(1,2)}$ (Figure 4.3c). The displacement of each reference point is calculated using the difference in position of the same point before (yellow crosses) and after (red crosses) deformation, *e.g.* $\Delta a_{(1,2)} = A_{(1,2)} - a_{(1,2)}$, taking contraction with reference to the bottom-left corner as positive (Figure 4.3d). These displacements are then used to determine the inelastic deformation within each near-square cell, where the

grain-scale, inelastic, vertical strain is given: ε_{11}^{grain} = ([$\Delta b_1 - \Delta a_1$] + [$\Delta d_1 - \Delta c_1$]) / ([$b_1 - a_1$] + [$d_1 - c_1$]), and the grain-scale, inelastic, horizontal, strain is obtained using ε_{22}^{grain} = ([$\Delta c_2 - \Delta a_2$] + [$\Delta d_2 - \Delta b_2$]) / ([$c_2 - a_2$] + [$d_2 - b_2$]). The grain-scale, inelastic shear strains are similarly obtained, where: ε_{21}^{grain} = ([$\Delta b_2 - \Delta a_2$] + [$\Delta d_2 - \Delta c_2$]) / ([$b_1 - a_1$] + [$d_1 - c_1$]), while ε_{12}^{grain} = ([$\Delta c_1 - \Delta a_1$] + [$\Delta d_1 - \Delta b_1$]) / ([$c_2 - a_2$] + [$d_2 - b_2$]). Error propagation based on the limited accuracy of ± 1 pixel of each reference point measurement implies that the absolute, standard errors on ε_{11}^{grain}, ε_{22}^{grain}, ε_{21}^{grain} and ε_{12}^{grain} are each ± 0.6% strain. The quantities $\bar{\varepsilon}_{11}^{grain}$ and $\bar{\varepsilon}_{22}^{grain}$ listed in Table 4.1 refer to the mean, grain-scale, inelastic, vertical and horizontal strains, respectively, of the 288 near-square regions analysed. The standard errors on these mean values are 0.03% strain. The inelastic deformation of each 2 x 2 strain marker cell is described further using the area strain in 2D, given by ε_{11}^{grain} + ε_{22}^{grain}, and the average- or effective shear strain (*i.e.* the 2nd invariant of the grain-scale, inelastic, deviatoric strain tensor in 2D), given: $\varepsilon_e^{grain} = \sqrt{\frac{1}{4}\left(\varepsilon_{11}^{grain} - \varepsilon_{22}^{grain}\right)^2 + \left(\varepsilon_{12}^{grain}\right)^2}$.

4.4.3 Chemical element mapping

4.4.3.1 Electron dispersive X-ray spectrometry method

Post-experiment, Sample Z1 was analysed further through electron dispersive X-ray spectrometry (EDX) chemical element mapping in the Helios instrument. First, the grid-marked sample halve was cast in Araldite 20:20 resin. After curing for 48 hours, the flat, axis-parallel surface was lightly ground, and subsequently polished using a 1 µm diamond suspension to even out the deformed surface and to fully remove the Pt/Pd coating. This procedure led to an average removal of the top 10 - 15 µm of the imaged sample surface. Virtually all grains visible in the SE micrographs obtained before grinding were still clearly identifiable in a reflected light microscope, though the marker grid is no longer present. The polished surface was then re-coated with a 5 - 20 µm layer of carbon. We analysed a rectangular area measuring 2 by 11 mm, located in the bottom center of the sample and oriented with its long side parallel to the main compression direction (green box in Figure 4.2c). This rectangular area was chosen to overlap with a series of strain marker grids, thus allowing evaluation of the effect of mineralogy on (local) deformation. EDX element maps were obtained by collecting mosaic micrographs, using an Oxford Instruments X-Max 150 silicon drift detector (acceleration voltage: 10 kV; beam current: 1.6 nA; working distance: 4.0 mm; horizontal field width of 0.8 mm). The elements mapped included Al, Ba, Ca, Cl, Fe, K, Mg, Mn, Na, S and Si, forming the main constituents of the sample, except for Cl, which we used to filter out the background (noise) signal [*cf. Verberne and Spiers*, 2017]. Element

maps were recorded at a resolution of 2 µm per pixel, and stitched automatically using Aztec software.

4.4.3.2 EDX data processing

To reduce noise, all EDX single element maps obtained from the microstructurally investigated cylinder half of Z1 were subjected to an edge-preserving, mean shift filter [*Fukunaga and Hostetler*, 1975], at a spatial radius of 2 pixels. Subsequently, filtered single element maps were processed to yield the main constituent minerals, notably quartz, feldspars, clays, carbonates and sulphates on the basis of their stoichiometry [*cf. Verberne and Spiers*, 2017]. The obtained mineral maps were converted to binary images through an Otsu threshold [*Otsu*, 1979], resulting in black and white colored images. These binary clay maps were processed further to isolate the clays present within grain contacts (*i.e.* where quartz, feldspar, carbonate and sulfate grains are juxtaposed within ~10 µm proximity from each other), thus excluding clays present in the pore space or coating the pore walls, as they do not contribute to the load-bearing framework. This was done by manually delineating each grain contact in a quartz + feldspar + carbonate + sulphate map using ImageJ. The resulting grain contact map was overlain (*i.e.* multiplied) with the binary clay map to produce a map showing the clays within grain contacts. This map was used to determine the area percentage of grain contact clay minerals.

4.5 Results - Mechanical data

A list of the experiments performed, the testing conditions, and the key-mechanical and microstructural data obtained is given in Table 4.1.

4.5.1 Sequential stress-cycling experiments performed on split-cylinder Sample Z1

P versus $\Delta\varphi_t$ and *Q* versus ε_t plots showing the mechanical data obtained in each of the five consecutive experiments imposed on split-cylinder Sample Z1 are shown in Figure 4.4. Throughout the sequence of experiments, Z1 showed typical Stage 1 (non-linear, concave-up), Stage 2 (near-linear) and Stage 3c (non-linear, concave-down) mean effective stress (*P*) versus total porosity reduction ($\Delta\varphi_t$) behavior (*cf.* Figures 4.1 and 4.4a). During loading, deformation consistently was compactive ($\Delta\varphi_t$ incremented monotonically). During unloading, all *P* - $\Delta\varphi_t$ and differential stress (*Q*) versus total axial strain (ε_t) curves (Figure 4.4b) showed higher stiffness than seen in successive experiments in the foregoing loading curve at the same stress. Total (finite) inelastic porosity reduction ($\Delta\varphi_i$) and inelastic compressive axial strain (ε_i) were measured at the end of each experiment (Table 4.1), *i.e.*

upon unloading to the reference stress conditions of P = 5 MPa and Q = 0 MPa (for $\Delta\varphi_i$), or P = 40 MPa and Q = 0 MPa (for ε_i). During the constituent reloading steps of Experiments 2-5, the observed Q - ε_t and/or P - $\Delta\varphi_t$ behavior was similar to that seen during the preceding unloading step.

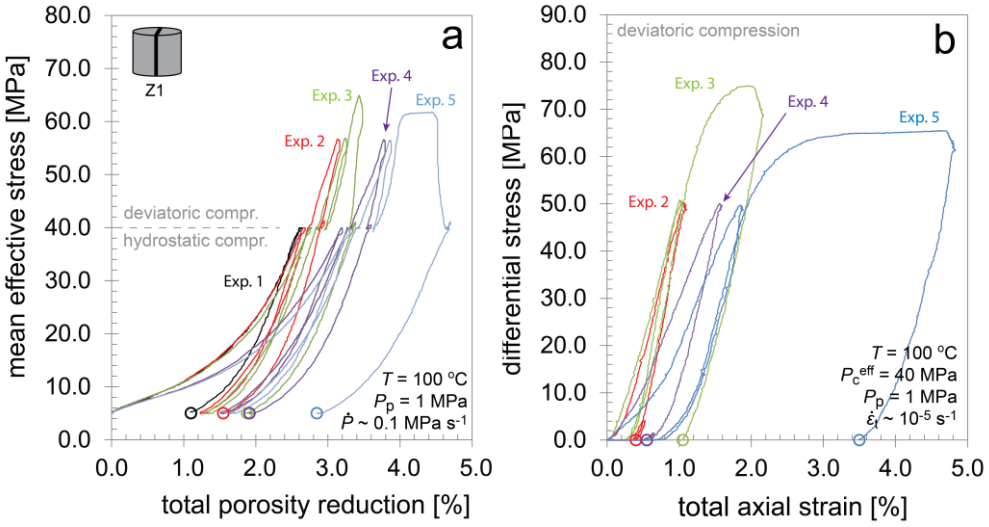

Figure 4.4 Plots showing **a)** mean effective stress (P) versus total porosity reduction ($\Delta\varphi_t$) and **b)** differential stress (Q) versus total axial strain (ε_t) data, obtained during the five consecutive experiments imposed on the split-cylinder Sample Z1 used for microstructural analysis. After each experiment, the sample was removed from the testing vessel for imaging. Stage 1 (non-linear, concave-up), Stage 2 (near-linear) and Stage 3c (non-linear, concave down) type P - $\Delta\varphi_t$ behavior was seen during Experiments 1, 2 and 3 and 5, respectively (refer Figure 4.1). The open circles indicate the inelastic porosity reduction (a) and inelastic axial strain (b) measured at the corresponding stress conditions.

During hydrostatic stress-cycling in Experiment 1, the P - $\Delta\varphi_t$ behavior was non-linear and concave-up (*cf.* Stage 1 – see Figure 4.1), up to the maximum applied P_c^{eff}, hence P of 40 MPa. The corresponding inelastic porosity reduction ($\Delta\varphi_i$) was 1.1%. During Experiment 2, the hydrostatic stress-cycle up to 40 MPa showed similar behavior to Experiment 1, in terms of the P - $\Delta\varphi_t$ behavior, leading to a $\Delta\varphi_i$ of 1.2%. During deviatoric compression in Experiment 2 (Q up to 50 MPa, at P_c^{eff} = 40 MPa), the sample exhibited near-linear P - $\Delta\varphi_t$ behavior (*cf.* Stage 2 of Figure 4.1) and near-linear Q - ε_t behavior, leading to $\Delta\varphi_i$ = 1.6% and ε_i = 0.4%. During Experiment 3, the P - $\Delta\varphi_t$ and Q - ε_t behavior was similar to that observed during Experiment 2, up to the maximum Q of 50 MPa explored in

the previous experiment. At Q > 50 MPa, the behavior remained linear up to $P \approx 62$ MPa, and $Q \approx 65$ MPa. Beyond this point, both the P - $\Delta\varphi_t$ and Q - ε_t curves showed strain-hardening at decreasing rates (*cf.* Stage 3c) until a maximum supported Q of 75 MPa was reached at $\Delta\varphi_t \approx 3.4\%$ and $\varepsilon_t \approx 2.0\%$. Permanent strains obtained in Experiment 3 amounted to 1.9% for $\Delta\varphi_i$ and 1.0% for ε_i. During Experiment 4, the P - $\Delta\varphi_t$ and Q - ε_t data showed significantly more compliant loading and unloading behavior than observed during the foregoing stress-cycling experiments. At the highest stress applied (Q = 50 MPa) the $\Delta\varphi_t$ value of 3.8% and the ε_t value of 1.6% indicated increased porosity reduction, but less sample shortening, than seen in Experiment 3. In Experiment 4, the final inelastic porosity reduction of 1.9%, measured at the reference P_c^{eff} of 5 MPa, was similar to that seen in the foregoing experiment, though the inelastic axial strain of 0.6% was reduced. In the final stress-cycling test, *i.e.* Experiment 5, the P - $\Delta\varphi_t$ and Q- ε_t behavior obtained were slightly more compliant than observed in Experiment 4. At P > 58 MPa and Q > 55 MPa, strongly non-linear strain-hardening trends were seen, which transitioned into near-strain neutral (~steady-state) behavior at $\Delta\varphi_t \approx 4.1\%$ and $\varepsilon_t \approx 3.4\%$. At the end of Experiment 5 (*i.e.* in the reference condition P_c^{eff} = 5 MPa, Q = 0 MPa), $\Delta\varphi_i$ and ε_i were both much larger than the values seen in the foregoing experiments, yielding 2.9% and 3.5%, respectively. Note that, post-test calliper measurements performed after removal of the Z1 sample from the experimental apparatus after each of Experiments 1 through 5 yielded inelastic axial strains (ε_i^{cal}) that were significantly smaller than the corresponding inelastic axial strains (ε_i) measured after deviatoric unloading, *i.e.* in the reference condition where Q = 0 MPa and P_c^{eff} = 40 MPa (see Table 4.1). No macroscopically visible deformation features were seen after any of the stress-cycling experiments.

4.5.2 Control experiments on samples Z2 and Z3

Plots showing P - $\Delta\varphi_t$ data obtained during our control experiments on split-cylinder sample Z2 and cylindrical plug Z3 are presented in Figure 4.5. Overall, these two samples showed closely similar behavior, though slightly more total porosity reduction was observed in Z2 than Z3 at each of the mean effective stresses explored. Both samples showed broadly similar behavior to that obtained for split-cylinder Sample Z1 (Figure 4.4). In Z2 and Z3, deformation was strictly compactive and stiffer behavior was again seen during unloading, than during the preceding uploading step. During reloading, the observed P - $\Delta\varphi_t$ behavior was similar to that seen during the preceding unloading step. Both, Z2 and Z3 showed non-linear, concave-up P - $\Delta\varphi_t$ behavior up to P ~ 30 to 40 MPa. After the initial hydrostatic stress-cycle up to 40 MPa, the inelastic porosity reduction ($\Delta\varphi_i$) measured at the reference

P_c^{eff} of 5 MPa was 1.1% (Z2) and 0.9% (Z3). During deviatoric compression at P_c^{eff} = 40 MPa, near linear behavior was seen up to P ~ 60 MPa, after which the compaction rate increased, leading up to the maximum supported P of 63.2 MPa (Z2) and 64.3 MPa (Z3). Hereafter, both samples showed minor strain-softening to strain-neutral P - $\Delta\varphi_t$ behavior. At the end of these tests, the ε_i value measured in Z2 and Z3 at the reference stress for deviatoric cycling (Q = 0 MPa, P_c^{eff} = 40 MPa) was 3.8 and 3.1%, respectively, while at the reference stress for hydrostatic cycling (Q = 0 MPa, and P_c^{eff} = 5 MPa), $\Delta\varphi_i$ were 2.5 and 1.9%, respectively. After removal of the sample from the vessel, calliper measurements showed ε_i^{cal} values of 3.2 ± 0.1% for Z2 and 2.8 ± 0.1% for Z3. No macroscopically visible deformation features were seen after testing.

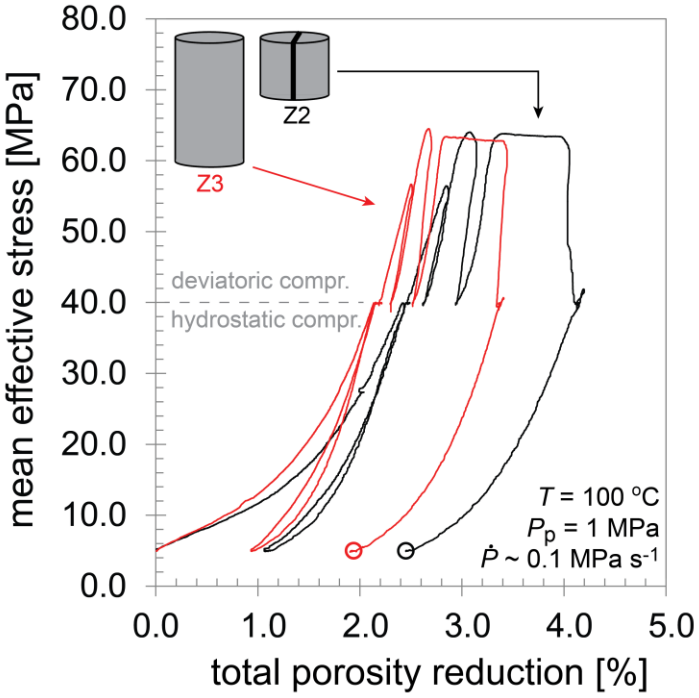

Figure 4.5 Plot showing mean effective stress (P) versus total porosity reduction ($\Delta\varphi_i$) data obtained during our control tests performed on split-cylinder Z2 and cylindrical plug Z3. The open circles indicate the inelastic porosity reduction measured at the reference P of 5 MPa and Q = 0 MPa.

4.6 Results - Microstructural data obtained from Sample Z1

4.6.1 Inelastic deformation field at the millimeter-scale

In Figure 4.6 we present contour maps of the mm-scale, vertical (ε_{11}^{mm}), and

horizontal inelastic strain (ε_{22}^{mm}), and of the corresponding rigid body rotation (ω_{12}^{mm}) obtained from PIV analysis of the surface of the imaged half of split-cylinder Sample Z1 after each experiment. Mean values of these quantities ($\bar{\varepsilon}_{11}^{mm}$, $\bar{\varepsilon}_{22}^{mm}$and $\bar{\omega}_{12}^{mm}$) are listed in Table 4.1. Note from Table 4.1 that, for each experiment, the value of the mean, mm-scale, inelastic vertical strain $\bar{\varepsilon}_{11}^{mm}$ (up to 2.3%) is similar to the axial inelastic strain measured by calliper (ε_i^{cal} values up to 2.7%), but generally smaller than the inelastic axial strains (ε_i up to 3.5%) measured at the end of each experiment at the reference stress state of P_c^{eff} = 40 MPa and Q = 0 MPa. Recall that in the consecutive Experiments 1, 2, 3 and 5 performed on Z1, the P – $\Delta\varphi_t$ behavior shown reached Stage 1, Stage 2, Stage 3c and Stage 3c (post-failure) respectively, as illustrated in Figure 4.1.

After Experiment 1 (experiment reaching Stage 1 of Figure 4.1), most of the mm-scale, vertical, inelastic strains were smaller than the minimum measurable strain of 0.06% (Figure 4.6a). The horizontal inelastic contraction was minor ($\bar{\varepsilon}_{22}^{mm}$ = 0.1%) and distributed roughly uniformly across the sample surface (Figure 4.6b). No significant rigid body rotation was seen (*i.e.* ω_{12}^{mm}< 0.03%; Figure 4.6c). After Experiment 2 (*i.e.* deviatoric compression conform the near-linear Stage 2, of Figure 4.1), uniform compaction was seen (Figures 4.6d and e), with the mean vertical strain $\bar{\varepsilon}_{11}^{mm}$ of 0.4% being larger than the mean horizontal strain $\bar{\varepsilon}_{22}^{mm}$ of 0.1%. Little to no rigid body rotation was detected (Figure 4.6f). After Experiment 3, in which Stage 3c behavior was reached (*cf.* Figure 4.1), the strains were significantly larger and more heterogeneously distributed. Vertical contractions as large as 4.0% localized within a ~2 mm wide band running diagonally across the sample at 43° to the main compression direction, and within two ~1 mm conjugate bands, oriented roughly perpendicular to the wider band (Figure 4.6g). All sets of conjugate bands showed horizontal expansion, with values of ε_{22}^{mm} reaching up to -1.5%, while $|\varepsilon_{11}^{mm}|$ was generally larger than $|\varepsilon_{22}^{mm}|$, indicating overall area reduction within the deformation bands, and suggesting that these bands are compaction bands. The main deformation band crossing the entire diagonal of the sample surface showed counterclockwise rigid body rotations of up to 0.4°, while the two smaller, conjugate bands yielded opposing, clockwise rotations of up to -0.5°. Compaction plus shear is therefore implied in the three bands. Outside these bands, vertical and horizontal strains were significantly smaller, with ε_{11}^{mm} ranging from 0.1 to 0.5% and ε_{22}^{mm} showing both contraction and expansion in the range of -0.3 to 0.3%, with only minor rotation. Reloading the sample to lower stresses (Experiment 4), produced vertical and horizontal strains that were much smaller and generally contractive, while body rotations were negligible (Figure 4.6j-l).

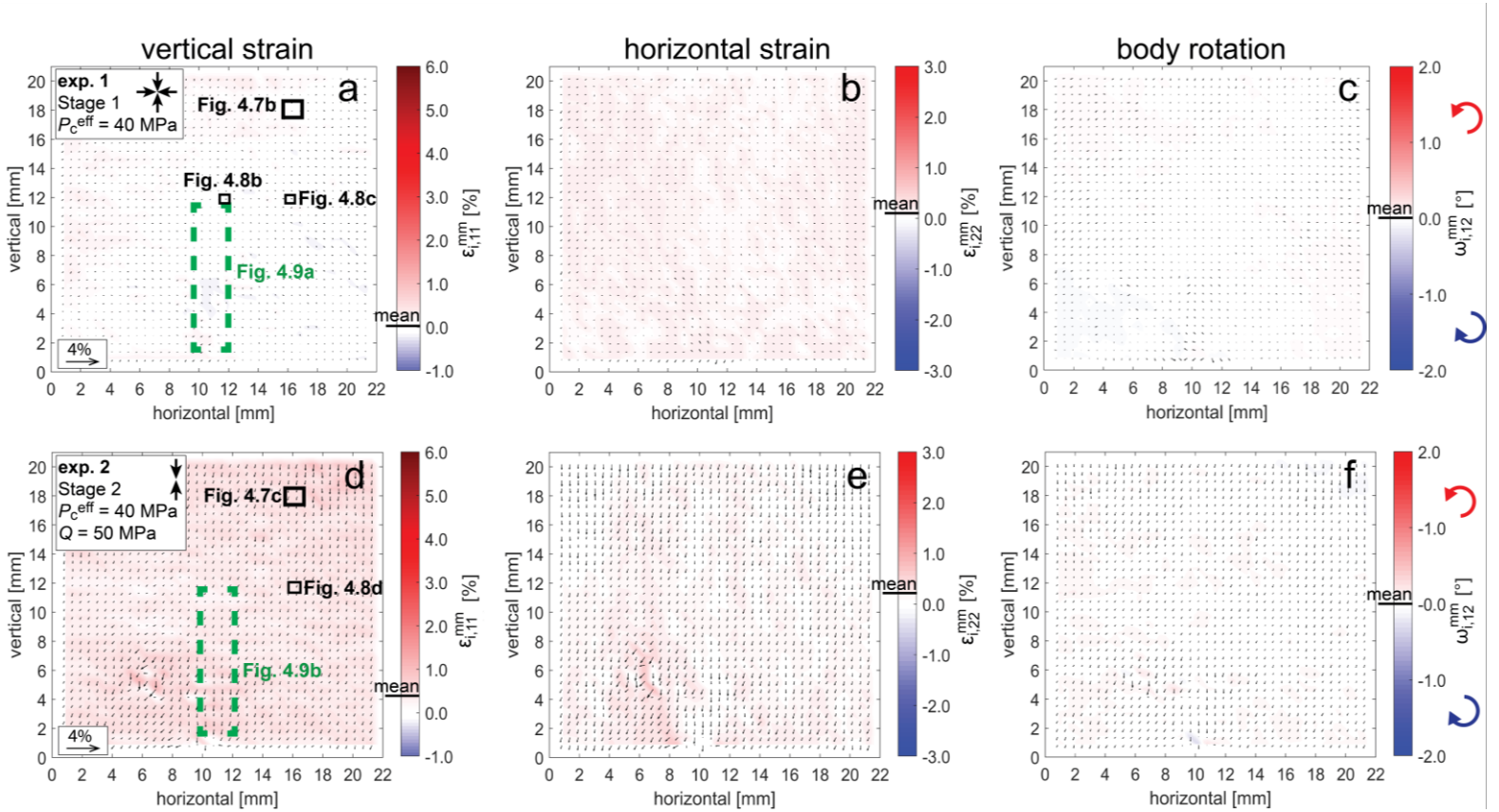

Figure 4.6 (Caption follows)

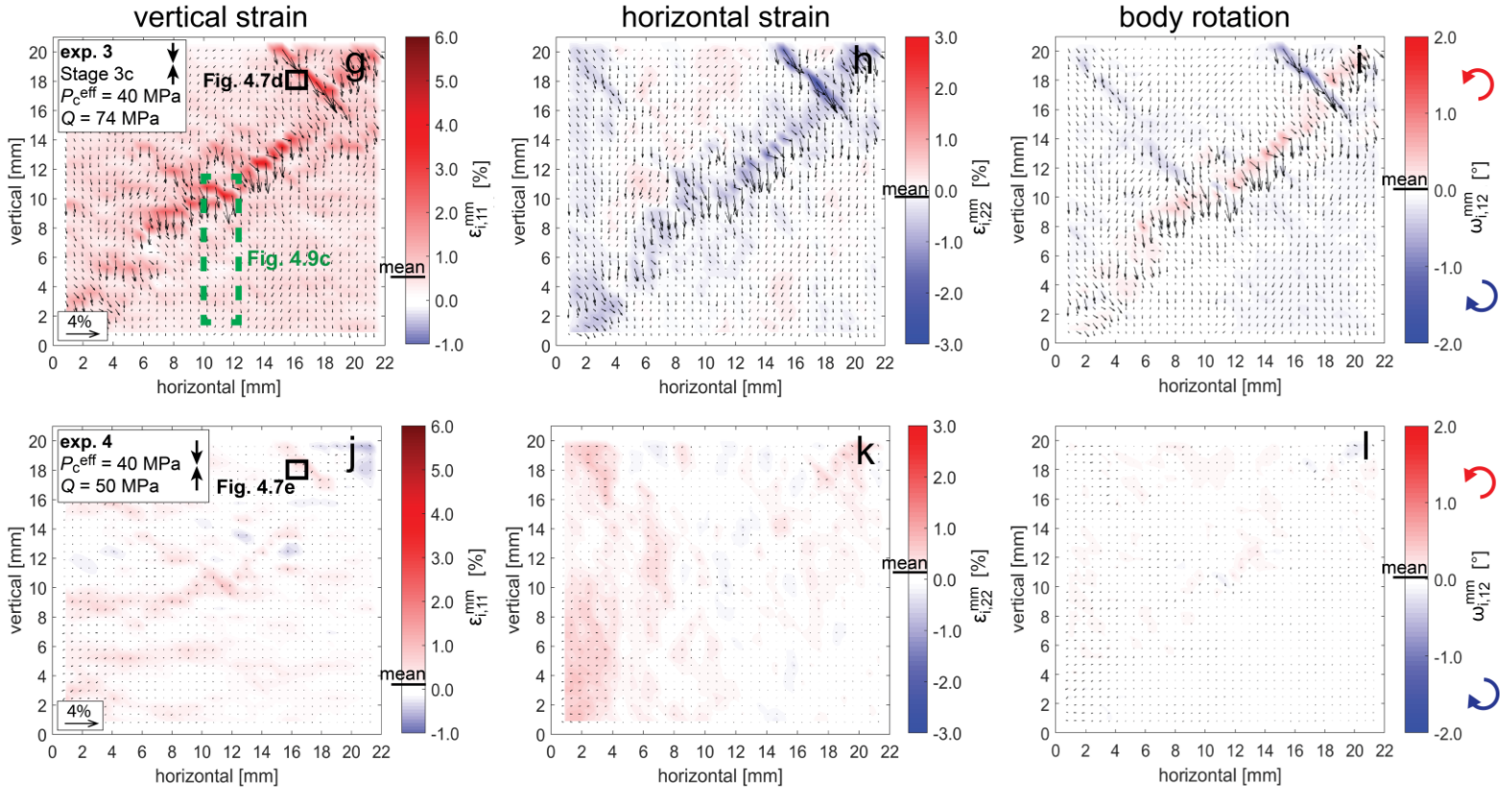
vertical strain
horizontal strain
body rotation
exp. 3
Stage 3c
P_c^{eff} = 40 MPa
Q = 74 MPa
Fig. 4.7d
Fig. 4.9c
exp. 4
P_c^{eff} = 40 MPa
Q = 50 MPa
Fig. 4.7e
4%
mean
vertical [mm]
horizontal [mm]
$\varepsilon_{i,11}^{mm}$ [%]
$\varepsilon_{i,22}^{mm}$ [%]
$\omega_{i,12}^{mm}$ [°]

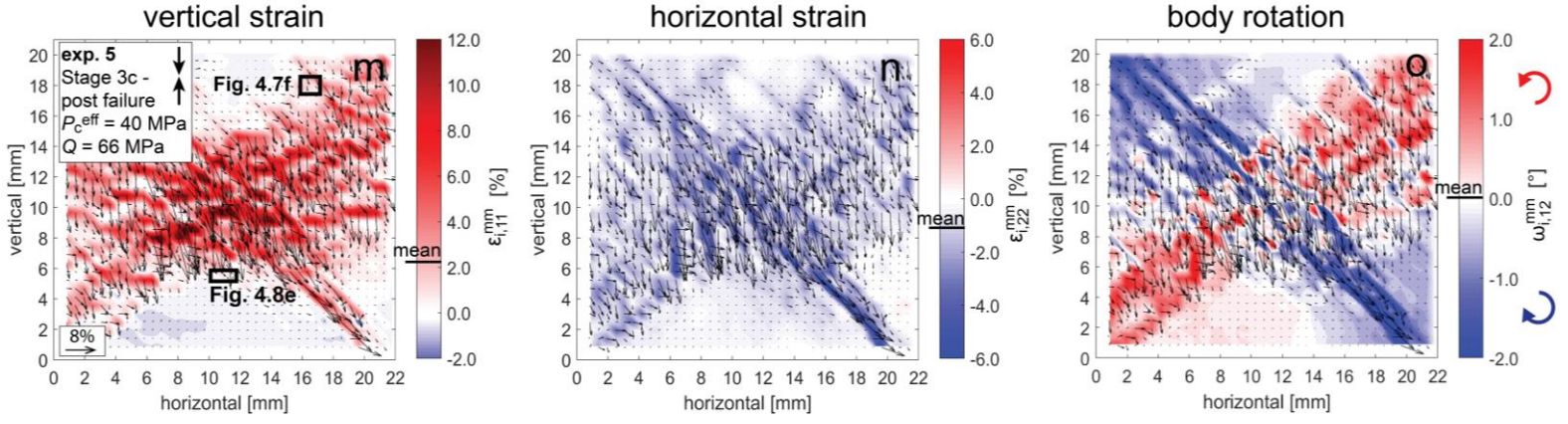

Figure 4.6 Plots showing contoured values of the mm-scale, inelastic, vertical strain (ε_{11}^{mm}; left column), the inelastic, horizontal strain (ε_{22}^{mm}; middle column), and the inelastic rotation (ω_{12}^{mm}; right column) components of the displacement gradients (black vectors) determined from micrographs covering the splitcylinder (Z1) face, obtained after each experiment on Z1. In the left two columns, red and blue colours indicate contraction and expansion, respectively, whereas in the right column they imply counterclockwise and clockwise rotations, respectively. Note the different scales for Experiment 1-4 and Experiment 5. **a-c)** Experiment 1 (*cf.* Stage 1 - see Figure 4.1); **d-f)** Experiment 2 (*cf.* Stage 2); g-i) Experiment 3 (*cf.* Stage 3); j-l) Experiment 4 (reloading to lower stresses and strains than previously explored); m-o) Experiment 5 (*cf.* Stage 3 - post-failure). Note the uniform, predominantly vertical contraction of stress-cycling Experiment 2 and the localized, compactive shear bands seen after stress-cycling experiments 3 and 5. Locations of the micrographs used for grain-scale strain analysis as shown in Figures 4.7 and 4.8 and the EDX-investigated portion (Figure 4.9) are indicated in the left column.

The largest vertical contractions obtained in Experiment 4 (up to 0.5%) were seen within the high-strain conjugate deformation bands which first developed during Experiment 3, and within three ~1 mm wide horizontal bands located at the bottom-left corner of the sample (Figure 4.6j). Horizontal strains resulting from Experiment 4 showed the highest values (~ 0.4%) patchily distributed throughout the sample-half above the main deformation band (Figure 4.6k). After the final stress-cycling test, Experiment 5 (experiment reaching Stage 3c, post-failure), large vertical contractions (up to 12%; Figure 4.6m) and horizontal expansions (up to -5%; Figure 4.6n) were recorded in two conjugate 4 to 10 mm wide deformation bands, oriented at 40 to 45° to the main compression direction, and running from corner to corner, diagonally across the sample face. These bands have developed along, and significantly widened the deformation bands first seen after Experiment 3. The top-right to bottom-left band yielded counterclockwise rotations of up to 2.0°, whereas the top-left to bottom-right band showed rotations of up to -2.0°, *i.e*. in the opposite direction (Figure 4.6o). Again, within these bands, $|\varepsilon_{11}^{mm}| > |\varepsilon_{22}^{mm}|$, implying net area reduction and suggesting the bands are compactive shear bands. Outside these bands, vertical and horizontal deformation and rotation were approximately an order of magnitude smaller, with ε_{11}^{mm} < 0.4%, ε_{22}^{mm} within -0.3 and 0.3%, and ω_{12}^{mm} ranging from -0.2 to 0.2°.

Figure 4.7 (see next page) Secondary electron micrographs obtained from Sample Z1 at the same location, before deformation and after each experiment, illustrating the microstructural evolution throughout the sequence of experiments. **a)** Undeformed sample, the intergranular clays are indicated; **b)** Experiment 1, in which Stage 1 was reached (compare Figures 4.1 and 4.4); **c)** Experiment 2, in which Stage 2 was reached; **d)** Experiment 3, in which Stage 3c was reached; **e)** Experiment 4 (reloading to lower stresses and strains than previously explored); and **f)** Experiment 5, in which the Stage 3c, post-failure behavior was explored (Figure 4.4). Yellow and red crosses indicate the location of reference points within the ion-milled grid before and after each experiment, respectively. Cross positions are referenced to the bottom left cross, so that down and left cross displacements imply contractions. Black arrows indicate intragranular cracks not present in the foregoing stress-cycling experiment. White and yellow arrows indicate the intergranular shear- and normal displacements, respectively, in panels b,c and e. Green arrows indicate extrusion of intergranular material (seen only after Experiment 5 –see: f). Note that at the end of Experiments 1 and 2, deformations are small and predominantly intergranular. After experiments 3 and 5, grain-scale displacements within the deformation bands are larger and accompanied by pervasive intragranular cracking, grain slip and grain rotation.

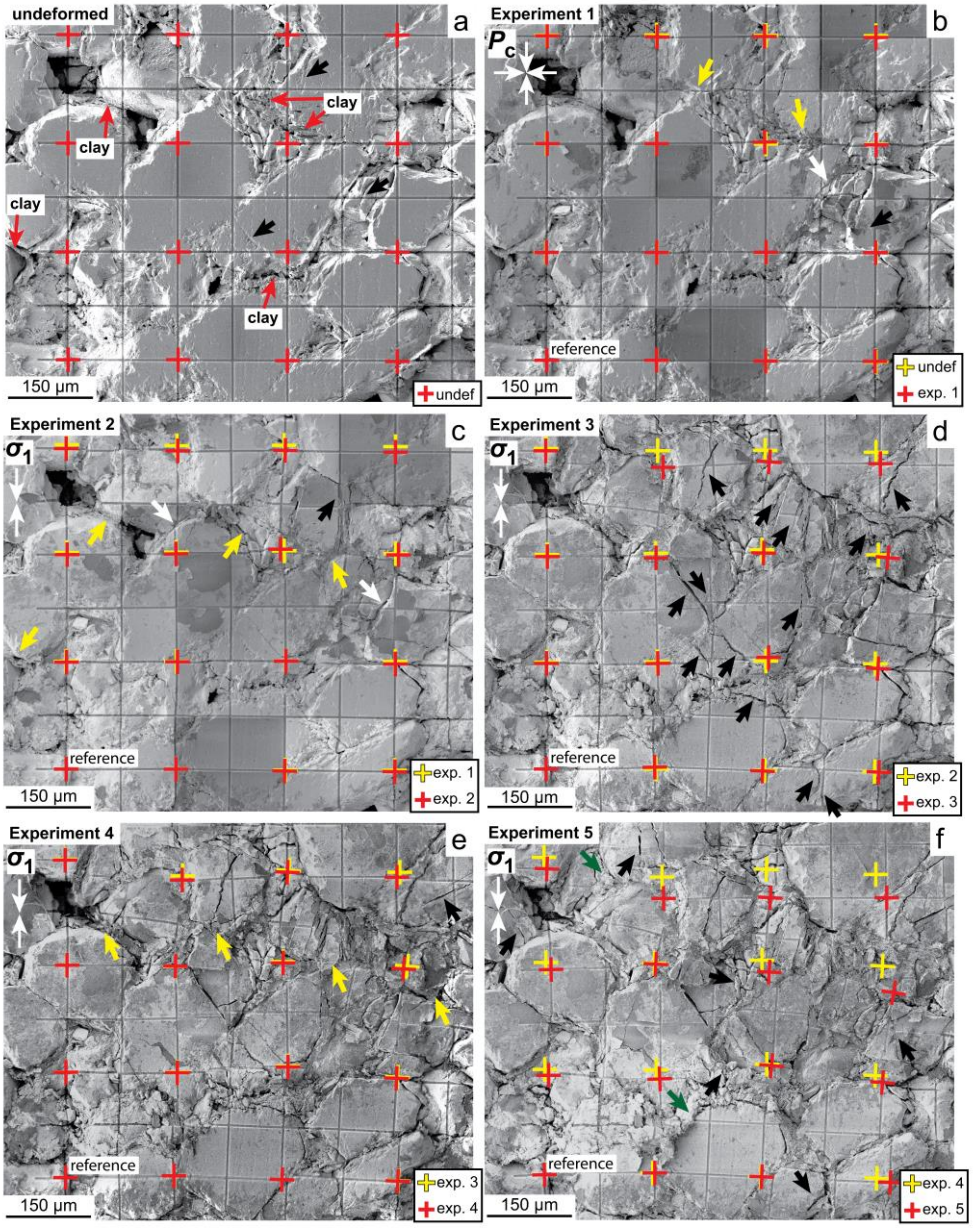

Figure 4.7 (Caption on previous page)

4.6.2 Microstructural evolution at the grain-scale

To illustrate the microstructural evolution at the scale of individual grains in Sample Z1, we present six secondary electron micrographs in Figure 4.7. The images are taken before deformation and after each experiment at the locations indicated in Figure 4.6 and include ion-milled strain marker gridding. The incremental deformation of the marker grid is highlighted using yellow and red cross symbols, which indicate the positions of reference points within the grid before and after each experiment, respectively. The micrographs shown are representative for the progressive, microstructural evolution seen in regions that will ultimately develop marked, localized deformation bands, as seen after experiments 3 and 5. To highlight the smaller deformations seen in the earlier stages of deformation, Figures 4.8a-d show two sets of higher magnification micrographs obtained before and after Experiments 1 and 2, which showed Stage1 and 2 behavior, respectively. In addition, an EDX map showing the clay films present within grain contacts, filling pores, and coating pore walls at the location indicated in Figure 4.6m is given in Figure 4.8e.

With reference to Figure 4.7a, the undeformed sample was predominantly composed of subrounded, slightly elongated quartz (~80 vol%) and feldspar grains (~15 vol%), with lesser amounts of clay (~5 vol%) being present in the pore space or as grain-coating films. Clay films are present on most of the pore walls (5-20 µm thick) and within many grain contacts (1 - 5 µm thick; Figures 4.7a and 4.8a). Intragranular cracks are present even in the undeformed material (black arrows). These features are typical for Slochteren sandstone of the Groningen field [*Gaupp and Okkerman*, 2011; *Waldmann and Gaupp*, 2016]. After hydrostatic stress-cycling (Experiment 1, *cf.* Stage 1 of Figure 4.1), grain-scale displacements are frequently small (typically < 1 µm across individual grains, *i.e.* < 0.5% strain – see Figure 4.7b), while newly formed intragranular cracks are rare. Rather, deformation is predominantly intergranular, showing contraction and expansion normal to grain contacts (yellow arrows, in Figure 4.7b) and slip tangential to grain contacts (white arrow). These intergranular deformations appear often to be more prominent in grain contacts that are clay-filled (Figure 4.8a,b). After Experiment 2 (*i.e.* deviatoric compression within the near-linear Stage 2 regime of Figure 4.1), permanent grain-scale displacements are larger (several µm per 200 by 200 µm grid cell, *i.e.* > 1 to 3% strain; Figure 4.7c). These displacements are predominantly accommodated through intergranular contraction and shear, while grain contact expansions and newly formed intragranular cracks are limited (Figure 4.7c). Intergranular deformation again appear to be larger in or near grain boundaries filled with clay films (Figure 4.8c,d). After compression to the highest supported stress (Experiment 3, *cf.* Stage 3c of Figure 4.1), displacements are much larger (up to 10 µm

measured per 200 by 200 µm grid cell, *i.e.* up to 5% strain; Figure 4.7c). Downward and right-directed displacements of the reference points within the marker grid (compare yellow and red cross-symbols) and clockwise rotations of the strain markers located in the top-right of the micrograph indicate an overall right-lateral shear movement (*cf.* Figure 4.6i). Within the regions of high shear mapped in Figure 4.6g-i, intragranular cracks are ubiquitous and intergranular slip is widespread, as evidenced by the distortion of the grid cells (Figure 4.7d). Within lower-strain regions away from this strongly deformed zone, intragranular cracks are far fewer (not shown). After reloading the sample in Experiment 4 to lower stresses and axial strains than explored in Experiment 3, small, intergranular contractions occur through rearrangement of grains and grain fragments. Newly formed intragranular cracks are rare (Figure 4.7d). After Experiment 5 (which reached Stage 3c, post-failure), grain-scale displacements within the high-strain bands mapped in Figures 4.6m and 4.6n are very large (up to 30 µm per 200 by 200 µm grid cell, *i.e.* up to 15% strain). Here, downward and right-directed displacement plus clockwise rotation of the strain markers (see yellow and red crosses) again point to a general right-lateral shear movement (Figure 4.7e; see also Figures 4.6m-o). These large displacements are accompanied by intragranular cracking, intergranular slip and extrusion of intergranular material into the pore-space and, in a few locations, normal to sample surface (green arrows, Figure 4.7f).

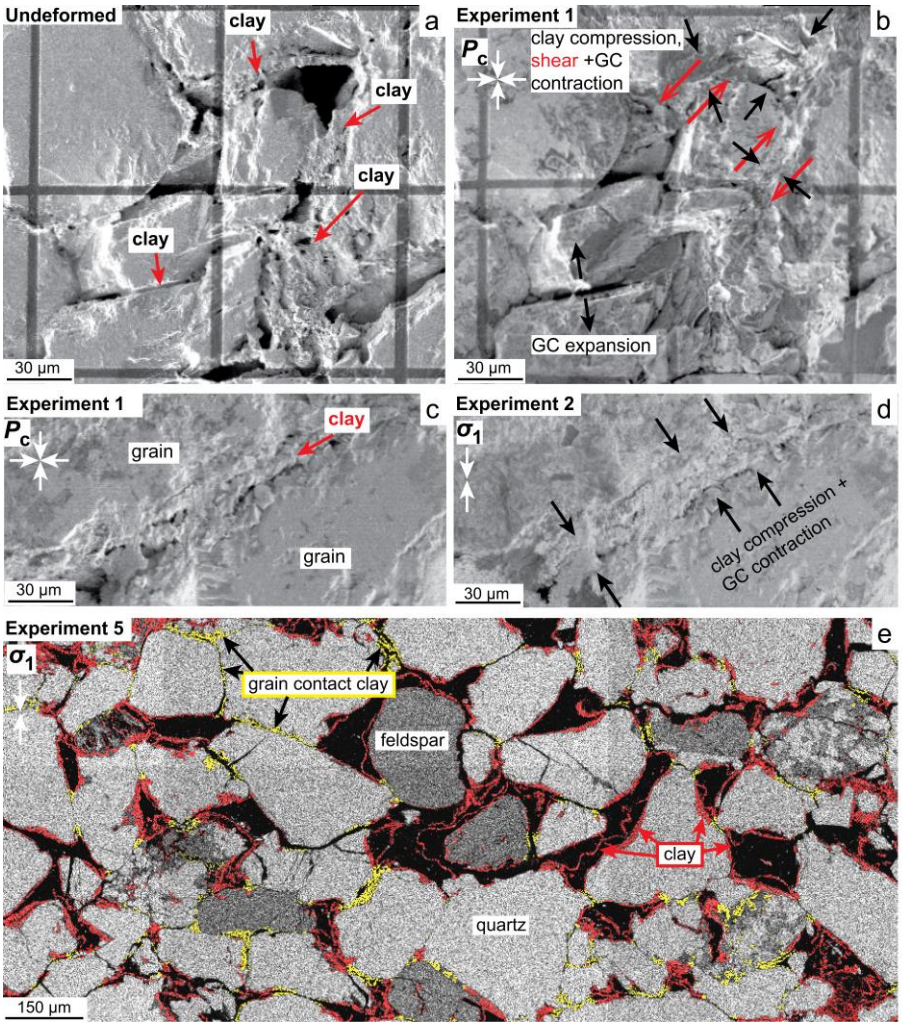

Figure 4.8 Detailed micrographs obtained from Sample Z1, highlighting the intergranular clays and their role played in accommodating inelastic strain during Experiments 1 and 2, in which Stages 1 and 2 were explored (see Figure 4.1); **a)** Secondary electron (SE) micrograph of the undeformed sample (location shown in Figure 4.6a), showing the strain marker grid and quartz grains coated by clay films. **b)** SE micrograph of the same location, after Experiment 1. In some locations, shear and compression of clay films lead to grain displacement and closure of pore space. In other locations, clay-coated grain contacts (GC) expand. **c)** SE image obtained after Experiment 1 at the location indicated in Figure 4.6d. **d)** SE image of the same location, after Experiment 2. Normal compression of intergranular clay leads to grain contact contraction. **e)** Electron dispersive X-ray spectrometry image obtained after Experiment 5 from the location indicated in Figure 4.6m. Pore-filling/coating clays are mapped in red, while clays present within grain contacts are shown in yellow (see text).

4.6.3 Data on clay content versus inelastic deformation at the grain-scale

We explored if a relationship exists between the grain-scale deformations seen after Experiments 1-3 on Sample Z1 and the grain-scale mineralogy. To do this, we used the incremental distortions of the strain marker grid seen after each of these experiments (see Section 4.4.2), plus the mineral maps obtained after Experiment 5 (*e.g.* Figure 4.8e). Within the area of interest indicated in Figure 4.2c, the mean values of the grain-scale inelastic vertical ($\bar{\varepsilon}_{11}^{grain}$) and horizontal strains ($\bar{\varepsilon}_{22}^{grain}$) obtained after each experiment are similar to the corresponding mean values of inelastic strains determined at the mm-scale using the full mosaic images (Table 4.1). The region of investigation shows no clear correlation between grain-scale, inelastic, area strain, or effective shear strain (ε_e^{grain}) and mineralogical content, *i.e.* quartz, feldspar, carbonate, sulfate and/or total clay content. However, there is a correlation between ε_e^{grain} and the abundance of clays present within grain contacts (Figure 4.9). For Experiments 1 (Figure 4.9a) and 2 (Figure 4.9b), ε_e^{grain}-values show a rough, positive correlation to the grain contact clay content, especially after Experiment 2. For Experiment 3, which showed significant intragranular cracking (Figure 4.7d), no such correlation could be inferred (Figure 4.9c).

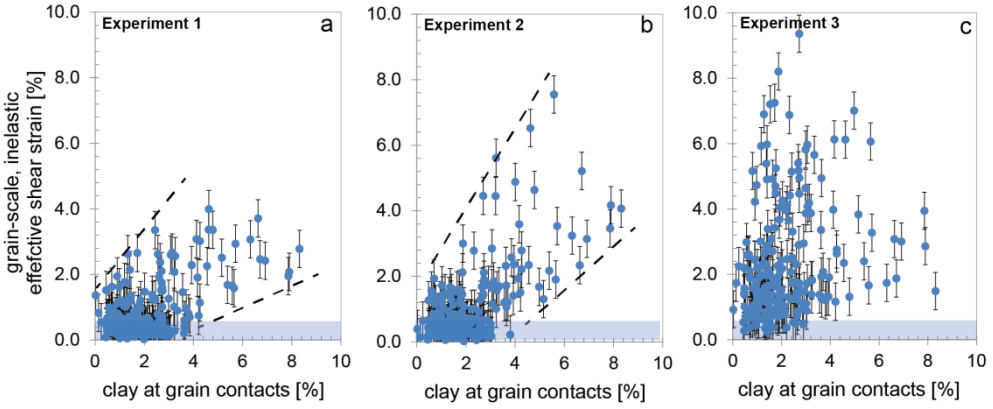

Figure 4.9 Plots showing grain-scale, inelastic effective shear strain data (*i.e.* 2nd invariant of the corresponding deviatoric strain tensor), versus the percentage of area covered by clay at grain contacts, obtained on Sample Z1 within the area mapped by EDX (see Figure 4.2c). Error bars and mean values of the principal, grain-scale inelastic strains are indicated. Grain-scale strain data were collected for **a)** Experiment 1, **b)** Experiment 2) and **c)** Experiment 3. Experiments 4 and 5 were not analysed. These data show rough, positive trends after Experiment 1 and 2, while such a trend is absent after Experiment 3. The blue shaded areas indicate the strains falling below the limit of strain determination.

4.7 Discussion

Mean effective stress (P) versus total porosity reduction ($\Delta\varphi_t$) data obtained in the five consecutive stress-cycling experiments performed on split-cylinder Z1 (Figure 4.4) showed the typical transition seen in sandstones from initial, non-linear, concave-up behavior in Experiment 1 (*cf.* Stage 1 of Figure 4.1), to near-linear behavior in Experiment 2 (*cf.* Stage 2) and to non-linear, concave-down behavior in Experiment 3 and 5 (cf. Stage 3c). Inelastic deformation played a significant role in each experiment. The maximum, total porosity reduction measured before final unloading of each experiment performed on Z1 ranged from 2.5 to 4.4%, of which 1.1 to 2.9% was inelastic after unloading, *i.e.* at the reference P_c^{eff} of 5 MPa (Table 4.1). Similarly, total axial strains measured in the deviatoric portions of Experiments 2 - 5 ranged from 1.1 to 4.8%, with inelastic components of 0.4 to 3.5%, as measured at the reference stresses of Q = 0 MPa and P_c^{eff} = 40 MPa. The concomitant, inelastic deformation of the face of one of the Z1 cylinder halves was recorded using high resolution (0.54 µm per pixel) electron microscopy. PIV-derived data obtained at the mm-scale implied little to no inelastic deformation after Experiment 1, uniform, predominantly vertical contraction after Experiment 2, and markedly localized deformation after experiments 3 and 5, where significant compaction (ε_{11}^{mm} up to 12%) and rigid body rotation was seen within 1 to 10 mm wide, conjugate bands, oriented at 40° to 45° to the main compression direction (Figures 4.6g-i, m-o). More detailed micrographs (Figures 4.7b,c; 8a-d) and strain-marker grid deformations at the grain-scale (Figures 4.9a-c) showed that the inelastic deformations recorded in Z1 reflected mostly intergranular displacements during the first two experiments, particularly in intergranular clay-rich regions, while intragranular cracking was found to be more dominant in experiments 3 and 5 (Figures 4.7d,f). Crucially, we demonstrated similar P- $\Delta\varphi_t$ behavior in control experiments on a second split-cyclinder sample (Z2) and an intact plug (Z3; Figure 4.5), indicating that the split-cylinder Sample Z1 behaved in a representative way, not affected by its construction, at least at the sample scale.

In the following, we first discuss the potential cause for the mismatch between the inelastic axial strains measured in Sample Z1 in the triaxial testing machine (*i.e.* under reference stresses of Q = 0 MPa and P_c^{eff} = 40 MPa) versus those measured after removing Sample Z1 from the apparatus. Subsequently, we use the microstructural data obtained after experiments 3 and 5 on Sample Z1 to evaluate whether the observed micromechanical behavior is representative for the Stage 3c behavior typically reported in sandstones. Finding the similarity to be satisfactory, we go on to explore the processes controlling inelastic deformation in Z1 at strains more relevant to producing reservoirs ($\varepsilon_t \leq 1.0\%$). Once identified, these mechanisms are incorporated into a simple model for sandstone compaction,

in order to assess whether they quantitatively account for the inelastic deformation measured in our experiments and are consistent with compaction strains inferred for the Slochteren reservoir during depletion of the Groningen gas field. We go on to evaluate the rate-sensitivity of these mechanisms, in order to assess their potential to drive ongoing compaction, subsidence and seismicity after production of the field stops in 2022.

4.7.1 Effect of loading history on strain recovery in Sample Z1

At the end of the hydrostatic stress-cycling Experiment 1, an inelastic porosity reduction of 1.1% was measured at the reference P_c^{eff} of 5 MPa. Assuming isotropic compaction, this would imply an inelastic axial strain of about 0.4%. By contrast, calliper measurements performed after removal of the sample from the deformation apparatus showed no detectable change in sample length (ε_i^{cal} = 0.0 ± 0.1%; Table 4.1). The post-test PIV data also showed virtually no resolvable, mm-scale, inelastic deformation ($\bar{\varepsilon}_{11}^{mm}$= 0.0% and $\bar{\varepsilon}_{22}^{mm}$= 0.1%; Figure 4.6a-c). Similarly, contractions and expansions were seen within grain-to-grain contacts after Experiment 1 (Figures 4.7b and 4.8a,b) but on average these produced little to no grain-scale strain ($\bar{\varepsilon}_{11}^{grain}$= -0.1% and $\bar{\varepsilon}_{22}^{grain}$= 0.1%). Notably, the control experiment performed on the intact cylindrical sample Z3 showed similar P - $\Delta\varphi_t$ and P - $\Delta\varphi_i$ behavior during the first hydrostatic stress-cycle to Experiment 1 on Z1 (Figure 4.5). This suggests that the strain recovery effect seen after removing Sample Z1 from the deformation apparatus after Experiment 1 is not due to the anomalous geometry of the split-cylinder. Instead, this behavior is more likely to reflect hysteresis in the stress-strain curve, whereby the inelastic porosity reduction measured at the reference P_c^{eff} of 5 MPa is largely recovered during further reduction of P_c^{eff} to ambient values, and/or possibly during subsequent drying of the sample. By contrast, after Experiments 2, 3 and 5, inelastic deformation was more prominent.

Hysteretic stress-strain behavior is widely documented for sandstone [*McKavanagh and Stacey*, 1974; *Shalev et al.*, 2014] and is thought to reflect semi-recoverable slip along- and contraction/expansion of grain contacts [*Tutuncu et al.*, 1998] or pre-existing cracks [*David et al.*, 2012; *Walsh*, 1965]. Such behavior is generally perceived to persist up to a previously supported state of stress [*Holt et al.*, 1994; *Pijnenburg et al.*, 2018], beyond which newly induced, inelastic deformation may occur. For the Slochteren sandstone samples used here, the previously supported state of stress is given by that prevalent in the reservoir at the time of core extraction [*Van Eijs*, 2015], with the *in-situ P* being 35 ± 2 MPa. This *P*- value is closely similar to the maximum *P* of 40 MPa explored during Experiment 1 performed on Sample Z1. Hence, the nominally recoverable deformation behavior seen in Experiment 1 is

considered to reflect a return to its approximate *in-situ* state. In subsequent Experiments 2 through 5, the stresses and axial strains explored were larger, and the ε_i^{cal}, $\bar{\varepsilon}_{11}^{mm}$ and $\bar{\varepsilon}_{11}^{grain}$ values measured (up to 2.7% - Table 4.1) demonstrate more prominent inelastic deformation. For these experiments, the quasi-inelastic contribution to the inelastic axial strain (ε_i) measured at the end of each experiment (*i.e.* at Q = 0 and P_c^{eff} = 40 MPa) may be removed by taking the difference in the ε_i values measured at the end of each experiment relative to that obtained at the end of the previous experiment. The resultant, experiment-specific increases in inelastic axial strain ($\Delta\varepsilon_i$ – Table 4.1) are in rough agreement with the corresponding values of ε_i^{cal}, $\bar{\varepsilon}_{11}^{mm}$ and, where obtained, $\bar{\varepsilon}_{11}^{grain}$, particularly for Experiments 2, 3 and 5 (Table 4.1). In Experiment 4, where lower stresses and strains were explored than previously applied, $\Delta\varepsilon_i$ shows no increase in inelastic axial strain ($\Delta\varepsilon_i$ = -0.4%), which is in accordance with the low values ε_i^{cal} and $\bar{\varepsilon}_{11}^{mm}$ measured after this experiment. On this basis, we infer that the discrepancy between the inelastic axial strains measured inside and outside of the deformation apparatus is largely caused by hysteresis in the sample loading and unloading behavior at stresses and strains smaller than those previously accessed.

4.7.2 Micromechanical behavior at high strains: Localization

The similar P - $\Delta\varphi_t$ behavior shown by our split-cylinder samples (Z1, Z2) and the intact plug (Z3) (Figure 4.5) demonstrates representative mechanical behavior of Z1 with respect to intact samples, at least at the sample scale. To evaluate whether the micromechanical/microstructural behavior shown by Z1 is similarly representative, we now compare the inelastic deformation behavior shown by this sample to the inelastic deformation features most commonly reported in the literature, *i.e.* for the inelastic, Stage 3c deformations seen at high axial strains (1.5 to 15%). At these high strains, high porosity samples (20 – 25%), tested in deviatoric compression at similar effective confining pressures (30 - 50 MPa) as used in the present study often show shear-associated compaction bands of one to several mm in thickness [*Baud et al.*, 2004; *Fortin et al.*, 2005; *Wong et al.*, 1997]. These bands are typically oriented at an angle of 45 - 65° to the main compression direction and contain highly fractured grains, such as observed after Stage 3c deformation of split-cylinder Sample Z1, *i.e.* after stress-cycling experiments 3 and 5 (see: Figure 4.6g-i, m-o and Figure 4.7c,e). While the orientation of the high strain bands seen in Sample Z1 may be partly controlled by its lower length-to-diameter ratio (1:1, as opposed to the more conventional 2:1; *e.g. Hawkes and Mellor*, 1970), their similarity to the bands formed in conventionally-sized samples suggests that the micromechanical behavior observed at high

axial strains (> 1.4%) is representative for that of Slochteren sandstone under the investigated experimental conditions. This provides confidence that the inelastic deformations shown by Sample Z1 at the lower strain Stages 1 and 2 ($\varepsilon_t \leq 1\%$), for which to date the governing processes remain largely unidentified, are also representative for intact samples.

4.7.3 Inelastic mechanisms governing small-strain deformation: Role of intergranular clay films

As noted in the Introduction, the total axial strains (1.5 to 15%) associated with typical Stage 3c behavior far exceed the vertical strains (< 1%) relevant for most upper crustal (< 5 km) sandstone reservoirs undergoing pore pressure reduction during oil or gas extraction. The relevance of Stage 3c deformation in this context is limited. Similarly, Stage 1 behavior, in which the sample is thought to return to its *in-situ* state (see Section 4.7.1) is also of limited field importance as it is unlikely to occur in the reservoir. Instead, the *in-situ* compaction behavior occuring during pore pressure reduction is most likely best represented by the behavior seen during the near-linear Stage 2 part of the P - $\Delta\varphi_t$ curve, *i.e.* during the deviatoric stress-cycle of stress-cycling Experiment 2 (Figure 4.4a). Here, the increase in inelastic axial strain ($\Delta\varepsilon_i$ = 0.4% - Table 4.1) was manifested mostly by small, intergranular normal- (Figure 4.7c; yellow arrows; Figures 4.8c and d) and shear displacements (Figure 4.7c; white arrows). These inelastic deformations were found to be larger in areas where more grain contact clay is present (Figure 4.9b). By comparison, the role played by intragranular cracking appeared to be small (Figure 4.7c; black arrow), in accordance with the quantitative data on crack densities presented in Chapter 3 [*Pijnenburg et al.*, 2019]. These observations, in combination with the widespread occurrence of intergranular clays (*e.g.* Figures 4.7a and 4.8) and the uniform inelastic deformation measured across the full Z1 sample face (Figure 4.6d-f) after Experiment 2 (Stage 2 deformation in Figure 4.1) suggest that Stage 2 deformation is predominantly intergranular, with an important role played by intergranular clays.

The above observations and inference are in agreement with previous, more general inferences, whereby Stage 2 inelastic deformation of sandstone was proposed to be governed by intergranular grain rearrangements [*Bernabe et al.*, 1994; *DiGiovanni et al.*, 2007; *Menéndez et al.*, 1996; *Shalev et al.*, 2014]. However, to our knowledge, our study is the first to explicitly demonstrate that, at least in the clay-bearing Slochteren sandstone, such intergranular deformations are for a large part accommodated by normal compression (*i.e.* consolidation) of and slip on the clay films present in grain contacts (Figures 4.8a-d; Figures

4.9a,b).

The presence of clays in grain contacts is not unique to the Slochteren reservoir. Indeed, similar films have been reported to occur in a large number of reservoir sandstones around the world. These include the M'Bya field (Gabon), the Malih X1 field (Oman), the Kahar field (Syria), the Haltenbanken field (Norway) [all four reported in: *Billault et al.*, 2003] and the Sawan field (Pakistan) [*Berger et al.*, 2009], as well as several fields in the North Sea [*Glennie et al.*, 1978; *McHardy et al.*, 1982; *Wilson*, 1992], Texas and Louisiana [*Dutton et al.*, 2017] and in the Changqing [*Yang et al.*, 2016] and Sulige fields of China [*Wang et al.*, 2017]. Further quantification of the contribution clay-film deformation can make to the overall deformation of clay-bearing sandstones accordingly deserves further attention.

4.7.4 Quantifying the role played by clay films in the Stage 2 inelastic deformation relevant to producing reservoirs

It remains difficult to quantify the extent to which Stage 2 inelastic strains are accommodated by clay deformation, as opposed to other inelastic processes such as intragranular cracking, which operate at least to a lesser degree during Stage 2 (see also: *Pijnenburg et al.*, [2019]). Mainly, this is because of the limited resolution of the present grain-scale strain (0.6% for grain-scale strains of up to 10%) and clay thickness determinations (EDX pixel size 2 μm). Nonetheless, a major contribution of clay-film deformation at the small, depletion-relevant strains, would strongly impact our understanding of the *in-situ* compaction behavior of the Groningen gas field, since intergranular clays are widely observed in the Slochteren reservoir [*Gaupp et al.*, 1993; *Gaupp and Okkerman*, 2011; *Pijnenburg et al.*, 2019; *Waldmann*, 2011; *Waldmann and Gaupp*, 2016; *Wilson*, 1992]. This is particularly so at the center of the field, which experiences the largest amount of subsidence and the most frequent and largest induced earthquakes [*NAM*, 2016].

We now present a first attempt to quantify the inelastic strains expected to develop in clay-bearing sandstone, deforming by consolidation of and slip on intergranular clay, for the stress changes applied in our Experiment 2 on Z1 (in which Stage 2 of Figure 4.1 was reached), and for the increase in effective stress representing that in the Groningen gas field. We make use of the simple sandstone model shown in Figure 4.10. The model consists of quasi-spherical quartz grains with flattened, circular grain contacts that are each coated with clay. The detrital grain diameter from contact to contact is taken as 180 μm, while the thickness of the clay film (z) is taken to be 4 μm, similar to the average grain diameter and clay film thickness described for Slochteren sandstone (see Section 4.2). The external,

effective vertical- (σ_1^{eff}) and horizontal (σ_3^{eff}) stresses are transmitted onto the clay-filled, grain-to-grain contacts, where these are markedly enhanced due to the smaller contact area. For a porosity of 20% typical for the center of the Groningen field, the enhancement of the contact normal stress ($\tilde{\sigma}$) and the contact shear stress ($\tilde{\tau}$) typically amounts to a factor of 3 [*e.g. van den Ende et al.*, 2018]. For our model configuration, this gives: $\tilde{\sigma} \approx 3\ (\sigma_1^{eff} + \sigma_3^{eff})/2$ and $\tilde{\tau} \approx 3\ (\sigma_1^{eff} - \sigma_3^{eff})/2$. Any grain contact-normal consolidation strain developing within the clay film at B ($\tilde{\varepsilon}_B$ – see Figure 4.10) requires a shear strain of the clay film at A ($\tilde{\gamma}_A$), and vice versa. Hence, consolidation and slip are serial deformation processes, meaning that one cannot occur without the other. Consequently, in the present, symmetrical configuration $\tilde{\varepsilon}_B = \tilde{\gamma}_A = \tilde{\varepsilon}_A = \tilde{\gamma}_B$. The inelastic vertical strain of the bulk can then be written as: $\varepsilon_1^{inel} = 2z\ \tilde{\varepsilon}\ /d$.

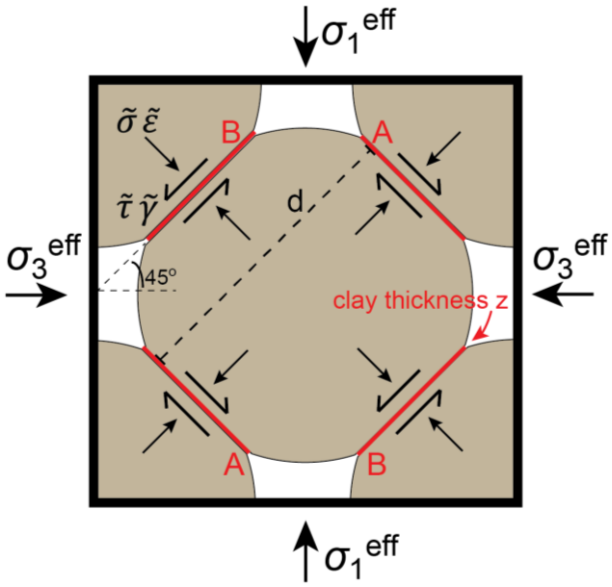

Figure 4.10 Assumed model microstructure for a clay-bearing sandstone, inelastically deforming by clay slip and consolidation. The clay films are indicated in red. The effective, external stresses (σ_1^{eff} and σ_3^{eff}) imply normal ($\tilde{\sigma}$) and shear stresses ($\tilde{\tau}$) on each of the grain contacts. Note that in this configuration, consolidation at B ($\tilde{\varepsilon}$) requires slip and shear strain ($\tilde{\gamma}$) on A, and vice versa, meaning these processes are serial.

In Experiment 1 on Sample Z1, hydrostatic stresses were explored with P_c^{eff} up to 40 MPa. In Experiment 2, the maximum stress conditions explored were Q = 50 MPa and P_c^{eff} = 40 MPa. Hence, between Experiments 1 and 2, σ_1^{eff} was incremented from 40 MPa to 90 MPa, at constant σ_3^{eff} (=P_c^{eff}). The corresponding increment in inelastic strain ($\Delta\varepsilon_i$) was 0.4% (see Table 4.1: Experiment 2 on Z1). For an increase in σ_1^{eff} from 40 to 90 MPa at

constant σ_3^{eff} of 40 MPa, the above relations imply an increase in the effective normal stress ($\tilde{\sigma}$) supported by the clay-filled grain contacts from 120 to 195 MPa. For this change in effective normal stress, drained, 1D consolidation test data performed on wet illite gouges show a decrease in void ratio ($e = \varphi/[1-\varphi]$) from 0.22 to 0.15 [*Brown et al.*, 2017]. Note that this highly compliant densification behavior is largely inelastic. For 1D compression, this decrease in void ratio implies a normal consolidation strain in the clay films of $\tilde{\varepsilon} \approx 6\%$. In turn, this means that for the increase in effective stress explored during Experiment 2, the increase in inelastic vertical strain at the sample scale would be $\varepsilon_1^{inel} \approx 0.3\%$. This value is similar to increase in inelastic axial strain ($\Delta\varepsilon_i$) of 0.4% measured in Experiment 2, confirming that inelastic deformation in Experiment 2 (*i.e.* Stage 2 – Figure 4.1) can indeed be largely accounted for by consolidation of- and slip on intergranular clay films. In addition, intragranular cracking may have played a smaller role, particularly towards the end of Experiment 2 [*Pijnenburg et al.*, 2019].

Depletion of the Groningen gas field between 1963 and now (P_p decrease from 35 to 8 MPa) implies an accompanying increase in σ_1^{eff} from 30 to 57 MPa, and of σ_3^{eff} from 8 MPa [*Breckels and Van Eekelen*, 1982] to roughly 27 MPa [± 2 MPa; *Van Eijs*, 2015]. For these effective stress changes, the effective normal stress acting on the clay-filled grain contacts ($\tilde{\sigma}$) increases from 57 to 126 MPa. In turn, for this increase in effective normal stress, the data obtained by *Brown et al.*, [2017] show a decrease in void ratio of 0.27 to 0.21, implying a normal strain of 4%. In turn, this means that for the above *in-situ* effective stress changes, the inelastic vertical strain yields: $\varepsilon_1^{inel} \approx 0.2\%$. To compare the value obtained with the *in-situ* total (elastic + inelastic) compaction, we must first estimate the poroelastic strain that would occur for the above porosity and vertical effective stress changes ($\Delta\sigma_1^{eff}$). We assume a Biot coefficient of 1 (*i.e.* similar elastic pore and bulk volume responses, *cf.* Figure 3.4, Chapter 3), and we use a Young's modulus E of 14 GPa, as has been described for Slochteren sandstone with a similar porosity of 21.5% [*Pijnenburg et al.*, 2019]. The elastic strain thus yields $\Delta\sigma_1^{eff}/E = 0.2\%$. Summing up the elastic and inelastic contributions, we estimate a total vertical strain of 0.4% will have accumulated over the past 50 years of depletion. As can be seen, the inelastic component contributes approximately 50% to the total amount of deformation, which falls within the range previously reported in experimental studies on the strain partitioning in Slochteren sandstone during simulated pore pressure reduction [30 - 70% - *Hol et al.*, 2015, 2018; *Pijnenburg et al.*, 2018]. Moreover, the modelled total strain of 0.4% corresponds suitably to the value of 0.3% estimated from *in-situ* compaction measurements in the Zeerijp-3 well [*Cannon and Kole*, 2017; *NAM*, 2015]. This suggests that the inelastic contribution to the total deformation of Slochteren

sandstone can be realistically accounted for through the deformation of grain contact clay films, at least at the center of the Groningen field where the reservoir is known to contain a significant portion of clay-coated grain contacts.

4.7.5 Rate-sensitivity

As noted in our introduction, it remains unclear whether compaction of the reservoir of the Groningen field and other fields is time-dependent, *i.e.* whether ongoing compaction and/or associated seismicity should be expected after production has been stopped. Some evidence has been presented for time-dependent effects during changes in production (rate) [*Hettema et al.*, 2002; *Thienen-Visser et al.*, 2015; see also: *Mallman and Zoback*, 2007], but it is not clear if these are caused by reservoir creep, or other effects, such as transient fluid flow in the faulted reservoir [*Postma and Jansen*, 2018; *Zbinden et al.*, 2017], time-dependent deformation of the overlying evaporites [*Marketos et al.*, 2016] or pore pressure re-equilibration of the underlying shale-rich formation. Here, we briefly examine to what extent sandstone deformation due to clay film consolidation and slip can be expected to be rate-sensitive. We again make use of the model shown in Figure 4.10. The serial nature of consolidation and slip implied by model configuration means that the slowest process controls the overall deformation rate. To examine which of these processes is slowest, we explore the rates of both, at the state of effective stress currently prevalent in the reservoir (σ_1^{eff} = 57 MPa, σ_3^{eff} = 27 MPa).

Ignoring any changes in the microstructural state of the illite film during slip, this sensitivity of the slip velocity vs to the grain contact shear stress $\tilde{\tau}$, expressed through the friction coefficient $\mu = \tilde{\tau}/\tilde{\sigma}$, can be described through [*Marone*, 1998]:

$$v_s = v_0 \exp\left(\frac{\mu-\mu_0}{a-b}\right) \qquad \text{(Eq. 4.3)}$$

Here μ_0 is the reference friction coefficient at a reference slip velocity v_0, and a and b are constants reflecting the magnitudes of the so-called direct and evolution effects of friction upon an experiment-change in slip velocity, respectively. For relatively pure (~95vol%) illite gouges, tested at room temperature and an effective normal stress of 40 MPa, μ_0 = 0.26 at v_0 = 1 µm/s, while (a - b) ~0.005 [*Tembe et al.*, 2010]. During grain contact slip at static equilibrium, the grain contact friction must be roughly equal to the ratio of the shear and normal contact stresses supported on this contact. Hence, $\mu \approx \tilde{\tau}/\tilde{\sigma}$ = 0.36. For these values of μ, μ_0, v_0, and (a - b), Equation 4.3 yields a slip velocity of several hundreds of

meters per second, implying that at these conditions, slip occurs virtually instantaneously.

Consolidation of clay by dewatering is dependent on the drainage path, hence on the size of the clay examined [*Brown et al.*, 2017; *Fitts and Brown*, 1999]. As far as we are aware, no experimental data are available on time-dependent consolidation appropriate for consolidation of grain contact clay films with dimensions of ~50 µm radius and several µm thickness. To explore the consolidation rate of the very small clay films present on grain contacts, we developed a model based on Poiseuille outflow of the fluids present between rigid illite plates [*Batchelor*, 2000], as outlined in detail in Appendix 4.A3. This model implies that the consolidation rate normal to each grain contact is given by:

$$v_c = \frac{z{h_w}^3}{(h_w+h_{il})\eta r^2}\left(\sigma_1^{eff}+\sigma_3^{eff}\right) \qquad \text{(Eq. 4.4)}$$

where z is the clay film thickness, h_w and h_{il} are the thicknesses of the water films and (rigid) clay plates within each hosting clay film, respectively (see Figure 4.A3), η is the water viscosity and r is the grain contact radius. For realistic values of each of these parameters of z = 4 µm, h_w = 3 nm, h_{il} = 3 nm, $\eta = 10^{-3}$ Pa s and r = 50 µm and the current state of effective stress in the Groningen field, Equation 4.4 yields a consolidation velocity of roughly 0.5 mm/s. This rate is much slower than the slip rate, such that consolidation will be rate-controlling at these conditions. However, for the decade time-scales relevant to producing reservoirs, the consolidation rate again implies near-instantaneous deformation. Therefore, consolidation of- and slip on intergranular clays are not expected to contribute to ongoing compaction of the field once production has stopped in 2022. We note further that a recent microstructural investigation of undepleted versus depleted core material from the Groningen field showed no evidence that much slower creep processes, such as stress corrosion cracking [*e.g. Brantut et al.*, 2013] or pressure solution [*e.g. Spiers et al.*, 2004] contributed significantly to reservoir compaction, during 50 years of production [*Verberne et al.*, in prep.]. It remains difficult, though, to rule out that these creep processes may start to contribute to ongoing reservoir compaction and possibly seismicity in the decades/centuries beyond field closure.

4.8 Conclusions

This study analysed the microphysical mechanisms accommodating inelastic (permanent) deformation in Slochteren sandstone from the seismogenic center of the Groningen gas field in the Netherlands. This was done by performing a sequence of five

triaxial stress-cycling experiments on a single, porous (20.4%) split-cylinder sample of Slochteren sandstone (*cf. Spiers*, 1979; *Quintanilla-Terminel et al.*, 2017). In each experiment, the sample was first subjected to a hydrostatic stress-cycle, in which the imposed effective confining pressure (P_c^{eff}) was varied between 5 and 40 MPa. In the case of Experiments 2 through 5, this hydrostatic cycle was followed by deviatoric stress-cycling, during which we explored differential stresses (Q) up to 75 MPa. Throughout the sequence of experiments, we imposed increasingly larger stresses and/or axial strains, chosen to systematically explore the main stages in mean effective stress (P) versus total porosity reduction ($\Delta\varphi_t$) behavior typically reported in the literature [*e.g. Wong and Baud*, 2012], and to include the small strains relevant for producing reservoirs (ε < 1%). A pore pressure of 1 MPa was applied, using demineralized water as the pore fluid. The experiments were conducted at an axial strain rate of 10^{-5} s^{-1}, a loading rate ($\dot{P}$) of ~0.1 MPa s^{-1} and a temperature of 100 °C similar to the temperature in the Groningen reservoir. To record the microstructural evolution throughout the sequence of experiments, we removed the split-cylinder sample from the triaxial testing machine after each experiment and imaged the face of one of the cylinder halves in full, at a resolution of 0.54 µm/pixel. Inelastic deformation at the mm- and grain-scale was analysed using Particle Image Velocimetry (PIV) and an ion-milled strain marker grid, respectively. In addition, two control experiments were performed to test if split-cylinders exhibit the same mechanical behavior as a conventional, intact plug. We concluded the following:

1) Our split-cylinder samples (Z1 and Z2) and the intact cylindrical plug (Z3) showed similar P- $\Delta\varphi_t$ behavior (Figures 4.4 and 4.5). In addition, the data obtained showed similar Stage 1, 2 and 3c behavior to that frequently reported in the literature (refer Figure 4.1). The observed consistency implies that our split-cylinder tests show representative behavior for an intact sample.
2) In the microstructurally investigated Sample Z1, Stage 3c behavior was seen at total axial strains (ε_t) between 1.4 to 4.8%. Micrographs obtained after Stage 3c revealed markedly localized, inelastic deformation (Figures 4.6g-i and m-o), where large vertical contractions (ε_{11}^{mm} up to 12%), horizontal expansions (ε_{22}^{mm} up to –5%), rotations (-2° > ω_{12}^{mm} > 2°), and many intragranular cracks (Figures 4.7d,f) were seen in conjugate shear compaction bands. Similar bands are widely reported to occur after Stage 3c deformation of intact plug samples, which further evidences that the micromechanical behavior shown by our split-cylinders is representative for intract plugs.
3) In Experiments 1 and 2 of Sample Z1, smaller axial strains were explored (ε_t < 1.0%), while the P- $\Delta\varphi_t$ behavior reached showed typical Stage 1 and Stage 2 behavior,

respectively. Here, intragranular cracking played a much diminished role, while inelastic deformation was mostly intergranular (Figures 4.7a-c and 4.8a-d).

4) The grain-scale, inelastic effective shear strain (ε_e^{grain}) seen after Experiments 1 and 2 (hence for Stages 1 and 2) was larger in regions where more grain contact clay was present (Figures 4.9a and b). Such a trend could not be discerned after Stage 3c.

5) The mechanical behavior shown during Stage 2 of our experiments is thought to be most relevant to *in-situ* compaction in the Groningen field. Using a simple microphysical model for a clay-bearing sandstone deforming by clay consolidation and slip (Figure 4.10), we showed that the increase in inelastic axial strain of 0.4% measured at the end of Experiment 2 on Sample Z1 (*cf.* Stage 2), and that inferred to have occurred in the Groningen reservoir during depletion (~ 0.1 to 0.2%) can be roughly accounted for by consolidation of- and slip on intergranular clay films.

6) Based on this, the micrographical evidence for clay slip and consolidation after Experiment 2 (*i.e.* Stage 2; Figures 4.7c and 4.8c,d), the direct relation between ε_e^{grain} and grain contact clay content (Figure 4.9a,b), the widespread occurrence of intergranular clays in Sample Z1 (*e.g.* Figures 4.7a and 4.8a,e), and the uniform, inelastic deformation measured across the full Z1 sample face after Experiment 2 (Figure 4.6d-f), we infer that Stage 2 inelastic deformation in Sample Z1 was dominated by clay film deformation. We accordingly expect that inelastic deformation of the Groningen reservoir is largely controlled by the behavior of intergranular clays.

7) Intergranular clay deformation was shown to be virtually instantaneous and dependent only on stress. This implies that ongoing reservoir compaction by this mechanisms is not expected when gas production from the Groningen field stops. In the periods of reduced production, or after production, other time-dependent processes (*e.g.* pressure solution, stress-corrosion cracking) may start to play a role, although it remains unclear whether these will lead to significant compacting in the coming decades, or even centuries after field closure.

8) Clay-bearing reservoir sandstones similar to the Slochteren sandstone are widely reported to occur in fluid reservoirs worldwide, implying a direct relevance of our findings to a large number of fields.

Acknowledgements

This research was carried out in the context of the research program funded by the Nederlandse Aardolie Maatschappij (NAM). This program aims to fundamentally improve the physical understanding of production-induced reservoir compaction and seismicity in the seismogenic Groningen gas field. We thank the teams at NAM and Shell Global Solutions for providing the samples used in this study, and for numerous insightful and energetic interactions. Colin Peach and Martyn Drury are thanked for their instructive advice regarding the applied experimental and imaging techniques. We thank UU employees Gert Kastelein, Thony van der Gon-Netscher and Floris van Oort for technical assistance, and Maartje Hamers for acquiring the chemical element maps used in this study.

Appendix 4.A1: Image distortion and resolution correction

Images obtained in an electron microscope are subject to distortion, *i.e.* misrepresentation of the physical position and size of the area covered by each pixel [*e.g. Nolze*, 2007]. In each image, the extent of distortion increases outward from the center of the analyzed area, and can therefore be expected to be small at the small horizontal field width of 0.828 mm used in this study [*Kammers and Daly*, 2013]. However, distortion is also known to be affected by the degree of surface charging [*Grella et al.*, 2003; *Seeger et al.*, 2006], which itself is controlled by: 1) the acceleration voltage used; 2) the composition, thickness and lateral continuity of the conducting layer coating the sample surface (in our case: 20 nm of Pt/Pd coating); and 3) the surface topography. In the present image data, distortion effects due to surface charging can be expected, since: a) Different acceleration voltages were used during imaging after stress-cycling experiment 0, 1 and 2 (2 kV), versus that used after stress-cycling Experiment 3, 4 and 5 (1 kV); b) The Pt/Pd coating was subject to damage, after each stress-cycling experiment; and c) The imaged sample is porous and thus inherently rough, while this roughness is likely enhanced with increasing deformation. Furthermore, calibration imaging on an FEI quartz standard sample showed that the horizontal and vertical extent of an image obtained at a working distance (WD) of 4.0 mm was smaller by ~1-2 µm, compared to that covered at a WD of 4.5 mm, even though the set horizontal field width was maintained constant at 828 µm. This implies that the resolution (µm/pixel) will be slightly different in the undeformed sample (WD = 4.5 mm), relative to that in all images obtained after compression (WD = 4.0 mm). It further means that any tilting of the sample will lead to a gradient in working distance, and hence in scaling across the surface.

Before we can use the present image data in a quantitative manner, we must first analyze and correct for any differences in the actual resolution obtained, both across the

sample surface, and between the different imaging sessions, and for any effects on these of image distortions. The axis-parallel and axis-perpendicular distances traveled by the stage to collect each image mosaic tile were a constant 497 and 746 µm, respectively, to ensure a ~10% overlap with the neighboring tile in each direction. These distances are identical to, respectively, the distance between the centers of images juxtaposing in the axis-parallel direction, and to the distance between the centers of images juxtaposing in the axis-perpendicular direction. If the area covered in a single tile is relatively large, whether due to a relatively large WD, or due to distortion effects, then the overlap with its neighboring tiles will be slightly larger. In that case, the number of pixels between the centers of overlapping tiles is reduced, meaning that the resolution at these locations (in µm/pixel) is coarser. To systematically analyze this effect across the sample surface, and between imaging sessions, we sampled 18 subsets from the image tiles obtained before the first, and after each stress-cycling experiment (Figure 4.A1). Each subset consisted of 3 by 3 image tiles. Subsets were chosen to cover 9 juxtaposing areas along a left-to-right row through the center of the sample, and 9 more areas covering the top-to-bottom column, through the center of the sample surface (Figure 4.A1a). For each subset, the 3 by 3 image tiles were stitched automatically in ImageJ to obtain a rectangular subset stitch, and the subset stitch height (SSH) and width (SSW) were measured in pixels (Figure 4.A1b). Note that the real distance between the center points of the subset tiles on the far left, and the center points of the subset tiles on the far right is given by two horizontal stage displacements, *i.e.* by 2 times 746 = 1492 µm.

The real number of pixels present between these points is obtained by subtracting the width of one image tile (1536 pixels) from the SSW (see Figure 4.A1b). The uncorrected horizontal resolution (res_{corr}^{h}) is then obtained for each subset by dividing the distance covered between these center points, by the number of pixels present between these center points. Similarly, the uncorrected vertical resolution (res_{corr}^{v}) is obtained by dividing the distance covered between the center points of the top and bottom tiles of each subset (2*497 = 994 µm), by the number of pixels present between these points, given by subtracting the height of one tile (1024 pixels) from the SSH (Figure 4.A1b).

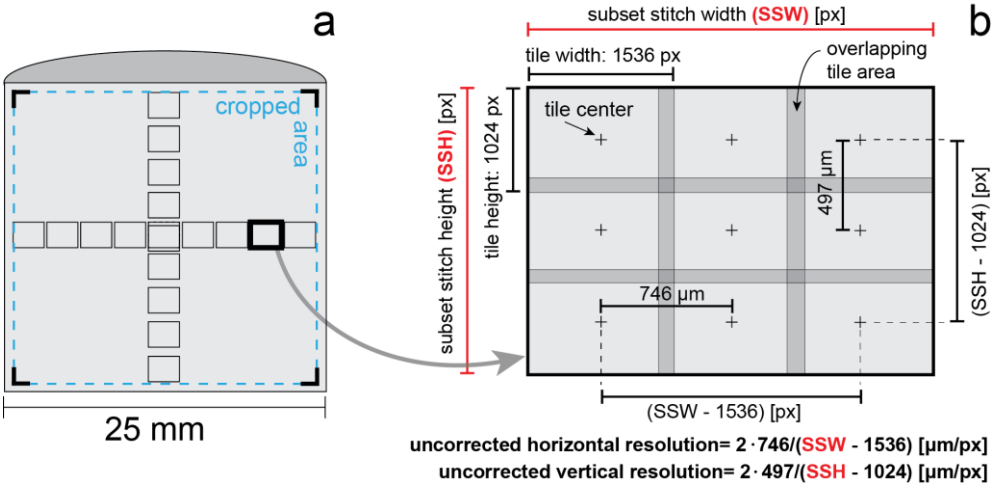

Figure 4.A1: a) Illustration of the imaged face of split-cylinder Z1, showing the locations from where the 18 subsets of 9 image tiles each were sampled. These subsets are used to measure the uncorrected resolution of each subset, which is subsequently employed to correct for the variations in resolution seen across the surface and between the imaging sessions following each stress-cycling experiment. **b)** Illustration showing the stitched image tiles of each subset, and the procedure adopted to measure its uncorrected horizontal (res_{corr}^{h}) and vertical resolutions (res_{corr}^{v}).

The uncorrected horizontal and vertical resolutions obtained in this way for the various locations across the sample surface, and for the six imaging experiments are presented in Figure 4.A2. The following trends are shown: 1) From the top to the bottom of the sample, res_{corr}^{h} and res_{corr}^{v} obtained for each stress-cycling experiment show a roughly linear decrease along similar slopes (Figure 4.A2a,c); 2) From the left to the right of the sample, res_{corr}^{h} and res_{corr}^{v} both show a small, linear increase, again along an approximately similar slope (Figure 4.A2b,d); 3) Between imaging sessions, these roughly linear trends are offset. This offset is particularly apparent for stress-cycling experiments 0, 1 and 2, while experiments 3, 4 and 5 are more similar with respect to each other; 4) For each stress-cycling experiment, scatter around the above noted, roughly linear trends can be up to 1 nm per pixel, while more scatter is seen in later stress-cycling experiments.

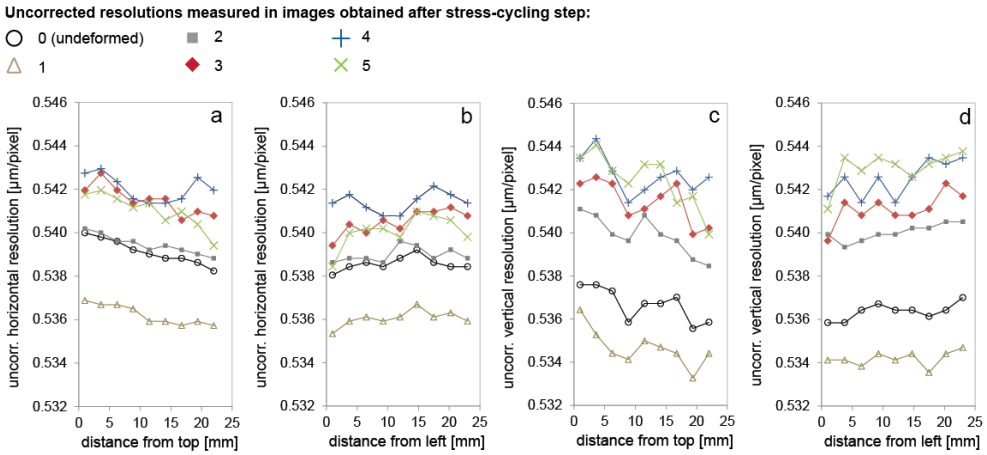

Figure 4.A2 Plots showing the uncorrected horizontal (a,b) and vertical (c,d) resolution data versus the corresponding position on the split-cylinder face (see Figure 4.A1a), obtained for each stress-cycling experiment.

These observations indicate the following. The decrease in uncorrected vertical and horizontal resolution seen from top to bottom, and the increase seen in these quantities from left to right indicate that the sample surface was slightly tilted forward (top side down) and to the right (right side down), with respect to a plane lying perpendicular to the SEM column. However, since the decreasing trends seen from top to bottom and increasing trends from left to right were approximately similar for each imaging experiment, the sample tilt is inferred to be similar in each imaging experiment. The offsets shown by the subset width and height data obtained between imaging experiments are attributed to small differences in the working distance used in the various experiments and to variations in surface charging. In turn, variations in surface charging are likely to have been caused by a different acceleration voltage used in different imaging sessions (0, 1 and 2 [2 kV] versus 3, 4 and 5 [1 kV]), plus partial removal of the Pt/Pd layer coating the sample surface after each stress-cycling experiment. The scatter around the roughly linear trends shown by subset width and height versus location data may again be due to partial removal of the Pt/Pd coating, and/or due to an increasing roughness of the sample with increasing deformation.

In this study we are interested in the relative displacements recorded before and after each stress-cycling experiment, rather than in the absolute position of a particular point in any one of the individual images. Since the sample showed similar tilting in all imaging sessions, our image data do not have to be corrected for any distortion effects due to tilting. Rather, to account for the offset shown in the uncorrected vertical and horizontal resolutions between imaging experiments, we normalized the uncorrected resolutions obtained at each

location in each imaging experiment by the corresponding, uncorrected resolution obtained of the undeformed sample. For each imaging experiment, the mean values of the normalized, uncorrected horizontal resolution ($\overline{res}_{corr,0}{}^{h}$) and of the normalized, uncorrected vertical resolution ($\overline{res}_{corr,0}{}^{v}$), and their corresponding standard deviations are determined, and listed in Table A1. These quantities are then used to adjust the size of all sample-scale, cropped, stitched images, through multiplying the width and height of these images (measured in pixels) with $\overline{res}_{corr,0}{}^{h}$ and $\overline{res}_{corr,0}{}^{v}$, respectively. The standard deviations (SD) of $res_{corr,0}{}^{h}$ and $res_{corr,0}{}^{v}$ are used as the error on each of these size adjustment. The error on the strain calculation due to distortion effects is then obtained through SD$res_{corr,0}{}^{h,v}$ /√(width or height of the imaged region analyzed), which yielded negligible errors on the strain of < 0.01%. After size adjustment, all images were scaled using the same scaling factor of 0.54 μm/pixel.

Table 4.A1 List of the factors used to correct the resolution of the images for distortion effects. The factors $\overline{res}_{corr,0}{}^{h}$ and $\overline{res}_{corr,0}{}^{v}$ denote the mean values of the uncorrected horizontal and vertical resolutions measured in the 18 subsets of the image tiles obtained after each stress-cycling experiment (Figures 4.A1 and 4.A2), normalized to the corresponding uncorrected resolutions measured in images of the undeformed sample. Factors $\overline{res}_{corr,0}{}^{h}$ and $\overline{res}_{corr,0}{}^{v}$ are used to correct the total width and height of the stitched images, respectively, thus correcting the resolution of the stitched image. The standard deviation (SD) of $res_{corr,0}{}^{h}$ and $res_{corr,0}{}^{v}$ are used as the error on this resolution correction and hence on the displacement measured after each stress-cycling experiment.

Stress-cycling experiment	$\overline{res}_{corr,0}{}^{h}$	$\overline{res}_{corr,0}{}^{v}$	SD $res_{corr,0}{}^{h}$	SD $res_{corr,0}{}^{v}$
	[pixel/pixel]	[pixel/pixel]	$\cdot 10^{-3}$ [pixel/pixel]	$\cdot 10^{-3}$ [pixel/pixel]
0	1.000	1.000	0.00	0.00
1	0.996	0.996	0.99	0.82
2	1.001	1.006	0.80	0.90
3	1.004	1.009	1.75	0.90
4	1.005	1.011	1.99	1.20
5	1.003	1.012	1.76	1.63

Appendix 4.A2

The error resultant from the PIV analysis is estimated following the method outlined by *Wieneke* [2015]. For each interrogation window of each imaging experiment, the displacement was computed for 16 smaller sub-windows (128 by 128 pixels in size). These

sub-windows are each subject to a higher noise level due to fewer pixels present. The error is then estimated by the standard deviation of the displacement vectors obtained for the 16 sub-windows, divided by the square root of the number of sub-windows used [*Wieneke*, 2015]. This method assumes no internal displacement gradient within the interrogation window for which the error is analysed. Since each interrogation window used in this study contains multiple grains that could potentially be displaced, the assumption of no internal displacement likely leads to an overestimation of the error.

Appendix 4.A3

Here we outline the steps taken to obtain an expression for the consolidation velocity (v_c) normal to a clay film upon application of an effective grain contact normal stress ($\tilde{\sigma}$). Each clay film is assumed to consist of a number (N) of rigid illite plates, each of thickness h_{il}, interbedded with incompressible water films (Figure 4.A3). Clay plates and water films are stacked in parallel and have a disc-shaped top surface area equal to that of the host clay film (*i.e.* πr^2). We assume that the consolidation rate normal to the clay film is controlled by radial outflow of the interbedded fluids, which is described by Poiseuille laminar flow between parallel plates [*Batchelor*, 2000]. The Poiseuille formulation states that in a single water film, the average flow velocity (u) in the radial film-parallel direction x (x increases outward) is:

$$u = \frac{{h_w}^2}{12\eta}\left(-\frac{dP_p^{film}}{dx}\right) \qquad \text{(Eq. 4.A1)}$$

where η is the viscosity of the pore fluid films, h_w is the water film thickness, and $\frac{dP_p^{film}}{dx}$ is the pore pressure gradient within the water film. Mass balance implies that at any radius x within a single water film, the volume of water displaced per second by vertical compression at a velocity v_c^* must be equal to the volume of water flowing out radially in each second, so that:

$$v_c^* = -\frac{h_w}{6\eta x}\left(\frac{dP_p^{film}}{dx}\right) \qquad \text{(Eq. 4.A2)}$$

The fluid pressure within clay films (P_p^{film}) at radial distance x is obtained by integrating Equation 4.A2, and taking into account that at $x = r$, P_p^{film} must be equal to the fluid

pressure in the sandstone pore space (P_p). This then yields:

$$P_p^{film}(x) = P_p + \frac{3\eta v_c^*}{{h_w}^3}(r^2 - x^2) \quad \text{(Eq. 4.A3)}$$

Balancing the total (*i.e.* not effective) normal force acting on the water film with the force carried by the fluid pressure within the water film gives:

$$\tilde{\sigma}_{tot}\pi r^2 = \int_0^r P_p^{film}(x)\ 2\pi x\ dx \quad \text{(Eq. 4.A4)}$$

Combining Equations 4.A3 and 4.A4, integrating over the distance *x* and rearranging to give the vertical consolidation velocity (v_c^*) due to radial outflow of a single fluid film at a given effective normal stress, to be:

$$v_c^* = \frac{2{h_w}^3}{3\eta r^2}\ \tilde{\sigma} \quad \text{(Eq. 4.A5)}$$

where $\tilde{\sigma}$ is the effective normal contact stress. For any number (N) of fluid films, the cumulative vertical consolidation speed is given by: $v_c = v_c^*$, so that:

$$v_c = N\frac{2{h_w}^3}{3\eta r^2}\ \tilde{\sigma}. \quad \text{(Eq. 4.A6)}$$

In turn, N is equal to z / (h_w + h_{il}), where z is the clay film thickness (*i.e.* including all clay plates plus intermittent water films). Inserting this relation and $\tilde{\sigma}$ = [σ_1^{eff}+σ_3^{eff}] /2 (see main text) in Equation 4.A6, we obtain:

$$v_c = \frac{z{h}^3}{(h_w+h_{il})\eta r^2}\ \left(\sigma_1^{eff} + \sigma_3^{eff}\right) \quad \text{(Eq. 4.A7)}$$

Here, the thickness of each water film (h_w) is taken to be 3 nm, conform the estimated thickness of the water films trapped between illite plates at effective normal stresses of 100 – 180 MPa [*Brown et al.*, 2017]. We assume that the thickness of individual illite plates (h_{il}) can be approximated by also 3 nm, which would be similar to the thickness of individual montmorillonite platelets [*Carrier et al.*, 2016]. The water film viscosity η is taken to be 10^{-3}

Pa s, which has been shown to be valid for fluid film thicknesses down to ~1 nm [*Israelachvili*, 1986]. Finally, the micrographs obtained on the present Z1 sample, having an initial porosity of 20.4% show that the grain contact radius r typically is 50 ± 20 µm (*e.g.* Figure 4.8 of the main text).

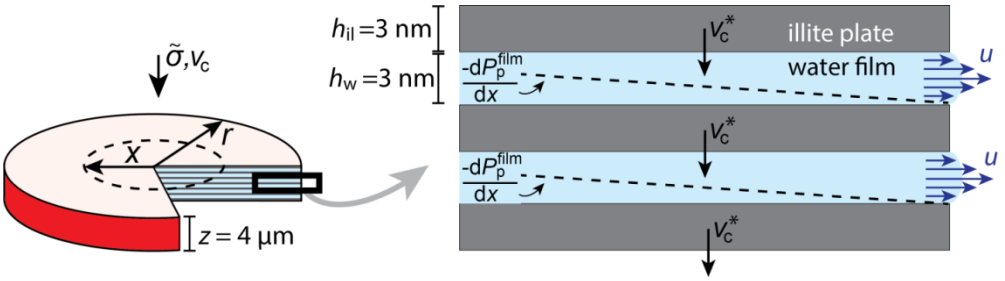

Figure 4.A3: Diagram illustrating the factors used in deriving the consolidation rate model. Each illite film (red) is assumed to consist of a stack of parallel, rigid illite plates, interbedded with films of incompressible water. Consolidation of the illite films at velocity v_c is controlled by radial outflow of these constituent water films due to application of the effective normal contact stress $\tilde{\sigma}$. The consolidation velocity normal to each individual water film (v_c^*) is taken to be controlled by laminar (Poiseuille) flow in the radial direction x, at an average velocity u.

Chapter 5

Microphysics of inelastic deformation in reservoir sandstones from the seismogenic center of the Groningen gas field

Abstract

Physics-based assessment of the long-term effects of hydrocarbon production from sandstone reservoirs on induced subsidence and seismicity hinges on understanding the processes governing compaction of the reservoir. Compaction strains are typically small (ε < 1%) and may be partly elastic (recoverable) and partly inelastic (permanent). To describe the inelastic contribution to reservoir deformation in the seismogenic Groningen gas field, and its effect on *in-situ* stress evolution and energy dissipation versus storage, a Cam-clay-type plasticity model was recently reported by the present team and calibrated to fit triaxial test data obtained for Slochteren sandstone samples from the Groningen reservoir. Here, we develop a microphysical model to underpin this empirical description, based on the deformation mechanisms observed in triaxial experiments at *in-situ* conditions and compaction strains (ε < 1%). These mechanisms include consolidation of and slip on µm-thick, grain boundary clay films, plus intragranular cracking. The microphysical model obtained predicts mechanical behaviour that agrees favourably with our experimental data and Cam-Clay description. A simple analysis shows that grain boundary clay film consolidation and slip are time- or rate-insensitive deformation processes at stresses pertaining to the depletion of the Groningen reservoir, so that reservoir compaction by these mechanisms is also expected to be time or rate-insensitive. The Cam-clay plasticity model is accordingly anticipated to describe the main trends in compaction behavior at the decade time-scales relevant to the field, though compaction strains and lateral stresses may be slightly underestimated due to other, minor (decelerating) creep effects seen in the experiments. To constrain the long-term (decades - centuries) effect of very slow creep processes (*e.g.* stress-corrosion cracking, pressure solution) not seen in lab experiments of conventional (hours/days) duration, further work is needed.

5.1 Introduction

A physics-based assessment of the short- and long-term effects of hydrocarbon production from sandstone reservoirs, in terms of induced subsidence and seismicity, requires an understanding of the processes operating in the reservoir system [*Mallman and Zoback*, 2007; *Spiers et al.*, 2017; *Van Thienen-Visser and Breunese*, 2015; *De Waal et al.*, 2015; *Van Wees et al.*, 2018]. It is generally understood that the increase in effective stress accompanying pore pressure (P_p) reduction leads to elastic and possibly inelastic compaction of the reservoir, resulting in small vertical strains (ε) totaling 0.1 to 1.0%, derived from surface subsidence [*Mallman and Zoback*, 2007; *Morton et al.*, 2001], or from *in-situ* compaction measurements [*Cannon and Kole*, 2017]. Even though these strains are small, they may induce sufficiently high shear tractions on pre-existing faults to trigger seismogenic rupture [*Bourne et al.*, 2014; *Buijze et al.*, 2017; *Mulders*, 2003]. However, from an experimental perspective, the magnitude of the *in-situ*, or internal reservoir strain, and particularly of the inelastic contribution remains poorly constrained. In part, this is because most experimental studies investigating sandstone deformation [*Wong and Baud*, 2012- and references therein] have focused on deformation behavior seen at high axial compression strains (ε of 1 to 10%), *i.e.* strains exceeding those relevant to producing reservoirs. It is also unclear to what extent the inelastic and elastic behavior seen in experiments at typical laboratory time scales (hours – months), and using typical experimental boundary conditions (*e.g.* triaxial compression at constant confining pressure), can be extended to the decade time-scales and uniaxial strain boundary conditions pertaining to many hydrocarbon reservoirs. Improving our understanding of the contribution of inelastic versus elastic deformation to the *in-situ* behavior of the reservoir is crucial for realistic geomechanical modelling of induced subsidence and seismicity [*Buijze et al.*, 2017; *Candela et al.*, 2019; *Lele et al.*, 2016; *Smith et al.*, 2019; *Van Thienen-Visser and Fokker*, 2017]. This is because: 1) The inelastic versus elastic strain partitioning controls the strain energy available in the reservoir for seismic rupture and associated processes [*Cooke and Madden*, 2014; *Pijnenburg et al.*, 2018]; 2) It governs the evolution of the stresses that prevail in the reservoir and that act on faults [*Chan et al.*, 2004; *Pijnenburg et al.*, 2019]; and 3) Many inelastic deformation processes exhibit a rate-sensitivity [*e.g. Spiers et al.*, 2004; *Brantut et al.*, 2013], that may therefore influence compaction, stress evolution and seismicity during production [*Hettema et al.*, 2002; *Mallman and Zoback*, 2007], or even lead to ongoing compaction, subsidence and seismicity beyond field closure. Extrapolation of lab-derived constraints on the reservoir compaction behavior and inelastic-elastic strain partitioning [*Hol et al.*, 2018; *Pijnenburg et al.*, 2018, 2019; *Schutjens et al.*, 1995], to field time-scales and conditions also requires

underpinning by a much better understanding of the governing processes [*Spiers et al.*, 2017].

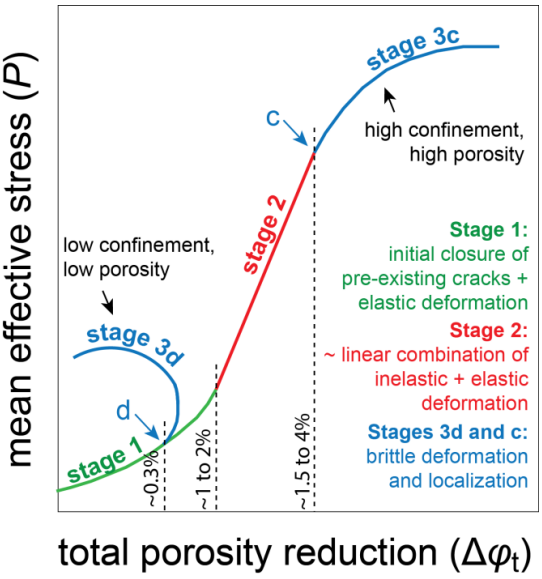

Figure 5.1 Schematic diagram showing the different stages in mean effective stress (P) versus total porosity reduction ($\Delta\varphi_t$) behavior typically seen in mechanical tests on porous sandstones. Note the effects of low porosity and confining pressure, and of low porosity and high confining pressure, on Stage 3 behavior (dilation – suffix "d" versus compaction - "c"). The onset of Stages 3d and 3c is indicated with "d" and "c", respectively. The deformation mechanisms inferred in the literature are shown per stage, as are typical values of $\Delta\varphi_t$ measured at the end of each stage.

Experimental studies investigating the compaction behavior of sandstone widely report a characteristic, trimodal sequence in stress-strain behavior, usually expressed using plots of mean effective stress ($P = [\sigma_1 + \sigma_2 + \sigma_3]/3$ – pore pressure P_p) versus total porosity reduction ($\Delta\varphi_t$) [*Wong and Baud*, 2012 - and references therein]. This sequence (Figure 5.1) typically includes an initial stage of non-linear, concave-up P- $\Delta\varphi_t$ behavior (Stage 1), which at high confining pressures (≥ 20 MPa) is followed by near-linear behavior (Stage 2) and finally non-linear, concave-down behavior, characterized by compaction (Stage 3c). Alternatively, at low confining pressures (< 20 MPa) dilation (Stage 3d) may set in after Stage 1 (see also: Chapters 3 and 4). Most previous research on the inelastic sandstone deformation of sandstone [*e.g. Wong et al.*, 1997; *Baud et al.*, 2006; *Rutter and Glover*, 2012] has focused on Stage 3d and Stage 3c behavior, typically seen at high strains (ε = 1.0 to 10%),

that usually exceed those relevant for producing hydrocarbon reservoirs. The onset of Stage 3d is often delineated by a porosity (virtually-) insensitive yield envelope [*Wong et al.*, 1997] describing an approximately linear, Coulomb-type dependence of the differential stress ($Q = \sigma_1 - \sigma_3$) on P [*Paterson and Wong*, 2005]. By contrast, at the onset of Stage 3c, the corresponding differential stresses are inversely dependent on P, strongly sensitive to porosity, and delineated by a yield envelop which may be either elliptical [*Baud et al.*, 2004; *Skurtveit et al.*, 2013; *Wong et al.*, 1997] or linear in a Q - P plot [*Fortin et al.*, 2006; *Guéguen and Fortin*, 2013]. Stages 3c and 3d are both strongly associated with brittle deformation behavior, involving localized shear fracturing (Stage 3d), or pervasive intra- or transgranular cracking (Stage 3c) [*Baud et al.*, 2004; *DiGiovanni et al.*, 2007; *Fortin et al.*, 2005; *Wu et al.*, 2000].

Most previous microphysical models developed for inelastic deformation of sandstone are based on the brittle phenomena observed during Stage 3d and Stage 3c. Such models invoke combined frictional slip plus intergranular or intragranular cracking to describe dilatant Stage 3d behaviour [*Ashby and Sammis*, 1990; *Baud et al.*, 2014; *Guéguen and Fortin*, 2013] or intragranular cracking in the case of Stage 3c [*Einav*, 2007; *Guéguen and Fortin*, 2013; *Sammis and Ashby*, 1986; *Wong et al.*, 1997; *Zhang et al.*, 1990]. Typically, cracks are assumed to emanate from stress-concentrators within the microstructure, such as grain boundaries, pores and other pre-existing flaws [*e.g. Sammis and Ashby*, 1986], or from flaws at the periphery of assumed Hertzian contacts [*Brzesowsky et al.*, 2014b; *Wong et al.*, 1997; *Zhang et al.*, 1990]. They are taken to grow according to the Griffith equilibrium condition [*Griffith*, 1921]. While these models significantly enhance understanding of the high strain Stages 3d and 3c, they may not apply to the lower (Stage 2) strains more relevant to producing reservoirs ($\varepsilon \sim 0.1$ to 1.0%). In Stage 2, shear fracturing is not observed, while intragranular cracking is similarly absent, or far less common [*Menéndez et al.*, 1996; *Pijnenburg et al.*, 2019; *Wu et al.*, 2000].

In recent years, seismic activity in the vast (30 by 30 km) and densely populated Groningen gas field in the Netherlands has led to an urgent need to understand better the compaction behavior of the Slochteren reservoir sandstone at production-relevant strains ($\varepsilon \leq$ 1%) [*Spiers et al.*, 2017; *De Waal et al.*, 2015; *Van Wees et al.*, 2018]. The latest experiments performed on the Slochteren sandstone, including the short term (hours) stress-cycling tests reported in Chapter 3 of this thesis and published by *Pijnenburg et al.*, [2019], demonstrate similar Stage 1, 2, 3c and 3d behavior as typically reported for sandstone. The small strain behavior ($\varepsilon \leq 1\%$) seen during Stage 2 was found to be the most relevant to *in-situ* compaction. At these small Stage 2 strains, one third, or up to one half of the total strain was

found to be inelastic (see also: Chapter 2; *Pijnenburg et al.*, 2018). Similar elastic versus inelastic strain partitioning data were obtained in simulated depletion experiments performed on Slochteren sandstones under 1-D (i.e. uniaxial) strain boundary conditions [*Hol et al.*, 2018]. The Stage 2 inelastic deformation behavior was found to be well-described by a constitutive, Cam-clay-type plasticity model, implying isotropic strain-hardening accompanying inelastic porosity reduction (Chapter 3 - *Pijnenburg et al.*, 2019). Application of this constitutive model to depletion of the Groningen field yielded similar stress evolution estimates (within 25%) to the values measured over the past 30 years in the reservoir, suggesting a controlling role of inelastic deformation on the *in-situ* stress evolution [*Pijnenburg et al.*, 2019]. However, a mechanistic basis for this empirical model and the underlying experimental data is still lacking, and it remains unclear if the same controlling mechanisms operate *in-situ* and at field time-scales, as in the laboratory.

A recent microstructural study by *Pijnenburg et al.*, (Chapter 4) showed that Stage 2, inelastic deformation of Slochteren sandstone is accompanied by consolidation of and slip on µm-thick, intergranular clay films, plus minor intragranular cracking. A rough estimate of the inelastic strain magnitude associated with clay film deformation ($\varepsilon \approx 0.3\%$), at the experimentally explored stress changes (σ_1 from 41 to 91 MPa, σ_3 = 41 MPa, P_p = 1 MPa), showed similar results to the values measured during testing (0.4%). However, a more thorough microphysical description of the observed behavior is still lacking. Moreover, while the criteria for the onset of pervasive intragranular cracking have been established [*Guéguen and Fortin*, 2013; *Wong et al.*, 1997; *Zhang et al.*, 1990], the role played by intragranular in determining the σ - ε behavior seen in experiments has so far only been considered in thermodynamically based models [*Einav*, 2007; *Tengattini et al.*, 2014], while any influence on this of the intergranular clays present in the Slochteren sandstone has not yet been analyzed. This limits application of the experimental results and the plasticity model reported by *Pijnenburg et al.*, [2019] (Chapter 3) to the conditions and boundary conditions pertaining to the field.

In this study, we develop and test a series of microphysical models addressing the inelastic deformation processes observed in the conventional triaxial compression experiments on Slochteren sandstone reported in Chapter 3, and by *Pijnenburg et al.*, [2019]. First, we evaluate more rigorously whether intergranular clay consolidation and slip can quantitatively account for the inelastic behavior governing the Stage 1 and Stage 2 behavior seen in these experiments. The possible effects of the presence of the intergranular clays on the higher strain Stage 3d (*i.e.* dilatant, intergranular slip) and Stage 3c (intragranular cracking) is also considered. We investigate model behavior for Slochteren sandstones with

porosities of 13.4%, 21.5% and 26.4%, as tested in the experiments. Our aim is to obtain quantitative insights into the physical processes governing inelastic deformation in our experiments and so to enhance understanding and underpin geomechanical modelling of the contribution of inelastic deformation to producing subsidence and seismicity in the Groningen reservoir (and in other, similar clay-bearing reservoir sandstones).

5.2 Decoupling of elastic and inelastic deformation

We adopt the convention that compressive stresses and strains are positive. To avoid unnecessary subcripting of symbols, all stresses and pressures supported by the sandstone framework addressed are understood to be Terzaghi effective values, *i.e.* total stress minus the pore pressure. A list of the symbols used is given in Table 5.1. Assumed values for key quantities are listed in Table 5.2.

In any material, the total principal strains (ε_i^t, with i = 1, 2 or 3) due to changes in the principal effective stresses (σ_i) and/or time-dependent deformation are given as the sum of the elastic (ε_i^{el}) and inelastic (ε_i^{inel}) components, as:

$$\varepsilon_i^t = \varepsilon_i^{el} + \varepsilon_i^{inel} \qquad \text{(Eq. 5.1)}$$

where ε_i^{inel} includes both time-independent and time-dependent inelastic strain. In this study, we consider ε_i^{inel} to be time-independent and hence determined by changes in stress only. We also assume that the elastic and total inelastic contributions are decoupled, so that each can be evaluated without affecting the other.

5.3 Quantifying the elastic contribution

The elastic strain contribution is quantified here using poroelasticity theory [*Wang*, 2000]. We assume that the compressibility of the grains constituting the Slochteren sandstone is negligible compared to that of the grain framework (*i.e.*the Biot coefficient is assumed close or equal to 1 – *cf. Hettema et al.*, [2000]; *Pijnenburg et al.*, [2019], see also: Figure 3.4 of Chapter 3). We further assume that the sandstone can be treated as elastically isotropic. Poroelasticity then prescribes that the principal elastic strain increments ($d\varepsilon_i^{el}$) are related to changes in the principal effective stresses ($d\sigma_i$) and mean effective stresses ($dP = [d\sigma_1 + d\sigma_2 + d\sigma_3] /3$) via:

$$d\varepsilon_i^{el} = \frac{d\sigma_i - dP}{2G} - \frac{dP}{3K} \qquad \text{(Eq. 5.2)}$$

Here, G is the shear modulus and K is the bulk modulus of the sandstone. In Chapter 3 [*Pijnenburg et al.*, 2019], it was shown that the elastic behavior of the Slochteren sandstone is non-linear and that the values of K and of the Young's modulus (E) obtained for Slochteren sandstone samples with initial porosity φ_0 = 13.4, 21.5 and 26.4%, increase with decreasing φ_0 and with increasing P, up to $P \approx 50$ MPa, beyond which they were roughly constant. At low $P < 30$ MPa, the elastic behavior was shown to be slightly anisotropic, but this anisotropy was not apparent at higher P. For present purposes, we obtained an average value of K at P in the range of 5 to 50 MPa, using the following, linear relation between K and P:

$$K = C_1^K + C_2^K P \qquad \text{(Eq. 5.3a)}$$

Here, C_1^K and C_2^K are constants obtained for each sample set tested (*i.e.* each initial porosity φ_0), through linear regression using the $K - P$ data presented in Figure 3.4 of Chapter 3. The values obtained are listed in Table 5.2. The E values measured at each P and φ_0 were combined with Equation 5.3a to obtain the corresponding shear moduli, using $G = 3KE/(9K - E)$ [*Wang*, 2000]. This showed a similar P- and φ_0 dependence of G, as shown by K. For $5 \leq P \leq 50$ MPa, the shear moduli are described through:

$$G = C_1^G + C_2^G P \qquad \text{(Eq. 5.3b)}$$

where C_1^G and C_2^G are porosity-sensitive constants obtained through linear regression of the $G - P$ data derived as described above. For values obtained, see Table 5.2. At $P \geq 50$ MPa, the experimentally observed K and G values were found to be roughly constant (within 0.5 GPa), taking values of $K \approx 11.7$, 9.4 and 6.1 GPa and $G \approx 7.5$, 6.0 and 4.5 GPa, for initial porosities of 13.4, 21.5 and 26.4%, respectively.

Table 5.1 Explanation of the symbols used

σ_i	Principal effective stress (i =1,2,3) [Pa]	$\tilde{\sigma}_h$	Value of $\tilde{\sigma}_0$ after hydros. compression [Pa]
Q	Differential stress (σ_1 - σ_3) [Pa]	ε^{clay}	Grain contact consolidation (normal) strain [-]
P	Mean effective stress (σ_1 + σ_2+ σ_3)/3 [Pa]	B	Constant for consolidation behavior of illite [-]
P_c	Effective confining pressure [Pa]	μ	Friction coefficient of illite [-]
P_p	Pore pressure [Pa]	σ_1^{slip}	Eff. vert. stress on unit cell to activate intergr. slip [Pa]
θ	Angle between σ_1 and the unit cell top normal [°]	σ_1^{dil}	Eff. vertical stress on unit cell at dilatant intergr. slip [Pa]
σ_{top}	Eff. normal stress on unit cell top/bottom [Pa]	F^*	Contact normal force needed for intragr. splitting [N]
τ_{top}	Shear stress on unit cell top/bottom [Pa]	$\tilde{\sigma}^*$	Contact normal stress needed for intragr. splitting [Pa]
σ_{side}	Eff. normal stress on unit cell side [Pa]	P_c^*	P_c value on unit cell needed for intragr. splitting [Pa]
τ_{side}	Lateral shear stress on unit cell [Pa]	$\sigma_1^*\|_{no\ slip}$	σ_1 value on unit cell at splitting absent intergr. slip [Pa]
ε_i^t	Total strain in direction i =1,2,3 [-]	$\sigma_1^*\|_{slipAC}$	σ_1 value on unit cell at splitting during intergr. slip [Pa]
ε_i^{el}	Elastic strain in direction i =1,2,3 [-]	z^*	Contact clay film thickness upon splitting [m]
ε_i^{inel}	Inelastic strain in direction i =1,2,3 [-]	b,w,D	Geometric factors used by Kendall [m]
ε_i^{clay}	Inelastic strain due to clay deform. [-]	Y	Fracture energy of quartz per unit area [J/m^2]
$\varepsilon_i^{cr,s}$	Inelastic strain by intragr. splitting [-]	u_{exp}	Expansion normal to contact due to splitting [m]
$\varepsilon_i^{cr,m}$	Inelastic strain by multi-edge cracking [-]	u_{cont}^o	Contraction normal to contact at opened crack end [m]
E	Young's modulus [Pa]	u_{cont}^c	Contraction normal to contact at closed crack end [m]
K	Bulk modulus [Pa]	u_{net}	Net displacement normal to contact due to splitting [m]
G	Shear modulus [Pa]	c	Half crack opening upon meridional splitting [m]
E_c	Constrained modulus of clay [Pa]	β	Grain half rotation angle upon splitting [°]
E_q	Young's modulus quartz grain [Pa]	x	Distance along-contact from margin to crack [m]
C_1^K	Constant for non-linear *K-P* behavior [Pa]	m	x value at limit of clay indentation at opened crack end [m]
C_2^K	Constant for non-linear *K-P* behavior [-]	n	x value at limit of clay indentation at closed crack end [m]
C_1^G	Constant for non-linear *G-P* behavior [Pa]	$\Delta l_o(x)$	Clay contraction at x due to crack opening (open end) [m]
C_2^G	Constant for non-linear *G-P* behavior [-]	$\Delta l_c(x)$	Clay contr. at x due to crack opening (closed end) [m]
φ_0	Initial porosity [-]	$\hat{\sigma}_o(x)$	Normal stress at x upon crack opening (opened end) [Pa]
$\Delta\varphi_t$	Total porosity reduction [-]	$d\hat{F}_o(x)$	Normal force increment at x (opened end) [N]
$\Delta\varphi_i$	Inelastic porosity reduction [-]	$\hat{\varepsilon}_o(x)$	Normal strain at x (opened end) [-]
ε	Total axial/vertical strain [-]	$\hat{\sigma}_c(x)$	Normal stress at x (closed end) [Pa]
R	Quartz grain radius towards pore [m]	$d\hat{F}_c(x)$	Normal force increment at x (closed end) [N]
r	Grain contact radius [m]	$\hat{\varepsilon}_c(x)$	Normal strain at x (closed end) [-]
q	Constant used in estimating r at given φ [-]	$S(x)$	Crack-parallel width of grain contact, at x [m]
R_c	Quartz grain radius towards grain contact [m]	dW_{ext}	External work increment per unit vol. [J/m^3]
z	Initial clay film thickness [m]	dW_{int}	Internal work increment per unit vol. [J/m^3]
d	Initial flaw spacing at grain contact [m]	$\tilde{\sigma}_{edge}$	Normal stress acting on uplifted contact edge [Pa]
$\tilde{\sigma}$	Grain contact normal stress [Pa]	$\tilde{\sigma}_{edge}^*$	Normal stress for edge crack propagation [Pa]
$\tilde{\tau}$	Grain contact shear stress [Pa]	φ_{cr}	2D porosity in the intragranular crack [-]
$\tilde{\sigma}_0$	Reference value of $\tilde{\sigma}$ at onset of loading [Pa]		

Table 5.2: Input parameters used to construct the plots shown in Figures 5.9 and 5.10. φ_0 denotes the initial porosity; z denotes the characteristic initial clay film thickness at each of these porosities, as was estimated from corresponding micrographs; C_1^K, C_2^K, C_1^G and C_2^G are empirically obtained constants describing the *P*-sensitivity of the bulk modulus (superscript *K*) or of the shear modulus (superscript *G*), shown in the experiments of Chapter 3; r is the grain contact radius (see Equation 5.4); R and R_c refer to the radii of the quartz grain measured from grain center to pore wall and the grain contact, respectively. d denotes the assumed grain contact flaw spacing in 2-D, chosen to be equivalent to the characteristic interspacing of grain contact surface irregularities seen in micrographs; μ denotes the assumed friction coefficient of the intergranular illite; B is a constant describing the consolidation behavior of illite (see Figure 5.5b); E_q is the Young's modulus of quartz grains; Y is the fracture energy of quartz and φ_{cr} is the intragranular porosity fraction assumed to prevail after multi-edge cracking (see Figure 5.8a).

Porosity-sensitive			
φ_0	13.4%	21.5%	26.4%
z [µm]	3	4	6
C_1^K [GPa]	1.37	0.92	0.71
C_2^K	0.19	0.12	0.11
C_1^G [GPa]	5.74	2.53	0.82
C_2^G	0.08	0.07	0.07
r [µm]	51.6	43.0	36.9
R_c [µm]	85.7	90.3	93.0
Porosity-insensitive			
R [µm]	100	E_q [GPa]	95
d [µm]	3	Y [J/m^2]	5
μ	0.26	φ_{cr}	0.5
B	0.05		

5.4 Microstructural model for inelastic deformation

5.4.1 Key microstructural observations

We start model development by summarizing key microstructural features observed in Slochteren sandstone samples from the Groningen field. These features are illustrated in Figure 5.2, using scanning electron microscope micrographs of samples recovered from the Stedum (SDM)-1 and Zeerijp (ZRP)-3a wells in the Groningen field, which were used in the experimental studies reported in Chapters 2, 3 and 4 (Figure 5.2).

The undeformed Slochteren sandstone is highly porous, with porosities ranging from 10 to 27% [*NAM*, 2013]. It consists predominantly of quartz (72 – 90 vol%), with lesser amounts of feldspar (8 – 25 vol%) and clay (0.5 – 5.5 vol%) [*Waldmann et al.*, 2014; *Waldmann and Gaupp*, 2016]. Quartz and feldspar grains are typically 200 ± 50 µm in size

[*Hol et al.*, 2015a; *Pijnenburg et al.*, 2018] and are flattened at grain-to-grain contacts. The clay is predominantly present in the pore space (Figure 5.2a), and is further found as thin films coating the pore walls and many of the grain contacts, where they constitute part of the load-bearing framework [Chapter 4; *Gaupp et al.*, 1993; *Waldmann*, 2011]. The clay present within grain contacts consist predominantly of illite and is inferred to have been largely present already prior to burial [*Gaupp and Okkerman*, 2011; *Waldmann*, 2011]. Diagenetic feldspar dissolution led to precipitation of kaolinite and additional illite in the pore space and on pore walls [*Desbois et al.*, 2016; *Waldmann and Gaupp*, 2016], while concomitant compaction and associated grain-rearrangements may have caused further trapping of these later clays within grain contacts. Grain contact clay films are up to 10 µm thick. Qualitative microstructural analysis of the limited number of samples inspected in Chapter 2 (8 samples), Chapter 3 (14 samples) and Chapter 4 (2 samples) shows that these grain-contact clay films are thicker in the more porous sandstones. Roughly estimating these thicknesses from the micrographs recovered from the undeformed counterparts of the samples mechanically tested in Chapter 3, having porosities of 13.4% (Figure 5.2b), 21.5% and 26.4% (Figure 5.2c), reveals that these typically range between 2.5 ± 1.5 µm, 4 ± 2 µm and 6 ± 2 µm, respectively. Further quantification of (any porosity sensitivity of) the clay film thickness would be desirable, but is not attempted here, since any statistically meaningful analysis would require an elaborate, 3D, and high resolution (< 1 µm) microstructural study of a large number of grain contacts [*e.g*. *Desbois et al.*, 2016], which is not feasible in the present study.

After experimental deformation of the three porosity ranges of samples, a variety of permanent, inelastic microstructural changes were observed (Chapters 2, 3 and 4), and shown to depend on the Stage of P - $\Delta\varphi_t$ behavior explored in the experiment (refer Figure 5.1; Chapters 3 and 4). During Stage 1, inelastic deformation was found to develop mostly through compression (*i.e.* consolidation) of, and local slip on the intergranular clay films (Figures 5.2d,e), with no role being played by intragranular cracking (see Chapter 3- Figure 3.8b). During the near-linear Stage 2, inelastic deformation was found to be governed by a combination of consolidation of and slip on intergranular clays films (Figure 5.2f), with only a small role being played by intragranular cracking (Chapter 3; Figure 3.8c). Samples deformed into Stage 3d often revealed one or more sample-scale fractures, oriented at an angle between 10 and 45 degrees to the axial compression direction (Figure 5.2g). These fractures are dilated at the time of inspection, and are predominantly intergranular at low confining pressure (< 20 MPa) and high φ_0 (> 20%). At higher P and lower φ_0, they are

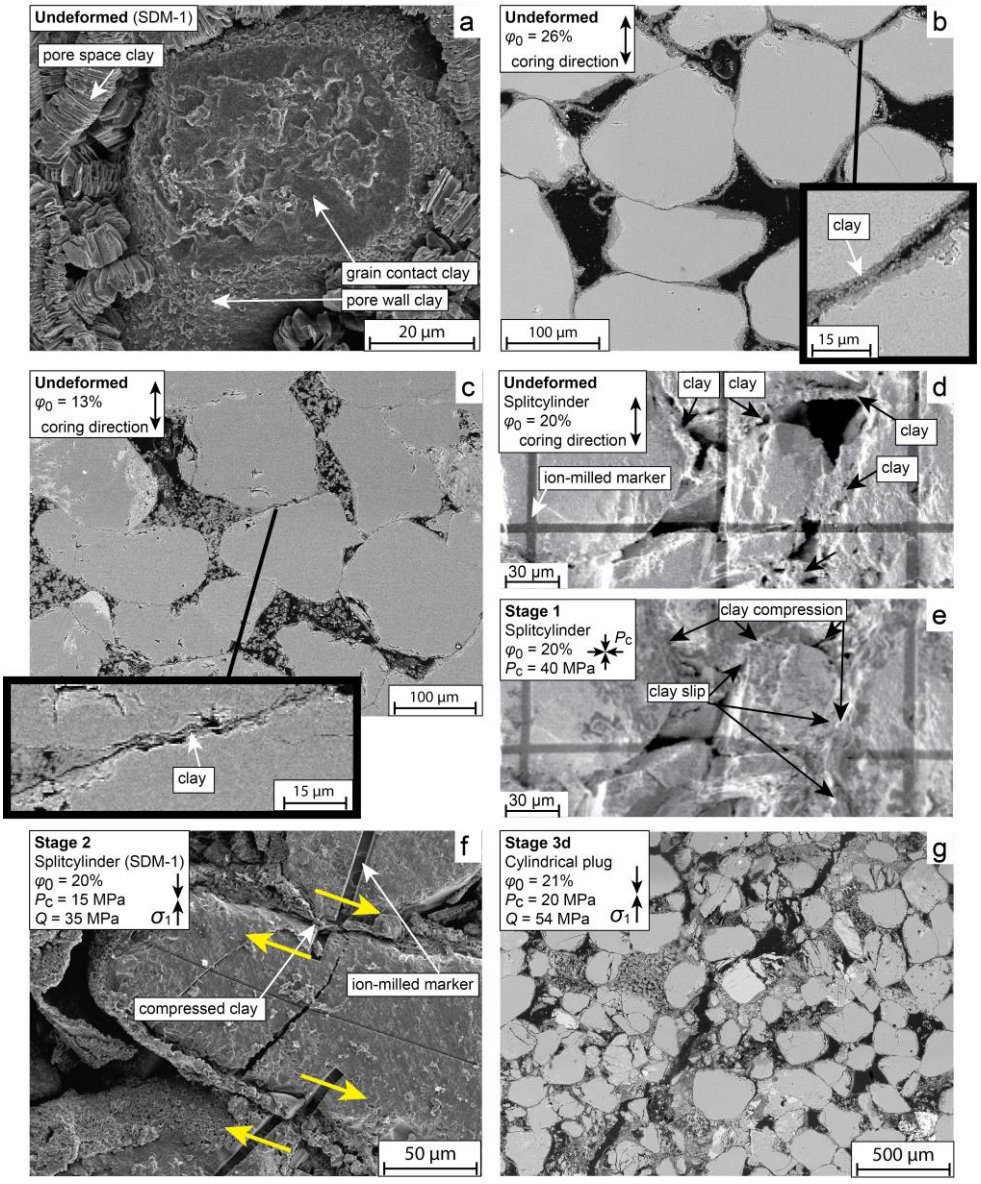

Figure 5.2 Representative micrographs of undeformed Slochteren sandstone samples having similar initial porosity (φ_0), and of samples deformed up to Stages 1, 2, 3d or 3c (refer Figure 5.1). Deformed samples are either cylindrical plugs (Chapter 3) or else split-cylinders (Chapter 4). Both types were tested at a P_p of 0.1 or 1 MPa, a strain rate of 10^{-5} s^{-1} and/or a rate of P increase of 0.1 MPa/s, up to the maximum stress conditions indicated. The samples used were obtained from the Stedum (SDM)-1 well (where indicated), or else from the Zeerijp-3a well, both in the Groningen gas field. *(Caption continued on next page)*

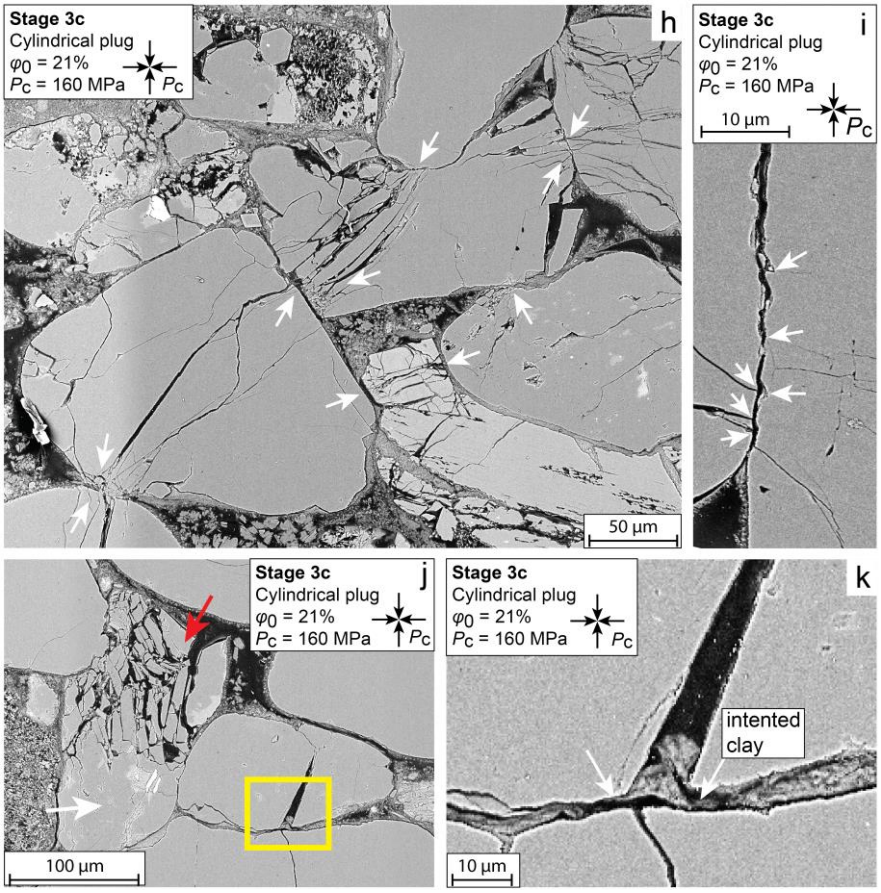

Figure 5.2 (cont.) a) Clays are present in the pore space, on the pore walls and within grain-contacts; **b, c)** Clay films, including those within the grain contacts (inset) appear thicker at higher sample porosity, than at low porosity ; **d, e)** During Stage 1, inelastic deformation is mostly accommodated by compression of clay; **f)** During Stage 2, inelasticity is thought to be predominantly accommodated by slip and compression of grain contact clays, with a smaller role played by intragranular cracking. This micrograph was obtained after a pilot-test for the experiments of chapter 4 and was tested and imaged following the same procedure as described in that chapter; **g)** After Stage 3d, sample-scale, shear fractures are often seen, which at low P_c and high φ_0 (*e.g.* here) are mostly intergranular; **h)** After Stage 3c, intragranular cracks are ubiquitous, emanating from grain-to-grain contacts, **i)** typically from µm-scale asperities within the contact; **j)** Cracked grains are either split by a single, meridional crack (yellow box), or else more pervasively crushed through multiple, roughly parallel, or convergent cracks (red arrow), referred to here as multi-edge cracks. Cracks typically open towards the pore space, while in more densely-packed (parts of) grains (white arrow), cracks are absent or closed; **k)** Close-up of (j). The boundaries of the split grain can be seen to indent into the clay film coating the contact.

typically surrounded by a damage zone up to 1 mm wide, in which intragranular cracks are abundant. In samples deformed into Stage 3c, such dilatant fractures are absent, while in these samples, pervasive intragranular cracking occurs within 1 to 10 mm wide bands, oriented at 45 to 90 degrees to the main compression direction (see Chapters 3 and 4). Where observed, intragranular cracks emanate from grain-to-grain contacts (Figure 5.2h, white arrows), frequently from or opposing micrometer-sized contact asperities, which are typically interspaced by 3 ± 2 μm (Figure 5.2i, white arrows). Cracked grains are either split by a single, meridional crack (Figure 5.2j, yellow box), or else fragmented by multiple, roughly parallel, or convergent cracks, interspaced by several micrometers (Figure 5.2h and 1j, red arrow). These will be referred to as multi-edge cracks. Cracks are typically opened by 0.1 to 10 μm. Where markedly opened, the boundaries of the split grain, or grain fragments can be seen to indent into the clay film coating the contact (Figure 5.2k). Crack opening is seen more readily in the direction of surrounding pores (Figure 5.2j, red arrow), whereas fewer cracks and reduced crack opening are seen in more densely packed parts of the microstructure (Figure 5.2j, white arrow).

5.4.2 Assumed deformation processes

On the above basis, we infer that inelastic deformation during each of the four stages of $P - \Delta\varphi_t$ behavior seen during triaxial compression of Slochteren sandstone is dominated by the following inelastic processes: (i) Stages 1 and 2: slip and/or consolidation of intergranular clays; (ii) Stage 3d: intergranular slip and dilatant opening of grain contacts (*i.e.* shear failure); and (iii) Stage 3c: intragranular cracking. In describing intragranular cracking, we differentiate between intragranular (meridional) splitting and intragranular multi-edge cracking, with reference to the dominant crack types seen (*e.g.* Figure 5.2j - yellow box, and red arrow, respectively). For reference, these deformation processes assumed to dominate each Stage are schematically illustrated in Figure 5.3.

In subsequent Sections 5.5 to 5.7, we develop a series of model components describing stress-criteria and accompanying stress-strain relations for the above processes. The behavior predicted by these models is then briefly evaluated by comparison with the experiments presented in Chapter 3, *i.e.* for hydrostatic compression ($\sigma_1 = \sigma_2 = \sigma_3$ = confining pressure P_c) up to P_c values in the range of 5 to 80 MPa, followed by deviatoric compression at constant P_c ($\sigma_1 > \sigma_2 = \sigma_3 = P_c$). Finally, in Section 5.8 we integrate the different model components to evaluate the total inelastic deformation behavior that results.

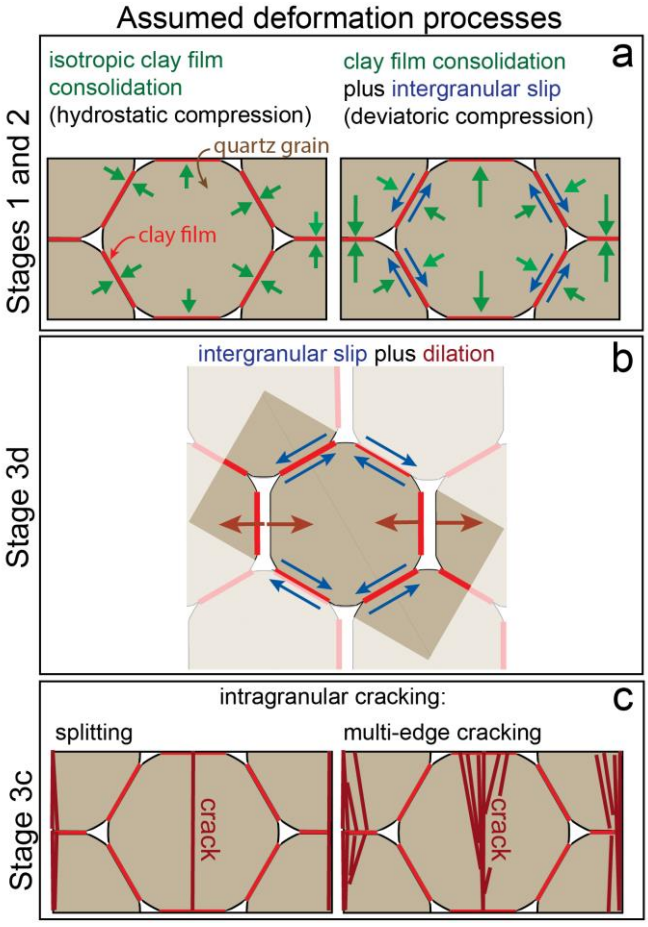

Figure 5.3 Schematic illustration of the deformation processes assumed to dominate each Stage of $P - \Delta\varphi_t$ behavior (*cf.* Figure 5.1).

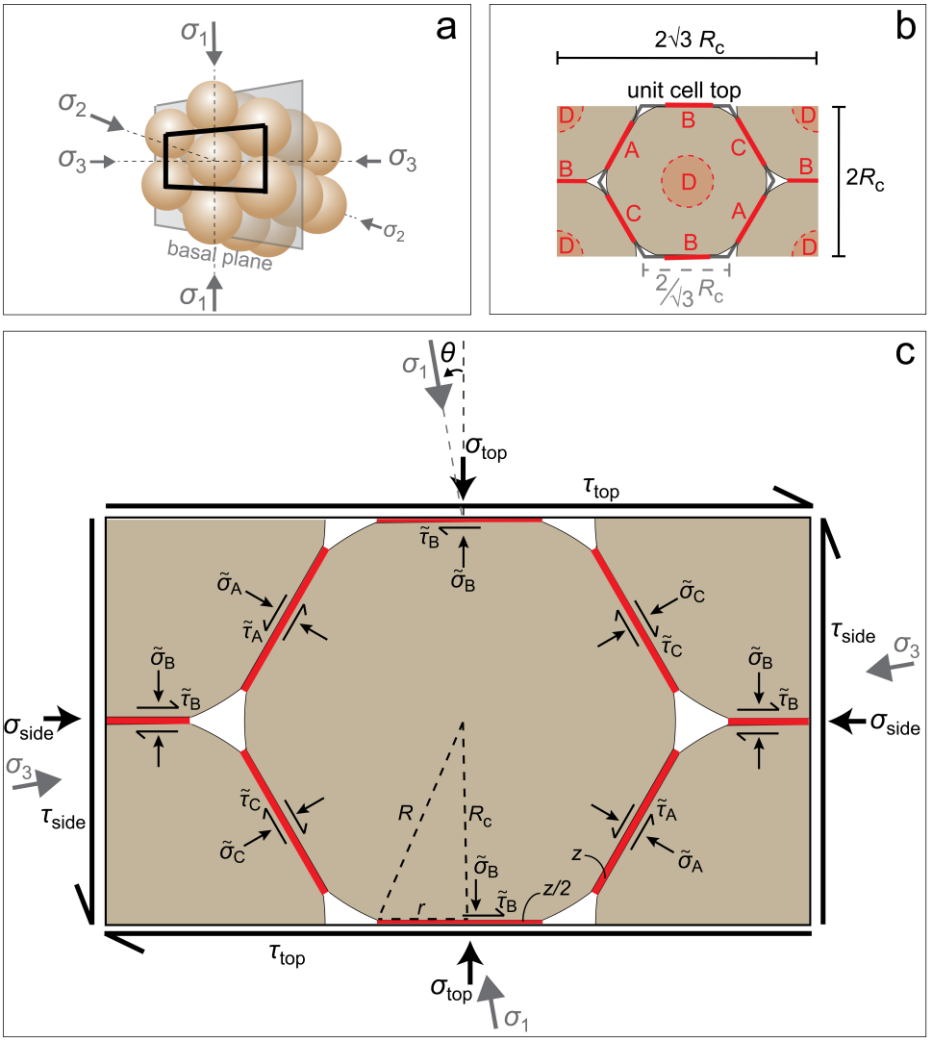

Figure 5.4 Assumed model microstructure for inelastic deformation of the clay-bearing Slochteren sandstone undergoing triaxial compression. The microstructure constitutes a simple hexagonal pack of quasi-spherical quartz grains with flattened contacts, each covered with illite clay films (indicated red). **a)** The simple hexagonal grain pack. The basal plane is oriented perpendicular to σ_2. **b)** Basal plane-parallel view on the representative, unit cell volume, taken to be one grain (2 R_c) deep. The unit cell contains grain contact A, B, C and D; **c)** The maximum vertical stress (σ_1) acts at an angle θ to the top of the unit cell, implying (external) normal and shear stresses on the top (σ_{top}, τ_{top}) and side (σ_{side}, τ_{side}) of the unit cell. These external stresses imply normal ($\tilde{\sigma}$) and shear stresses ($\tilde{\tau}$) on grain contacts A, B and C. which, if sufficiently large, may cause consolidation of- and/or slip on the intergranular clay (thickness z), and/or cracking of the quartz grains. R and R_c refer to the radii of the quartz grain measured from grain center to pore wall and the grain contact, respectively, while r is the grain contact radius.

5.4.3 Idealized microstructure and microstructural unit cell

Our idealized model for the Slochteren sandstone deforming by the inelastic processes shown in Figure 5.3 is shown in Figure 5.4. In the $\sigma_1 - \sigma_3$ plane, we assume a simple, 2-D hexagonal pack of quasi-spherical quartz grains (Figure 5.4a) with flat, or truncated, circular grain contacts, coated by clay films (Figures 5.4b and 5.4c – colored red). In the third dimension, or σ_2 direction, this 2-D pack is assumed to be stacked grain-on-grain (Figure 5.4a). The grain radius to the pore walls (R) is taken to be 100 μm (Table 5.2). The grain contact radius (r) is approximated for a given initial porosity (φ_0) through [*Gundersen et al.*, 2002; *Renard et al.*, 1999]:

$$r = 2R\sqrt{\frac{q-2\varphi_0}{k}} \qquad \text{(Eq. 5.4)}$$

where q is a constant assumed to be equal to 0.8 [*cf. Spiers et al.*, 2004], and k is the grain coordination number, here equal to 8. The distance between grain centers and flattened contacts is then given by $R_c = \sqrt{(R^2 - r^2)}$ (see Figure 5.4c). We ignore clays not present within grain-contacts, as these fall outside the load-bearing framework. Grain contact clay films are taken to consist of illite (see Section 5.4.1), and are disc-shaped, having the same top and bottom surface area as that of the contact (πr^2) and a thickness z of 3, 4 and 6 μm for porosities of 13.4, 21.5 and 26.4%, respectively (Table 5.2), following the clay film thicknesses estimated earlier for these porosities (Section 5.4.1). The unit cell of this regular pack is one grain deep (*i.e.* ~$2R_c$) and shown in Figure 5.4. It incorporate four sets of two parallel grain contacts, referred to as grain contacts A, B, C and D (see Figure 5.4b).

5.4.4 Stresses at the unit cell and grain contact scales

The maximum (σ_1) and minimum (σ_3) principal stresses act at an angle θ to the normal of the unit cell top and side, respectively, while the intermediate principal stress (σ_2) acts perpendicular to σ_1 and σ_3, hence perpendicular to grain contact D (Figures 5.4a, b). By varying θ between 0 and 30 degrees, grain contacts A, B and C are rotated such that all possible grain contact orientations (0 to 90°) with respect to σ_1 and σ_3 are described. In real sandstone, all of these grain contact orientations, hence all angles θ, will be present in different parts of the microstructure. During deformation of such a sandstone, we assume that the inelastic response of the bulk due to each given inelastic process will be dominated by the weakest parts of the microstructure, *i.e.* by those grain contacts oriented most favorably for a given inelastic process to occur [see for instance: weakest link theory - *e.g. Brzesowsky*

et al., 2011; *Lu et al.*, 2002]. To evaluate at which orientation θ a given inelastic process is easiest, we explore the unit cell behavior for the two end-member angles θ of 0 and 30° (Figure 5.4c). In doing so, we effectively explore the two extremes in mechanical behavior expected, where the behavior at intermediate angles is anticipated to fall in between. In addition, the onset of dilation (Stage 3d) is explored for the full range of θ, since the strength at the onset of Stage 3d dilation (*i.e.* at or approaching shear failure) is well-known to be markedly orientation-sensitive [*Jaeger et al.*, 2007].

Assuming a homogeneous stress distribution throughout the sandstone microstructure, then at a given angle θ, the normal (σ_{top}) and shear stresses (τ_{top}) acting on the top and bottom planes of the unit cell (Figure 5.4c), as well as the normal (σ_{side}) and shear stresses (τ_{side}) acting on the lateral planes of the unit cell, are related to the principal stresses at the sandstone sample scale [*Jaeger et al.*, 2007] through:

$$\sigma_{top} = \tfrac{1}{2}(\sigma_1 + \sigma_3) + \tfrac{1}{2}(\sigma_1 - \sigma_3)\cos(2\theta) \quad \text{(Eq. 5.5a)}$$

$$\sigma_{side} = \tfrac{1}{2}(\sigma_1 + \sigma_3) - \tfrac{1}{2}(\sigma_1 - \sigma_3)\cos(2\theta) \quad \text{(Eq. 5.5b)}$$

$$\tau_{top} = \tau_{side} = \tfrac{1}{2}(\sigma_1 - \sigma_3)\sin(2\theta) \quad \text{(Eq. 5.5c)}$$

These stresses, and the intermediate principal stress σ_2 are transmitted onto grain contacts A, B, C and D, producing shear ($\tilde{\tau}$) and/or effective normal ($\tilde{\sigma}$) stresses on each contact. Ignoring the thickness of the intergranular clay films (*i.e.* taking $z << R$, as observed), force balance considerations imply that the stresses acting on the unit cell and grain contacts (Figure 5.4c) are related by:

$$\sigma_{top} 4\sqrt{3}R_c^2 = \pi r^2 \left(2\tilde{\sigma}_B + \tfrac{1}{2}\tilde{\sigma}_A + \tfrac{1}{2}\tilde{\sigma}_C + \tfrac{\sqrt{3}}{2}\tilde{\tau}_A + \tfrac{\sqrt{3}}{2}\tilde{\tau}_C\right) \quad \text{(Eq. 5.6a)}$$

$$\tau_{top} 4\sqrt{3}R_c^2 = \pi r^2 \left(2\tilde{\tau}_B + \tfrac{\sqrt{3}}{2}\tilde{\sigma}_A - \tfrac{\sqrt{3}}{2}\tilde{\sigma}_C - \tfrac{1}{2}\tilde{\tau}_A + \tfrac{1}{2}\tilde{\tau}_C\right) \quad \text{(Eq. 5.6b)}$$

$$\sigma_{side} 4R_c^2 = \pi r^2 \left(\tfrac{\sqrt{3}}{2}\tilde{\sigma}_A + \tfrac{\sqrt{3}}{2}\tilde{\sigma}_C - \tfrac{1}{2}\tilde{\tau}_A - \tfrac{1}{2}\tilde{\tau}_C\right) \quad \text{(Eq. 5.6c)}$$

$$\tau_{side} 4R_c^2 = \pi r^2 \left(\tfrac{1}{2}\tilde{\sigma}_A - \tfrac{1}{2}\tilde{\sigma}_C + \tfrac{\sqrt{3}}{2}\tilde{\tau}_A - \tfrac{\sqrt{3}}{2}\tilde{\tau}_C\right) \quad \text{(Eq. 5.6d)}$$

$$\sigma_2 4\sqrt{3}R_c^2 = 2\pi r^2 \tilde{\sigma}_D \quad \text{(Eq. 5.6e)}$$

Here, the subcripts to $\tilde{\sigma}$ and $\tilde{\tau}$ denote the specific grain contact stress components (see Figure 5.4c). We assume that these force balance relations are satisfied within each cell-sized grain cluster during deformation. The magnitude of the contact stresses, for any given cell orientation θ, depends on the loading conditions (σ_i), and on the capacity of the intergranular illite films to support shear and normal load. This will be evaluated in the following.

5.5 Inelastic deformation mechanism 1: Clay consolidation and slip

5.5.1 Consolidation behavior of illite within grain contacts

The consolidation (*i.e.* compaction) behavior of illite powder has been investigated by *Brown et al.*, [2017]. These authors performed long-term (months), drained, 1-D consolidation tests on discs (1 to 2 mL in volume) of brine-saturated illite powder (purity 65 to 85%) at room temperature, exploring effective axial stresses in the range of 5 to 180 MPa. They found that the void ratio (= φ/[1 - φ]), hence the porosity of the illite decreased approximately logarithmically with increasing effective normal stress (Figure 5.5a). Similar behavior has been reported for many other clays [*Allman and Atkinson*, 1992; *Marcial et al.*, 2002; *Smith et al.*, 1992] and shales [*Favero et al.*, 2016; *Ferrari et al.*, 2016], though generally with uncertainties in degree of drainage versus test duration. Assuming constant pore fluid density, the total pore volume reduction is in 1-D compression equal to the fluid volume expelled, and thus gives axial strain when normalized with respect to a given reference disc thickness. We estimate the inelastic contribution to these data by subtracting the axial elastic strain expected for the corresponding changes in effective stress (*i.e.* $\Delta\sigma E$). We assume a constrained (oedometric) modulus E_c of 10 GPa, as measured at an effective axial stress of 100 MPa, in wet Opalinus shales with porosities in the appropriate range [10 - 20%; *Ferrari et al.*, 2016], and a Biot coefficient of 1. After subtracting the elastic strain contribution (< 10% of total), the residual inelastic strain due to clay consolidation is found to increase again roughly logarithmically with increasing effective normal stress (Figure 5.5b). Applying these data to our model, finite inelastic normal strain ($\tilde{\varepsilon}^{clay}$) occurring within a grain contact illite film due to consolidation accompanying an increase in grain contact normal stress to a value $\tilde{\sigma}$, from a reference value $\tilde{\sigma}_0$ is described by:

$$\tilde{\varepsilon}^{clay} = B \ln\left(\frac{\tilde{\sigma}}{\tilde{\sigma}_0}\right) \qquad \text{(Eq. 5.7)}$$

Here, B is a constant estimated from the data treatment illustrated in Figure 5.5b to be equal to about 0.05. The use of Equation 5.7 of course assumes that inelastic compression of illite

films in quartz grain contacts can be treated as 1-D, drained consolidation behavior. Given the small radius of grain contacts (10 to 50 µm in the Slochteren sandstone), hence very short fluid expulsion/drainage path, and the frictional constraints imposed on the clay film surfaces by the enclosing quartz grain contacts, we consider this assumption to be reasonable.

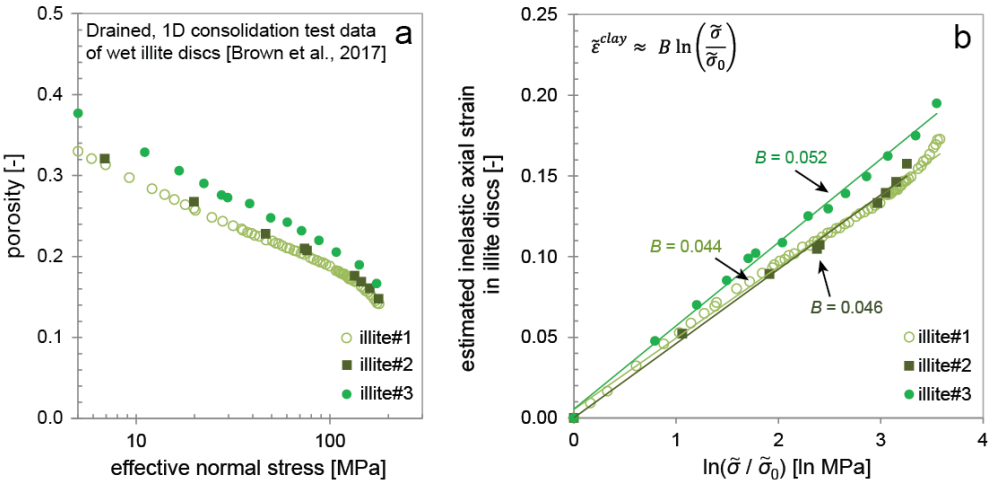

Figure 5.5 a) Plot showing the porosity (φ) evolution of wet illite discs (1-2 mL) with increasing effective axial stress (σ), calculated from the void ratio (= φ/[1 - φ]) versus σ data obtained in the drained, 1D consolidation tests performed by *Brown et al.*, [2017]; **b)** After subtraction of the expected elastic component (see text), the estimated 1-D, inelastic porosity reduction, or inelastic axial strain of the illite films (in our model denoted: $\tilde{\varepsilon}^{clay}$) can be described by a log-linear relation, as shown. In our model, the illite films are present on grain contacts, whereby σ is given by the effective contact normal stress ($\tilde{\sigma}$) and $\tilde{\sigma}_0$ is an initial, reference contact effective normal stress.

5.5.2 Clay film response to hydrostatic loading and effects at unit cell scale

Under hydrostatic effective stress conditions, $\sigma_1 = \sigma_2 = \sigma_3 = \sigma_{top} = \sigma_{side}$ = effective confining pressure P_c, while all shear stresses at the unit cell boundaries and grain contacts are zero (Figure 5.4c). In this case, Equations 5.6a and 5.6c imply that the normal stresses acting on grain contacts A, B and C in Figure 5.4c are given:

$$\tilde{\sigma}_A = \tilde{\sigma}_B = \tilde{\sigma}_C = \frac{4R_c^2}{\sqrt{3}\pi r^2} P_c \qquad \text{(Eq. 5.8a)}$$

At the same time, Equation 5.6e implies that:

$\tilde{\sigma}_D = (3/2)\tilde{\sigma}_{A,B,C}$ (Eq. 5.8b)

which highlights contact loading anisotropy in the model geometry chosen. Despite this anisotropy, Equations 5.7 plus 5.8a or 5.8b show that any increase in isotropic confining pressure to a value P_c from a reference confining pressure P_c^0 results in the same inelastic strain response $\Delta\tilde{\varepsilon}_{A,B,C,D}^{clay}$ at all contacts, *i.e.* at A through D. At the scale of the unit cell (Figure 5.4c) and above, the principal inelastic strains developing due to clay consolidation during hydrostatic compression can now be written as: $\Delta\varepsilon_1^{clay} = \Delta\varepsilon_2^{clay} = \Delta\varepsilon_3^{clay} = z\,\Delta\tilde{\varepsilon}_{A-D}^{clay}/(2R_c)$, where z is the grain contact clay film thickness. Combining these relations with Equations 5.7, 5.8a and 5.8b, we obtain the following expressions for the inelastic strains produced by consolidation during an increase in isotropic effective confining pressure from a value P_c^0 to a value P_c:

$$\Delta\varepsilon_1^{clay} = \Delta\varepsilon_2^{clay} = \Delta\varepsilon_3^{clay} = \frac{zB}{2R_c}\ln\left(\frac{P_c}{P_c^0}\right) \quad \text{(Eq. 5.9)}$$

5.5.3 Criterion for the onset of serially coupled, intergranular slip and clay film consolidation

During deviatoric compression at θ = 0° (refer Figure 5.4c), the model geometry dictates that any consolidation of the clays present at contact type B must be accompanied by slip and consolidation of the clay films present at A and C. During deviatoric loading at θ = 30°, consolidation of the clays at A and B requires slip along both of these contacts. Hence, during deviatoric loading at both orientations, consolidation and slip are serially coupled deformation processes, meaning that one process cannot occur without the other. Ignoring cohesion in the clay films, and noting the symmetry of the unit cell at θ = 0°, slip on grain contacts A and C during deviatoric compression at θ = 0° occurs when the criterion for frictional slip is obeyed, *i.e.* when:

$\tilde{\tau}_A = \tilde{\tau}_C = \mu\tilde{\sigma}_A = \mu\tilde{\sigma}_C$ (Eq. 5.10a)

Here, μ is the friction coefficient of illite. Similarly, during deviatoric loading at θ = 30°, A and B slip when:

$\tilde{\tau}_A = \tilde{\tau}_B = \mu\tilde{\sigma}_A = \mu\tilde{\sigma}_B$ (Eq. 5.10b)

Wet shear tests performed on relatively pure (95 vol%) illite "fault gouge" layers at room temperature, an effective normal stress of 40 MPa, and a shear velocity of 1 μm/s have shown that the value of μ is mildly strain dependent, increasing roughly linearly from 0.22 to 0.30 as the shear strain increases from 0.4 to 8.0, likely reflecting hardening due to densification and associated planar fabric development [*Tembe et al.*, 2010]. For present purposes, we use an intermediate μ-value of 0.26, reported by *Tembe et al.*, [2010] at a shear strain of 2.3%. We later discuss to what extent the model behavior changes if a variable, shear strain- or consolidation-strain dependent value of μ is assumed.

At deviatoric stresses where Equations 5.10a and b are not satisfied, *i.e.* where $\tilde{\tau}_x < \mu\tilde{\sigma}_x$, no clay film consolidation and no inelastic deformation of the unit cell can occur, at least until intragranular cracking is activated. Since the elastic response was decoupled from the present inelastic model, the distribution of the stresses acting within the σ_1 - σ_3 plane on the unit cell boundaries and on the grain contacts is not rigorously constrained under these "inelastically rigid" conditions, and is here assumed to be uniform, following *Guéguen and Fortin*, [2013]. This assumption implies an isotropic stress state within the unit cell, such that the normal and shear forces supported on grain contact B are one third of the normal and shear forces supported on the top and bottom of the unit cell, and hence given by $4R_c^2\sigma_{top}/\sqrt{3}$ and $4R_c^2\tau_{top}/\sqrt{3}$, respectively (refer Figure 5.4b). The corresponding stresses are obtained by dividing by the grain contact area (πr^2). Combining these relations with Equations 5.5a and b, we obtain descriptions of $\tilde{\sigma}_B$ and $\tilde{\tau}_B$ as these develop during deviatoric compression prior to slip, in terms of σ_1, σ_3 and θ, yielding:

$$\tilde{\sigma}_B|_{no\ slip} = \frac{2R_c^2}{\sqrt{3}\pi r^2}\left(\sigma_1 + \sigma_3 + (\sigma_1 - \sigma_3)\cos(2\theta)\right) \quad \text{(Eq. 5.11a)}$$

$$\tilde{\tau}_B|_{no\ slip} = \frac{2R_c^2}{\sqrt{3}\pi r^2}\left(\sigma_1 - \sigma_3\right)\sin(2\theta) \quad \text{(Eq. 5.11a)}$$

When $\tilde{\tau}_x < \mu\tilde{\sigma}_x$, the normal and shear stresses acting on A and C can then similarly be described in terms of the applied σ_1, σ_3 and θ, by:

$$\tilde{\sigma}_A|_{no\ slip} = \frac{2R_c^2}{\sqrt{3}\pi r^2}\left(\sigma_1 + \sigma_3 + (\sigma_1 - \sigma_3)\cos(120 - 2\theta)\right) \quad \text{(Eq. 5.11c)}$$

$$\tilde{\tau}_A|_{no\ slip} = \frac{2R_c^2}{\sqrt{3}\pi r^2}\left(\sigma_1 - \sigma_3\right)\sin(120 - 2\theta) \quad \text{(Eq. 5.11d)}$$

$$\tilde{\sigma}_C|_{no\ slip} = \frac{2R_C^2}{\sqrt{3}\pi r^2}\left(\sigma_1 + \sigma_3 + (\sigma_1 - \sigma_3)\cos(120 + 2\theta)\right) \quad \text{(Eq. 5.11e)}$$

$$\tilde{\tau}_C|_{no\ slip} = \frac{2R_C^2}{\sqrt{3}\pi r^2}\left(\sigma_1 - \sigma_3\right)\sin(120 + 2\theta) \quad \text{(Eq. 5.11f)}$$

Note that for the hydrostatic case when $\sigma_1 = \sigma_3 = P_c$, then $\tilde{\tau}_A$, $\tilde{\tau}_B$ and $\tilde{\tau}_C$ are all zero, and the values of $\tilde{\sigma}_A$, $\tilde{\sigma}_B$ and $\tilde{\sigma}_C$ given by Equations 5.11a, c and e are equivalent to those given by Equation 5.8.

At $\theta = 0°$, intergranular slip on A and C, and accompanying serial consolidation at A, B and C occurs when $\tilde{\tau}_A|_{no\ slip} = \tilde{\tau}_C|_{no\ slip}$ satisfy the criterion given in Equation 5.10a. Hence, for this orientation, the criterion of serially coupled intergranular slip plus consolidation is obtained by inserting Equations 5.11c-f into Equation 5.10a, which gives:

$$\sigma_1^{slip}\big|_{(\theta = 0°)} = \sigma_3\left(\frac{\sqrt{3}+3\mu}{\sqrt{3}-\mu}\right) \quad \text{(Eq. 5.12a)}$$

Similarly, inserting Equations 5.11a-d into Equation 5.10b gives the criterion for slip on and serial consolidation at A and B when $\theta = 30°$:

$$\sigma_1^{slip}\big|_{(\theta = 30°)} = \sigma_3\left(\frac{\sqrt{3}+\mu}{\sqrt{3}-3\mu}\right) \quad \text{(Eq. 5.12b)}$$

For values of μ in the range of 0 to $1/\sqrt{3}$ (≈ 0.58), including the presently assumed value of 0.26, Equations 5.12a and b show that $\sigma_1^{slip}\big|_{(\theta = 0°)} < \sigma_1^{slip}\big|_{(\theta = 30°)}$, indicating that for these values of μ, slip plus consolidation is easier at $\theta = 0°$, than it is at $\theta = 30°$, provided that consolidation is the easier serial step. The inelastic strains developing by these processes at $\theta = 0°$ will dominate over the corresponding strain contributions at $\theta = 30°$, as these develop earlier in the former orientation. Therefore, we will focus on describing the stress-strain behavior associated with serially coupled consolidation and slip at $\theta = 0°$ only.

5.5.4 Deviatoric stress vs. strain behavior due to serially coupled consolidation and slip at $\theta = 0°$

When the vertical stress σ_1 applied during deviatoric compression at $\theta = 0°$ exceeds

$\sigma_1^{slip}\big|_{(\theta = 0°)}$ (see Equation 5.12a), the unit cell deforms by slip and consolidation of A and C, and by consolidation of B. The normal stress acting on B is then obtained by combining Equations 5.5a, 5.5b, 5.6a, 5.6c and 5.10a, which gives:

$$\tilde{\sigma}_B|_{slipAC} = \frac{2R_c^2}{\pi r^2}\left(\sqrt{3}\sigma_1 - \left(\frac{1-\mu\sqrt{3}}{\sqrt{3}+\mu}\right)\sigma_3\right) \qquad \text{(Eq. 5.13)}$$

Note that during deviatoric compression at constant σ_3, $\tilde{\sigma}_B$ is larger during slip and consolidation of A and C (Equation 5.13), than it is when A and C do not slip and consolidate (Equation 5.11a).

With reference to Figure 5.4c, the kinematic constraints imposed by the unit cell geometry at $\theta = 0°$ require that the inelastic normal strains developing due to consolidation of the clay films at A, B and C due to consolidation are related to the vertical principal strain (ε_1) and the horizontal principal strain (ε_3) via:

$$\tilde{\varepsilon}_B^{clay} = \frac{2R_c}{z}\,\varepsilon_1 \qquad \text{(Eq. 5.14a)}$$

$$\tilde{\varepsilon}_A^{clay} = \tilde{\varepsilon}_C^{clay} = \frac{R_c}{2z}\varepsilon_1 + \frac{3R_c}{2z}\varepsilon_3 \qquad \text{(Eq. 5.14b)}$$

In turn, Equation 5.7 can be employed to evaluate the magnitudes of $\tilde{\varepsilon}_A^{clay}$, $\tilde{\varepsilon}_B^{clay}$ and $\tilde{\varepsilon}_C^{clay}$ developing during deviatoric compression, in terms of the corresponding normal contact stress ($\tilde{\sigma}_A$, $\tilde{\sigma}_B$ or $\tilde{\sigma}_C$). This is best done by normalizing the contact stresses with respect to a reference contact stress ($\tilde{\sigma}_h$) acting on grain contacts A, B and C at hydrostatic conditions ($\sigma_i = P_c$) before the onset of deviatoric compression. Hence, $\tilde{\sigma}_h$ is equal to $\tilde{\sigma}_A = \tilde{\sigma}_B = \tilde{\sigma}_C$ at the $\sigma_1 = \sigma_2 = \sigma_3 = P_c$ conditions applied before deviatoric loading, and is given $\tilde{\sigma}_h = \frac{4R_c^2}{\sqrt{3}\pi r^2}\sigma_3$ (*cf.* Equation 5.8). Replacing the initial reference stress $\tilde{\sigma}_0$ used in Equation 5.7 by $\tilde{\sigma}_h$, and by combining this equation with Equations 5.14a, 5.14b, and subsequently with Equations 5.5a, 5.5b, 5.6a, 5.6c and 5.10a, we obtain relations describing the changes in maximum and minimum principal inelastic strains ($\Delta\varepsilon_1$ and $\Delta\varepsilon_3$), occurring in the unit cell in response to increasing σ_1 up to and beyond $\sigma_1^{slip}\big|_{(\theta = 0°)}$. The result obtained for serially coupled slip

plus consolidation at θ = 0°, is given:

$$\Delta\varepsilon_1 = \frac{zB}{2R_c}\ln\left(\frac{3\sigma_1}{2\sigma_3} - \frac{\sqrt{3}+3\mu}{2(\sqrt{3}-\mu)}\right) \quad \text{(Eq. 5.15a)}$$

and:

$$\Delta\varepsilon_3 = \frac{zB}{6R_c}\left(4\ln\left(\frac{\sqrt{3}}{(\sqrt{3}-\mu)}\right) - \ln\left(\frac{3\sigma_1}{2\sigma_3} - \frac{\sqrt{3}+3\mu}{2(\sqrt{3}-\mu)}\right)\right) \quad \text{(Eq. 5.15b)}$$

where $\Delta\varepsilon_1$ and $\Delta\varepsilon_3$ are measured relative to the hydrostatic reference state $\sigma_i = P_c$.

5.5.5 Effect of θ on the onset of dilation

For deviatoric loading at θ = 0°, the granular unit cell microstructure cannot dilate (*e.g.* compare Figures 5.3b and 5.4c). By contrast, deviatoric compression at θ = 30° may lead to dilation, with slip on A and B causing opening of grain contact C (Figure 5.6a, *cf.* Figure 5.3b). This occurs when the normal stress acting on C ($\tilde{\sigma}_C$) is reduced to zero, or perhaps to a small, negative (tensile) value corresponding to the tensile strength of the intergranular clay films. For deviatoric stresses driving slip and consolidation of A and B at θ = 30° (*i.e.* those satisfying Equation 5.12b), the normal stress acting on C is obtained by combining Equations 5.5a-c, Equations 5.6a-d and Equation 5.10b. This gives:

$$\tilde{\sigma}_C = \frac{2R_c^2}{\pi r^2}\left(\sqrt{3}\sigma_3 - \left(\frac{1-\mu\sqrt{3}}{\sqrt{3}+\mu}\right)\sigma_1\right) \quad \text{(Eq. 5.16)}$$

Ignoring any tensile strength of the intergranular illite, and setting $\tilde{\sigma}_C$ = 0 in accordance with the onset of dilatation caused by slip on A and B, plus opening of C now yields the following dilation criterion for θ = 30°:

$$\sigma_1^{dil}\big|_{(\theta = 30°)} = \frac{3+\sqrt{3}\mu}{1-\sqrt{3}\mu}\sigma_3 \quad \text{(Eq. 5.17)}$$

For our chosen value of μ = 0.26, this equation reduces to: $\sigma_1^{dil}\big|_{(\theta = 30°)} \approx 6.3\sigma_3$. The stress conditions at which dilation is easiest at given μ can be more generally considered for θ in

the range between 0 and 30°, by considering opening of C due to slip on A only (Figure 5.6b). For the contact stresses corresponding to this scenario, *i.e.* for $\tilde{\tau}_A = \mu\tilde{\sigma}_A$, $\tilde{\sigma}_C = 0$ and $\tilde{\tau}_C = 0$, Equations 5.6a-d deliver the criterion for the onset of dilation due to slip on A only, plus opening of C, for $0 < \theta \leq 30°$:

$$\sigma_1^{dil}\big|_{(0<\theta\leq 30°)} = \sigma_3 \frac{1+\sqrt{3}\mu+(1+\sqrt{3}\mu)\cos(2\theta)+(\sqrt{3}-\mu)\sin(2\theta)}{-1-\sqrt{3}\mu+(1+\sqrt{3}\mu)\cos(2\theta)+(\sqrt{3}-\mu)\sin(2\theta)} \qquad \text{(Eq. 5.18)}$$

Note that for $\theta = 30°$, $\sigma_1^{dil}\big|_{(0<\theta\leq 30°)} \equiv \sigma_1^{dil}\big|_{(\theta=30°)}$. For $\mu = 0.26$, differentiation of Equation 5.18 with respect to θ, to obtain the minimum value of σ_1^{dil}, demonstrates that dilation is easiest at $\theta = 23°$, with $\sigma_1^{dil}\big|_{(\theta=23°)} \approx 5.7\sigma_3$. Hence, this orientation is most favorable for slip-coupled dilation in our model, such that Equation 5.18 and $\theta = 23°$ will be used in subsequent model integration (Section 5.8) to describe the onset of dilation.

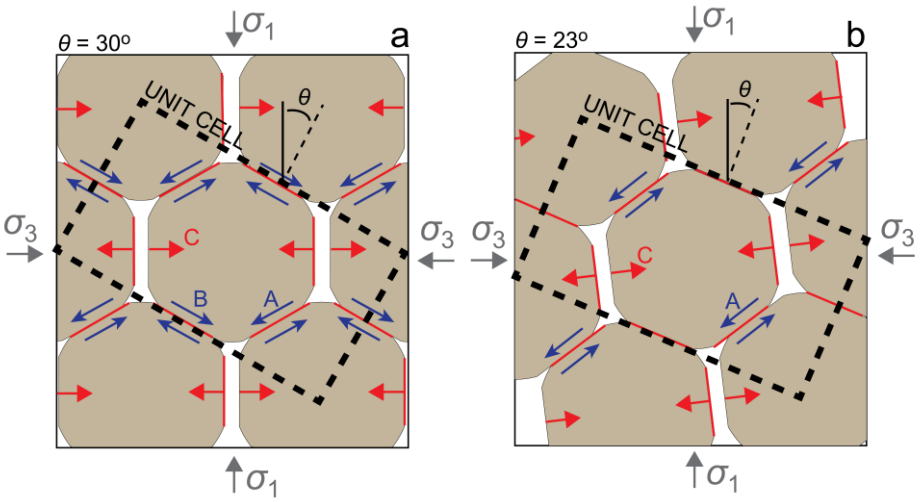

Figure 5.6 Diagrams illustrating the mode of failure at the onset of dilation (Stage 3d) when σ_1 acts at an angle θ of **a)** 30°; and **b)** 23° to the top of the unit cell. Dilation is easiest in the latter orientation, for a grain contact clay film friction coefficient μ of 0.26.

5.6 Inelastic deformation mechanism 2: Intragranular splitting

We now derive descriptions of the stress conditions and the instantaneous strain increment associated with the onset of intragranular cracking (Figure 5.7a; see also: Figure 5.3c), which in our experiments (Chapter 3; *Pijnenburg et al.*, 2019) was assumed to mark the end of Stage 2 and the onset of Stage 3c.

5.6.1 Assumed grain contact properties and behavior at the onset of Stage 3c

As a first approximation, we base this analysis on the following assumptions and simplifications:

1) Pre-existing stress concentrators and flaws are assumed present at the micro-scale within the flat grain contacts featured in our microstructural model. In 2D, (*i.e.* in the σ_1 and σ_3 plane) these flaws have a characteristic mean spacing (d) of 3 μm (Table 5.2), corresponding to the typical wavelength of grain contact asperities and irregularities from which intragranular cracks were observed to emanate in our experiments (Figure 5.2i).
2) Since the amplitude of grain contact asperities seen in the Slochteren sandstones is small (< 1 % of the grain diameter), the above grain contact roughness and flaw distribution is assumed to have negligible influence on the state of stress in the bulk of the grain, and that the average grain contact stresses are sufficiently well-described in terms of total traction acting over the presently assumed, flat grain contact geometry.
3) The criterion for propagation of grain contact flaws as cracks traversing the full grain diameter is assumed to be controlled by the normal stress ($\tilde{\sigma}$) supported on grain contacts, in line with the particle splitting model of *Kendall*, [1978], as applied to grain failure/cracking by *Sammis and Ben-Zion*, [2008]. Any effect of the grain contact shear stress ($\tilde{\tau}$) is to be negligible, as is any effect of lateral (confining) stresses acting normal to the crack propagation direction. The latter assumption is based on the notion that crack opening will preferentially occur towards unloaded pore walls (*cf*. Figure 5.2j – red arrow).
4) Since the highest normal load will be supported on grain contacts oriented perpendicular to σ_1, intragranular cracking will generally be easiest at grain contact B when θ = 0°. Therefore, intragranular cracking is evaluated for this orientation only.

5) We ignore the anisotropy implied by the stacked, 2-D model geometry (see Section 5.2). Hence, during hydrostatic compression, $\tilde{\sigma}_D$ is taken to be equal to $\tilde{\sigma}_A$, $\tilde{\sigma}_B$ and $\tilde{\sigma}_C$, thus being described by Equation 5.8a.

We note that excluding an effect of a lateral confining stress (assumption 3) effectively means that we only consider intragranular cracking in grains that are not loaded by other grains in at least one direction, which may lie out of the $\sigma_1 - \sigma_3$ plane. In this sense, the crack opening represented in Figure 5.7a is schematic. Micrographs of our experimentally deformed samples indeed show that intragranular cracks open more readily towards open pore spaces (Figure 5.2j – red arrow), while remaining closed in more densely packed parts of the microstructure (Figure 5.2j – white arrow). Still, assumption 3 is likely only reasonable at earlier stages of intagranular cracking (early Stage 3c).

5.6.2 Grain splitting criterion at the grain-scale

Kendall [1978] developed a criterion for meridional, mode I crack propagation of an incipient crack present at the narrow, flat end of a prismatic-shaped grain. The normal grain contact force (F^*) required for such crack propagation is given:

$$F^* = \frac{b}{1-\frac{w}{D}}\sqrt{2/3\, E_q Y D} \qquad \text{(Eq. 5.19)}$$

where E_q is the Young's modulus of the grain, Y is the fracture energy, D and b are the width and depth of the cross-section of the thick part of the grain, respectively and w is the width of the rectangular contact region. We take E_q to be equal to 95 GPa for quartz grains [*cf. Wong and Wu*, 1995], while Y is taken to be 5 J/m^2 (Table 5.2), which lies midway in the experimentally obtained range of 0.1 to 11.5 J/m^2 reported for quartz by *Atkinson and Meredith*, [1984]. Equation 5.19 is applied to the truncated spherical grains represented in our model microstructure, taking $D \approx 2R$, $b \approx 2R_c$ and $w \approx 2r$. We thus obtain the following expression for the effective normal contact stress ($\tilde{\sigma}^*$) required for mode I, meridional crack propagation from a flaw near the grain contact center:

$$\tilde{\sigma}^* \approx \frac{4R_c\sqrt{E_q Y R}}{\sqrt{3}\pi r^2\left(1-\frac{r}{R}\right)} \qquad \text{(Eq. 5.20)}$$

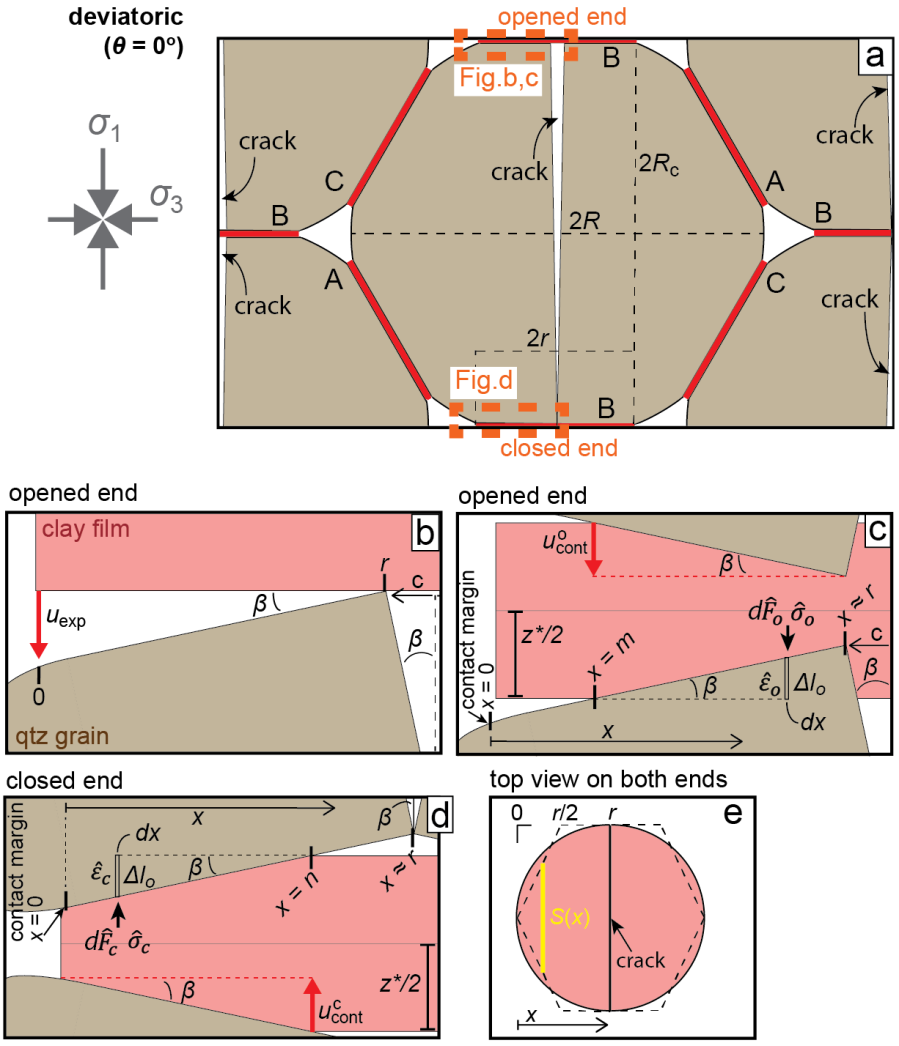

Figure 5.7 Diagrams illustrating the geometry and geometrical parameters considered in our analysis of the inelastic strain increment associated with intragranular splitting. **a)** During deviatoric compression, splitting at grain contacts B leads to transgranular cracking normal to these contacts. Crack opening is schematically represented here as occurring normal to σ_3, but will in reality occur towards open pores (see: Figure 5.2j – red arrow). Note the wedge-shaped opening defined by each intragranular crack; **b)** On the one hand, such opening causes expansion (u_{exp}) at the quartz-clay interface. On the other hand, it leads to contractions of the clay films present at: **c)** the opened end of the crack (u^o_{cont}); and at: **d)** the closed end of the crack (u^c_{cont}). The factors used in obtaining these contractions are indicated. **e)** Top view on contact B at either end of the crack. By approximating the circular grain contact to be hexagonally shaped, the crack-parallel, grain contact width (L) is simplified to a bi-linear function of the distance towards the crack (x).

5.6.3 Grain splitting criterion in terms of stresses at the unit cell scale

During deviatoric compression at θ = 0°, prior to slip on A and C $\left(\sigma_1 < \sigma_1^{slip}\big|_{(\theta = 0°)}\right)$, the vertical stress ($\sigma_1^*|_{no\ slip}$) required for intragranular crack propagation at grain contact B (*i.e.* when $\tilde{\sigma}_B = \tilde{\sigma}^*$) is obtained by combining Equations 5.11a and 5.20, which gives:

$$\sigma_1^*|_{no\ slip} = \frac{\sqrt{E_q Y R}}{R_c\left(1-\frac{r}{R}\right)} \qquad \text{(Eq. 5.21a)}$$

Note that for hydrostatic compression, the confining pressure (P_c^*) required for splitting of grain contacts A, B, C and/or D is equivalent to σ_1^*. At deviatoric stresses driving slip on A and C and consolidation on A, B and C $\left(\sigma_1 \geq \sigma_1^{slip}\big|_{(\theta = 0°)}\right)$, the vertical stress ($\sigma_1^*|_{slipAC}$) required for intragranular cracking at grain contact B is obtained by combining Equations 5.13 and 5.20. This gives:

$$\sigma_1^*|_{slipAC} = \frac{2\sqrt{E_q Y R}}{3R_c(1-\frac{r}{R})} + \frac{1+\sqrt{3}\mu}{3-\sqrt{3}\mu}\sigma_3 \qquad \text{(Eq. 5.21b)}$$

5.6.4 Strain due to grain splitting

5.6.4.1 Model development

When either one of the above criteria for grain splitting is reached, transgranular cracks are produced. In the deviatoric case, these cracks propagate diametrically from B to B (see schematic Figure 5.7a), in reality opening preferentially towards open pore space (*cf.* Figure 5.2j- red arrow). In the hydrostatic case, all grain contact types (*i.e.* A, B, C and D) are equally stressed, while transgranular cracks will form normal to any one pair of grain contacts of the unit cell, *i.e.* normal to A, B, C or D, assuming that one of these fails slightly earlier than the others. Here, we explore the magnitude of crack opening (2*c*) for the deviatoric case, the strain increment that may develop because of it, and the effect it has on the subsequent loading behavior and intragranular crack evolution. The hydrostatic scenario can be evaluated in a similar way, as will be briefly shown at the end of this section.

The assumed geometry of crack opening, and the geometrical factors considered in our analysis are defined in Figures 5.7b-e. On the one hand, crack opening by an amount 2*c* (*c* = half opening) will cause vertical expansion (u_{exp}) normal to the failing contact by

opening space between the contact and the overlying clay film (Figure 5.7b). This expansion is given by: u_{exp}= -sin(β)r = -cr/(2R_c) (Figure 5.7b). On the other hand, vertical contraction occurs, at the same site, due to indentation of the split grain halves into the overlying clay films, as seen in micrographs of lab-deformed, Slochteren sandstone (Figure 5.2k). At the opened end of the crack (Figure 5.7c), this contraction is given by: u^o_{cont} = sin(β)(r - m). At the opposite (closed) end of the crack (Figure 5.7d), indentation of the tilted contact margin into the contact clay film yields a contraction: u^c_{cont} = sin(β)n. The net contraction (u_{net}) parallel to a single meridional crack, due to its opening, is then the sum of these contraction and expansion effects, given: $u_{net} = u^o_{cont} + u^c_{cont} + u_{exp}$, or: $u_{net} = \frac{c}{2R_c}(n-m)$. In the limit of small c, the resultant vertical strain increment of the unit cell can hence be written as

$$d\varepsilon_1^{cr,s} = \frac{c(n-m)}{4R_c^2} \qquad \text{(Eq. 5.22)}$$

Since intragranular splitting is considered for laterally unconfined grains (see Section 5.6.1), opening will not induce any lateral strains, so that $d\varepsilon_3^{cr,s}$ = 0.

The values of c, m and n in Equation 5.22 are found by balancing the forces supported by the grain contacts at both ends of the crack prior to opening, versus those supported after opening, *i.e*. by the portions of the clay contact films that are indented by the split grain halves. The locally increased clay film consolidation strains implied by the indentations shown at both the opened and closed cracks ends in Figures 5.7c and 5.7d are additive to the reference consolidation strain accumulated in the clay films at the B contacts up to the point of intragranular splitting. This reference strain is given: $\tilde{\varepsilon}^*$ = $B\ln(\tilde{\sigma}^*/\tilde{\sigma}_h)$, while the corresponding reference clay film thickness is: z^* = z(1 - $\tilde{\varepsilon}^*$). Assuming crack opening is symmetric on both sides of each failing grain contact, only half of the clay film thickness is indented on each side (*i.e*. $z^*/2$ – see Figures 5.7c and d). At the opening end of the crack, the contraction of the half clay film at a distance x from the contact margin is: $\Delta l_o(x)$ = (x-m) sin(β) (Figure 5.7c). This implies that at this end, the increase in normal strain ($\hat{\varepsilon}_o(x)$) within the half film at location x is given:

$$\hat{\varepsilon}_o(x) = \frac{\Delta l_0(x)}{z^*/2} = \frac{(x-m)\sin(\beta)}{z^*/2} = \frac{c(x-m)}{R_c z^*} \qquad \text{(Eq. 5.23a)}$$

Similarly, at the closed end of the crack, the increase in normal strain in the half clay film at

distance *x* from the contact margin is:

$$\hat{\varepsilon}_c(x) = \frac{c(n-x)}{R_c z^*} \quad \text{(Eq. 5.23b)}$$

Combining Equations 5.23a and 5.23b with Equation 5.7, and inserting $\tilde{\sigma}^* \approx \frac{4R_c\sqrt{E_q Y R}}{\sqrt{3}\pi r^2\left(1-\frac{r}{R}\right)}$ (*cf.* Equation 5.20) as the reference normal contact stress $\tilde{\sigma}_0$, we obtain the grain contact normal stresses supported by the clay films present at the opened ($\hat{\sigma}_o(x)$) and closed ends ($\hat{\sigma}_c(x)$) of the crack, as a function of *x*:

$$\hat{\sigma}_o(x) = \tilde{\sigma}^* \exp\left(\frac{c(x-m)}{BR_c z^*}\right) \quad \text{(Eq. 5.24a)}$$

$$\hat{\sigma}_c(x) = \tilde{\sigma}^* \exp\left(\frac{c(n-x)}{BR_c z^*}\right) \quad \text{(Eq. 5.24b)}$$

In the clay film present at the opened end of the crack, the normal force acting on a constant element *dx*, at position *x* is given: $d\hat{F}_o(x) = S(x)\,\hat{\sigma}_o(x)dx$. Here, *S*(*x*) is the crack-parallel width of the circular grain contact, at *x* (see Figure 5.7e). At the closed end, the normal force contribution at *x* is $d\hat{F}_c(x) = S(x)\,\hat{\sigma}_c(x)dx$. The normal force ($\tilde{\sigma}^*\pi r^2$) supported on grain contact B upon splitting must be equal to the force supported after opening, given the assumed microstructure. At the opening end of the crack (Figure 5.7c), this force balance means:

$$\tilde{\sigma}^*\pi r^2 = 2\int_m^r S(x)\,\hat{\sigma}_o(x)dx \quad \text{(Eq. 5.25a)}$$

while at the closed end (Figure 5.7d), we obtain:

$$\tilde{\sigma}^*\pi r^2 = 2\int_0^n S(x)\,\hat{\sigma}_c(x)dx \quad \text{(Eq. 5.25b)}$$

For easy integration, we approximate the circular grain contact area as being hexagonally shaped (see Figure 5.7e), such that for $x \leq r/2$, then $S(x) = 4x$, while for $r/2 < x \leq r$, $S(x) = 2r$. The hexagonal area is similar to the circular solution within 5%. The description of *S*(*x*) in Equations 5.25a and b thus depends on whether *m* and *n* are larger or smaller than *r*/2, *e.g.* if $0 < m < r/2$, then *S*(*x*) is equal to 4*x* within the bounds of $m \leq x < r/2$, and to 2*r* when $r/2 \leq x$

$< r$. If $m \geq r/2$, then $S(x) = 2r$. For the opened end of the crack, we will assume, for now, that $0 < m \leq r/2$ (see Figure 5.7e). Later calculations demonstrate that this is indeed the case. The force balance for the grain contact at the open end of the crack is then obtained by inserting Equation 5.24a along with the two simplified descriptions given above for $S(x)$, into Equation 5.25a, which gives:

$$\tilde{\sigma}^* \pi r^2 = 2\tilde{\sigma}^* \left[\int_m^{r/2} 4x \ \exp\left(\frac{c(x-m)}{BR_c z^*}\right) dx + \int_{r/2}^{r} 2r \ \exp\left(\frac{c(x-m)}{BR_c z^*}\right) dx \right] \qquad \text{(Eq. 5.26a)}$$

where the first integral term represents the force contribution within the bounds of $m \leq x < r/2$, and the second integral term represents the force contribution along $r/2 \leq x < r$. After integration, we obtain:

$$1 = \frac{4z^* R_c B}{c\pi r^2} \left[\frac{2z^* R_c B}{c} \left(1 - \exp\left(\frac{c(r/2-m)}{BR_c z^*}\right)\right) + r \exp\left(\frac{c(r-m)}{BR_c z^*}\right) - 2m \right] \qquad \text{(Eq. 5.26b)}$$

Similarly, assuming that at the closed end of the crack, $r/2 \leq n < r$, and inserting Equation 5.24b and the above two simplified descriptions of $S(x)$ into Equation 5.25b leads to:

$$\tilde{\sigma}^* \pi r^2 = 2\tilde{\sigma}^* \left[\int_0^{r/2} 4x \ \exp\left(\frac{c(n-x)}{BR_c z^*}\right) dx + \int_{r/2}^{n} 2r \ \exp\left(\frac{c(n-x)}{BR_c z^*}\right) dx \right] \qquad \text{(Eq. 5.27a)}$$

which on integration gives:

$$1 = \frac{4z^* R_c B \ \tilde{\sigma}^*}{c\pi r^2} \left[\frac{2z^* R_c B}{c} \left(\exp\left(\frac{cn}{BR_c z^*}\right) - \exp\left(\frac{c(n-r/2)}{BR_c z^*}\right)\right) - r \right] \qquad \text{(Eq. 5.27b)}$$

Equations 5.26b and 5.27b can be numerically solved to yield the values of m and n, corresponding to an arbitrary half crack opening c. An additional constraint is provided by the fact that c, and the corresponding values of m and n, must be such that the total external work increment per unit volume (dW_{ext}) done through deforming the unit cell by intragranular splitting is approximately equal to the internal work increment per unit volume (dW_{int}) done (dissipated) by indenting all B-type clay films within the cell upon crack opening, *i.e.* assuming that the energy required to create new crack surface is provided by elastic energy released as described by the Kendall criterion [*Kendall*, 1978]. For the

presently considered, deviatoric case with zero $d\varepsilon_3^{cr,s}$, dW_{ext} is given:

$$dW_{ext} = d\varepsilon_1^{cr,s}\sigma_1^* \qquad \text{(Eq. 5.28)}$$

At the opened end of the crack (Figure 5.7c), the work done to achieve clay indentation over a clay film strip of width dx (length $S(x)$), at location x is given by the product of the local force acting on this strip at x (*i.e.* $S(x)\,\hat{\sigma}_o(x)dx$), and the corresponding indentation displacement ($\Delta l_o(x) = \hat{\varepsilon}_o(x)(z^*/2)$), *i.e.* by the product: $dT_o = \left[\hat{\varepsilon}_o(x)\left(\frac{z^*}{2}\right)S(x)\hat{\sigma}_o(x)dx\right]$. Similarly, at the closed end of the crack (Figure 5.7d), the work done by clay indentation at location x is given: $dT_c = \left[\hat{\varepsilon}_c(x)\left(\frac{z^*}{2}\right)S(x)\,\hat{\sigma}_c(x)dx\right]$. Recalling that two intragranular cracks are formed in each unit cell (Figure 5.7a), each indenting the clay on both sides, and at both ends, the corresponding internal work per unit volume dW_{int} is given:

$$dW_{int} = \frac{1}{8\sqrt{3}R_c^3}\left(4\int_m^r dT_0 + 4\int_0^n dT_c\right)$$

$$= \frac{1}{2\sqrt{3}R_c^3}\left(\int_m^r \hat{\varepsilon}_o(x)(z^*/2)S(x)\hat{\sigma}_o(x)dx + \int_0^n \hat{\varepsilon}_c(x)(z^*/2)S(x)\,\hat{\sigma}_c(x)dx\right) \qquad \text{(Eq. 5.29a)}$$

Here, $8\sqrt{3}R_c^3$ is the volume of the unit cell, while the first and second integral terms reflect the internal work contributions due to indentation of the clay films at the opening and closed ends of the two cracks, respectively. Inserting Equations 5.23a, 5.23b, 5.24a and 5.24b and the relations given above for $S(x)$, in Equation 5.29a, and integrating over x gives:

$$dW_{int} = \frac{(z^*B)^2\sigma^*}{c\sqrt{3}R_c^2}\left[\exp\left(\frac{c(r/2-m)}{z^*R_cB}\right)\left(\frac{2m-r}{2}+\frac{2z^*BR_c}{c}\right)+\exp\left(\frac{c(r-m)}{z^*R_cB}\right)\left(\frac{c(r^2-rm)}{2z^*R_cB}-\frac{r}{2}\right)+m-\right.$$

$$\left.\frac{2z^*BR_c}{c}+\exp\left(\frac{c\left(n-\frac{r}{2}\right)}{z^*R_cB}\right)\left(\frac{2z^*BR_c}{c}-n+\frac{r}{2}\right)+\frac{r}{2}+\exp\left(\frac{cn}{z^*R_cB}\right)\left(n-\frac{2z^*BR_c}{c}\right)\right] \qquad \text{(Eq. 5.29b)}$$

For the hydrostatic case, transgranular cracks may form normal to any pair of the contact types A, B, C or D, all of which are equally likely to fail. The external and internal work increments per unit volume associated with crack opening plus indentation at A, C and D will be the same to the corresponding work increments associated with failure of B described above, while the orientation of the strain increments developing in the unit cell due

to cracking will depend on which of the contacts fail. Assuming that at the sample scale, all contacts fail at roughly equal proportions, the average, principal, inelastic strain increments $d\varepsilon_i^{cr,s}$ (i = 1,2,3), developing during hydrostatic compression are approximately uniform, and each ~equal to a third of the vertical strain increment given for the deviatoric case by Equation 5.22.

5.6.4.2 Model implementation to estimate strain magnitude associated with grain splitting

We now briefly apply the above equations to the case of deviatoric loading at an effective confining pressure of 40 MPa, to explore whether our analysis implies realistic magnitudes of crack opening (2c), and what increments in vertical strain ($d\varepsilon_1^{cr,s}$) should be associated with such opening. We first employ Equations 5.26b, 5.27b, 5.28 and 5.29b, to numerically yield the values of m, n, dW_{ext} and dW_{int} corresponding to a range of c values between 10 nm and 10 µm. We use the input parameters corresponding to initial porosities of 13.4%, 21.5% and 26.4%, listed in Table 5.2. For these initial porosities, the values obtained for half opening c, at which the external and internal work increments per unit volume are balanced ($dW_{ext} = dW_{int}$) yield 0.1, 0.3 and 0.5 µm, respectively. These values of c imply maximum crack openings ($2c$) between 0.2 to 1.0 µm, which are similar, although perhaps on the low side, of the crack openings typically seen in micrographs (0.1 to 10 µm; Figure 5.2h-k). The corresponding, splitting induced, vertical strain increments ($d\varepsilon_1^{cr,s}$) ranged between 0.01 and 0.03%, being again higher with increasing porosity. We further test whether the values calculated for the indentation limits m and n indeed fall within the ranges of $0 < m < r/2$, and $r/2 \leq n < r$, as previously assumed in deriving Equations 5.26a, 5.26b, 5.27a and 5.27b. For the full range in stress changes considered here, *i.e.* for deviatoric compression at P_c = 5 to 80 MPa and for hydrostatic compression up to P_c^*, the obtained magnitude of m always fell in between 0 to $r/2$, while the resultant values of n ranged between $r/2$ and r. This validates the previously assumed bounds on m and n. Based on these results, we infer that our analysis of the inelastic strain associated with grain splitting, as outlined in Section 5.6.4.1, leads to representative magnitudes of crack opening, and hence of the strain increments developing because of it.

5.7 Inelastic deformation mechanism 3: Progressive multi-edge cracking of split grains

Micrographs show that cracked grains often host multiple, intragranular cracks, oriented roughly parallel, or convergent to one another (Figure 5.2h). The stress-strain behavior, and the associated microstructural evolution following the formation of the initial split will depend on the boundary conditions imposed. At constant strain rate, the increase in strain due to initial intragranular splitting ($d\varepsilon_1^{cr,s}$ -see Section 5.6.4) will lead to a drop in the stress carried by the unit cell. At a constant loading rate, the subsequent behavior hinges on the capacity of the loading system to adjust to the instantaneous increase in strain, *i.e.* it depends on the stiffness of the sandstone plus loading system. For the purpose of giving a rough estimate of the strain that would develop upon intragranular cracking in our model for clay-bearing sandstone, we will assume that the stress acting on the unit cell upon initial splitting at $\theta = 0°$ remains constant.

5.7.1 Criterion for edge cracking

For given contact stress (*e.g.* at B in the $\theta = 0°$ configuration), the normal stresses acting around a newly formed, meridional crack will be elevated where the clay film is indented the most, notably around the opened crack end (Figure 5.7c), and near the grain contact periphery at the closed end (Figure 5.7d). Near the grain contact periphery at the closed end, the elevated contact stress lead to elastic compression within the bulky volumes constituting the sides of the split grain, and are otherwise likely of little effect. However, at the opened end, the normal stress ($\tilde{\sigma}_{edge}$; Figures 5.8a,b) acting on the most uplifted edge (area: $S(x)d$) within one flaw spacing (d) of the initial meridional crack will be strongly enhanced and will tend to extend the first neighboring contact flaws to produce an edge crack running parallel to the initial crack surface [*Lawn*, 1993; *Tada et al.*, 2000]. An estimate of the enhanced edge stress ($\tilde{\sigma}_{edge}$) acting over an edge width d is obtained by subtracting the normal force acting on one split grain contact half between $m < x < r-d$, from the nominal force supported by the full grain contact half (*i.e.* $1/2\ \tilde{\sigma}_B\ \pi r^2$). Using the approximate relations for $S(x)$ outlined in the previous section, an expression for the normal stress acting on the most uplifted edge ($\tilde{\sigma}_{edge}$) alongside the opened end of the meridional crack can hence be written as:

$$\tilde{\sigma}_{edge} = \frac{1}{2rd}\left[\frac{\tilde{\sigma}_B\,\pi r^2}{2} - \sigma^* \int_m^{r/2} 4x\ exp\left(\frac{c(x-m)}{z^* R_c B}\right) dx - \sigma^* \int_{r/2}^{r-d} 2r\ exp\left(\frac{c(x-m)}{z^* R_c B}\right) dx\right]$$

(Eq. 5.30a)

which after integration yields:

$$\tilde{\sigma}_{edge} = \frac{1}{2rd}\left[\frac{\tilde{\sigma}_B\,\pi r^2}{2} - \frac{2\sigma^* z^* R_c B}{c}\left(\frac{2z^* R_c B}{c}\left(1 - \exp\left(\frac{c(r/2-m)}{z^* R_c B}\right)\right) + r\exp\left(\frac{c(r-d-m)}{z^* R_c B}\right) - 2m\right)\right] \quad \text{(Eq. 5.30b)}$$

Here, c and m can be obtained at given stress conditions, grain size and porosity by following the approach outlined in Section 5.6.4. Mode I edge crack propagation occurs from the first pre-existing flaw adjacent to the meridional crack, when $\tilde{\sigma}_{edge}$ reaches or exceeds a critical value $\tilde{\sigma}^*_{edge}$, described by [*Thouless et al.*, 1987]:

$$\tilde{\sigma}^*_{\mathrm{edge}} = 0.87\,\frac{K_{Ic}}{\sqrt{d}} = 1.23\sqrt{\frac{YE_q}{d}} \quad \text{(Eq. 5.31)}$$

Here, K_{Ic} is the Griffith critical stress intensity for mode I crack propagation. For the E_q, Y and d values listed in Table 5.2, $\tilde{\sigma}^*_{edge}$ = 489 MPa. For the values of c and m implied by the analysis of Section 5.6.4, for the porosities and input parameter values listed in Table 5.2, and at vertical stress conditions (σ_1^*) corresponding to initial, intragranular splitting during deviatoric loading at P_c between 5 and 80 MPa, or at confining pressures (P_c^*) associated with splitting during hydrostatic loading, Equation 5.30b yields values of $\tilde{\sigma}_{edge}$ in the range of 480 and 928 MPa, being higher with increasing P_c and porosity. Hence, for virtually all presently considered porosities and stresses, the value of $\tilde{\sigma}_{edge}$ obtained upon opening of the initial, intragranular split exceeds the critical value $\tilde{\sigma}^*_{edge}$, implying that initial meridional splitting and crack opening is spontaneously followed by edge cracking, at assumed constant stress.

5.7.2 Strain increment associated with multi-edge cracking

Once $\sigma_{edge} = \sigma^*_{edge}$ is met (at θ = 0°), the two grain slices located on both sides of the initial split between r-$d < x < r$ will break off (Figure 5.8c) and be displaced into the gaps opened by the initial, intragranular split, notably the opened split itself, and the gap present at the closed end of the split (Figure 5.8a). If the broken-off slices do not sufficiently fill this gap, they will not support load. At constant stress, this would imply that the remaining portions of the split grain halves indent further into the clay to compensate for the reduced load-supporting area (Figure 5.8c). At fixed applied stress, the portions of the split grains that then indent into the clay film will support the same force as those indenting it

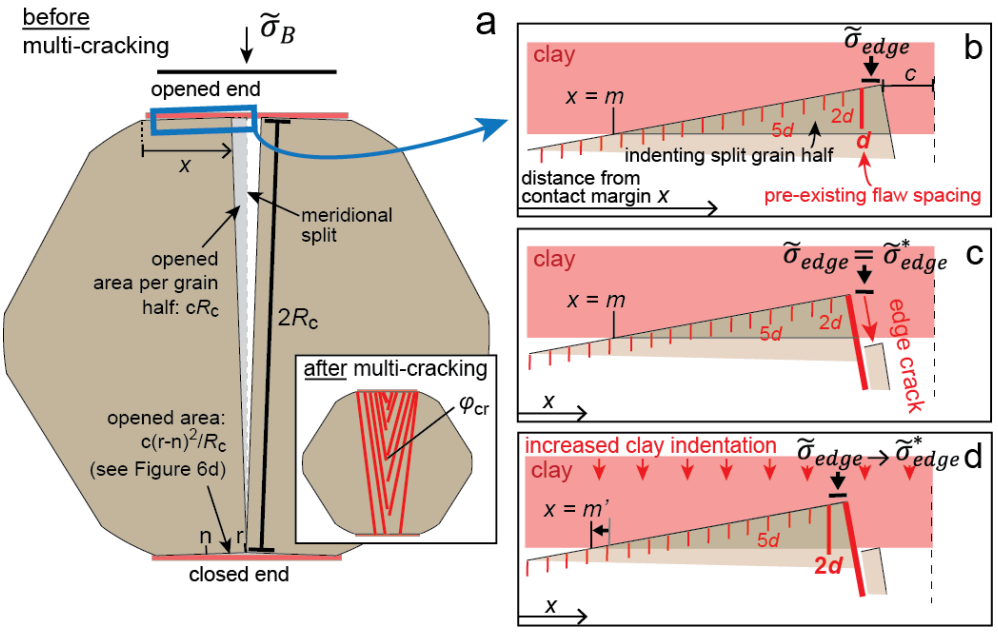

Figure 5.8 Diagrams illustrating the geometry and geometrical parameters considered in our analysis of intragranular, multi-edge cracking, following initial meridional splitting at assumed constant grain contact stress $\tilde{\sigma}_B$ during deviatoric compression at $\theta = 0°$. **a)** After splitting, the cross-sectional area of the opened gap is the sum of the opened cross-sectional area of the split, plus that at the closed end of the crack, along $n > x \geq r$ (refer Figure 5.7d). **b)** Detailed view on one side of the split grain contact, at the opened end. Along this contact, pre-existing flaws are assumed present at a regular distance d. The normal stress ($\tilde{\sigma}_{edge}$) acting on the most uplifted edge within one flaw spacing (d) of the initial meridional crack will be strongly enhanced due to clay indentation and will tend to extend the first neighboring contact flaws to produce an edge crack. **c)** When $\tilde{\sigma}_{edge}$ equals the critical value $\tilde{\sigma}^*_{edge}$ for edge crack propagation, two slices alongside the meridional split will break off, be displaced into the gap opened by the split, and seize to support load; **d)** At assumed constant applied stress, the reduction in supported load causes the grain halves to indent further into the clay, leading to again enhanced loading of the next edge, between $(r - 2d) > x \geq (r - d)$, which then instantly reaches $\tilde{\sigma}^*_{edge}$. At constant stress, this instable sequence of clay-indentation and breaking off slices progresses until the opened gap is filled such that the broken-off slices start to support load.

before edge cracking, implying that the value of $\tilde{\sigma}_{edge}$ acting on the now most uplifted edge (*i.e.* between r-$2d$ < x < r-d) will again exceed σ^*_{edge}, resulting in the propagation of the next pair of flaws to form edge cracks (Figure 5.8c). Two more, roughly crack parallel slices are then broken off the central crack face, and will again be displaced into the opened gap. Thus, at constant stress, an instable sequence of multiple stages of edge cracking is expected, which will progress until the gap opened by the initial split is filled such that the broken-off slices will start to support load.

The strain increment developing up to this point is estimated here by considering the gap filling process in the 2D plane shown in Figure 5.8a. Here, the combined cross-sectional area of the gaps present on either side of the split is given by $cR_c + c(r\text{-}n)^2/R_c$. The 2D porosity fraction φ_{cr} characterizing the 2D gap cross section before the cracked grain starts to support load is taken to be 0.5, *i.e.* equivalent to a typical porosity fraction of loosely packed, angular sand (0.4 – 0.5; *Mavko et al.*, 2009). The contraction normal to the critically stressed grain contacts is then obtained by dividing the solid area within the gap, notably $(1 - \varphi_{cr})\ (cR_c + c\ (r\text{-}n)^2/R_c)$, by the grain contact radius (r). During deviatoric loading, the vertical strain increment due to multi-edge cracking ($d\varepsilon_1^{cr,m}$) of grain contact B is then given by:

$$d\varepsilon_1^{cr,m} \approx \frac{(1-\varphi_{cr})\left(cR_c+\frac{c}{R_c}(r-n)^2\right)}{2rR_c} \qquad \text{(Eq. 5.32)}$$

while $d\varepsilon_3^{cr,m}$ is again zero. For the values and porosities listed in Table 5.2, the value of $d\varepsilon_1^{cr,m}$ obtained for deviatoric compression at P_c = 5 to 80 MPa ranges between 0.08% and 0.40%. During hydrostatic compression, multi-edge cracking occurs at whichever grain contacts A, B, C or D an initial meridional crack was formed. As it was assumed that the unit cells including initial meridional cracks from any one of the contact types A, B, C or D, are equally present throughout the microstructure at the sample scale (*cf.* Section 5.6.4), the average, principal inelastic strain increments ($d\varepsilon_i^{cr,m}$, i = 1,2,3) developing due to multi-edge cracking at the sample scale are then each equivalent to a third of the deviatoric, vertical strain increment $d\varepsilon_1^{cr,m}$, described by Equation 5.32. Note that the sum of the strain increments due to initial splitting, and those resulting from subsequent multi-edge cracking developing at constant stress, constitutes the total inelastic strain increment developing at the vertical stress (σ_1^*) corresponding to initial intragranular splitting (Equations 5.21a and b).

5.8 Multi-mechanism model integration and comparison with experimental data

We have developed a series of models for inelastic deformation in Slochteren sandstone, based on the grain-scale processes assumed to operate during each of the main Stages 1, 2, 3d and 3c of mean effective stress (P) versus total ($\Delta\varphi_t$) and inelastic ($\Delta\varphi_i$) porosity reduction behavior seen in our experiments of Chapter 3 [*Pijnenburg et al.*, 2019]. We have obtained equations for the (yield) stresses required to activate these processes, notably for: 1) Isotropic consolidation of intergranular clay during hydrostatic compression; 2) Serially coupled, intergranular clay consolidation and slip (Equation 5.12a); 3) intergranular clay slip, leading to dilation (Equation 5.18); and 4) Intragranular cracking (*i.e.* meridional splitting, followed by multi-edge cracking at constant stress), whether operating with or without intergranular slip (Equations 5.21a,b). The contribution of each of these processes to the inelastic deformation behavior of the sandstone was assumed to be determined by the inelastic response of the unit cell oriented most favorably for this process to occur, *i.e.* for the value of θ at which the corresponding activation stress is lowest. Most of these processes were found to be easiest at a unit cell orientation θ of 0°, except for dilatant intergranular slip (Equation 5.18), which for $\mu = 0.26$ was shown to be easiest at $\theta = 23°$. For all compactive processes ($\theta = 0°$), approximate stress-strain relations are obtained (Equations 5.9, 5.15a, 5.15b, 5.22 and 5.32), so that the model hardening behavior due to inelastic densification can be evaluated. Elastic deformation is considered to develop independently and in parallel to the inelastic response (*cf.* Equation 5.1), and is described independently (additively) through the non-linear poroelasticity relations given in Equations 5.2, 5.3a and 5.3b.

We now integrate the above models by compiling the full set of equations using Matlab software to calculate the implied, integrated stress versus elastic and inelastic strain behavior. The integrated behavior is computed for the initial porosities (φ_0 = 13.4, 21.5 and 26.4%) used in the experimental study of Chapter 3, and the corresponding input parameter values listed in Table 5.2, employing the numerical solvers embedded in Matlab where needed. We first compute the model behavior for the same stress conditions as those explored in the hydrostatic plus deviatoric experiments of Chapter 3 [*Pijnenburg et al.*, 2019; Figure 3.3], allowing for a direct comparison between the predicted and observed behavior. We then compare the stress conditions predicted to mark the onset of Stages 3d and 3c with the corresponding stresses reported in the literature, and we assess to what extent the hardening behavior seen during the preceding Stages 1 and 2 in our experiments is captured by our model. These comparisons are used to identify the agreement and discrepancies between the model predictions and experimental observations, and so to discuss to what extent the

underlying processes modelled account for the inelastic deformation observed. Finally, we employ the newly obtained understanding of these processes to evaluate to what extent the empirical plasticity model calibrated to the short-term experimental data of Chapter 3 (see Section 5.1) may be applied to describe the induced compaction behavior at field time-scales.

5.8.1 Total and inelastic deformation behavior: model versus experiments

The triaxial stress-cycling experiments of Chapter 3 were performed on Slochteren sandstone samples with initial porosities (φ_0) of 13.4%, 21.5% and 26.4%. These samples were either deviatorically compressed at a constant effective confining pressure P_c of 5 MPa from the outset, or else first hydrostatically compressed from an initial 5 MPa, to 20, 40 or 80 MPa, followed by deviatoric compression at constant P_c until Stage 3d or Stage 3c behavior was seen. The modeled mean effective stress ($P = [\sigma_1 + \sigma_2 + \sigma_3]/3 = [\sigma_1 + 2\sigma_3]/3$) versus inelastic porosity reduction ($\Delta\varphi_i \approx \varepsilon_1^{inel} + 2\varepsilon_3^{inel}$) behavior and the P versus total porosity reduction ($\Delta\varphi_t \approx \varepsilon_1^{el} + 2\varepsilon_3^{el} + \Delta\varphi_i$) behavior obtained for the chosen initial porosities and stresses are shown in Figure 5.9. Again, all processes governing the modeled inelastic deformation during deviatoric compression ($Q > 0$) are described at an orientation θ of 0°, except intergranular slip plus dilation, which for a μ value of 0.26 was found to be easiest at θ = 23° (Equation 5.18). The model results are compared in Figure 5.9 with the corresponding experimental data. The experimental data are represented by circular symbols, each reflecting the maximum P explored in each stress-cycle, versus the corresponding value of $\Delta\varphi_t$ (closed circle) or $\Delta\varphi_i$ (open circle).

The modeled and experimentally obtained P versus $\Delta\varphi_t$ and $\Delta\varphi_i$ curves obtained for each of the initial sandstone porosities investigated are typically similar within 0.1 to 0.2% porosity reduction (Figure 5.9). An exception is seen at the lowest P_c of 5 MPa tested, where the model significantly overestimates the $P - \Delta\varphi_t$ behavior by a factor of 1.5 to 2, particularly for $\varphi_0 \geq 21.5\%$ (Figures 5.9b,c). The experimental behavior likely reflects the anisotropic elastic behavior shown to occur at these low values of P_c [*Pijnenburg et al.*, 2019], which is at present not included in our model (Section 5.3). Still, during hydrostatic compression up to P_c = 20, 40 or 80 MPa, the modeled and experimental P - $\Delta\varphi_t$ and $P - \Delta\varphi_i$ are closely similar. During subsequent deviatoric compression, the model initially shows no inelasticity, reflecting the inability of the model to compact by serially coupled clay consolidation and slip, when slip is not yet activated (*i.e.* when $P_c < \sigma_1 < \sigma_1^{slip}\big|_{(\theta = 0°)}$; Equation 5.12a). Note, though, that during this episode of "inelastically rigid" model behavior, contact stresses do increase, *cf.* Equations 5.11a-f. In our experiments, $\Delta\varphi_i$ is never fully absent. However,

within the first 5 MPa mean effective stress of deviatoric compression at a P_c of 20, 40 or 80 MPa, the experimental data obtained for samples with φ_0 of 13.4%, 21.5% and 26.4% show markedly increased (*i.e.* stiff) hardening rates, with $\Delta P/\Delta(\Delta\varphi_i)$ falling in the ranges of, respectively, 33 to 95 GPa, 46 to 52 GPa and 27 to 97 GPa, compared to the corresponding $dP/d\Delta\varphi_i$ values of 28, 17 and 10 GPa seen during subsequent deviatoric loading [*i.e.* for Stage 2; *Pijnenburg et al.*, 2019]. In our model, the onset of inelastic deformation during deviatoric compression (*i.e.* when $\sigma_1 = \sigma_1^{slip}\big|_{(\theta = 0°)}$) is accompanied by an instantaneous increase in $\Delta\varphi_i$ of about 0.02 to 0.05% (Figure 5.9). This reflects the re-equilibration of the clay films by clay consolidation and slip to the elevated contact stresses (*cf.* Equation 5.15a and b). During subsequent compression, the model shows more gradual, P - $\Delta\varphi_t$ and P – $\Delta\varphi_i$ behavior, yielding similar, roughly linear (Stage 2) hardening rates to those shown by the experimental data at the same P. Stages 1 and 2 are then followed by Stage 3d or Stage 3c behavior. The dilatant (suffix d) or compactive (suffix c) nature of these Stages as seen in our experiments (solid arrows in Figure 5.9), is in most cases well-predicted by the model (open arrows), except for φ_0 = 13.4%, at P_c = 40 MPa, and for φ_0 = 26.4%, at P_c = 20 MPa. For these two cases, Stage 3c is predicted, while Stage 3d was observed. Where described correctly, the predicted mean effective stress marking the onset of Stage 3d or Stage 3c falls within 10 MPa from the experimentally obtained value. In our experiments, Stage 3c is associated with concave-down P – $\Delta\varphi_i$ behavior, while our model implies an instantaneous increase in $\Delta\varphi_i$ at constant stress. Still, the inelastic porosity reduction seen at the onset of Stage 3c in our experiments (indicated by *c*-arrows), is closely similar to the modeled inelastic porosity reduction after initiating Stage 3c, *i.e.* within a relative difference of 5%.

The above comparison has highlighted several discrepancies between the modeled and experimental results, including the fully inhibited inelastic deformation implied by the model at the onset of deviatoric compression and the instantaneous increase in $\Delta\varphi_i$ implied upon initiating Stage 3c in the model, where more continuous behavior was shown in the experiments. Still, the onset of Stages 3d and 3c was in most cases well-described. Moreover, the P - $\Delta\varphi_t$ and P – $\Delta\varphi_i$ associated with Stages 1, 2 and 3c were typically found closely similar. On this basis, we conclude that the processes assumed to describe the inelastic deformation behavior seen in our experiments during Stages 1 and 2 (clay consolidation and slip), Stage 3d (slip-assisted dilation) and Stage 3c (intragranuar cracking) can account for the main trends in the experimental inelastic deformation behavior shown.

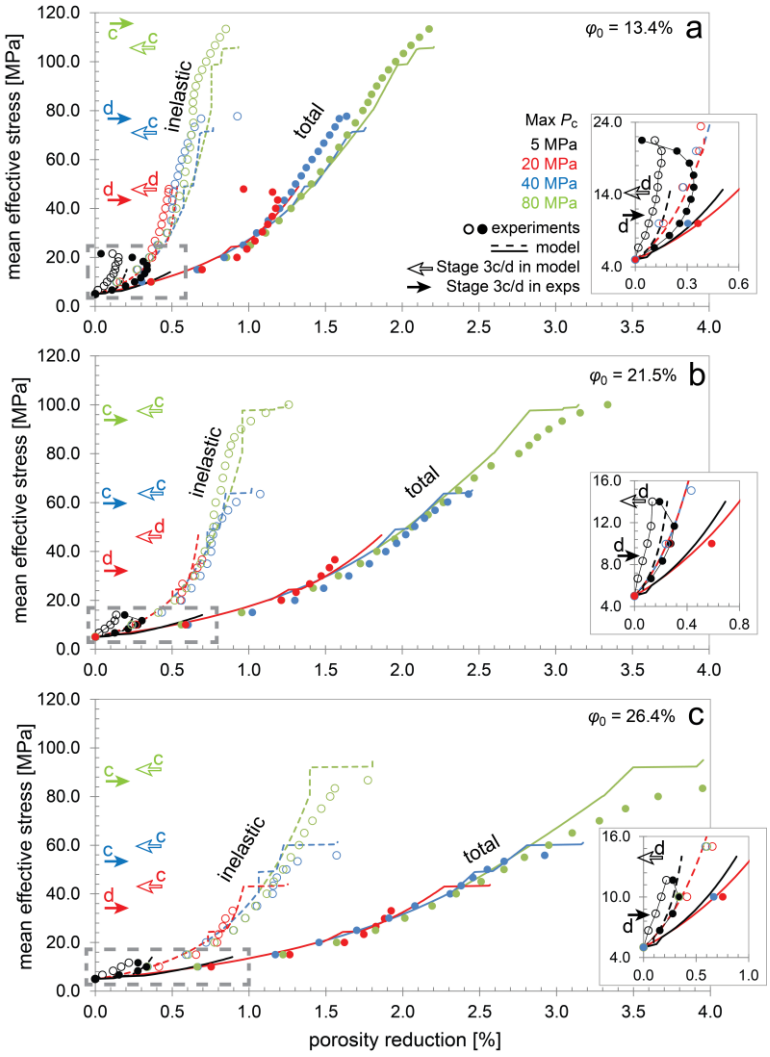

Figure 5.9 Comparison between the mean effective stress (P) versus total- ($\Delta\varphi_t$) and inelastic porosity reduction ($\Delta\varphi_i$) data implied by the model (continuous and dashed lines) and the corresponding experimental data (dots) obtained in our stress-cycling tests of Chapter 3 (see Figure 3.3 of that chapter), for initial porosities (φ_0) of: **a)** 13.4%; **b)** 21.5%; and **c)** 26.4%. We explored hydrostatic compression up to the maximum effective confining pressures (max P_c) indicated, followed by deviatoric compression up to the onset of dilation (Stage 3d indicated "d"- *cf*. Figure 5.1) or up to and including the onset of enhanced compaction (Stage 3c – indicated "c"). The experimental data reflect the maximum P conditions and the corresponding values of $\Delta\varphi_t$ and $\Delta\varphi_i$ explored in each stress-cycle. The modeled and experimental data show roughly similar, Stage 1, 2 and 3c P - $\Delta\varphi_t$ and $\Delta\varphi_i$ behavior. Note that at $\varphi_0 \geq 21.5\%$, the experimental data show dilation prior to that predicted by the model (see inset figures).

5.8.2 Integration of process-specific yield conditions

Yield envelopes describing the differential stress ($Q = \sigma_1 - \sigma_3$) versus mean effective stress ($P = (\sigma_1 + \sigma_2 + \sigma_3)/3$) conditions required to activate each of the assumed, inelastic (combination of) processes obtained for initial porosities of 13.4%, 21.5% and 26.4% are shown in Figure 5.10. For reference, the model kinematics corresponding to each yield envelope are illustrated in this figure.

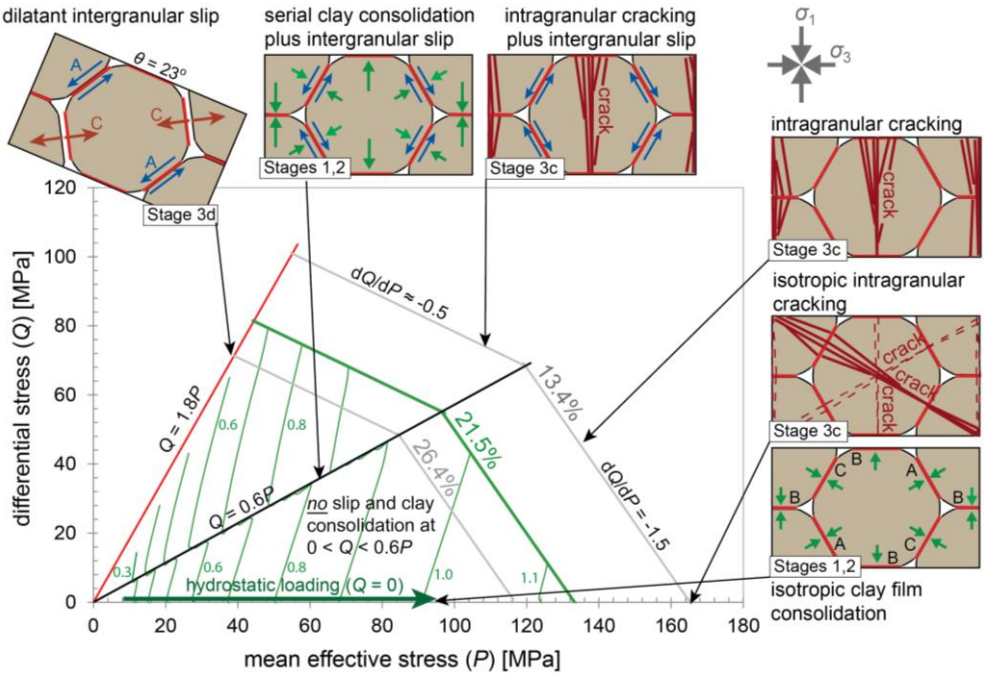

Figure 5.10 Differential stress ($Q = \sigma_1 - \sigma_3$) versus mean effective stress ($P = [\sigma_1 + \sigma_2 + \sigma_3]/3$) conditions delineating the yield conditions for each of the (combination of) inelastic processes assumed to govern the indicated Stage of P-$\Delta\varphi_t$ behavior in our model, at initial porosities (φ_0) of 13.4%, 21.5% and 26.4%. All processes are described at θ = 0° (refer Figure 5.4c), except for dilatant intergranular slip (shown at top-left) which for the assumed intergranular illite friction coeffecient μ = 0.26 was found to be easiest at θ = 23°. Stress conditions delineating fixed values of the inelastic porosity reduction ($\Delta\varphi_i$) computed for φ_0 = 21.5% are contoured with thin green lines ($\Delta\varphi_i$ values in % are indicated). At $0 < Q < 0.6P$, no inelastic deformation by intergranular slip and serially coupled clay film consolidation occurs, while fixed $\Delta\varphi_i$ stress-contours have a slope dQ/dP equal to 3, equivalent to that of the stress path implied for deviatoric loading (increasing σ_1) at constant $\sigma_2 = \sigma_3$. Upon intragranular cracking (Stage 3c), fixed $\Delta\varphi_i$ stress-contours follow the cracking envelopes towards lower P.

5.8.2.1 Comparison withwith experimentally obtained Stage 3d and 3c yield envelopes

The yield envelopes obtained for dilatant intergranular slip (*i.e.* Stage 3d) and for (serially coupled) clay slip plus clay consolidation are insensitive to φ_0, while the envelopes obtained for intragranular cracking (Stage 3c) envelopes are markedly φ_0-sensitive (Figure 5.10). Furthermore, the combined outline of the predicted envelopes marking Stages 3d and 3c describes a tri-linear, or roughly elliptical shape in *Q*-*P* space, transecting the *P* axis at the origin and at the hydrostatic confining pressure for isotropic grain crushing (P_c^*). This shape, and the predicted φ_0-(in)sensitivities characterizing Stages 3d and 3c in our model are in qualitative agreement with the behavior seen in experiments performed on Slochteren sandstones [*Pijnenburg et al.*, 2019] and on many other sandstones [*Wong and Baud*, 2012 - see also our Introduction]. Hence, at least for these high strain Stages 3d and 3c ($\varepsilon > 1\%$), the agreement between predicted and observed stress conditions is found to be satisfactory. This implies that the dilatant behavior is well-captured by considering the onset of tension at grain boundaries developing during intergranular slip [see also: *Guéguen and Fortin*, 2013], while Stage 3c initiation can be accounted for by considering intragranular cracking, which at $Q > 0.6P$ is made easier by accompanying intergranular slip. We now go on to discuss whether the model captures the inelastic yield envelope expansion implied for Stages 1 and 2 of our Chapter 3 experiments [*Pijnenburg et al.*, 2019]. In that way, we evaluate to what extent the associated hardening behavior due to inelastic densification is accounted for by consolidation of- and slip on the intergranular clay films.

5.8.2.2 Processes governing yield envelope expansion during Stages 1 and 2

To constrain the model hardening behavior (*i.e.* the yield envelope expansion) due to inelastic porosity reduction, we show contour lines delineating fixed values of inelastic porosity reduction in Figure 5.10 (thin green lines; magnitude indicated in %), obtained for a φ_0 value of 21.5%. These contours were obtained by interpolating the *Q* and *P* data corresponding to fixed values of $\Delta\varphi_i$, obtained during consecutive model runs in which hydrostatic- plus subsequent deviatoric loading was simulated. The maximum P_c used to compute the deviatoric portion was incremented by 1 MPa in each run, thus exploring P_c in the range between 5 and 133 MPa, *i.e.* up to the isotropic confining pressure P_c^* required for intragranular cracking during hydrostatic compression. Similar $\Delta\varphi_i$-contour lines were obtained for initial porosities of 13.4 and 26.4%. These are not shown, as the behavior was highly similar to that seen for $\varphi_0 = 21.5\%$, albeit less- and more compliant, respectively.

Overall, the modeled inelastic porosity reduction contours obtained for a φ_0 value of 21.5% at the Stage 1 and 2 *Q* and *P* conditions enveloped by Stage 3d (dilation) and Stage 3c

(intragranular cracking) yield envelopes are positive, and steeply inclined (Figure 5.10), indicating that inelastic compaction is primarily sensitive to *P*, not to *Q*. The interspacing between the lines decreases with increasing *P*, reflecting stiffening of the clay films as these consolidate. Recall that throughout hydrostatic compression, the unit cell deforms by inelastic clay consolidation (*cf*. Equation 5.9). However, at deviatoric stress conditions below those required to activate intergranular slip ($Q < 0.6P$) and intragranular cracking, the unit cell cannot deform inelastically. Therefore, at these deviatoric stresses corresponding to inelastically rigid behavior, the slope (dQ/dP) of the inelastic porosity reduction contours is equal to 3, and thus equivalent to the slope dQ/dP implied during deviatoric loading at constant confining pressure. Upon activating intergranular slip plus clay consolidation ($Q = 0.6P$), all contours shift along the corresponding envelope to lower *Q* and *P*, reflecting the instantaneous increase in $\Delta\varphi_i$ accompanying the onset of serially coupled, intergranular slip and clay film consolidation (see also Section 5.8.1). At $Q > 0.6P$, contour lines are steeper ($dQ/dP = 5 \pm 1$), reflecting increasing inelastic compaction at these loading conditions. Where $\Delta\varphi_i$ contours intersect the intragranular cracking envelopes (Figure 5.10), their orientation changes to follow these envelopes towards lower *P* values, implying negative slopes (dQ/dP) of -0.5 (if accompanied by intergranular slip), or -1.5 (no intergranular slip). Hence, the onset of intragranular cracking in our model marks a sharp change from primarily *P*-sensitive- to *P*- and *Q*-sensitive, inelastic porosity reduction behavior.

The experiments of Chapter 3 showed a similar transition from *P*-sensitive $\Delta\varphi_i$ behavior during Stage 1 and the initial portions of Stage 2, to *P*- and *Q*-sensitive behavior at higher *P* and *Q*, *i.e.* towards the end of Stage 2, and into Stage 3c (Figure 3.11 of Chapter 3). Indeed, this behavior was inferred to reflect a transition in the governing inelastic deformation processes, where, at the time unidentified, intergranular compaction processes were thought to govern the initial, *P*-sensitive behavior, while at higher *P* and *Q*, intragranular cracking would lead to more *Q*-sensitive, or shear-enhanced compaction behavior [*cf. Curran and Carroll*, 1979]. However, in our experiments, the transition from primarily *P*-sensitive, to *P*- and *Q*-sensitive hardening behavior was more gradual than implied by our model, developing already at values of $\Delta\varphi_i$ corresponding to the later portions of Stage 2 behavior. In addition, micrographs obtained from samples deformed up to Stage 2 showed a small increase in intragranular crack density (see Chapter 3; Figure 3.8c), demonstrating a small role played by intragranular cracking during Stage 2.

Our model provides a physical basis to underpin the above inferences made in Chapter 3. The dominantly *P*-sensitive inelastic porosity reduction behavior seen during Stage 1 and the bulk of Stage 2 of our experiments is shown to be well-accounted for by slip

on- and/or consolidation of the intergranular clay films (Figure 5.10). Our model predicts a sharp transition from primarily *P*-sensitive, to *Q*- and *P*-sensitive inelastic porosity reduction behavior upon intragranular cracking (*i.e.* Stage 3c; Figure 5.10), which in our experiments is seen to occur more gradually throughout the later portion of Stage 2, becoming dominant in Stage 3c.

5.8.3 Model evaluation and suggestions for future steps

We showed that the main experimental trends in $Q - P$ - $\Delta\varphi_i$ behavior seen in our experiments on Slochteren sandstones can be accounted for by the present model. However, discrepancies were also found, including the discontinuous P - $\Delta\varphi_i$ behavior implied by the model at the onset of serially coupled, intergranular slip plus clay consolidation, and at the onset of intragranular cracking, but not seen in experiments. These discrepancies mainly arise from the discrete yield conditions implied by the assumed, uniform model microstructure and microscale strength parameters, *i.e.* the regular array of quartz grains and intermittent clay films with uniform size, contact geometry and strength. In natural sandstone, these microstructural features will be distributed [*Brzesowsky et al.*, 2011; *Cook et al.*, 2015; *McDowell et al.*, 1996], so that the P-$\Delta\varphi_i$ behavior is likely to be smoothed out. A more complete quantification of the stress-strain behavior exhibited by Slochteren sandstone may require accounting for such microstructural and microscale strength parameter variations and distributions. For instance, the empirical plasticity model reported in Chapter 3 predicts fully balanced dilation and compaction (*i.e.* critical state) for $\varphi_0 \geq 21.5\%$, at $Q = (1.7 \pm 0.1)P$. This means that for these porosities, dilation occurs prior to the onset of dilation implied by the present microphysical model at the assumed constant grain contact friction coefficient μ of 0.26 ($Q = 1.8P$). If the value of μ is taken to vary across the microstructure, for instance due to variations and changes in the consolidation state of and/or shear strain within the intergranular clay, then the onset of dilation will accordingly be spatially variable. For the smallest μ-value of 0.22 within the range described by *Tembe et al.*, [2010] ($\mu = 0.22$ to 0.30, at shear strains between 0.4 to 8.0% - see Section 5.3) Equation 5.18 implies that dilation occurs at $Q = 1.7P$ and $\theta = 24°$, hence at similar stress conditions to those implied by the plasticity model at critical state. At the limit of no intergranular friction ($\mu = 0$), which may locally be the case when grains are unconstrained in the slip direction, Equation 5.18 implies dilation when $Q = 1.2P$ and $\theta = 0°$. Note that in this end-member case, the resistance to dilation is controlled by the dilatancy angle implied by the model packing [see: *Niemeijer and Spiers*, 2007]. In general, the effect of structural heterogeneity on the inelastic deformation behavior may in future work be investigated by incorporating a (statistically)

distributed grain/grain contact strength in this model [*e.g. Brzesowsky et al.*, 2014b], through discrete element modelling [*e.g. Marketos and Bolton*, 2009], or by adopting the thermodynamically-based approach outlined by *Einav*, [2007] and *Tengattini et al.*, [2014]. In its present form, though, the model contributes to understanding of the processes governing inelastic deformation, and can so be used to evaluate the applicability of existing geomechanical models at field conditions and time-scales.

5.8.4 Implications for modelling in the context of the Groningen gas field

5.8.4.1 Implications for 1-D reservoir compaction modelling

In Chapter 3, we showed that the inelastic deformations seen in our short-term (hours), constant strain rate ($\dot{\varepsilon} \approx 10^{-5}$ s^{-1}) experiments at the Stage 2 strains relevant to producing reservoirs, were well-described by an isotropic, Cam-clay-type plasticity model. When applied to describe induced, 1-D (uniaxial) compaction in the Groningen gas field, this plasticity model, combined with a poroelastic model to describe the concomitant elastic contribution, significantly improves predictions of the *in-situ* stress evolution, notably by up to 40% with respect to purely poroelastic estimates [*Pijnenburg et al.*, 2019]. In addition, the strain energy budget available for release through seismicity and associated rupture processes is more realistically represented by this empirical elastic/inelastic model (*i.e.* 30 - 50% dissipated). However, since the mechanisms underlying the empirical model remained at the time unidentified, it was left unclear to what extent the experimental data, and hence the model, could be realistically applied at field time-scales.

Longer-term stress relaxation experiments (one week; *Pijnenburg et al.*, [2019]), and constant stress creep tests (weeks- months; *Hol et al.*, [2015]) conducted on the Slochteren sandstone at *in-situ* conditions of stress (σ_1 = 30 to 65 MPa, σ_3 = 8 to 30 MPa), temperature (100 °C) and pore fluid chemistry (4M salt brine), showed that the bulk of the inelastic contribution to the near-linear stress - strain behavior relevant to producing reservoirs (*cf.* Stage 2) is time-independent, *i.e.* in these experiments, decelerating creep strains were observed, which in total contributed only 10 to 20% to the inelastic strain accumulated during active loading. Moreover, the present study demonstrates that the inelastic deformation behavior seen during Stage 2 in our short-term experiments can be largely accounted for by consolidation of- and slip on intergranular clay films, with perhaps a small role played by intragranular cracking. The analysis outlined in Section 4.7.5 (Chapter 4) shows that compaction by intergranular slip plus clay consolidation is virtually time- or rate-insensitive at stresses pertaining to the current state of depletion of the Groningen reservoir (σ_1 = 57 MPa; σ_3 = 27 MPa), so that reservoir compaction by these mechanisms is

expected to be largely time or rate-insensitive. The time-independent plasticity plus poroelasticity model outlined in Chapter 3 is accordingly anticipated to capture the main trends of the *in-situ* compaction behavior at the decade time-scales relevant to the field, though compaction strains and lateral stresses may be slightly underestimated due to the above minor (decelerating) creep effects seen in the experiments. Still, to fully constrain the long-term compaction behavior, these small creep effects need to be scrutinized in future work. This can be achieved by microphysical modelling of the underlying slow creep processes, such as stress-corrosion cracking [*e.g. Brantut et al.*, 2013] and pressure solution [*e.g. Spiers et al.*, 2004], followed by validation of the modelling results using long-term (weeks – months) compaction (creep) experiments performed at the reservoir-relevant small strains (ε = 0.1 to 1.0%) [*e.g. Hol et al.*, 2015; *Pijnenburg et al.*, 2018], and by subsequent extrapolation of the modelling results to the decade time-scales relevant to the (post-)production phase.

5.8.4.2 Implications for modelling reservoir deformation near faults

The empirical, poroelasticity plus plasticity model of Chapter 3 not only applies to the reservoir body, but also close to faults, and to modest irregularities within faults. At these locations, deformation departs from 1-D (uniaxial) compaction, but remains in the isotropic, small strain (Stage 2) regime where the model applies. The elastic and inelastic deformations developing near such faults will influence the stress development before and up to the point of fault slip, and thus control the onset of fault rupture. However, upon (and possibly before) fault rupture, stresses acting on particularly large-amplitude fault irregularities or asperities may locally be sufficiently large to imply Stage 3c behavior, *i.e.* to lead to pervasive cracking within, or crushing of these asperities, which is not accounted for by the empirical (Stage 2) model. Still, if significant fault roughness is included in a fault rupture model, then energy dissipation associated with inelastic deformation in Stages 2 and 3c will decrease the energy available for seismic release [*Cooke and Madden*, 2014]. This again indicates that accounting for the inelastic contribution to reservoir deformation has a key role to play in future geomechanical modelling.

5.9 Conclusions

In this study, a series of microphysical models has been derived to explain the inelastic deformation behavior shown in triaxial experiments performed under in-situ conditions of temperature (100 °C), stress and pore fluid chemistry (~4 *M* brine), on Slochteren sandstone samples from the seismogenic center of the Groningen field, as

reported in Chapter 3 [*Pijnenburg et al.*, 2019]. In particular, we sought a mechanistic basis for the continuous inelastic (permanent) deformation seen at small strains ($\varepsilon \leq 1.0\%$) relevant to the field, *i.e.* during Stage 2 of the experiments considered (*i.e.* the near-linear mean effective stress P versus total porosity reduction $\Delta\varphi_t$ behavior). On the basis of microstructural evidence obtained in previous experiments, inelastic deformation was inferred to be governed by intergranular slip and consolidation of intergranular clay films during Stage 1 (concave-up P-$\Delta\varphi_t$ behavior) and Stage 2. The subsequent dilatant (Stage 3d) and non-linear compaction behavior (Stage 3c) were inferred to be governed by dilatant, frictional slip and intragranular cracking, respectively. The model microstructure was taken to consist of a regularly packed array of quartz grains (radius 100 μm) with flattened/dissolved contacts and intergranular clay films (thickness 3 to 6 μm). The integrated model behavior was explored for the same initial sample porosities (φ_0 = 13.4%, 21.5% and 26.4%) used in our experiments, and for stress conditions covering the bulk of those explored in our tests, *i.e.* differential stresses (Q) up to 130 MPa and effective confining pressures up to 165 MPa. This allowed for a direct comparison between the model-implied, and experimentally obtained behavior. We draw the following main conclusions:

1) Our model captures the main trends in P versus total ($\Delta\varphi_i$) and inelastic porosity reduction ($\Delta\varphi_i$) seen in experiments on Slochteren sandstone under simulated *in-situ* (depletion) conditions, showing a similar progression in Stage 1, Stage 2 and Stage 3d or Stage 3c P – $\Delta\varphi_t$ and P versus inelastic porosity reduction ($\Delta\varphi_i$) behavior.
2) During Stages 1 and 2, the model implies a yield envelope that expands with increasing $\Delta\varphi_i$ from the onset of compression, reflecting hardening due to intergranular clay consolidation. The hardening behavior was found to be primarily P-sensitive when governed by clay consolidation and slip, and markedly Q-sensitive upon intragranular cracking (*i.e.* upon Stage 3c). This behavior is qualitatively similar to that seen in our experiments.
3) The yield envelope describing Stage 3d (dilatant intergranular slip) is φ_0-insensitive and describes a direct dependence of Q on P (*i.e.* $Q = 1.8P$). The yield envelopes obtained for Stage 3c (intragranular cracking) are φ_0-sensitive and show an inverse dependence of Q on P, being shallower when accompanied by intergranular slip (dQ/dP = -0.5, compared to dQ/dP = -1.5 absent slip). The φ_0-(in)sensitivities, and the orientations described in Q-P space are in qualitative agreement with the Stage 3d and Stage 3c seen in the Slochteren sandstone and in many other sandstones.

4) We infer that the processes assumed in the present model, *i.e*. clay consolidation, intergranular slip and intragranular cracking can indeed account for the main trends in inelastic deformation behavior seen in our experiments. The discrepancies between the model predictions and the observations are attributed to the discontinuous inelastic deformation behavior implied by our model, which in reality is likely to be more smoothed out due to distributed values of grain (-contact) strength, or due to variations in packing.
5) The present model provides a mechanistic basis for the empirical, constitutive (poroelastic plus plastic) compaction model reported in Chapter 3 [*Pijnenburg et al.*, 2019], where at the small strains relevant to reservoir compaction ($\varepsilon \leq 1\%$), the inelastic contribution is largely governed by serially coupled intergranular slip and clay film consolidation.
6) At constant effective stresses (σ_1 = 57 MPa; σ_3 = 27 MPa) pertaining to the current state of depletion (P_p = 8 MPa, in 2016) of the Groningen gas reservoir, deformation by intergranular slip plus clay film consolidation is very fast (order: mm/s) and hence virtually rate-insensitive at the time-scales of the reservoir. Creep effects due to other (minor) processes are seen in experiments, though their added contribution to the instantaneous inelastic strain accumulated during loading is small (10 to 20% of instantaneous value) [*Hol et al.*, 2015a; *Pijnenburg et al.*, 2018].
7) This means that the constitutive model reported in Chapter 3 is expected to capture the main trends of the *in-situ* compaction behavior at the decade time-scales relevant to the field, though compaction strains and lateral stresses may be slightly underestimated due to minor (decelerating) creep effects seen in the experiments. Hence, the Chapter 3 model can be incorporated in geomechanical models investigating the effects of field production, where it will improve estimates of the stress evolution in the reservoir bulk, as well as near faults, the elastic strain energy budget available in the reservoir for seismic release, and the magnitude of subsidence.
8) Therefore, the empirical model, underpinned by the present microphysical model, contributes directly to a more realistic, physics-based description of induced seismicity at relevant decade time-scales. To fully constraint the long-term compaction behavior, the minor creep effects seen in experiments at reservoir-relevant stresses and strains need to be investigated further in future work.

Acknowledgements

This research was carried out in the context of the research program funded by the Nederlandse Aardolie Maatschappij (NAM). This program aims to fundamentally improve understanding the physics of production-induced reservoir compaction and seismicity in the seismogenic Groningen gas field.

Chapter 6

Conclusions, implications and suggestions for further research

This thesis has reported an experimental study aimed at investigating the elastic versus the inelastic deformation behavior and energy budget of Slochteren sandstones from the seismogenic center of the Groningen gas field in the Netherlands. The samples used were obtained from the Stedum (SDM)-1 well, which was drilled in 1965, prior to major production of the field (pore pressure ~35 MPa), and from the Zeerijp (ZRP)-3a well, drilled in 2015 after depletion to a pressure of ~8 MPa. The mechanical behavior was studied by means of short-term (hours to one week) axi-symmetric compression experiments, conducted in a conventional triaxial testing machine. The experiments were performed at *in-situ* conditions of temperature and pore fluid chemistry, exploring stresses and strains covering and exceeding those occurring during depletion of the field. Progressive stepwise loading and relaxation tests conducted up to differential stresses of 50 MPa, on SDM-1 samples with porosities in the range 12.7 to 24.6% showed elastic and inelastic deformation developing continuously throughout compression, with elastic axial strains reaching up to 0.3 to 0.6%, while inelastic axial strains ranged between 0.1 to 0.8% at the end of each test. The magnitude of the inelastic contribution was found to be modestly rate-sensitive, being larger by 10 to 20% at $\dot{\varepsilon} \approx 10^{-9}$ s^{-1}, compared to the values obtained at $\dot{\varepsilon} \approx 10^{-5}$ s^{-1}. Cyclic loading experiments performed at constant strain rate ($\dot{\varepsilon} \approx 10^{-5}$ s^{-1}) on samples with porosities of 13.4, 21.5 and 26.4% showed inelastic behavior that can be characterized by an expanding yield/compaction envelope truncated by a shear failure envelope. The data obtained were used to calibrate an isotropic, Cam-clay-type plasticity model, describing the small strain (<1%), time-independent inelastic deformation behavior seen in the experiments and expected during gas production from the Groningen field. This model does not account for the above described rate-sensitivity, such that the compaction strains and lateral stresses may be underestimated by 10 to 20%. In addition, state-of-the-art, microstructural and microscale strain analyses were performed, aimed at elucidating the mechanisms governing the inelastic deformation seen in our experiments. On the basis of the microstructural data obtained, a microphysical model for inelastic deformation of Slochteren sandstone by intergranular clay film deformation and grain fracturing was developed, and used to assess the applicability of the above empirical model at the decade time-scales relevant to producing reservoirs. This model shows that the inelastic contribution to the small strains relevant to producing reservoirs can be largely accounted for by clay consolidation plus intergranular slip. A simple analysis shows that these mechanisms are virtually time- or rate-insensitive at stresses pertaining to the depletion of the Groningen reservoir, so that reservoir compaction by these mechanisms is also expected to be largely rate-insensitive, though small (decelerating) creep effects due to other processes (*e.g.* stress-corrosion

cracking, pressure solution) may occur.

The work done has provided some of the first insights into elastic versus inelastic strain and strain energy partitioning in the Slochteren reservoir sandstone at the small strains ($\varepsilon \approx 0.1$ to 1.0%) relevant for production of, and induced seismicity in the Groningen gas field. In addition, the research presented in this thesis provides new insights into the effect of loading-rate on inelastic deformation, and the mechanisms governing the behavior observed in the Slochteren Sandstone. The results are also relevant to similar gas and oil reservoirs elsewhere. In the following, the principal conclusions will be integrated and summarized and the overall implications for induced reservoir compaction, subsidence and seismicity in Groningen (and beyond) will be assessed. Finally, remaining questions are identified and suggestions are made for future research.

6.1 Main findings

6.1.1 Total versus inelastic deformation behavior observed in cyclic loading experiments

Combined hydrostatic and deviatoric cyclic loading tests were performed on ZRP-3a samples (Chapter 3). The samples tested had initial porosities (φ_0) between 13.4% and 26.4%. I explored effective hydrostatic or confining pressures (P_c^{eff} = confining pressure minus pore pressure) up to 320 MPa and differential stresses ($Q = \sigma_1 - \sigma_3$) up to 135 MPa and employed relatively rapid strain rates of $\dot{\varepsilon} \approx 10^{-5}$ s^{-1}, and loading rates of ~0.1 MPa/s. It was shown that the stress-cycling method employed to quantify the inelastic contribution to deformation did not impact the overall stress-strain behavior through effects such as damage accumulation. The mean effective stress ($P = [\sigma_1 + \sigma_2 + \sigma_3]/3$ – pore pressure) versus total porosity reduction ($\Delta\varphi_t$) data obtained showed the typical progression of Stage 1 (non-linear, concave-up), to Stage 2 (near-linear) and to Stage 3d (non-linear dilatant shear failure) or Stage 3c (non-linear compaction) behavior, often reported for sandstones (*cf.* Figure 1.4, Chapter 1). Inelastic deformation contributed significantly to each of these stages, where at the reference P_c^{eff} values of 5, 20 40 and 80 MPa, 30 to 50% of the total porosity reduction ($-0.4\% < \Delta\varphi_t < 7.4\%$) and total axial strains (ε_t up to 3.4%) were inelastic. The total and inelastic porosity reductions were larger with increasing P_c^{eff} and φ_0. However, the inelastic porosity reduction measured at the end of Stage 1, at the reference P_c^{eff} of 5 MPa, was largely recovered upon full depressurization and removal of the sample from the vessel (Chapter 4). This suggests that the inelastic porosity reductions measured in the experiments of Chapters 3 and 4 at the end of Stage 1 at $P_c^{eff} = 5$ MPa are in fact apparent values, reflecting hysteresis in the Stage 1 loading/unloading behavior. Stage 1 behavior was shown to persist up to mean effective stresses of 30 to 40 MPa, which are similar to the previously supported, *in-situ*

mean effective stress of 35 ± 2 MPa prevalent in the reservoir at the time of core extraction [*Van Eijs*, 2015]. Therefore, the nominally recoverable, hysteretic behavior seen during Stage 1 likely reflects closure of pre-existing damage (*i.e.* dilated grain boundaries and pre-existing cracks – or "core damage"; *Holt et al.*, 2000). Inelastic strains developing beyond Stage 1, hence during the subsequent Stages 2 and 3c were shown to be truly permanent after retrieval of the sample from the vessel (Chapter 4).

The results of Chapter 3 show that during the near-linear Stage 2, the increase in total axial strain reached up to 1.0% (φ_0 = 13.4%–13.9%), 0.7% (φ_0 = 21.4%–21.5%), and 0.7% (φ_0 = 25.6%–26.4%). The corresponding increases in inelastic axial strain reached up to 0.3%, 0.3% and 0.4%, respectively. Similarly, total Stage 2 porosity reduction reached up to 1.1%, 1.3%, and 1.9%, respectively, to which inelastic deformation contributed up to 0.6%. Hence, during the near-linear Stage 2, assumed to be poroelastic in many studies [*e.g. Baud et al.*, 2004; *Guéguen and Fortin*, 2013; *Brantut et al.*, 2014], a significant 30 to 50% is found to be inelastic, *i.e.* permanent. The truly elastic Young's moduli (E) obtained during Stage 2 deformation (*i.e.* at P = 50 MPa) were 22.0 GPa, 13.4 GPa and 10.1 GPa, corresponding to initial porosities of 13.4, 21.5 and 26.4%, respectively. The Stage 2 P - $\Delta\varphi_t$ and P – $\Delta\varphi_i$ behavior was isotropic, being similar during both hydrostatic and deviatoric compression. Moreover, the inelastic deformation behavior shown during Stage 2 was found to be well-described by a plasticity model that utilizing an expanding (hardening) Cam-clay yield envelope, while obeying the normality condition. During Stages 3d (non-linear dilatant shear failure) and 3c (non-linear compaction), deformation was predominantly inelastic, with the P - $\Delta\varphi_t$ and P – $\Delta\varphi_i$ behavior being markedly anisotropic and poorly fitted by the above plasticity model.

6.1.2 Experimental constraints on the time-dependence of inelastic deformation behavior

The strain rate-sensitivity of deformation of the Slochteren sandstone was experimentally explored in Chapter 2, using samples retrieved from the SDM-1 well with initial porosities (φ_0) in the range of 12.7 to 24.6%. To remove any pre-existing (Stage 1) core damage or other damage effects, these samples were first pre-equilibrated for 2-3 days at stress conditions estimated to be prevalent in the reservoir before significant depletion in 1965 (vertical stress = 65 MPa, horizontal stresses ≈ 43 MPa, gas/pore pressure = 35 MPa, so that Q = 22 MPa and P_c^{eff} = 8 MPa). They were then subjected to a series of consecutive steps of active deviatoric loading ($\dot{\varepsilon} \approx 10^{-5}$ s^{-1}), each followed by a stress relaxation phase at fixed load point position (~ 1 day), during which $\dot{\varepsilon}$ decreased gradually from 10^{-5} s^{-1}, to 10^{-9}

s^{-1} or even 10^{-10} s^{-1}. In this way, the stress supported by the samples was explored across 4 to 5 orders of magnitude, with the lowest rates falling within 2 to 3 orders of magnitude of the total production-related strain rate inferred for the Groningen field (~10^{-12} s^{-1}) from subsidence measurements [*NAM*, 2013], or from *in-situ* compaction measurements [*Cannon and Kole*, 2017; *NAM*, 2015].

Throughout the sequence of loading plus relaxation steps, samples with φ_0 < 20% showed Stage 2 behavior up to the highest differential stress explored (Q = 50 MPa, ε_t up to 0.5%), as implied by the roughly linear trends in $Q - \varepsilon_t$ and $\Delta\varphi_t$ - ε_t data obtained. The strain rate ($\dot{\varepsilon}$) versus Q data obtained during Stage 2 relaxation intervals showed an exponential relation of the form $\dot{\varepsilon} \propto \ln[Q]$, which was found to be consistent with the $\dot{\varepsilon}$- Q relation predicted by a model based on rate-and-state-friction, including a reference grain boundary friction coefficient of 0.28, at a reference slip velocity of 1 μm/s. This suggests that the Stage 2 relaxation rate was controlled by rate-sensitive, intergranular slip. For φ_0 > 20%, Stage 2 behavior was seen up to Q = 30 to 40 MPs and ε_t up to ~0.6%, beyond which Stage 3d behavior (*i.e.*a transition from compaction towards dilatant shear failure) was seen. For the relaxation intervals initiated in Stage 3d, the $\dot{\varepsilon} - Q$ data again showed an exponential relation of the form $\dot{\varepsilon} \propto \ln[Q]$, but here was found to be consistent with previously reported creep data obtained on sandstones tested at high strains (*cf.* Stages 3c and 3d; ε_t = 0.6 to 5.0%) where stress-corrosion cracking resulting in grain-scale failure was inferred to be the main, rate-controlling mechanism [*Heap et al.*, 2009, 2015]. In all our samples, and for loading plus relaxation in all Stages, the rate-sensitivity of inelastic deformation was found to be modest, with the inelastic axial strains produced at $\dot{\varepsilon} \approx 10^{-9}$ s^{-1} being typically higher by 10 to 20% relative to the corresponding inelastic values obtained at $\dot{\varepsilon} \approx 10^{-5}$ s^{-1}. Accordingly, at $\dot{\varepsilon} \approx 10^{-9}$ s^{-1}, the inelastic contribution to total axial strain is 30 to 55% during Stage 2, which is slightly larger than time-independent inelastic strain partitioning results of 30 to 50% obtained at $\dot{\varepsilon} \approx 10^{-5}$ s^{-1} in our stress-cycling experiments performed on the ZRP-3a samples (see previous section). This means that the Cam-clay type model calibrated to the data obtained at $\dot{\varepsilon} \approx 10^{-5}$ s^{-1} will underestimate the stresses and strains developing due to inelastic deformation by 10 to 20%. Whether, or to what extent the model can be applied at field strain rates ($\dot{\varepsilon} \approx 10^{-12}$ s^{-1}) will be discussed shortly.

6.1.3 Microstructures after deformation into Stages 1, 2, 3c or 3d

Undeformed (as received) SDM-1 and ZRP-3a sandstone samples showed similar microstructural features as reported in previous work [*Gaupp et al.*, 1993; *Gaupp and Okkerman*, 2011; *Waldmann*, 2011; *Waldmann and Gaupp*, 2016; *Wilson*, 1992], which

suggests they are representative for much of the Slochteren sandstone formation across the Groningen field. Both suites of samples investigated consist predominantly of quartz grains (70 - 90 vol%), with lesser amounts of feldspar (10 - 25 vol%) and clays (up to ~5 vol%). The detrital grains are well- to sub-rounded, range from 100 – 250 μm in diameter and exhibit mostly flattened, or truncated contacts. The observed clays are present in the pore space and within a large proportion of grain contacts. At least in the samples inspected in this study (total number ~ 24), the thickness of these grain contact clay films increased from 1-4 μm in low porosity material (12 - 13%) to 4-8 μm in high porosity samples (24 - 26%). Undeformed SDM-1 and ZRP-3a samples both showed an intragranular crack density in detrital grains of 0.10 ± 0.05 cracks/mm^2. After deformation into equivalent Stages (*i.e.* 1, 2, 3d or 3c), similar microstructural changes were shown by all samples. Hence, we observed no microstructural difference reflecting the undepleted (SDM-1) versus depleted (ZRP-3a) state of the cores from which our samples were retrieved, nor any difference caused by the various strain rates explored in the SDM-1 tests ($\dot{\varepsilon} \approx 10^{-5}$ to 10^{-10} s^{-1}; Chapter 2), versus those employed in the ZRP-3a experiments ($\dot{\varepsilon} \approx 10^{-5}$ s^{-1}; Chapters 3 and 4).

The microstructures of ZRP-3a samples (Chapter 3) deformed to high strains ($\varepsilon >$ 1%; Stages 3d and 3c) showed similar features to typical Stage 3d and 3c sandstone microstructures reported in the literature [*Dresen and Gueguen*, 2004; *Wong and Baud*, 2012]. After reaching Stage 3d (dilatant shear failure regime), our samples typically showed one, or several, sample-scale fractures, oriented at 20 to 40° to the main compression direction. Micrographs recovered from one sample (φ_0 = 21.5%) deformed into Stage 3d showed that the main fracture (width ~0.1 mm) predominantly exhibited intergranular grain fracturing and was surrounded by a ~1 mm wide damage zone where intragranular cracks were abundant (crack density 40 cracks/mm^2). Nonetheless, the increase in intragranular crack density over the full, axial cross-section of the sample (55 by 1 mm) was modest, yielding an average value of 10 cracks/mm^2, compared to the undeformed average value of 8 cracks/mm^2. After Stage 3c deformation (compactive regime) of samples with φ_0-values of 13.4, 21.5, 21.9 and 26.4%, average crack densities were markedly higher, with values reaching up to 72 cracks/mm^2. In Stage 3c, most cracks were seen within diffuse, 2 to 10 mm wide bands, oriented at 45 to 90° to the main compression direction. Hence, after both Stages 3d and 3c, deformation was brittle, and markedly localized, where particularly Stage 3c was accompanied by significant intragranular cracking. By contrast to Stages 3c and d, the role played by intragranular cracking in accommodating deformation during Stages 1 and 2 was much smaller. In our incremental loading plus stress relaxation tests of Chapter 2, the intragranular crack density increased from ~7 ± 3 cracks/mm^2 (undeformed) to ~12 ± 4

cracks/mm^2 after Stage 2 deformation, and locally to 40 ± 10 cracks/mm^2 after Stage 3d deformation. To further quantify the role played by intragranular cracking in accommodating strain during Stages 1 and 2 versus higher strain Stages 3c/d, we analyzed the microstructures of a set of ZRP-3a cylindrical samples (φ_0 = 21.9%) recovered after deformation up to Stage 1, Stage 2 and Stage 3c. The stage-specific increase in mean crack density, normalized to the increase in inelastic porosity reduction measured at the reference P_c^{eff} of 5 MPa was negligible after Stage 1 (1.1 cracks mm^{-2}/% porosity reduction), small after Stage 2 (32.4 cracks mm^{-2}/% porosity reduction), and high (110.7 mm^{-2}/% porosity reduction) after Stage 3c. Hence, the hysteretic stress-strain behavior seen during Stage 1 (see Section 6.1.1), and the inelastic deformation demonstrated for Stage 2, must have been accommodated, in part at least, by a mechanism or by mechanisms other than grain fracture and failure.

To elucidate this mechanism, a sequence of five stress/strain-cycling plus strain-marker-imaging experiments was performed on a single split-cylinder sample (φ_0 = 20.4%) of Slochteren sandstone from the ZRP-3a well (Chapter 4). In consecutive experiments, increasingly high stresses and strains were investigated, to systematically explore Stages 1, 2 and 3c. In particular, the experiments involved a) hydrostatic compression up to P_c^{eff} = 40 MPa (Experiment 1; Stage 1), chosen to approximate the mean effective stress of 35 ± 2 MPa prevalent in the reservoir upon core extraction, b) deviatoric compression at P_c^{eff} = 40 MPa and up to Q = 50 MPa (Experiment 2; Stage 2), and c) deviatoric compression at P_c^{eff} = 40 MPa and up to Q = 75 MPa (Experiment 3; Stage 3c). The micrographs obtained after Experiment 1 (~end of Stage 1) showed both opening and closure of grain contacts, particularly those filled with clay. At the scale of the sample, these grain-scale deformations produced little area change with respect to the undeformed sample, as revealed by particle image velocimetry analysis (PIV), suggesting nominally recoverable behavior due to opening/closure of clay-filled grain contacts. After Experiment 2 (~end of Stage 2), PIV analysis revealed uniform, mostly vertical contraction across the full split-cylinder sample face. These contractions were frequently accommodated by consolidation of and/or slip on clay films present within grain-to-grain contacts. Moreover, grain-scale deformation was found to be larger where more clay (*i.e.* thicker clay coating) was present in grain contacts. Hence, during both Stages 1 and 2, deformation was largely accommodated by consolidation of and slip on intergranular clay films, which led to nominally recoverable stress-strain behavior (Stage 1), until a previously supported stress state was exceeded (Stage 2). After Experiment 3 (within Stage 3c), micrographs showed pervasive intragranular cracking plus intergranular shear displacements within localized,

conjugate compaction bands orientated at 40 to 45 degrees to the main compression direction, as typically reported for Stage 3c deformation of cylindrical plugs, at similar stress conditions [*Baud et al.*, 2004; *Fortin et al.*, 2006; *Tembe et al.*, 2008]

6.1.4 Mechanisms governing inelastic deformation of Slochteren sandstone

On the basis of the above microstructural observations, we inferred that the inelastic deformation behavior, seen during each of the main Stages 1, 2, 3d and 3c observed in the present load-cycling experiments (Chapters 3 and 4), was dominated by the following processes. Stages 1 and 2: intergranular slip plus consolidation of intergranular clay films, leading to nominally recoverable behavior at the sample-scale, until a previously supported state of stress was exceeded; Stage 3d: intergranular slip, leading to dilation (*cf.* shear fracturing); and Stage 3c: intragranular cracking. To test whether these processes can account for the $P - \Delta\varphi_i$ behavior shown in the experiments of Chapter 3, a series of microphysical models was developed for Slochteren sandstone deforming by these processes (Chapter 5). The constitutive model microstructure was taken to consist of a simple hexagonal pack of uniformly sized, quasi-spherical quartz grains with flattened/truncated grain-contacts, covered by illite clay films. The initial clay film thickness was taken to increase from 3 to 6 μm, as the model porosity increases from 13.4 to 26.4%, in line with microstructural observations. Within this model framework, the clay film consolidation behavior is described using long-term (months), drained, 1-D consolidation test data obtained on discs (1 – 2 mL) of wet illite powders (purity 65-85%; *Brown et al.*, 2017). The frictional behavior exhibited by the intergranular illite (μ = 0.26) is constrained using shear testing data obtained on high purity (95%), wet illite gouges (effective normal stress = 40 MPa, shear velocity v = 1 μm/s, shear strain 2.3%; *Tembe et al.*, 2010). During deviatoric loading, consolidation and slip are shown to be serially coupled deformation processes. To constrain the onset of intragranular cracking (Stage 3c), we used a criterion for grain splitting due to unconfined, axial compression [*Kendall*, 1978]. Upon entering Stage 3c, inelastic strain develops by indentation of the split and crack-tilted grain halves into the overlying grain contact clay films, plus subsequent, unstable crack formation and reorganization of grain fragments with no further stress change (*i.e.* stress assumed constant). Stage 3d (*i.e.* dilatant shear) is implied when frictional slip on one or more favorably orientated grain contacts leads to extension at, and opening of another. At present, the model does not include a strain-hardening or softening relation during Stage 3d dilation, nor does it account for any rate-sensitivity. The integrated model behavior was computed for the same initial porosities (φ_0) of 13.4%, 21.5% and 26.4%, and stress conditions used in the experiments of Chapter 3, allowing for a direct

comparison between modeled and experimental results.

The main trends in inelastic deformation behavior predicted by this model are in good agreement with the Stage 1, 2, 3d and 3c behavior seen in our load cycling experiments of Chapter 3. During Stages 1 and 2 (*i.e.* clay consolidation and slip), the model predicts a yield envelope that expands with increasing $\Delta\varphi_i$, implying hardening due to clay film densification. During these initial stages, $\Delta\varphi_i$ is primarily sensitive to P, not to Q, while the Q-sensitivity increases drastically at the onset of stage 3c, *i.e.* upon intragranular cracking. The onset of Stage 3d (dilation) is found to be insensitive to φ_0, while Stage 3c is encountered at lower Q and P, at higher values of φ_0. The yield envelope delineating the onset of Stage 3d shows a Coulomb-type, linear dependence of Q on P. At the onset of Stage 3c, an inverse Q-P dependence is shown, revealing a gentle slope (dQ/dP) of -0.5 when intragranular cracking is accompanied by intergranular slip (at approximately $0.5\ P_c^* < P < 0.8P_c^*$, where P_c^* is the hydrostatic grain crushing pressure), and a steeper slope of -1.5 when cracking occurs in the absence of intergranular slip (when $0.8\ P_c^* < P < P_c^*$). The porosity (in)sensitivities implied by the modeled Stage 3d and 3c yield envelopes, and their orientation in Q-P space are consistent with the porosity (in)sensitivity and broadly elliptical outline in Q-P space characterizing the Stage 3d/3c yield envelopes reported in experimental studies on the Slochteren sandstone (see Chapter 3), and on many other types of sandstone (*Wong and Baud*, 2012 - see also the Introduction, Chapter 1). The results suggest that the inelastic deformation behavior of Slochteren sandstone is indeed largely governed by intergranular slip, clay film consolidation and intragranular cracking. The main discrepancies between the predictions and observations are attributed to the discontinuous transitions in the deformation behavior implied at the onset of (Stage 2) deviatoric loading, and upon Stage 3c, which in reality is expected to be more smoothed out, due to distributed values of grain (-contact) strength, or due to variations in packing.

We employed a similar modelling approach to explore the rate-sensitivity implied by serially coupled intergranular slip and clay consolidation (Chapter 4). In such a serially coupled system, the slowest process determines the overall deformation rate. It was found that under constant effective stress conditions pertaining to the current state of depletion in the Groningen gas field (σ_1^{eff} = 57 MPa; σ_3^{eff} = 27 MPa, at a pore pressure of 8 MPa), consolidation is rate controlling, while the overall deformation rate is very rapid (order: mm/s), and virtually rate-insensitive on the time-scale of the experiments or field. By contrast, during the Stage 2 stress relaxation intervals of our Chapter 2 experiments, the applied stress was not constant. As noted earlier, these experiments showed that time-dependent relaxation of the differential stress (Q) by only 1 to 3 MPa led to an

exponential reduction in $\dot{\varepsilon}$ from 10^{-5} s^{-1} to 10^{-10} s^{-1} over 24 hours. The implied exponential relation, where $\dot{\varepsilon} \propto \ln[Q]$, was found to be consistent with a rate-and-state friction model (see Figure 2.8), suggesting that intergranular slip was rate-controlling during relaxation. Note that the grain boundary friction coefficient of 0.28 used in the rate-and-state friction-based model of Chapter 2 is closely similar to the friction coefficient of 0.26 assumed to apply to the clay-filled grain contacts in our microphysical model of Chapter 5. By comparison, the deformation rate implied by clay consolidation was far less sensitive to the applied stress (see Section 4.7.5). This means that during stress relaxation, intergranular slip rates decrease much faster than serially coupled clay consolidation rates, becoming rate-controlling virtually from the onset of stress relaxation. Thus, both the time-dependent, Stage 2 relaxation stress-versus strain behavior reported in Chapter 2 and the time-independent Stage 2 stress-strain behavior reported in Chapters 3 and 4 can be largely accounted for by serially coupled intergranular slip plus clay consolidation.

6.2 Implications

To assess the impact of current and future production strategies in the Groningen gas field (and in similar fields) on subsidence and induced seismicity, geomechanical models require a description of the deformation behavior within the reservoir, and of any time-dependence thereof. The experiments reported in this thesis demonstrate significant inelastic (dissipative) deformation (30 to 50% of total) throughout compressive deformation on time-scales of hours to around one week (Chapters 2 and 3). This means that the assumption of a fully poroelastic reservoir response to depletion, as frequently employed in current geomechanical models [*e.g. Van den Bogert*, 2015; *Candela et al.*, 2019; *Lele et al.*, 2016; see also Section 1.3], will lead to a significant overestimation of the stored strain energy available in the reservoir for release through seismicity and associated rupture processes, and to a potential misrepresentation of the *in-situ* stresses developing in the reservoir and acting on faults. Instead, geomechanical treatments should incorporate a constitutive model that accounts for both the inelastic and elastic contributions. Such a model should be validated and calibrated against experimental data obtained at the small strains (ε = 0.1 to 1.0%) relevant to producing reservoirs - as conducted here in Chapter 3 using constant strain rate ($\dot{\varepsilon} \approx 10^{-5}$ s^{-1}), conventional triaxial compression tests, and in Chapter 2, where the elastic versus time (in)dependent deformation behavior was quantified at strain rates between $\dot{\varepsilon} \approx 10^{-5}$ s^{-1} and $\dot{\varepsilon} \approx 10^{-9}$ s^{-1}. In addition, such a model should adequately describe *in-situ* reservoir behavior under the prevailing 1-D (*i.e.* uniaxial strain) boundary conditions expected in the bulk of the reservoir (*i.e.* remote from faults and other discontinuities).

Ideally, it should also capture any time-dependent deformation that contributes additional strain on the decade time-scales relevant to the (post-)production phase of the field. Clearly, field-relevant time-scales, reaching >50 years in the case of Groningen, cannot be explored in laboratory tests. Therefore, assessment of whether the laboratory data, and any model tested and calibrated against these data, can be extrapolated to longer time-scales requires a mechanistic (microphysical) model of the deformation mechanisms operating under laboratory conditions, ideally with evidence that the same mechanisms operate in the field. Chapters 4 and 5 contribute to our mechanistic understanding of the deformation behaviour observed in the laboratory experiments, demonstrating a major time/rate independent role of intergranular clay film deformation, in addition to subordinate time-dependent processes. Recent work by Verberne *et al.* [*Verberne et al., in prep*] on the microstructure of core recovered from the Stedum-1 well before local production (1965 - virgin pore pressure = 35 MPa), and from the ZRP-3 well in 2015 after reservoir depletion to 8-9 MPa [*NAM*, 2016], are consistent with this mechanism dominating *in-situ* compaction. Yet, application of the constitutive model obtained in Chapter 3 to the Groningen field and the implications of the present work for subsidence and induced seismicity clearly requires further analysis. The present section accordingly addresses the applicability of the model to describe 1-D (uniaxial strain) compaction experiments, and the implications of the model for induced seismicity when applied to the case of the Groningen field. I also evaluate more rigorously to what extent the time-dependence of reservoir compaction has been experimentally and/or mechanistically constrained, and to what degree the model is expected to apply at the decade time-scales pertaining to the field. In closing, we briefly discuss implications of our work to describing elastic versus inelastic deformation behavior outside the context of the Groningen field and of the Slochteren sandstone.

6.2.1 Present model for reservoir compaction and implications for subsidence and seismicity in the Groningen gas field

6.2.1.1 Elastic plus inelastic deformation behavior at reservoir-relevant strains: The model

Of the previously described Stages 1, 2, 3d and 3c of $P - \Delta\varphi_t$ behaviour (refer Fig 1.4), Stage 2 and the corresponding small strains (ε and $\Delta\varphi_t$ typically $\leq$ 1%) were judged most relevant to the behavior expected to accompany pore pressure depletion in the reservoir. The other stages are not, or to a much lesser extent expected, since: 1) Stage 1 was for a large part inferred to reflect damage removal and a return of the sandstone to its approximate, *in-situ* state, which is unlikely to be shown *in-situ*; 2) Any tendency of the reservoir rock to dilate upon incipient Stage 3d (dilatant shear failure) will lead to an increase in the

horizontal/confining stress, which curbs dilatancy; and 3) The total axial strains seen at the onset of Stage 3c (ε > 1.0%; compactive grain failure) frequently exceed the small compaction strains seen in reservoirs undergoing hydrocarbon extraction (0.1 to 1.0%), and in particular those inferred from geodetic and down-hole measurements [*Cannon and Kole*, 2017; *NAM*, 2015] in the Groningen field (up to 0.3%). To provide a general description of the inelastic and elastic deformation behavior corresponding to the reservoir-relevant Stage 2, Chapter 3 reported an empirical, plasticity plus (poro)elastic model, calibrated to the Stage 2 compression data obtained on the laboratory time scales investigated (hours). This model is expected to be relevant to deformation within a large part of the reservoir, including that in the seismogenic center (Figure 1.1), because intergranular clay films are widely reported to occur in the Groningen reservoir and particularly in the seismogenic center of the field [*Wilson*, 1992; *Gaupp et al.*, 1993; *Gaupp and Okkerman*, 2011; *Waldmann*, 2011; *Waldmann and Gaupp*, 2016; *Verberne et al.*, in prep.]. If applicable to the 1-D boundary conditions and decade time-scales relevant to the field, this model provides a convenient framework for quantifying the inelastic behavior of sandstone reservoir rocks, since both the plastic and poroelastic components are often already included in many finite element modelling packages used in geomechanics (*e.g.* Abaqus, Ansys, DIANA).

6.2.1.2 Comparison of the model with 1-D compaction/depletion experiments

The plasticity plus (poro)elasticity model of Chapter 3 is based on data obtained in compression experiments conducted at constant radial stress, hence laterally unrestricted strains. To test whether this model can be applied to describe compaction behavior under the 1-D (uniaxial strain) boundary conditions expected to prevail in the reservoir, it is important to compare the mechanical behavior implied by our model for 1-D compaction (*i.e.* for $\varepsilon_3^{total} = \varepsilon_3^{elastic} + \varepsilon_3^{inelastic} = 0$; see: Section 3.7.2) with data obtained in pore pressure depletion experiments conducted under uniaxial strain boundary conditions. Suitable data have been obtained on Slochteren sandstone samples from the ZRP-3a well by *Hol et al.*[2018], *i.e.* from the same core as used in the present study. In the experiments by Hol et al., samples were first loaded to initial total stress conditions of σ_1 = 65 MPa, $\sigma_2 = \sigma_3$ = 57 MPa, and a pore pressure (P_p) of 35 MPa, such that the initial effective stresses (σ_i - P_p) were σ_1^{eff} = 30 MPa and $\sigma_2^{eff} = \sigma_3^{eff}$ = 22 MPa. The pore pressure was then repeatedly cycled between 35 and 3 MPa, while σ_1 was maintained constant and while servo-controlling $\sigma_2^{eff} = \sigma_3^{eff}$ to maintain zero radial strain. The effective horizontal stress, total uniaxial strain and elastic uniaxial strain versus pore pressure data obtained in these experiments on samples with initial porosities (φ_0) of 16.3% (*i.e.* sample ZRP-3a_18CV), 20.8% (ZRP-3a_10AV) and 25.4%

(ZRP-3a_39CV) are plotted in Figure 6.1. This figure also shows the behavior implied by the constitutive model obtained in Chapter 3 for the same initial stress conditions, a monotonic reduction in P_p from 35 to 3 MPa, and similar initial porosities of 13.4%, 21.5% and 26.4% (Figure 6.1).

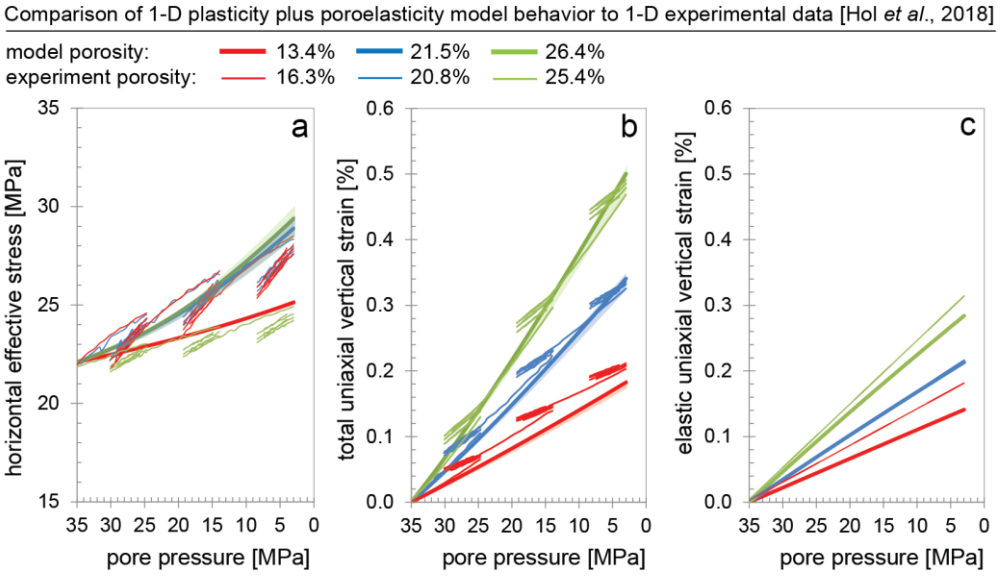

Figure 6.1 Comparison between the 1-D (uniaxial strain) behavior implied by the plasticity plus poroelasticity model reported in Chapter 3, and the data obtained in the 1-D cyclic pore pressure depletion experiments performed on Slochteren sandstone by *Hol et al.*, [2018], on samples with similar initial porosity (φ_0). The various panels show modeled and experimentally measured results for: **a)** horizontal effective stress; **b)** total (*i.e*. elastic plus inelastic) uniaxial vertical strain; and **c)** the elastic uniaxial vertical strain, versus pore pressure curves. The experimental data were retrieved from the data set supplementary to *Hol et al.*, [2018], corresponding to samples ZRP-3a_18CV (initial porosity φ_0 = 16.3%), ZRP-3a_10AV (φ_0 = 20.8%), and ZRP-3a_39CV (φ_0 = 25.4%).

Overall, the predicted and observed behavior agree favourably (Figure 6.1). The model and the experimental data both show a small increase in σ_3^{eff} of 3 – 6 MPa as the P_p is reduced from 35 to 3 MPa (Figure 6.1a). At intermediate porosities (φ_0 = 20.8 to 21.5% - blue curves), the predicted and observed σ_3^{eff} - P_p evolution is closely similar. However, at low porosities (φ_0 = 13.4 to 16.3% - red curves), the modelled increase is σ_3^{eff} accompanying P_p reduction is lower by 3 MPa than that experimentally observed, while at high porosities (φ_0 = 25.4 to 26.4% - green curves), the modelled increase in σ_3^{eff} is higher by 3 MPa than that experimentally shown. Nonetheless, the modelled and experimentally obtained total and

elastic uniaxial strain versus P_p data are closely similar within 0.03% strain (Figures 6.1b,c). Based on the broad agreement between our model and the experimental results obtained for 1-D compaction due to cyclic depletion, we infer that the present model adequately describes the elastic plus (near instantaneous) inelastic compaction behavior of Slochteren sandstone under the 1-D boundary conditions expected in the bulk of the Groningen reservoir and is likely applicable more generally (*e.g.* to small 3-D deformations in the neighbourhood of faults).

6.2.1.3 Effect of inelastic deformation on in-situ stress evolution and strain energy partitioning

In Chapter 3 (Section 3.7.3), we applied the model obtained to the Groningen field, to demonstrate the effect of accounting for the inelastic (versus elastic) contribution to reservoir compaction on the *in-situ* stress evolution and on strain-energy partitioning. Here, we re-iterate the outcome of this application, and the main implications for induced seismicity in the Groningen field. The relevance of the model at the decade time-scales applying to production from the field will be discussed shortly.

The initial (pre-depleted) horizontal stress in the Groningen reservoir is poorly constrained [*Van Eijs*, 2015], but was taken to be equal to 43 MPa, in line with estimates made at depths of 2800 to 3000 m using leak-off test data [*Breckels and Van Eekelen*, 1982]. The σ_3^{eff} evolution accompanying pore pressure reduction from 35 to the current 8 MPa was first evaluated for a 1-D, poroelastic base case, in which the total (elastic + inelastic) deformation behavior shown in experiments was taken to be fully governed by poroelasticity, as is commonly done in many geomechanical treatments (see our Introduction – Section 1.3). The resultant σ_3^{eff} - P_p estimates for φ_0 values of 13.4%, 21.5% and 26.4% are shown in Figure 6.2a. It is shown that the poroelastic σ_3^{eff} evolution is similar for the full range in φ_0 explored. However, the values obtained for the current pore pressure of 8 MPa significantly underpredict the corresponding σ_3^{eff} values of 24 to 29 MPa (*i.e.* by 25 to 50% of the measured values), determined on the basis of mud losses in the period of 2010 to 2014, in the more porous parts of the reservoir [*Van Eijs*, 2015], *i.e.* where the vertically averaged porosity is 18 ± 2% [*NAM*, 2013].

The corresponding σ_3^{eff} - P_p evolutions implied by our plasticity plus (poro)elasticity model during 1-D compression are shown in Figure 6.2b. The σ_3^{eff} values obtained at the current P_p of 8 MPa imply a marked φ_0-sensitivity, where the values obtained for the higher porosities ($\varphi_0 \geq 21.5\%$) correspond much better to the *in-situ* data measured in the high porosity (18 ± 2%) parts of the field (within 25% of the measured values). Hence, for $\varphi_0 \geq$

21.5%, the rate of σ_3^{eff} increase with decreasing P_p is higher when plasticity (*i.e.* inelasticity) is accounted for, compared to the fully (poro)elastic base-case. This indicates that at the explored *in-situ* stresses and 1-D boundary conditions, the tendency of the sandstone to expand radially upon pore pressure reduction is larger in the inelastic plus elastic case, than it is in the purely elastic case. In turn this increase in tendency for radial expansion due to inelastic deformation is likely governed by intergranular slip (plus serially coupled clay consolidation), which in Section 5.8.3 is argued to develop even at small Stage 2 strains, if distributed grain contact strength is accounted for. Furthermore, our model shows that again 30 to 50% of the total uniaxial strain energy (area under the elastic + inelastic strain curves in Figure 6.2c) is inelastic, hence dissipated and unavailable for release through seismic rupture and associated processes. This suggests that poroelastic reservoir compaction models significantly overestimate the energy budget available in the reservoir for seismicity. The impact of this on the magnitude-frequency distribution of earthquakes in Groningen requires further investigation, following the lead given for example by *Bourne et al.*, [2014].

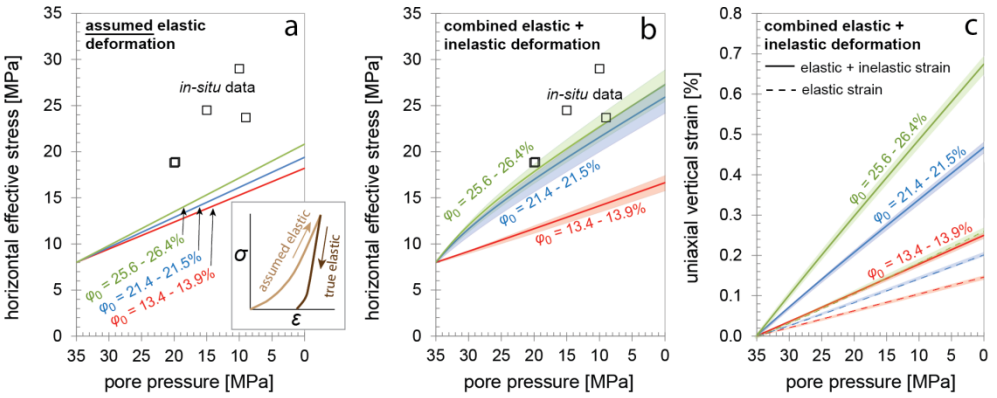

Figure 6.2 Plots showing the effect of accounting for the inelastic contribution to compaction of Slochteren sandstone with initial porosities (φ_0) of 13.4 – 26.4%, on predicted effective horizontal stress (σ_3^{eff}) changes and elastic versus inelastic strain partitioning during pore pressure (P_p) reduction under uniaxial strain conditions (after Figure 3.13 – Chapter 3; see also Section 3.7). Here, we show the horizontal effective stress versus pore pressure evolution, estimated **a)** while assuming that the total deformation is fully poroelastic (see inset), and **b)** by accounting for both the inelastic and elastic contributions, using the plasticity plus poroelasticity model outlined in Chapter 3. **c)** Total and elastic uniaxial vertical strain versus pore pressure curves.

6.2.1.4 Implications for seismicity in the Groningen field

The effective horizontal stress evolution towards relatively high values (24 to 29 MPa) predicted by our plasticity plus poroelasticity model for porosities ≥ 21.5% implies that the differential stress ($Q = \sigma_1 - \sigma_3$) prevailing in the reservoir in the seismogenic center of the field will be lower than estimated through poroelasticity, and lower than in lower porosity parts of the field (φ = 10 to 14%), *i.e.* at the field margins – refer Figure 1.1 (Chapter 1). The lower Q values inferred for high porosity parts of the reservoir imply that faults intersecting these parts may be less prone to rupture. On the other hand, the stresses and strains generated along faults with substantial offset, *i.e.* differential compaction with respect to juxtaposed, low-porosity units such as the Basal Zechstein or Carboniferous shales and siltstones [*e.g. Mulders*, 2003; *Buijze et al.*, 2017], and the elastic strain energy stored in the reservoir will be higher by a factor of two in high porosity areas (*e.g.* for a φ_0 of 21.5 to 26.4%, E = 13.4 to 10.1 GPa) than in low porosity areas (*e.g.* for φ_0 = 13.4%, E = 22.0 GPa). This increases the tendency for faults to rupture in high porosity regions of the reservoir, with respect to low porosity parts. In the Groningen field, this latter effect may be more important in controlling fault rupture than the effect caused by the reduced differential stress in high porosity parts of the field, since the most frequent and largest seismic events are seen in the central part of the reservoir (Figure 1.1, Chapter 1), where the reservoir is most porous (φ = 16 to 22%) and thickest (~200 m). Geomechanical modelling of compaction and fault rupture in the Groningen field has so far assumed elastic reservoir behaviour [*Bourne et al.*, 2014; *Dempsey and Suckale*, 2017; *Van Eijs et al.*, 2006; *Lele et al.*, 2016; *Smith et al.*, 2019; *Wassing et al.*, 2016; *Zbinden et al.*, 2017]. The present findings demonstrate that including the inelastic contribution to reservoir compaction has a key role to play in future geomechanical modelling, and in understanding induced seismicity.

It is further important to note that the plasticity plus poroelasticity model of Chapter 3 not only applies to the reservoir body, but also close to faults, and to modest irregularities within faults. At these locations, deformation may depart from 1-D (uniaxial) compaction, while remaining in the isotropic, small strain (Stage 2) regime where the model applies. The elastic and inelastic deformations developing near such faults will influence the stress development before and up to the point of fault slip, and thus control the onset of fault rupture. However, upon (and possibly before) fault rupture, stresses acting on particularly large-amplitude fault irregularities or asperities may locally be sufficiently large to imply Stage 3c behavior, *i.e.* to lead to pervasive cracking within, or crushing of these asperities, which is not accounted for by the empirical (Stage 2) model. Nonetheless, if significant fault roughness is included in a fault rupture model, then energy dissipation associated with

inelastic deformation in Stages 2 and 3c will decrease the energy available for seismic release [*Cooke and Madden*, 2014], again pointing to the importance of accounting for inelastic deformation.

6.2.2 An improved basis to assess the model relevance at field time-scales

6.2.2.1 Experimental constraints

The data obtained in the incremental loading plus stress relaxation experiments of Chapter 2 showed that the time-dependence or rate-sensitivity of Stage 2 behavior was modest, with only 10 to 20% more inelastic strain being developed during relaxation to $\dot{\varepsilon} \approx 10^{-9}$ s^{-1} (*i.e.* over the course of one week), than had accumulated at a strain rate that was faster by four orders of magnitude ($\dot{\varepsilon} \approx 10^{-5}$ s^{-1}). Of course, this strain rate value of 10^{-9} s^{-1} is still virtually instantaneous compared to the strain rates ($\dot{\varepsilon} \approx 10^{-12}$ s^{-1}) inferred from geodetic and *in-situ* measurements to pertain to accompany production of the Groningen gas field [*Cannon and Kole*, 2017; *NAM*, 2016], and the question remains as to what extent the stress-strain relations given by the model describes the field behavior at $\dot{\varepsilon} \approx 10^{-12}$ s^{-1}, *i.e.* underestimates the compaction strains and resultant horizontal stresses. Long-term (months) 1-D (*i.e.* uniaxial strain) creep experiments performed by *Hol et al.*, [2015a] on similar sandstones from a nearby field (*i.e.* from a Wadden Sea gas field, located within several tens of km from the Groningen field), showed that at constant effective stresses of σ_1^{eff} = 77 MPa and σ_3^{eff} = 23 MPa (*i.e.* at a similar differential stress Q of 44 MPa as the values between 22 and 50 MPa used in the experiments of Chapter 2), the axial strain rate decreased with time, reaching values below 10^{-11} s^{-1} after one to three months (see also the more extensive report by *Hol et al.*, 2015b). The axial strains developing over the course of these months ranged between 0.05 and 0.10%, and contributed a modest 10 to 20% relative to the near-instantaneous inelastic strains that had developed during active loading [*Hol et al.*, 2015b], *i.e.* similar to the time-dependent contributions of 10 to 20% reported in Chapter 2. These data suggest that little additional inelastic strain accumulates at the above noted stresses relevant to depleting reservoirs, over time-scales longer than one to several weeks. The inelastic and elastic stress-strain behavior predicted by the plasticity plus (poro)elasticity model is accordingly expected to be broadly similar at $\dot{\varepsilon}$ down to 10^{-9} s^{-1} (*i.e.* based on the Chapter 2 results), and likely even down to 10^{-11} s^{-1} (*cf.* the data reported by *Hol et al.*, 2015a,b), compared to that obtained at the $\dot{\varepsilon}$ value of 10^{-5} s^{-1} used in Chapter 3, with the model underestimating the inelastic component by perhaps 10 to 20% of the inelastic component. To further constrain the applicability of this model at reservoir-relevant strain rates ($\dot{\varepsilon} \approx 10^{-12}$ s^{-1}) and time scales (decades) which cannot be accessed in the lab,

understanding the processes underlying the Stage 2 experimental data is required.

6.2.2.2 Mechanistic constraints

The microphysical model, as presented in Chapter 5, contributes to understanding the role of time-dependent inelastic processes on field time scales. It was shown in Chapters 4 and 5 that Stage 2 inelastic deformation relevant to the Groningen reservoir can be largely accounted for by serially coupled intergranular slip and clay film consolidation, with a small role played by intragranular cracking. As explained in Section 6.1.4, serially coupled intergranular slip plus clay consolidation implies rapidly decelerating strain rates (from $\dot{\varepsilon} \approx 10^{-5}$ s^{-1} to $\dot{\varepsilon} < 10^{-9}$ s^{-1}, in 24 hours) accompanying the small reductions in differential stress (ΔQ = 1 to 3 MPa) seen in our stress relaxation experiments (Chapter 2), and rapid, virtually instantaneous deformation (rates of order: mm/s) at constant stresses (σ_1^{eff} = 57 MPa, σ_3^{eff} = 27 MPa) pertaining to depletion of the Groningen gas field (see Chapter 4). The virtually instantaneous deformation accommodated by these intergranular mechanisms at the above constant stresses suggests that the time-dependent strains developing during the creep experiments on similar sandstones performed by *Hol et al.*, [2015a] at similar, constant stresses (σ_1^{eff} = 77 MPa and σ_3^{eff} = 23 MPa) may be governed by a different mechanism, notably by stress corrosion (intragranular) cracking, as suggested by the authors. This inference is supported by the evidence reported in Chapter 2, where the role played by intragranular cracking was minor at low porosity and low Q, and increased with increasing porosity and increasing Q. However, the additional inelastic strain due to stress corrosion cracking measured by *Hol et al.*, [2015a], relative to that accumulated instantaneously during loading, was found to be small (10 – 20%), even while exploring strain rates down to 10^{-11} s^{-1}, *i.e.* one order of magnitude larger than that seen in the Groningen field (see previous Section). Therefore, the data in this thesis, and those obtained by *Hol et al.*, [2015a], indicate that while the bulk of the inelastic deformation developing at the small strains relevant to producing reservoirs is largely rate-insensitive at reservoir-relevant stresses, and is adequately accounted for by clay consolidation and intergranular slip, a smaller portion (10 – 20%) is likely accommodated by time-dependent (*i.e.* stress-corrosion) intragranular cracking. To what extent the long-term (decades- centuries) compaction behavior will be influenced by this slow creep process, or by other creep processes (*e.g.* pressure solution) still requires further investigation and quantification. However, the present experimental and mechanistic constraints suggest that reservoir compaction in the Groningen gas field is largely rate-insensitive. In turn, this means that the compaction rate is predominantly governed by the production rate (compaction strain governed by total depletion), while any

ongoing compaction due to stress-corrosion cracking, or other slow creep processes beyond the currently planned field closure in 2022 [*Wiebes*, 2019], is expected to be small. This inference is consistent with a recent microstructural investigation of undepleted (SDM-1) and depleted (ZRP-3a) reservoir sandstones from the Groningen field, which showed no detectable evidence that pressure solution, nor intragranular cracking contributed to compaction during more than 50 years of production [*Verberne et al.,* in prep]. Hence, at present, no microstructural evidence has been found that suggests a detectable time-dependent component of reservoir compaction in the Groningen field. Despite this, an absence of time-dependent reservoir compaction does not necessarily imply independence of subsidence and seismicity from production rate and strategy. Even if reservoir compaction is fully time-independent, subsidence and seismicity may be influenced by time-dependent (creep) deformation of the overlying Basal Zechstein and rock salt [*Marketos et al.*, 2016], and by pore pressure re-equilibration within/near the reservoir (*e.g.* the clay-rich Ten Boer and Ameland members), and/or the underlying low-permeable (Carboniferous) shales [*NAM*, 2017]. In addition, time dependent behavior may perhaps be caused by transient fluid flow along faults [*Postma and Jansen*, 2018; *Zbinden et al.*, 2017].

6.2.3 Implications for the description of small-strain inelastic deformation in other sandstones

Our results also bear important implications for the description of the elastic versus inelastic deformation behavior of sandstones in general, outside the context of the Groningen gas field. As noted in the Introduction (Chapter 1), the yield criterion frequently employed in the literature to mark the onset of inelastic deformation in sandstone corresponds to the departure from linear P - $\Delta\varphi_t$ behavior [*Wong and Baud*, 2012]. While this criterion was originally used to mark the onset of dilatancy, or (shear-)enhanced compaction in sandstone [*Wong et al.*, 1997], it is now frequently employed to delineate the stress conditions below which deformation is treated to be fully poroelastic [*e.g. Baud et al.*, 2004; *Guéguen and Fortin*, 2013; *Brantut et al.*, 2014]. The present data obtained on Slochteren sandstones consistently show inelastic strain development throughout compression, alongside poroelastic strains. Hence, at least for the present experiments, performed on this sandstone, the discrete yield criterion approach does not adequately describe the onset of inelastic behavior. Rather, the data point to a porosity-sensitive compactive yield envelope, that expands with increasing inelastic strain from the onset of compression [*cf. Karner et al.*, 2005], or at least when the applied stresses exceed a previously supported stress state (Section 6.1).

Microphysical modelling of the Slochteren sandstone showed that Stage 1 and Stage 2 yield envelope expansion and associated hardening was largely accommodated by intergranular slip plus serial clay film consolidation. Hence, in other (reservoir) sandstones containing clay films within grain contacts [*Berger et al.*, 2009; *Billault et al.*, 2003; *Dutton et al.*, 2017; *Louis et al.*, 2009], similar, continuous yielding can be expected. Interestingly, inelastic deformation has been reported to occur during Stages 1 and/or 2 (*i.e*. prior to Stage 3c and Stage 3d), in several other sandstones (*i.e*. Berea sandstone - *Wong et al.*, [1992]; *Shalev et al.*, [2014]; the Castlegate and Salt Wash sandstones - *Bernabe et al.*, [1994]; and the Darley Dale sandstone - *Shalev et al.*, [2014]). While all of these sandstones are described to contain clay, it is unclear whether the clay is present in the pore space only, or also within grain contacts, such that it contributes to the load-bearing framework and potentially accommodates inelastic strain during loading. If pre-Stage 3d/3c inelastic strains are not accommodated by clay consolidation and slip, they may possibly arise from grain-contact asperity crushing, plus subsequent grain re-arrangements, or from intragranular cracking of particularly weak grains [*Brzesowsky et al.*, 2014b].

Aside from the detailed mechanisms, it appears that many sandstones show continuous yielding behavior well before Stages 3d and 3c, in qualitatively similar manner to that shown by the Slochteren sandstone [*Bernabe et al.*, 1994; *Shalev et al.*, 2014; *Wong et al.*, 1992]. While the magnitude of these inelastic strains preceding Stages 3d and 3c may be small (< 0.5%) compared to the much larger inelastic strains accompanying Stages 3d and 3c (> 1 to 10%), they may constitute a significant portion of the total deformation (ε < 1%) accompanying pore pressure changes during hydrothermal energy production, hydrocarbon production, or CO_2 storage. Hence, in future studies investigating the mechanical response of sandstones at the small strains relevant to these sub-surface activities [*e.g*. *Schutjens et al.*, 2004; *Hangx et al.*, 2013; *Heap et al.*, 2019], the possibility of early inelastic strain development (*i.e*. pre-Stage 3d/3c), and concomitant, inelastic strain hardening should be considered, alongside the poroelastic response.

6.3 Remaining questions and suggestions for future research

The present research has provided a detailed investigation of the time-insensitive compaction behaviour of the Slochteren sandstone reservoir in the Groningen gas field, and of the controlling microphysical mechanisms. In addition, a first step towards quantifying these underlying microphysical mechanisms has been made. However, the work leaves behind a number of unanswered questions and has brought up a number of new issues that should be addressed in future. These are outlined below.

6.3.1 Unsolved issues and remaining data needs

A number of possible issues to address in future (experimental) work follow directly from the present research. In addition, the datasets are not in all cases complete and call for further work.

6.3.1.1 The effect of grain compressibility on effective stress estimates

In this thesis, the compressibility of the grain phases constituting the Slochteren sandstone has been assumed to be negligible compared to that of the grain framework (*i.e.* the Biot coefficient was assumed to be equal or close to 1). Previous experiments performed on Slochteren sandstones [*Hettema et al.*, 2000; *Hol et al.*, 2018 - see supplementary dataset], and the, similar responses of the bulk and pore volume data during increases in P observed in this study (*i.e.* within the limited absolute accuracy of ± 0.03% on the bulk volumetric strain; see Figure 3.4 of Chapter 3), all suggest that this is generally the case. However, the value and effect of the Biot coefficient being < 1 [*Lele et al.*, 2015] on the elastic and inelastic deformation behavior has not been rigorously quantified in this study. In future work, the significance of accounting for the compressibility of the grain phases constituting the Slochteren sandstone with respect to that of the grain framework can be explored by comparing the mechanical response during 1-D axial loading to the response shown during pore pressure depletion under (1-D) uniaxial strain boundary conditions. Of course, the Biot coefficient can also be measured directly [*e.g*. *Blöcher et al.*, 2014]. Evidently, the outcome may affect fault rupture models in which the Biot coefficient is similarly assumed to be 1, or close to 1 [*e.g. van den Bogert*, 2015; *Buijze et al.*, 2017], as the changes in the effective stresses acting on faults decrease, with decreasing Biot coefficient (see Section 2.4.2).

6.3.1.2 Effect of boundary conditions: conventional triaxial testing versus uniaxial strain experiments

It has been shown that the present plasticity plus (poro)elasticity model, calibrated to data obtained in triaxial compression testing conducted at constant radial stress (hence laterally unrestricted strain boundary conditions) renders similar 1-D behavior at the sample-scale, to that observed in 1-D compaction/depletion experiments (Figure 6.1). However, despite the general correspondence seen at the sample-scale, the underlying, micro-mechanical behavior may be (subtly) different. Under uniaxial strain boundary conditions, slip on grain contacts cannot occur without being accommodated by normal strain developing on the surrounding grain contacts, which in turn should then be accommodated by consolidation of clay films, or by intragranular cracking of surrounding

grains (Figure 6.3a). By contrast, in conventional triaxial compression experiments, intergranular slip is theoretically possible, even in the absence of any other inelastic processes (Figure 6.3b). The coupling between intergranular slip and consolidation or intragranular cracking, and the effect on this of the imposed boundary conditions may affect the outcome of future microphysical modelling of sandstone and should be investigated further. A more rigorous investigation of the effects of the imposed boundary conditions on the micro-mechanical compaction behavior would require a new set of stress-cycling experiments on sandstones with similar initial properties, conducted at both uniaxial strain boundary conditions and at constant confining pressure. The stress-strain behavior can then be compared for both boundary conditions, for instance by delineating fixed values of strain (*e.g.* inelastic porosity reduction, *cf.* Chapter 3) in *Q*-*P* space. These data can be subsequently used to further test and/or calibrate the model behavior at different boundary conditions, which in turn will benefit the reliability of the model to describe the general deformation behavior of the reservoir, both distal and proximal to faults and/or other discontinuities. With reference to Figure 6.3, it will also be interesting to explore whether the different boundary conditions lead to detectible differences in the microstructural evolution.

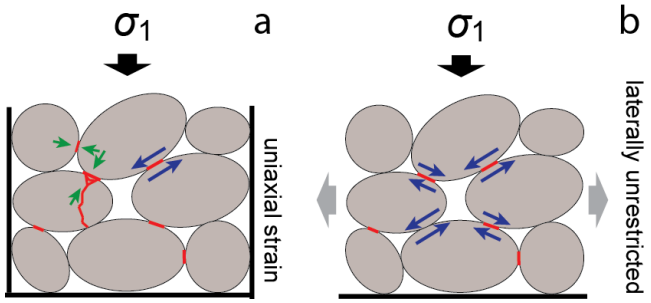

Figure 6.3 a) Under uniaxial strain boundary conditions, slip along one grain contact (blue arrows) requires intragranular cracking or consolidation at another (green arrows); **b)** At constant confining pressure, hence laterally unrestricted boundary conditions, intergranular slip can theoretically occur in the absence of any other process.

6.3.1.3 Improving the resolution of experimentally constrained yield envelope expansion

In Chapter 3, the shape and size evolution of the Cam-clay yield envelope was calibrated to the experimentally obtained, inelastic porosity reduction ($\Delta\varphi_i$) data contoured at fixed values in *Q*-*P* space. Owing to the limited number of samples available per core sections (core diameter ~10 cm) the resultant yield envelopes were typically constrained by only three data points. Because of this, the shape and size of the envelopes are subject to uncertainty due to the limited number of data points, and/or to sample variation. Evidently,

this restricts the reliability of the plasticity model used to estimate the *in-situ* stress evolution accompanying pore pressure reduction in the Groningen field. If the number of available samples is limited, as was the case in our study, the shape of the yield envelope may be delineated at higher resolution by following the method outlined by *Tembe et al.*, [2007]. These authors delineated fixed values of porosity reduction, using a single sample, by manipulating the confining pressure and axial stress imposed in a triaxial test, so as to maintain constant pore volume. Alternatively, envelopes of fixed inelastic porosity reduction can be mapped, again using a single sample, by combining the triaxial ('stress probing') testing methodology as outlined by *Bedford et al.*, [2019], with the stress-cycling procedure employed in Chapter 3. Here, a single sample may be subjected to stress-cycling to increasingly higher compressive stresses until a given value of $\Delta\varphi_i$ is measured. The sample is then partially unloaded, and subsequently cyclically reloaded along a different stress path, until the previously explored, maximum value of $\Delta\varphi_i$ increases. By employing such methods, the expansion of the yield envelope may be constrained at much higher resolution, which in turn will improve the accuracy of the stress-strain behavior predicted by empirical (plasticity) models calibrated to these data.

6.3.1.4 Effect of shear strain on Stage 2 hardening behavior and concomitant yield envelope expansion

The plasticity model used in Chapter 3 is calibrated to Stage 2 $\Delta\varphi_i$ data with hardening assumed to be sensitive only to $\Delta\varphi_i$, and not to the inelastic axial, or shear strain. While the Stage 2 behavior is well-described by this assumption, it likely constitutes a simplification, as, at least upon Stage 3d, hardening was shown to progress at constant, or increasing pore volume (*i.e.* dilation). Indeed, a more elaborate study investigating the evolution of the yield envelope during Stage 3d and 3c sandstone deformation [by *Bedford et al.*, 2019] showed that, at least for these high strain stages, the expansion of the yield envelope is sensitive to the imposed shear strain, hence not only to the volumetric strain, or porosity reduction. Whether similar behavior is shown during Stage 2 remains yet unclear, and should be investigated in more detail than presently explored.

6.3.2 Broader challenges for the future

In this thesis, several issues have been identified that are outside the scope of a direct follow-up study, adding to the data obtained in this one, but deserving attention in their own right.

6.3.2.1 Microphysical model developments: From unit cell to DEM and homogenization approaches

In Chapter 5, a basis is established for future microphysical modelling of elastic plus inelastic deformation of the Slochteren sandstone. In its present form, the main trends in time-independent, inelastic deformation behavior were shown to be accounted for by incorporating a role played by intergranular clay deformation. However, for faithful representation of the continuous stress versus elastic and inelastic deformation behavior seen in the present experiments, the model, or a similar, mechanistic-based model, still requires future development.

The uniformity of the simplified microstructure (*i.e.* the constant grain/grain contact strength and size, and the regular grain packing) considered in our model implies discrete, process-specific yield conditions, and concomitant, discontinuous stress-strain behavior, not shown in our experiments. Evidently, in natural Slochteren sandstones, the microstructure is heterogeneous, while the stress-strain behavior is more smoothed out. In future work, the effect of structural heterogeneity on the inelastic deformation behavior may be investigated by incorporating a statistically distributed grain strength [*Brzesowsky et al.*, 2014b], and/or grain contact clay strength, in the current model. Alternatively, the effect of heterogeneous grain and grain contact size distributions, and spatial variation in grain packing, and clay film thickness may be explored by discrete element method modelling [*e.g. Marketos and Bolton*, 2009]. Another approach would be a homogenization (volume averaging) approach incorporating appropriate internal variables, following authors such as *Sulem and Mühlhaus*, [1997], and *Stefanou et al.*, [2008].

If microstructural or micro-mechanical heterogeneity is included in future microphysical models for the Slochteren sandstone, dilatant intergranular slip and intragranular cracking may locally occur already during Stages 1 and 2. To evaluate the effect of these processes on the overall stress-strain behavior, particularly for the reservoir-relevant Stage 2, the local hardening or softening behavior implied by these processes should be considered in more detail. While we explored the strain increment arising from intragranular cracking, at least at constant stress conditions, the stress-strain response due to dilatant intergranular slip has so far not yet been described. This hampers a direct comparison of the Stage 2 behavior resultant from our microphysical model to the behavior predicted by the plasticity model of Chapter 3, in which a stress-controlled interplay between dilatant and compactive deformation is implied. Hardening during dilation may arise from slip-hardening behavior of the intergranular clay films [*Tembe et al.*, 2010]. Alternatively, it may be that local dilation may lead to elastic distortion of the surrounding

material, such that the dilatant hardening behavior is effectively governed by the elastic properties of the bulk. In particular, this last approach has some appeal, as the dilatant porosity reduction shown in our experiments during Stage 3d loading is generally found to be largely recovered during subsequent unloading, suggesting that dilation is in part elastic, at least until a shear fracture is formed. However, it may be challenging to quantify the extent to which locally induced dilation is accommodated by poroelastic compression of the surrounding volume, versus the portion that is transmitted to the outer edges of the modeled volume, leading to net, bulk dilation. This effect presumably depends on the size of the representative elementary volume considered, *i.e.* on the volume of poroelastically deforming material surrounding a dilatant point within the model microstructure. In future modelling efforts, these, or other dilatant hardening effects can perhaps be explored further.

6.3.2.2 Improving constraints on the intergranular clay film thickness and behaviour

The present microphysical model behavior was found to be markedly sensitive to the assumed thickness of the clay films present within the grain contacts. The typical thickness of grain contact clay films was estimated to range from 3 – 6 μm, by using 2-D section micrographs. Ideally, such thickness estimates should be verified using 3-D, X-ray scanning or neutron imaging, or (cryo-)FIB tomography. However, to achieve the sub-micron resolution required for such thickness determinations, state-of-the-art X-ray tomography methods require samples with a diameter of only several grains wide (≤ 1 mm). While preparing such samples is challenging, the small volume per sample imply that many samples need to be inspected for the outcome to be statistically significant. By contrast, FIB tomography (*i.e.* sequential ion-milling plus SEM imaging) will be able to achieve the required resolution to accurately measure the clay film thickness within sectioned grain contacts. However, to obtain a statistically large enough distribution of clay coating thickness, again this would mean the sectioning of a large number of grain boundaries. Hence, placing reliable constraints on the clay films present in grain contacts using current, state-of-the-art imaging techniques, remains highly challenging. We do note, though, that the contrast of the intergranular clays with respect to other phases in CT imaging may be improved by first saturating the sample with contrasting agents [*Nadeev et al.*, 2013], such as a Ba-solution or heavy (D_2O) water. Furthermore, qualitative analysis of the section micrographs recovered in this study suggested that the thickness of the grain contact clay films increases with increasing bulk sandstone porosity. Further quantification and explanation of this apparent trend was not pursued, as it would imply a rigorous microstructural study (as above), which was outside the present research scope.

6.3.2.3 Constraining the distribution of clay-bearing sandstones in a reservoir-scale facies model

We showed that Stage 2, inelastic deformation can largely be accounted for by slip on- and consolidation of intergranular clay films, present in the Slochteren sandstones from the center of the Groningen gas field (*i.e.* from the SDM-1 and ZRP-3a wells). In the absence of intergranular clay, Stage 2, inelastic deformation is anticipated to be less prominent, though this has not yet been verified, and other mechanisms, such as asperity crushing, may play a role. Once all operating grain-scale mechanisms are identified and described in terms of constitutive laws, it is key to incorporate such laws into numerical models that are capable of taking into account variations in porosity, grain size and grain composition, such as Discrete Element Method models [*Kawamoto et al.*, 2016; *Marketos and Bolton*, 2009]. Through volume averaging it may then be possible to upscale these simulated stress-strain and stress-strain rate behaviors to the reservoir scale.

However, to predict the elastic versus inelastic deformation over the entire Groningen gas field in a realistic and meaningful way, the reservoir model should includes the main variations in porosity, grain size and mineralogy. To this end, a depositional/diagenetic facies model of the reservoir is needed. Ideally, such a model should be based on petrographical constraints on the (expected) spatial distribution of intergranular clays, and in particular those present within grain contacts. Such a facies model may be applied to map out the parts of the field where significant Stage 2 inelastic deformations due to intergranular clay deformation should be expected, and where a larger poroelastic signature can be expected. Since the inelastic contribution to Stage 2 deformation was shown to affect the *in-situ* stress-evolution and the strain-energy budget available for seismicity, these effects will be directly influenced by the facies model.

6.3.2.4 Extrapolation to the decade time-scales and slow strain rates relevant to the Groningen gas field

Most of the experiments reported in this thesis were performed at loading rates ($\dot{P} \approx$ 0.1 MPa/s) and/or strain rates ($\dot{\varepsilon} \approx 10^{-5}$ s^{-1}) that are essentially instantaneous at the time-scales relevant to the reservoir, while the lowest strain rate experimentally explored ($\dot{\varepsilon} \approx 10^{-9}$ s^{-1}) is still a 1000 times faster than the strain rate seen in the Groningen gas field ($\dot{\varepsilon} \approx 10^{-12}$ s^{-1}) [*Cannon and Kole*, 2017]. The mechanistic constraints outlined in this thesis contribute to an improved mechanistic basis to assess to what extent the laboratory data apply to the much lower, field-relevant strain rates. The deformation mechanisms shown by using this model to largely accommodate the inelastic contribution to Stage 2 deformation in

our experiments (*i.e.* serially coupled, intergranular slip plus clay film consolidation), were found to be virtually time-independent, at constant effective stresses pertaining to the current state of depletion in the Groningen reservoir, while the time-dependent contribution of subordinate intragranular (stress-corrosion) cracking to the instantaneously accumulated inelastic strain was shown to be small (10 – 20% of the instantaneously accumulated inelastic strain) down to strain rates of 10^{-11} s^{-1}.

However, to constrain the rate-sensitivity of Stage 2 deformation behavior better, the role played by intragranular cracking in accommodating Stage 2 inelastic strains, and the rate-sensitivity thereof needs to be quantified further, as does the role of any deformation mechanisms not observed in the present, short-duration experiments. In part, this may be achieved by conducting a new set of long-term (weeks-months) experiments, exploring the elastic versus inelastic strain behavior, and the role played by intragranular (stress-corrosion) cracking or other slow creep processes (*e.g*. pressure solution), at strain rates as low as 10^{-10} s^{-1} or possibly even 10^{-11} s^{-1}. Experiments that can be considered include a) new, higher precision stress relaxation experiments, b) creep tests at *in-situ* stress, and c) both types of experiments, while exploring modestly higher temperatures or varied mean grain size to assess the role of thermally activated and grain size dependent processes. The data obtained can then be used to further develop and calibrate the microphysical model, so as to include the rate-sensitivity of Stage 2, inelastic deformation, resulting from intragranular cracking or mass transfer processes. This will improve the mechanistic basis for assessing the applicability of laboratory data at field time-scales, and may even allow for direct model extrapolation to field-relevant strain rates.

References

Allman, M.A., and Atkinson, J.H. (1992). Mechanical properties of reconstituted Bothkennar soil. *Géotechnique*. DOI:10.1680/geot.1992.42.2.289

Altmann, J.B., Müller, T.M., Müller, B.I.R., Tingay, M.R.P., and Heidbach, O. (2010). Poroelastic contribution to the reservoir stress path. *International Journal of Rock Mechanics and Mining Sciences*, *47*, 1104–1113. DOI:10.1016/j.ijrmms.2010.08.001

Amthor, J.E., and Okkerman, J. (1998). Influence of early diagenesis on reservoir quality of Rotliegend sandstones, Northern Netherlands. *American Association of Petroleum Geologists Bulletin*, *82*, 2246–2265.

Antonellini, M.A., and Pollard, D.D. (1995). Distinct element modeling of deformation bands in sandstone. *Journal of Structural Geology*. DOI:10.1016/0191-8141(95)00001-T

Ashby, M.F., and Sammis, C.G. (1990). The damage mechanics of brittle solids in compression. *Pure and Applied Geophysics*, *133*(3), 489–521. DOI:10.1007/BF00878002

Atkinson, B.K., and Meredith, P.G. (1987). Experimental fracture mechanics data for rocks and minerals. In Atkinson, B. K. (Ed.), *Fracture Mechanics of Rock*. Academic Press. DOI:10.1016/b978-0-12-066266-1.50016-8

Baranova, V., Mustaqeem, A., and Bell, S. (1999). A model for induced seismicity caused by hydrocarbon production in the Western Canada Sedimentary Basin. *Canadian Journal of Earth Sciences*, *36*(1), 47–64. DOI:10.1139/e98-080

Bardainne, T., Dubos-sallée, N., Sénéchal, G., Gaillot, P., and Perroud, H. (2008). Analysis of the induced seismicity of the Lacq gas field (Southwestern France) and model of deformation. *Geophysical Journal International*, *172*(3), 1151–1162. DOI:10.1111/j.1365-246X.2007.03705.x

Batchelor, G.K. (2000). Flow of a Uniform Incompressible Viscous Fluid. In *An Introduction to Fluid Dynamics* (pp. 174–263). Cambridge: Cambridge University Press. DOI:10.1017/CBO9780511800955.006

Baud, P., Zhu, W., and Wong, T. -f. (2000). Failure mode and weakening effect of water on sandstone. *Journal of Geophysical Research*, *105*, 371–389.

Baud, P., Klein, E., and Wong, T. -f. (2004). Compaction localization in porous sandstones: spatial evolution of damage and acoustic emission activity. *Journal of Structural Geology*, *26*(4), 603–624. DOI:10.1016/j.jsg.2003.09.002

Baud, P., Vajdova, V., and Wong, T. -f. (2006). Shear-enhanced compaction and strain localization: Inelastic deformation and constitutive modeling of four porous sandstones. *Journal of Geophysical Research: Solid Earth*, *111*(12). DOI:10.1029/2005JB004101

Baud, P., Wong, T. -f., and Zhu, W. (2014). Effects of porosity and crack density on the compressive strength of rocks. *International Journal of Rock Mechanics and Mining Sciences*, *67*, 202–211. DOI:10.1016/j.ijrmms.2013.08.031

Bedford, J.D., Faulkner, D.R., Leclère, H., and Wheeler, J. (2018). High-Resolution Mapping of Yield Curve Shape and Evolution for Porous Rock: The Effect of Inelastic Compaction on Porous Bassanite. *Journal of Geophysical Research: Solid Earth*. DOI:10.1002/2017JB015250

Bedford, J.D., Faulkner, D.R., Wheeler, J., and Leclère, H. (2019). High-resolution mapping of yield curve shape and evolution for high porosity sandstone. *Journal of Geophysical Research: Solid Earth*. DOI:10.1029/2018jb016719

Berger, A., Gier, S., and Krois, P. (2009). Porosity-preserving chlorite cements in shallow-marine volcaniclastic sandstones: Evidence from cretaceous sandstones of the sawan gas field, Pakistan. *AAPG Bulletin*. DOI:10.1306/01300908096

Bernabe, Y., Fryer, D.T., and Hayes, J.A. (1992). The effect of cement on the strength of granular rocks. *Geophysical Research Letters*, *19*(14), 1511–1514.

Bernabe, Y., Fryer, D.T., and Shively, R.M. (1994). Experimental-Observations of the Elastic and Inelastic Behavior of Porous Sandstones. *Geophysical Journal International*, *117*, 403–418.

Billault, V., Beaufort, D., Baronnet, A., and Lacharpagne, J.-C. (2003). A nanopetrographic and textural study of grain-coating chlorites in sandstone reservoirs. *Clay Minerals*. DOI:10.1180/0009855033830098

Blöcher, G., Reinsch, T., Hassanzadegan, A., Milsch, H., and Zimmermann, G. (2014). Direct and indirect laboratory measurements of poroelastic properties of two consolidated sandstones. *International Journal of Rock Mechanics and Mining Sciences*, *67*, 191–201. DOI:10.1016/j.ijrmms.2013.08.033

Van den Bogert, P.A.J. (2015). *Impact of various modelling options on the onset of fault slip and fault slip response using 2-dimensional Finite-Element modelling*. *NAM, SR.15.11455*. Assen.

Borg, I.Y., Friedman, M., Handin, J., and Higgs, D.V. (1960). Experimental Deformation of St. Peter Sand: A study of Cataclastic Flow. *Geological Society of America Memoris*, *79*, 133–192. DOI:10.1130/MEM79-p133

Bouckovalas, G.D., Andrianopoulos, K.I., and Papadimitriou, A.G. (2003). A critical state interpretation for the cyclic liquefaction resistance of silty sands. *Soil Dynamics and Earthquake Engineering*, *23*(2), 115–125. DOI:10.1016/S0267-7261(02)00156-2

Bourne, S.J., Oates, S.J., Van Elk, J., and Doornhof, D. (2014). A seismological model for earthquakes induced by fluid extraction from a subsurface reservoir. *Journal of Geophysical Research: Solid Earth*, *119*, 8991–9015. DOI:10.1002/2014JB011663

Bourne, S.J., Oates, S.J., Bommer, J.J., Dost, B., Van Elk, J., and Doornhof, D. (2015). A monte carlo method for probabilistic hazard assessment of induced seismicity due to conventional natural gas production. *Bulletin of the Seismological Society of America*, *105*(3), 1721–1738. DOI:10.1785/0120140302

Brantut, N., Heap, M.J., Meredith, P.G., and Baud, P. (2013). Time-dependent cracking and brittle creep in crustal rocks: A review. *Journal of Structural Geology*, *52*, 17–43. DOI:10.1016/j.jsg.2013.03.007

Brantut, N., Heap, M.J., Baud, P., and Meredith, P.G. (2014). Rate- and strain-dependent brittle deformation of rocks. *Journal of Geophysical Research: Solid Earth*, *119*(3), 1818–1836. DOI:10.1002/2013JB010448

Breckels, I.M., and Van Eekelen, H.A.M. (1982). Relationship Between Horizontal Stress and Depth in Sedimentary Basins. *Journal of Petroleum Technology*, *34*, 2191–2199. DOI:10.2118/10336-PA

Brouwer, A.S., Van den Broek, M., Zappa, W., Turkenburg, W.C., and Faaij, A. (2016). Least-cost options for integrating intermittent renewables in low-carbon power systems. *Applied Energy*, *161*, 48–74. DOI:10.1016/j.apenergy.2015.09.090

Brown, K.M., Poeppe, D., Josh, M., Sample, J., Even, E., Saffer, D., Tobin, H., Hirose, T., Kulongoski, J.T., Toczko, S., and Maeda, L. (2017). The action of water films at Å-scales in the Earth: Implications for the Nankai subduction system. *Earth and Planetary Science Letters*. DOI:10.1016/j.epsl.2016.12.042

Brzesowsky, R.H., Spiers, C.J., Peach, C.J., and Hangx, S.J.T. (2011). Failure behavior of single sand grains: Theory versus experiment. *Journal of Geophysical Research: Solid Earth*, *116*(March), 1–13. DOI:10.1029/2010JB008120

Brzesowsky, R.H., Hangx, S.J.T., Brantut, N., and Spiers, C.J. (2014a). Compaction creep of sands due to time-dependent grain failure: Effects of chemical environment, applied stress and grain size. *Journal of Geophysical Research: Solid Earth*, (119), 1–21. DOI:10.1002/2014JB011277

Brzesowsky, R.H., Spiers, C.J., Peach, C.J., and Hangx, S.J.T. (2014b). Time-independent compaction behavior of quartz sands. *Journal of Geophysical Research : Solid Earth*, (119), 5814–5829. DOI:10.1002/2014JB011151

Buijze, L., Van Den Bogert, P.A.J., Wassing, B.B.T., Orlic, B., and Ten Veen, J. (2017). Fault reactivation mechanisms and dynamic rupture modelling of depletion-induced seismic events in a Rotliegend gas reservoir. *Geologie En Mijnbouw/Netherlands Journal of Geosciences*, *96*(5), 131–148. DOI:10.1017/njg.2017.27

Buscarnera, G., and Laverack, R.T. (2014). Path dependence of the potential for compaction banding: Theoretical predictions based on a plasticity model for porous rocks. *Journal of Geophysical Research: Solid Earth*. DOI:10.1002/2013JB010562

Candela, T., Osinga, S., Ampuero, J.-P., Wassing, B., Pluymaekers, M., Fokker, P.A., van Wees, J.-D., de Waal, H.A., and Muntendam-Bos, A.G. (2019). Depletion-induced seismicity at the Groningen gas field: Coulomb rate-and-state models including differential compaction effect. *Journal of Geophysical Research: Solid Earth*. DOI:10.1029/2018JB016670

Cannon, M., and Kole, P. (2017). The First Year of Distributed Strain Sensing (DSS) Monitoring in the Groningen Gas Field, *SR.17.0093*(November).

Carrier, B., Vandamme, M., Pellenq, R.J.M., Bornert, M., Ferrage, E., Hubert, F., and Van Damme, H. (2016). Effect of Water on Elastic and Creep Properties of Self-Standing Clay Films. *Langmuir*. DOI:10.1021/acs.langmuir.5b03431

Chan, A.W., Hagin, P.N., and Zoback, M.D. (2004). Viscoplastic deformation in unconsolidated resevoir sands: field applications using dynamic DARS analysis. *ARMA/NARMS*.

Chang, C., Zoback, M.D., and Khaksar, A. (2006). Empirical relations between rock strength and physical properties in sedimentary rocks. *Journal of Petroleum Science and Engineering*, *51*, 223–237. DOI:10.1016/j.petrol.2006.01.003

Cheng, Y.P., Nakata, Y., and Bolton, M.D. (2003). Discrete element simulation of crushable soil. *Géotechnique*. DOI:10.1680/geot.53.7.633.37389

Chester, J.S., Lenz, S.C., Chester, F.M., and Lang, R.A. (2004). Mechanisms of compaction of quartz sand at diagenetic conditions. *Earth and Planetary Science Letters*, *220*, 435–451. DOI:10.1016/S0012-821X(04)00054-8

Chuhan, F.A., Kjeldstad, A., Bjørlykke, K., and Høeg, K. (2002). Porosity loss in sand by grain crushing - Experimental evidence and relevance to reservoir quality. *Marine and Petroleum Geology*, *19*(1), 39–53. DOI:10.1016/S0264-8172(01)00049-6

Cole, D.M., and Hopkins, M.A. (2017). The contact properties of naturally occurring geologic materials: contact law development. *Granular Matter*. DOI:10.1007/s10035-016-0683-4

Cook, J.E., Goodwin, L.B., Boutt, D.F., and Tobin, H.J. (2015). The effect of systematic diagenetic changes on the mechanical behavior of a quartz-cemented sandstone. *Geophysics*, *80*(2), D145–D160. DOI:10.1190/Geo2014-0026.1

Cooke, M.L., and Madden, E.H. (2014). Is the Earth Lazy? A review of work minimization in fault evolution. *Journal of Structural Geology*. DOI:10.1016/j.jsg.2014.05.004

Crawford, B.R., and Yale, D.P. (2002). Constitutive Modeling of Deformation and Permeability: Relationships between Critical State and Micromechanics. *Proceedings of SPE/ISRM Rock Mechanics Conference*. DOI:10.2118/78189-MS

Crawford, B.R., Sanz, P.F., Alramahi, B., and DeDontney, N.L. (2011). Modeling and Prediction of Formation Compressibility and Compactive Pore Collapse in Siliciclastic Rocks. *ARMA 45th US Rock Mechanics / Geomechanics Symposium*, *11*(384).

Cuisiat, F., Jostad, H.P., Andresen, L., Skurtveit, E., Skomedal, E., Hettema, M., and Lyslo, K. (2010). Geomechanical integrity of sealing faults during depressurisation of the Statfjord Field. *Journal of Structural Geology*, *32*(11), 1754–1767. DOI:10.1016/j.jsg.2010.01.006

Curran, J.H., and Carroll, M.M. (1979). Shear stress enhancement of void compaction. *Journal of Geophysical Research*, *84*(B3), 1105. DOI:10.1029/JB084iB03p01105

Dahm, T., Krüger, F., Stammler, K., Klinge, K., Kind, R., Wylegalla, K., and Grasso, J.R. (2007). The 2004 Mw 4.4 Rotenburg, northern Germany, earthquake and its possible relationship with gas recovery. *Bulletin of the Seismological Society of America*. DOI:10.1785/0120050149

Darling, T.W. (2004). Neutron diffraction study of the contribution of grain contacts to nonlinear stress-strain behavior. *Geophysical Research Letters*, *31*(16), 31–34. DOI:10.1029/2004GL020463

Das, A., Tengattini, A., Nguyen, G.D., Viggiani, G., Hall, S.A., and Einav, I. (2014). A thermomechanical constitutive model for cemented granular materials with quantifiable internal variables. Part II - Validation and localization analysis. *Journal of the Mechanics and Physics of Solids*, *70*, 382–405. DOI:10.1016/j.jmps.2014.05.022

David, C., Menendez, B., Zhu, W., and Wong, T. -f. (2001). Mechanical compaction, microstructures and permeability evolution in sandstones. *Physics and Chemistry of the Earth, Part A: Solid Earth and Geodesy*, *26*(1), 45–51. DOI:10.1016/S1464-1895(01)00021-7

David, E.C., Brantut, N., Schubnel, A., and Zimmerman, R.W. (2012). Sliding crack model for nonlinearity and hysteresis in the uniaxial stress–strain curve of rock. *International Journal of Rock Mechanics and Mining Sciences*, *52*, 9–17. DOI:10.1016/j.ijrmms.2012.02.001

Davies, R., Foulger, G., Bindley, A., and Styles, P. (2013). Induced seismicity and hydraulic fracturing for the recovery of hydrocarbons. *Marine and Petroleum Geology*. DOI:10.1016/j.marpetgeo.2013.03.016

Dempsey, D., and Suckale, J. (2017). Physics-based forecasting of induced seismicity at Groningen gas field, the Netherlands. *Geophysical Research Letters*, *44*(15), 7773–7782. DOI:10.1002/2017GL073878

Desai, C.S., and Siriwardane, H.J. (1984). *Constitutive laws for enginieering materials: with emphasis on geological materials*. Prentice-Hall.

Desbois, G., Urai, J.L., Hemes, S., Schröppel, B., Schwarz, J.O., Mac, M., and Weiel, D. (2016). Multi-scale analysis of porosity in diagenetically altered reservoir sandstone from the Permian Rotliegend (Germany). *Journal of Petroleum Science and Engineering*. DOI:10.1016/j.petrol.2016.01.019

Dewers, T., and Hajash, A. (1995). Rate laws for water-assisted compaction and stress-induced water-rock interaction in sandstones. *Journal of Geophysical Research*, *100*, 13093.

DOI:10.1029/95JB00912

Diaz, G., Kittl, P., and Rosales, M. (2003). Probabilistic design and quality control in probabilistic strength of materials. *International Journal of Solids and Structures*, *40*(19), 5001–5015.

Dieterich, J.H. (1972). Time-dependent friction in rocks. *Journal of Geophysical Research*, *77*(20), 3690. DOI:10.1029/JB077i020p03690

Dieterich, J.H. (1978). Time-dependent friction and the mechanics of stick-slip. *Pure and Applied Geophysics*, *116*(4–5), 790–806. DOI:10.1007/BF00876539

Digby, P.J. (1981). The Effective Elastic Moduli of Porous Granular Rocks. *Journal of Applied Mechanics*. DOI:10.1115/1.3157738

DiGiovanni, A.A., Fredrich, J.T., Holcomb, D.J., and Olsson, W.A. (2007). Microscale damage evolution in compacting sandstone. *Geological Society, London, Special Publications*, *289*(1), 89–103. DOI:10.1144/SP289.6

DiMaggio, F.L., and Sandler, I.S. (1971). Material Model for Granular Soils. *Journal of the Engineering Mechanics Division*, *97*(3), 935–950. Retrieved from http://cedb.asce.org/cgi/WWWdisplay.cgi?7100054

Dobereiner, L., and De Freitas, M.H. (1986). Geotechnical properties of weak sandstones. *Géotechnique*, *36*(1), 79–94. DOI:10.1680/geot.1986.36.1.79

Doser, D.I., Baker, M.R., and Mason, D.B. (1991). Seismicity in the War-Wink gas field, Delaware Basin, west Texas, and its relationship to petroleum production. *Bulletin of the Seismological Society of America*, *81*(3), 971–986. DOI:10.1016/0148-9062(92)93679-E

Dost, B., and Kraaijpoel, D. (2013). The August 16, 2012 earthquake near Huizinge (Groningen). *KNMI-Scientific Report*, (January), 1–26.

Dresen, G., and Gueguen, Y. (2004). Damage and rock physical properties. In Gueguen, Y. & Boutéca, M. (Eds.), *Mechanics of Fluid-Saturated Rocks* (pp. 169–217). Amsterdam: Elsevier. DOI:10.1016/S0074-6142(03)80020-7

Dutton, S.P., Ambrose, W.A., and Loucks, R.G. (2017). Diagenetic controls on reservoir quality variation in Jurassic Cotton Valley sandstones, Onshore Gulf of Mexico, USA. In *79th EAGE Conference and Exhibition 2017*.

Dzung, T.Q., Al-Harthy, M., Hunt, S., and Sayers, J. (2009). The impact of uncertainty on subsidence and compaction prediction. *Science and Technology Development*, *12*(06), 84–95.

Eberhart-Phillips, D., and Oppenheimer, D.H. (1984). Induced seismicity in The Geysers Geothermal Area, California. *Journal of Geophysical Research*, *89*(B2), 1191–1217. DOI:10.1029/JB089iB02p01191

Van Eck, T., Goutbeek, F., Haak, H., and Dost, B. (2006). Seismic hazard due to small-magnitude, shallow-source, induced earthquakes in The Netherlands. *Engineering Geology*, *87*(1–2), 105–

121. DOI:10.1016/j.enggeo.2006.06.005

Van Eijs, R.M.H.E. (2015). Neotectonic Stresses in the Permian Slochteren Formation of the Groningen Field EP201510210531. NAM.

Van Eijs, R.M.H.E., Mulders, F.M.M., Nepveu, M., Kenter, C.J., and Scheffers, B.C. (2006). Correlation between hydrocarbon reservoir properties and induced seismicity in the Netherlands. *Engineering Geology*, *84*(3–4), 99–111. DOI:10.1016/j.enggeo.2006.01.002

Einav, I. (2007). Breakage mechanics-Part I: Theory. *Journal of the Mechanics and Physics of Solids*, *55*(6), 1274–1297. DOI:10.1016/j.jmps.2006.11.003

Van den Ende, M.P.A., Marketos, G., Niemeijer, A.R., and Spiers, C.J. (2018). Investigating Compaction by Intergranular Pressure Solution Using the Discrete Element Method. *Journal of Geophysical Research: Solid Earth*. DOI:10.1002/2017JB014440

Estrada, N., Lizcano, A., and Taboada, A. (2010a). Simulation of cemented granular materials. I. Macroscopic stress-strain response and strain localization. *Physical Review E - Statistical, Nonlinear, and Soft Matter Physics*, *82*(1). DOI:10.1103/PhysRevE.82.011303

Estrada, N., Lizcano, A., and Taboada, A. (2010b). Simulation of cemented granular materials. II. Micromechanical description and strength mobilization at the onset of macroscopic yielding. *Physical Review E - Statistical, Nonlinear, and Soft Matter Physics*, *82*(1). DOI:10.1103/PhysRevE.82.011304

Evans, K.F., Zappone, A., Kraft, T., Deichmann, N., and Moia, F. (2012). A survey of the induced seismic responses to fluid injection in geothermal and CO2 reservoirs in Europe. *Geothermics*, *41*, 30–54. DOI:10.1016/j.geothermics.2011.08.002

Favero, V., Ferrari, A., and Laloui, L. (2016). On the hydro-mechanical behaviour of remoulded and natural Opalinus Clay shale. *Engineering Geology*. DOI:10.1016/j.enggeo.2016.04.030

Ferrari, A., Favero, V., and Laloui, L. (2016). One-dimensional compression and consolidation of shales. *International Journal of Rock Mechanics and Mining Sciences*. DOI:10.1016/j.ijrmms.2016.07.030

Fialko, Y., and Simons, M. (2000). Deformation and seismicity in the Coso geothermal area, Inyo County, California: Observations and modeling using satellite radar interferometry. *Journal of Geophysical Research*, *105*(B9), 21781. DOI:10.1029/2000JB900169

Fitts, T.G., and Brown, K.M. (1999). Stress-induced smectite dehydration: Ramifications for patterns of freshening and fluid expulsion in the N. Barbados accretionary wedge. *Earth and Planetary Science Letters*. DOI:10.1016/S0012-821X(99)00168-5

Fortin, J., Schubnel, A., and Guéguen, Y. (2005). Elastic wave velocities and permeability evolution during compaction of Bleurswiller sandstone. *International Journal of Rock Mechanics and Mining Sciences*. DOI:10.1016/j.ijrmms.2005.05.002

Fortin, J., Stanchits, S., Dresen, G., and Guéguen, Y. (2006). Acoustic emission and velocities associated with the formation of compaction bands in sandstone. *Journal of Geophysical Research: Solid Earth*, *111*(10). DOI:10.1029/2005JB003854

Fredrich, J.T., and Fossum, A.F. (2002). Large-scale three-dimensional geomechanical modeling of reservoirs: Examples from California and the deepwater gulf of Mexico. *Oil and Gas Science and Technology*, *57*(5), 423–441. DOI:10.2516/ogst:2002028

Fu, R., Hu, X., and Zhou, B. (2017). Discrete element modeling of crushable sands considering realistic particle shape effect. *Computers and Geotechnics*. DOI:10.1016/j.compgeo.2017.07.016

Fukunaga, K., and Hostetler, L.D. (1975). The Estimation of the Gradient of a Density Function, with Applications in Pattern Recognition. *IEEE Transactions on Information Theory*. DOI:10.1109/TIT.1975.1055330

Gaupp, R., and Okkerman, J.A. (2011). Diagenesis and reservoir quality of Rotliegend sandstones in the Northern Netherlands-a review. In Grötsch, J. & Gaupp, R. (Eds.), *The Permian Rotliegend of the Netherlands* (SEPM Speci). DOI:10.2110/pec.11.98.0193

Gaupp, R., Matter, A., Platt, J., Ramseyer, K., and Walzebuck, J. (1993). Diagenesis and fluid evolution of deeply buried Permian (Rotliegende) gas reservoirs, northwest Germany. *American Association of Petroleum Geologists Bulletin*. DOI:10.1306/BDFF8E0C-1718-11D7-8645000102C1865D

GEA. (2012). *Global Energy Assessment: Towards a Sustainable Future*. (Johansson, T. B., Patwardhan, A., Nakicenovic, N., & Echeverri, L. G., Eds.), *Towards a sustainable future*. Laxenburg, Austria: Cambridge University Press. DOI:10.1017/CBO9780511793677

Geertsma, J. (1973). Land subsidence above compacting oil and gas reservoirs. *Journal of Petroleum Technology*. DOI:10.2118/3730-PA

Genmo, Z., Huaran, C., Shuqin, M., and Deyuan, Z. (1995). Research on earthquakes induced by water injection in China. *Pure and Applied Geophysics PAGEOPH*. DOI:10.1007/BF00879483

Glennie, K.W. (1972). Permian Rotliegendes of Northwest Europe interpreted in the light of modern desert sedimentation studies. *American Association of Petroleum Geologists Bulletin*, *56*, 1048 – 1071.

Glennie, K.W., Mudd, G.C., and Nagtegaal, P.J.C. (1978). Depositional environment and diagenesis of Permian Rotliegendes sandstones in Leman Bank and Sole Pit areas of the UK southern North Sea. *Journal of the Geological Society*. DOI:10.1144/gsjgs.135.1.0025

Grasso, J.R. (1992). Mechanics of seismic instabilities induced by the recovery of hydrocarbons. *Pure and Applied Geophysics*, *139*(3–4), 507–534.

Gratier, J.P., and Guiguet, R. (1986). Experimental pressure solution-deposition on quartz grains: the crucial effect of the nature of the fluid. *Journal of Structural Geology*, *8*(8), 845–856.

DOI:10.1016/0191-8141(86)90030-1

Grella, L., Lorusso, G., and Adler, D.L. (2003). Simulations of Scanning Electron Microscopy Imaging and Charging in Insulating Structures. *Scanning*, *25*, 300–308. DOI:10.1002/sca.4950250606

Griffith, A.A. (1921). The Phenomena of Rupture and Flow in Solids. *Philosophical Transactions of the Royal Society*.

Grötsch, J., Sluijk, A., Van Ojik, K., De Keijzer, M., Graaf, J., and Steenbrink, J. (2011). The Groningen gas field: fifty years of exploration and gas production from a permian dryland reservoir. In Jürgen Grötsch, R. G. (Ed.), *The Permian Rotliegend of the Netherlands* (Vol. 98, pp. 11–33). Tulsa: Society for Sedimentary Geology.

Grünthal, G. (2014). Induced seismicity related to geothermal projects versus natural tectonic earthquakes and other types of induced seismic events in Central Europe. *Geothermics*, *52*, 22–35. DOI:10.1016/j.geothermics.2013.09.009

Guéguen, Y., and Fortin, J. (2013). Elastic envelopes of porous sandstones. *Geophysical Research Letters*, *40*(14), 3550–3555. DOI:10.1002/grl.50676

Gundersen, E., Dysthe, D.K., Renard, F., Bjorlykke, K., and Jamtveit, B. (2002). Numerical modelling of pressure solution in sandstone, rate-limiting processes and the effect of clays. *Geological Society, London, Special Publications*. DOI:10.1144/GSL.SP.2001.200.01.03

Guyer, R.A. (2005). Hysteretic elastic systems: Geophysical materials. In Bertotti, G. & Mayergoyz, I. (Eds.), *The Science of Hysteresis* (Vol. 3, pp. 555–688). Academic Press. DOI:10.1016/B978-012480874-4/50024-5

Han, G., Stone, T., Liu, Q., Cook, J., and Papanastasiou, P. (2005). 3-D elastoplastic FEM modelling in a reservoir simulator. *SPE Reservoir Simulation Symposium, Proceedings*, 9–19. Retrieved from http://www.scopus.com/inward/record.url?eid=2-s2.0-22344443672%7B&%7DpartnerID=tZOtx3y1

Hangx, S., Van der Linden, A., Marcelis, F., and Bauer, A. (2013). The effect of CO2 on the mechanical properties of the Captain Sandstone: Geological storage of CO2 at the Goldeneye field (UK). *International Journal of Greenhouse Gas Control*, *19*, 609–619. DOI:10.1016/j.ijggc.2012.12.016

Hangx, S.J.T., Spiers, C.J., and Peach, C.J. (2010a). Creep of simulated reservoir sands and coupled chemical-mechanical effects of CO2 injection. *Journal of Geophysical Research*, *115*(B9), B09205. DOI:10.1029/2009JB006939

Hangx, S.J.T., Spiers, C.J., and Peach, C.J. (2010b). Mechanical behavior of anhydrite caprock and implications for CO2 sealing capacity. *Journal of Geophysical Research*, *115*(B7), B07402. DOI:10.1029/2009JB006954

Hawkes, I., and Mellor, M. (1970). Uniaxial testing in rock mechanics laboratories. *Engineering*

Geology. DOI:10.1016/0013-7952(70)90034-7

Hawkins, A.B., and McConnell, B.J. (1992). Sensitivity of sandstone strength and deformability to changes in moisture content. *Quarterly Journal of Engineering Geology and Hydrogeology*. DOI:10.1144/gsl.qjeg.1992.025.02.05

Heap, M.J., Baud, P., Meredith, P.G., Bell, a. F., and Main, I.G. (2009). Time-dependent brittle creep in Darley Dale sandstone. *Journal of Geophysical Research*, *114*(B7), B07203. DOI:10.1029/2008JB006212

Heap, M.J., Faulkner, D.R., Meredith, P.G., and Vinciguerra, S. (2010). Elastic moduli evolution and accompanying stress changes with increasing crack damage: Implications for stress changes around fault zones and volcanoes during deformation. *Geophysical Journal International*. DOI:10.1111/j.1365-246X.2010.04726.x

Heap, M.J., Brantut, N., Baud, P., and Meredith, P.G. (2015). Time-dependent compaction band formation in sandstone. *Journal of Geophysical Research: Solid Earth*, n/a-n/a. DOI:10.1002/2015JB012022

Heap, M.J., Villeneuve, M., Kushnir, A.R.L., Farquharson, J.I., Baud, P., and Reuschlé, T. (2019). Rock mass strength and elastic modulus of the Buntsandstein: An important lithostratigraphic unit for geothermal exploitation in the Upper Rhine Graben. *Geothermics*. DOI:10.1016/j.geothermics.2018.10.003

Hettema, M., Schutjens, P.M., Verboom, B., and Gussinklo, H. (2000). Production-Induced Compaction of a Sandstone Reservoir: The Strong Influence of Stress Path. *SPE Reservoir Evaluation & Engineering*, *3*(August). DOI:10.2118/65410-PA

Hettema, M., Papamichos, E., and Schutjens, P.M. (2002). Subsidence delay: Field observations and analysis. *Oil and Gas Science and Technology*, *57*(5), 443–458. DOI:10.2516/ogst:2002029

Hol, S., Mossop, A.P., van der Linden, A.J., Zuiderwijk, P.M.M., and Makurat, A.H. (2015a). Long-term compaction behavior of Permian sandstones - An investigation into the mechanisms of subsidence in the Dutch Wadden Sea. *ARMA*, *15–618*.

Hol, S., Linden van der, A.J., Zuiderwijk, P.M.M., Marcelis, F.H.M., and Coorn, A.H. (2015b). *Mechanical characterization of Permian reservoir sandstone from the Moddergat-3 well in the Dutch Wadden Area (Report, Shell Global Solutions International B.V., Rijswijk)*. *Internal report*. Rijswijk. https://doi.org/SR.12.10541

Hol, S., van der Linden, A., Bierman, S., Marcelis, F., and Makurat, A. (2018). Rock physical controls on production-induced compaction in the Groningen Field. *Scientific Reports*.

Holt, R.M., Brignoli, M., and Kenter, C.J. (1994). Core damage effects on compaction behaviour. *Society of Petroleum Engineers Journal*, 55–62. Retrieved from http://www.onepetro.org/mslib/app/Preview.do?paperNumber=00028027&societyCode=SPE

Holt, R.M., Brignoli, M., and Kenter, C.J. (2000). Core quality: Quantification of coring-induced rock alteration. *International Journal of Rock Mechanics and Mining Sciences*, *37*, 889–907. DOI:10.1016/S1365-1609(00)00009-5

Hunfeld, L.B., Niemeijer, A.R., and Spiers, C.J. (2017). Frictional Properties of Simulated Fault Gouges from the Seismogenic Groningen Gas Field Under In Situ P-T Chemical Conditions. *Journal of Geophysical Research: Solid Earth*. DOI:10.1002/2017JB014876

IEA. (2016). Key world energy trends. In *World energy balances*. Paris: OECD Publishing.

Ingraham, M.D., Bauer, S.J., Issen, K.A., and Dewers, T.A. (2017). Evolution of permeability and Biot coefficient at high mean stresses in high porosity sandstone. *International Journal of Rock Mechanics and Mining Sciences*, *96*, 1–10. DOI:10.1016/j.ijrmms.2017.04.004

Israelachvili, J.N. (1986). Measurement of the viscosity of liquids in very thin films. *Journal of Colloid And Interface Science*. DOI:10.1016/0021-9797(86)90376-0

Issen, K., and Rudnicki, J. (2000). Conditions for compaction bands in porous rock. *J. Geophys. Res.*, *105*(B9), 21529–21536. DOI:10.1029/2000JB900185

Jaeger, J.C., Cook, N.G.W., and Zimmerman, R.W. (2007). *Fundamentals of rock mechanics (4th edition)*. Malden, USA: Blackwell Publishing.

De Jager, J., and Visser, C. (2017). Geology of the Groningen field - An overview. *Geologie En Mijnbouw/Netherlands Journal of Geosciences*. DOI:10.1017/njg.2017.22

De Jager, J., Doyle, M.A., Grantham, P.J., and Mabillard, J.E. (1996). Hydrocarbon habitat of the West Netherlands Basin. In Rondeel, H. E., Batjes, D. A. J., & Nieuwenhuijs, W. H. (Eds.), *Geology of Gas and Oil under the Netherlands* (p. 1996). Dordrecht: Kluwer Academic Publishers.

Ji, Y., Hall, S.A., Baud, P., and Wong, T. -f. (2015). Characterization of pore structure and strain localization in Majella limestone by X-ray computed tomography and digital image correlation. *Geophysical Journal International*, *200*, 699–717. DOI:10.1093/gji/ggu414

Kammers, A.D., and Daly, S. (2013). Digital Image Correlation under Scanning Electron Microscopy: Methodology and Validation. *Experimental Mechanics*. DOI:10.1007/s11340-013-9782-x

Karner, S.L., Chester, F.M., Kronenberg, A.K., and Chester, J.S. (2003). Subcritical compaction and yielding of granular quartz sand. *Tectonophysics*, *377*(3–4), 357–381. DOI:10.1016/j.tecto.2003.10.006

Karner, S.L., Chester, J.S., Chester, F.M., Kronenberg, A.K., and Hajash, A. (2005a). Laboratory deformation of granular quartz sand: Implications for the burial of clastic rocks. *AAPG Bulletin*, *89*(5), 603–625. DOI:10.1306/12200404010

Karner, S.L., Chester, F.M., and Chester, J.S. (2005b). Towards a general state-variable constitutive relation to describe granular deformation. *Earth and Planetary Science Letters*, *237*(3–4), 940–950. DOI:10.1016/j.epsl.2005.06.056

Kawamoto, R., Andò, E., Viggiani, G., and Andrade, J.E. (2016). Level set discrete element method for three-dimensional computations with triaxial case study. *Journal of the Mechanics and Physics of Solids*. DOI:10.1016/j.jmps.2016.02.021

Kemeny, J.M., and Cook, N.G.W. (1991). Micromechanics of Deformation in Rocks. In Shah, S. P. (Ed.), *Toughening Mechanisms in Quasi-Brittle Materials* (pp. 155–188). Dordrecht: Springer Netherlands. DOI:10.1007/978-94-011-3388-3_10

Kendall, K. (1978). The impossibility of comminuting small particles by compression. *Nature*. DOI:10.1038/272710a0

Ketelaar, V.B.H. (2009). *Satellite Radar Interferometry: subsidence monitoring techniques*. (Van der Meer, F. D. & Marcal, A., Eds.). New York City: Springer. DOI:10.1038/scientificamerican0297-46

Khalili, N., Russell, A., Khoshghalb, A., Zhang, Y., and Buscarnera, G. (2014). Model predictions of hydro-mechanical coupling in unsaturated crushable soils. In *Unsaturated Soils: Research & Applications*. DOI:10.1201/b17034-65

Klein, E., Baud, P., Reuschle, T., and Wong, T. -f. (2001). Mechanical behaviour and failure mode of Bentheim Sandstone under triaxial compression. *Phys. Chem. Earth.*, *26*(1–2), 21–25.

Kole, P. (2015). *In - situ compaction measurements using gamma ray markers*. Assen.

Koster, H.R.A., and Ommeren, J. van. (2015). A shaky business: Natural gas extraction, earthquakes and house prices. *European Economic Review*, *80*, 120–139. DOI:10.1016/j.euroecorev.2015.08.011

Lawn, B. (1993). *Fracture of Brittle Solids - second edition*. (Davis, E. A. & Ward, I. M., Eds.). Cambridge University Press. DOI:10.1017/CBO9780511623127

Lele, S., Hsu, Y.-S., Garzon, J.L., DeDontney, N., Searles, K.H., Gist, G.A., Sanz, P.F., Biediger, E.A.O., and Dale, B.A. (2016). Geomechanical Modeling to Evaluate Production-Induced Seismicity at the Groningen field. *SPE International*, (183554).

Lele, S.P., Garzon, J.L., Hsu, S.-Y., DeDontney, N.L., Searles, K.H., and Sanz, P.F. (2015). *Groningen 2015 Geomechanical Analysis*. Assen.

Liu, L., Zoback, M.D., and Segall, P. (1992). Rapid intraplate strain accumulation in the New Madrid seismic zone. *Science*. DOI:10.1126/science.257.5077.1666

Louis, L., Baud, P., and Wong, T. -f. (2009). Microstructural inhomogeneity and mechanical anisotropy associated with bedding in rothbach sandstone. *Pure and Applied Geophysics*. DOI:10.1007/s00024-009-0486-1

Lu, C., Danzer, R., and Fischer, F.D. (2002). Fracture statistics of brittle materials: Weibull or normal distribution. *Physical Review E - Statistical, Nonlinear, and Soft Matter Physics*, *65*(6). DOI:10.1103/PhysRevE.65.067102

Mallman, E.P., and Zoback, M.D. (2007). Subsidence in the Louisiana coastal zone due to hydrocarbon production. *Journal of Coastal Research*. DOI:10.2112/05-0553

Marcial, D., Delage, P., and Cui, Y.J. (2002). On the high stress compression of bentonites. *Canadian Geotechnical Journal*. DOI:10.1139/t02-019

Marketos, G., and Bolton, M.D. (2009). Compaction bands simulated in Discrete Element Models. *Journal of Structural Geology*, *31*(5), 479–490. DOI:10.1016/j.jsg.2009.03.002

Marketos, G., Spiers, C.J., and Govers, R. (2016). Impact of rock salt creep law choice on subsidence calculations for hydrocarbon reservoirs overlain by evaporite caprocks. *Journal of Geophysical Research: Solid Earth*, *121*(6), 4249–4267. DOI:10.1002/2016JB012892

Marone, C. (1998). Laboratory-Derived Friction Laws and Their Application To Seismic Faulting. *Annual Review of Earth and Planetary Sciences*, *26*(1), 643–696. DOI:10.1146/annurev.earth.26.1.643

Mavko, G., Mukerji, T., and Dvorkin, J. (2009). *The Rock Physics Handbook*. DOI:10.1017/CBO9780511626753

McBride, E.F. (1963). A classification of common sandstones. *Journal of Sedimentary Research*, *33*(3), 664–669. DOI:10.1306/74D70EE8-2B21-11D7-8648000102C1865D

McBride, E.F. (1989). Quartz cement in sandstones: a review. *Earth Science Reviews*, *26*(C), 69–112. DOI:10.1016/0012-8252(89)90019-6

McDowell, G.R., Bolton, M.D., and Robertson, D. (1996). The fractal crushing of granular materials. *Journal of the Mechanics and Physics of Solids*, *44*(12), 2079–2102. DOI:10.1016/S0022-5096(96)00058-0

McGarr, A. (1999). On relating apparent stress to the stress causing earthquake fault slip. *Journal of Geophysical Research*, *104*(1999), 3003–3011.

McHardy, W.J., Wilson, M.J., and Tait, M. (1982). Electron Microscope and X-ray Diffraction Studies of Filamentous Illitic Clay from Sandstones of the Magnus Field. *Clay Minerals*, *17*, 23–40. DOI:10.1180/claymin.1982.017.1.04

McKavanagh, B., and Stacey, F.D. (1974). Mechanical hysteresis in rocks at low strain amplitudes and seismic frequencies. *Physics of the Earth and Planetary Interiors*. DOI:10.1016/0031-9201(74)90091-0

Menéndez, B., Zhu, W., and Wong, T. -f. (1996). Micromechanics of brittle faulting and cataclastic flow in Berea sandstone. *Journal of Structural Geology*, *18*(1), 1–16. DOI:10.1016/0191-8141(95)00076-P

Menin, A., Salomoni, V.A., Santagiuliana, R., Simoni, L., Gens, A., and Schrefler, B.A. (2008). A mechanism contributing to subsidence above gas reservoirs and its application to a case study. *International Journal of Computational Methods in Engineering Science and Mechanics*.

DOI:10.1080/15502280802225234

Mitchell, J.K., and Green, R.A. (2017). Some induced seismicity considerations in geo-energy resource development. *Geomechanics for Energy and the Environment*, 1–9. DOI:10.1016/j.gete.2017.01.001

Morton, R.A., Purcell, N.A., and Peterson, R. (2001). Field evidence of subsidence and faulting induced by hydrocarbon production in coastal southeast Texas. *Gulf Coast Associaction of Geological Societies Transactions*, *L1*, 239–248.

Morton, R.A., Bernier, J.C., and Barras, J.A. (2006). Evidence of regional subsidence and associated interior wetland loss induced by hydrocarbon production, Gulf Coast region, USA. *Environmental Geology*, *50*(2), 261–274. DOI:10.1007/s00254-006-0207-3

Mossop, A. (2012). An explanation for anomalous time dependent subsidence. *ARMA*, *12*(518).

Mossop, A., and Segall, P. (1997). Subsidence at The Geysers Geothermal Field, N. California from a comparison of GPS and leveling surveys. *Geophysical Research Letters*, *24*(14), 1839–1842. DOI:10.1029/97GL51792

Muir Wood, D. (1991). *Soil Behaviour and Critical State Soil Mechanics*. Cambridge University Press. DOI:10.1017/CBO9781139878272

Mulders, F.M.M. (2003). *Modelling of stress development and fault slip in and around a producing gas reservoir*. *DUP Science*. Delft University, Delft, the Netherlands.

Nadeev, A., Mikhailov, D., Chuvilin, E., Koroteev, D., and Shako, V. (2013). Visualization of clay and frozen substances inside porous rocks using X-ray micro-computed tomography. *Microscopy and Analysis*, *27*(March), 8–10.

NAM. (2013). *Technical Addendum to the Winningsplan Groningen 2013 Subsidence, Induced Earthquakes and Seismic Hazard Analysis in the Groningen Field*.

NAM. (2015). *Bodemdaling door Aardgaswinning. NAM-gasvelden in Groningen, Friesland, en het noorden van Drenthe*.

NAM. (2016). *Technical Addendum to the Winningsplan Groningen 2016* (Vol. 1).

NAM. (2017). *Ensemble Based Subsidence application to the Ameland gas field – long term subsidence study part two (LTS II)*.

Nepveu, M., Van Thienen-Visser, K., and Sijacic, D. (2016). Statistics of seismic events at the Groningen field. *Bulletin of Earthquake Engineering*. DOI:10.1007/s10518-016-0007-4

Niemeijer, A.R., and Spiers, C.J. (2007). A microphysical model for strong velocity weakening in phyllosilicate-bearing fault gouges. *Journal of Geophysical Research: Solid Earth*, *112*, 1–12. DOI:10.1029/2007JB005008

Niemeijer, A.R., Spiers, C.J., and Bos, B. (2002). Compaction creep of quartz sand at 400-600C: experimental evidence for dissolution-controlled pressure solution. *Earth and Planetary Science*

Letters, *195*, 261–275.

Nolze, G. (2007). Image distortions in SEM and their influences on EBSD measurements. *Ultramicroscopy*. DOI:10.1016/j.ultramic.2006.07.003

Van Noort, R., Visser, H.J.M., and Spiers, C.J. (2008). Influence of grain boundary structure on dissolution controlled pressure solution and retarding effects of grain boundary healing. *Journal of Geophysical Research: Solid Earth*, *113*(3), 1–15. DOI:10.1029/2007JB005223

Olsson, W.A., and Holcomb, D.J. (2000). Compaction localization in porous rock. *Geophysical Research Letters*, *27*(21), 3537–3540. DOI:10.1029/2000GL011723

Ord, A., Vardoulakis, I., and Kajewski, R. (1991). Shear band formation in Gosford Sandstone. *International Journal of Rock Mechanics and Mining Sciences And*, *28*(5), 397–409. DOI:10.1016/0148-9062(91)90078-Z

Otsu, N. (1979). A Threshold Selection Method from Gray-Level Histograms. *IEEE Transactions on Systems, Man, and Cybernetics*. DOI:10.1109/TSMC.1979.4310076

Paterson, M.S., and Wong, T. -f. (2005). *Experimental rock deformation - The brittle field* (2nd ed.). New York City: Springer. DOI:10.1007/b137431

Peach, C.J. (1991). *Influence of deformation on the fluid transport properties of salt rocks*. Utrecht University, Utrecht, the Netherlands.

Pijnenburg, R.P.J., Verberne, B.A., Hangx, S.J.T., and Spiers, C.J. (2018). Deformation Behavior of Sandstones From the Seismogenic Groningen Gas Field: Role of Inelastic Versus Elastic Mechanisms. *Journal of Geophysical Research: Solid Earth*, (123). DOI:10.1029/2018JB015673

Pijnenburg, R.P.J., Verberne, B.A., Hangx, S.J.T., and Spiers, C.J. (2019). Inelastic deformation of the Slochteren sandstone: Stress-strain relations and implications for induced seismicity in the Groningen gas field. *Journal of Geophysical Research: Solid Earth*, (124). DOI:10.1029/2019JB017366

Postma, T., and Jansen, J.D. (2018). The Small Effect of Poroelastic Pressure Transients on Triggering of Production-Induced Earthquakes in the Groningen Natural Gas Field. *Journal of Geophysical Research: Solid Earth*. DOI:10.1002/2017JB014809

Potyondy, D.O., Cundall, P.A., and Lee, C.A. (1996). Modelling rock using bonded assemblies of circular particles. In *2nd North American Rock Mechanics Symposium, 19-21 June, Montreal, Quebec, Canada*.

Pratt, W.E., and Johnson, D.W. (1926). Local subsidence of the Goose Creek oil field. *The Journal of Geology*, *34*(7), 577–590. DOI:10.1086/521238

Preibisch, S., Saalfeld, S., and Tomancak, P. (2009). Globally optimal stitching of tiled 3D microscopic image acquisitions. *Bioinformatics*, *25*(11), 1463–1465. DOI:10.1093/bioinformatics/btp184

Pruiksma, J.P., Breunese, J.N., Van Thienen-Visser, K., and de Waal, J.A. (2015). Isotach formulation

of the rate type compaction model for sandstone. *International Journal of Rock Mechanics and Mining Sciences*, *78*, 127–132. DOI:10.1016/j.ijrmms.2015.06.002

Quintanilla-Terminel, A., Zimmerman, M., Evans, B., and Kohlstedt, D. (2017). Micro-scale and nano-scale strain mapping techniques applied to creep of rocks. *Solid Earth Discussions*, (March), 1–32. DOI:10.5194/se-2017-27

Renard, F., Park, A., Ortoleva, P., and Gratier, J.P. (1999). An integrated model for transitional pressure solution in sandstones. *Tectonophysics*, *312*(2–4), 97–115. DOI:10.1016/S0040-1951(99)00202-4

Renard, F., Cordonnier, B., Kobchenko, M., Kandula, N., Weiss, J., and Zhu, W. (2017). Microscale characterization of rupture nucleation unravels precursors to faulting in rocks. *Earth and Planetary Science Letters*. DOI:10.1016/j.epsl.2017.08.002

Rijken, M.C.M. (2005). *Modeling naturally fractured reservoirs: From experimental rock mechanics to flow simulation*. *ProQuest Dissertations And Theses; Thesis (Ph.D.)--The University of Texas at Austin*. The University of Texas, Austin.

Rudnicki, J.W., and Rice, J.R. (1975). Conditions for the localization of deformation in pressure-sensitive dilatant materials. *Journal of the Mechanics and Physics of Solids*, *23*(6), 371–394. DOI:10.1016/0022-5096(75)90001-0

Rutter, E.H. (1983). Pressure solution in nature, theory and experiment. *Journal of the Geological Society*, *140*(5), 725–740. DOI:10.1144/gsjgs.140.5.0725

Rutter, E.H., and Glover, C.T. (2012). The deformation of porous sandstones ; are Byerlee friction and the critical state line equivalent? *Journal of Structural Geology*, *44*, 129–140. DOI:10.1016/j.jsg.2012.08.014

Rutter, E.H., and Mainprice, D.H. (1978). The effect of water on stress relaxation of faulted and unfaulted sandstone. *Pure and Applied Geophysics*, *116*(4–5), 634–654. DOI:10.1007/BF00876530

Sackfield, A., and Hills, D.A. (1986). The strength of some non-hertzian plane contacts. *Journal of Tribology*, *108*(4).

Saidi, F., Bernabe, Y., and Reuschle, T. (2003). The mechanical behaviour of synthetic, poorly consolidated granular rock under uniaxial compression. *Tectonophysics*, *370*(1–4), 105–120. DOI:10.1016/S0040-1951(03)00180-X

Sakic, A., Nanver, L.K., Van Veen, G., Kooijman, K., Vogelsang, P., Scholtes, T.L.M., de Boer, W., Wien, W., Milosavljevic, S., Heerkens, C.T.H., Knezevic, T., and Spee, I. (2011). Solid-state backscattered-electron detector for sub-keV imaging in scanning electron microscopy. In *ICT Open: Micro Technology and Micro Devices SAFE* (pp. 1–4). Veldhoven: Technology Foundation STW.

Sammis, C.G., and Ashby, M.F. (1986). The failure of brittle porous solids under compressive stress states. *Acta Metallurgica*, *34*(3), 511–526. DOI:10.1016/0001-6160(86)90087-8

Sammis, C.G., and Ben-Zion, Y. (2008). Mechanics of grain-size reduction in fault zones. *Journal of Geophysical Research: Solid Earth*. DOI:10.1029/2006JB004892

Santarelli, F., Tronvoll, J., Svennekjaer, M., Skeie, H., Henriksen, R., and Bratli, R.K. (1998). Reservoir stress path: the depletion and the rebound. *Society of Petroleum Engineers Journal*, (47350), 1–7. DOI:10.2118/47350-MS

Santarelli, F.J., and Dusseault, M.B. (1991). Core quality control in petroleum engineering. In Roegiers (Ed.), *Rock Mechanics as a Multidisciplinary Science* (pp. 111–120). Rotterdam: Balkema.

Schofield, A., and Wroth, P. (1968). Critical State Soil Mechanics. *Soil Use and Management*, *25*(3), 128–105. DOI:10.1111/j.1475-2743.1987.tb00718.x

Scholz, C.H. (2002). *The Mechanics of Earthquakes and Faulting*. *Seismological Research Letters* (2nd ed., Vol. 74). Cambridge University Press. DOI:10.1785/gssrl.74.3.333

Schultz, R.A., and Siddharthan, R. (2005). A general framework for the occurrence and faulting of deformation bands in porous granular rocks. *Tectonophysics*, *411*(1–4), 1–18. DOI:10.1016/j.tecto.2005.07.008

Schutjens, P.M.T.M. (1991). Experimental compaction of quartz sand at low effective stress and temperature conditions. *Journal of the Geological Society*, *148*(3), 527–539. DOI:10.1144/gsjgs.148.3.0527

Schutjens, P.M.T.M., Fens, T.W., and Smits, R.M.M. (1995). Experimental observations of the uniaxial compactionn of quartz-rich reservoir rock at stresses up to 80 MPa. In Barends, Brouwer, & Schroder (Eds.), *Land Subsidence* (pp. 389–409). Rotterdam: Balkema.

Schutjens, P.M.T.M., Hanssen, T.H., Hettema, M.H.H., Merour, J., de Bree, P., Coremans, J.W. a., and Helliesen, G. (2004). Compaction-Induced Porosity/Permeability Reduction in Sandstone Reservoirs: Data and Model for Elasticity-Dominated Deformation. *SPE Reservoir Evaluation & Engineering*, *7*(June). DOI:10.2118/88441-PA

Seeger, A., Duci, A., and Haussecker, H. (2006). Scanning electron microscope charging effect model for chromium/quartz photolithography masks. *Scanning*. DOI:10.1002/sca.4950280307

Segall, P., and Fitzgerald, S.D. (1998). A note on induced stress changes in hydrocarbon and geothermal reservoirs. *Tectonophysics*, *289*, 117–128.

Shah, K.R., and Wong, T. -f. (1997). Fracturing at contact surfaces subjected to normal and tangential loads. *International Journal of Rock Mechanics and Mining Sciences*, *34*(5), 727–739. DOI:10.1016/S1365-1609(97)00007-7

Shalev, E., Lyakhovsky, V., Ougier-Simonin, A., Hamiel, Y., and Zhu, W. (2014). Inelastic compaction, dilation and hysteresis of sandstones under hydrostatic conditions. *Geophysical Journal*

International, *197*(2), 920–925. DOI:10.1093/gji/ggu052

Sharp, J.M., and Hill, D.W. (1995). Land subsidence along the northeastern Texas Gulf coast: Effects of deep hydrocarbon production. *Environmental Geology*, *25*(3), 181–191. DOI:10.1007/BF00768547

Shen, Z., Jiang, M., and Thornton, C. (2016). DEM simulation of bonded granular material. Part I: Contact model and application to cemented sand. *Computers and Geotechnics*, *75*, 192–209. DOI:10.1016/j.compgeo.2016.02.007

Shipton, Z.K., Evans, J.P., Abercrombie, R.E., and Brodsky, E.E. (2013). The Missing Sinks : Slip Localization in Faults , Damage Zones , and the Seismic Energy Budget. In Abercrombie, R., McGarr, A., Toro, G. Di, & Hiroo, K. (Eds.), *Earthquakes: Radiated Energy and the Physics of Faulting* (pp. 217–222). American Geophysical Union. DOI:10.1029/GM170

Sijacic, D., Pijpers, F., Nepveu, M., and Van Thienen-Visser, K. (2017). Statistical evidence on the effect of production changes on induced seismicity. *Geologie En Mijnbouw/Netherlands Journal of Geosciences*. DOI:10.1017/njg.2017.14

Skurtveit, E., Torabi, A., Gabrielsen, R.H., and Zoback, M.D. (2013). Experimental investigation of deformation mechanisms during shear-enhanced compaction in poorly lithified sandstone and sand. *Journal of Geophysical Research: Solid Earth*, *118*(8), 4083–4100. DOI:10.1002/jgrb.50342

Smith, J.D., Avouac, J., White, R.S., Copley, A., Gualandi, A., and Bourne, S. (2019). Reconciling the long-term relationship between reservoir pore pressure depletion and compaction in the Groningen region. *Journal of Geophysical Research: Solid Earth*. DOI:10.1029/2018jb016801

Smith, P.R., Jardine, R.J., and Hight, D.W. (1992). The yielding of Bothkennar clay. *Géotechnique*. DOI:10.1680/geot.1992.42.2.257

Spiers, C.J. (1979). Fabric Development in Calcite Polycrystals Deformed at 400°C. *Bulletin de Minéralogie*, *102*(2–3), 282–289.

Spiers, C.J., De Meer, S., Niemeijer, A.R., and Zhang, X. (2004). Kinetics of rock deformation by pressure solution and the role of thin aqueous films. In Nakashima, S. et al. (Ed.), *Physicochemistry of thin film water* (pp. 129–158).

Spiers, C.J., Hangx, S.J.T., and Niemeijer, A.R. (2017). New approaches in experimental research on rock and fault behaviour in the Groningen gas field. *Netherlands Journal of Geosciences*, *96*(05), s55–s69. DOI:10.1017/njg.2017.32

Stamhuis, E.J. (2006). Basics and principles of particle image velocimetry (PIV) for mapping biogenic and biologically relevant flows. *Aquatic Ecology*. DOI:10.1007/s10452-005-6567-z

Stefanou, I., Sulem, J., and Vardoulakis, I. (2008). Three-dimensional Cosserat homogenization of masonry structures: Elasticity. *Acta Geotechnica*. DOI:10.1007/s11440-007-0051-y

Suckale, J. (2009). Induced seismicity in hydrocarbon fields. In *Advances in Geophysics* (Vol. 51, pp. 55–106). Amsterdam: Elsevier Ltd. DOI:10.1016/S0065-2687(09)05107-3

Sulem, J., and Mühlhaus, H. (1997). A continuum model for periodic two-dimensional block structures. *Mechanics of Cohesive-frictional Materials*, *2*, 31–46.

Tada, H., Paris, P.C., and Irwin, G.R. (2000). *The Stress Analysis of Cracks Handbook; 3rd edition*. New York: ASME Press.

Tada, R., and Siever, R. (1989). Pressure solution during diagenesis. *Annual Review Earth and Planetary Sciences*, *17*, 89–118. DOI:10.1038/264511b0

Tapponnier, P., and Brace, W.F. (1976). Development of Stress-Induced Mlcrocracks m Westerly Granite. *International Journal of Rock Mechanics and Mining Sciences & Geomechanics*, *13*, 103–112.

Tembe, S., Vajdova, V., Baud, P., Zhu, W., and Wong, T. -f. (2007). A new methodology to delineate the compactive yield cap of two porous sandstones under undrained condition. *Mechanics of Materials*, *39*(5), 513–523. DOI:10.1016/j.mechmat.2006.08.005

Tembe, S., Baud, P., and Wong, T. -f. (2008). Stress conditions for the propagation of discrete compaction bands in porous sandstone. *Journal of Geophysical Research: Solid Earth*, *113*(9), 1–16. DOI:10.1029/2007JB005439

Tembe, S., Lockner, D.A., and Wong, T. -f. (2010). Effect of clay content and mineralogy on frictional sliding behavior of simulated gouges: Binary and ternary mixtures of quartz, illite, and montmorillonite. *Journal of Geophysical Research: Solid Earth*. DOI:10.1029/2009JB006383

Tengattini, A., Das, A., Nguyen, G.D., Viggiani, G., Hall, S.A., and Einav, I. (2014). A thermomechanical constitutive model for cemented granular materials with quantifiable internal variables. Part I—Theory. *Journal of the Mechanics and Physics of Solids*, *70*, 281–296. DOI:10.1016/j.jmps.2014.05.021

Van Thienen-Visser, K., and Breunese, J.N. (2015). Induced seismicity of the Groningen gas field: History and recent developments. *The Leading Edge*, *34*(6), 664–671. DOI:10.1190/tle34060664.1

Van Thienen-Visser, K., and Fokker, P.A. (2017). The future of subsidence modelling: Compaction and subsidence due to gas depletion of the Groningen gas field in the Netherlands. *Geologie En Mijnbouw/Netherlands Journal of Geosciences*. DOI:10.1017/njg.2017.10

Van Thienen-Visser, K., Pruiksma, J.P., and Breunese, J.N. (2015a). Compaction and subsidence of the Groningen gas field in the Netherlands. *Proceedings of the International Association of Hydrological Sciences*, *372*(10), 367–373. DOI:10.5194/piahs-372-367-2015

Van Thienen-Visser, K., Fokker, P.A., Nepveu, M., Hettelaar, J., and Van Kempen, B. (2015b). *Recent developments on the seismicity of the Groningen field in 2015 (TNO report 2015 R10755)*.

Utrecht.

Thouless, M.D., Evans, A.G., Ashby, M.F., and Hutchinson, J.W. (1987). The edge cracking and spalling of brittle plates. *Acta Metallurgica*. DOI:10.1016/0001-6160(87)90015-0

Tseng, Q., Duchemin-Pelletier, E., Deshiere, A., Balland, M., Guillou, H., Filhol, O., and Thery, M. (2012). Spatial organization of the extracellular matrix regulates cell-cell junction positioning. *Proceedings of the National Academy of Sciences*. DOI:10.1073/pnas.1106377109

Tutuncu, A.N., Podio, A.L., and Sharma, M.M. (1998). Nonlinear viscoelastic behavior of sedimentary rocks, Part II: hysteresis effects and influence of type of fluid on elastic moduli. *Geophysics*. DOI:10.1190/1.1444313

Underwood, E.E. (1970). *Quantitative stereology*. Reading, Mass.: Addison Wesley.

Verberne, B.A., and Spiers, C.J. (2017). A quantitative microstructural investigation of depleted and undepleted reservoir sandstones. *ARMA*, (966).

Verberne, B.A., Hangx, S.J.T., Pijnenburg, R.P.J., Hamers, M.F., Drury, M.R., and Spiers, C.J. (n.d.). Gas field drill core constrains mechanisms behind subsidence and induced seismicity. *In Preperation*.

Verberne, B.A., Spiers, C.J., Niemeijer, A.R., De Bresser, J.H.P., De Winter, D.A.M., and Plümper, O. (2013). Frictional Properties and Microstructure of Calcite-Rich Fault Gouges Sheared at Sub-Seismic Sliding Velocities. *Pure and Applied Geophysics*. DOI:10.1007/s00024-013-0760-0

Van der Voort, N., and Vanclay, F. (2015). Social impacts of earthquakes caused by gas extraction in the Province of Groningen, The Netherlands. *Environmental Impact Assessment Review*, *50*, 1–15. DOI:10.1016/j.eiar.2014.08.008

De Waal, J.A. (1986). *On the rate type compaction behaviour of sandstone reservoir rock*. Delft University, Delft, the Netherlands.

De Waal, J.A., Muntendam-Bos, A.G., and Roest, J.P.A. (2015). Production induced subsidence and seismicity in the Groningen gas field - can it be managed? *Proceedings of the International Association of Hydrological Sciences*, *372*, 129–139. DOI:10.5194/piahs-372-129-2015

De Waal, J.A., Muntendam-Bos, A.G., and Roest, J.P.A. (2017). From checking deterministic predictions to probabilities, scenarios and control loops for regulatory supervision. *Netherlands Journal of Geosciences*, *96*(05), s17–s25. DOI:10.1017/njg.2017.15

Waldmann, S. (2011). *Geological and mineralogical investigation of Rotliegend gas reservoirs in the Netherlands and their potential for CO2 storage*. Jena University, Jena.

Waldmann, S., and Gaupp, R. (2016). Grain-rimming kaolinite in Permian Rotliegend reservoir rocks. *Sedimentary Geology*, *335*, 17–33. DOI:10.1016/j.sedgeo.2016.01.016

Waldmann, S., Busch, A., Van Ojik, K., and Gaupp, R. (2014). Importance of mineral surface areas in Rotliegend sandstones for modeling CO2-water-rock interactions. *Chemical Geology*, *378*–

379(1), 89–109. DOI:10.1016/j.chemgeo.2014.03.014

Walsh, J.B. (1965). The effect of cracks on the compressibility of rock. *Journal of Geophysical Research*, *70*(2), 381. DOI:10.1029/JZ070i002p00381

Walton, K. (1987). The effective elastic moduli of a random packing of spheres. *Journal of the Mechanics and Physics of Solids*. DOI:10.1016/0022-5096(87)90036-6

Wang, B., Chen, Y., and Wong, T. -f. (2008). A discrete element model for the development of compaction localization in granular rock. *Journal of Geophysical Research: Solid Earth*. DOI:10.1029/2006JB004501

Wang, H.F. (2000). *Theory of linear poroelasticity with applications to geomechanics and hydrogeology*. Princeton Univ. Press, Mercer County, New Jersey.

Wang, M., Tang, H., Zhao, F., Liu, S., Yang, Y., Zhang, L., Liao, J., and Lu, H. (2017). Controlling factor analysis and prediction of the quality of tight sandstone reservoirs: A case study of the He8 Member in the eastern Sulige Gas Field, Ordos Basin, China. *Journal of Natural Gas Science and Engineering*. DOI:10.1016/j.jngse.2017.08.033

Wassing, B.B.T., Buijze, L., and Orlic, B. (2016). Modelling of fault reactivation and fault slip in producing gas fields using a slip-weakening friction law. *50th US Rock Mechanics / Geomechanics Symposium*.

Van Wees, J.D., Buijze, L., Van Thienen-Visser, K., Nepveu, M., Wassing, B.B.T., Orlic, B., and Fokker, P.A. (2014). Geomechanics response and induced seismicity during gas field depletion in the Netherlands. *Geothermics*, *52*, 206–219. DOI:10.1016/j.geothermics.2014.05.004

Van Wees, J.D., Osinga, S., Van Thienen-Visser, K., and Fokker, P.A. (2018). Reservoir creep and induced seismicity: Inferences from geomechanical modeling of gas depletion in the Groningen field. *Geophysical Journal International*. DOI:10.1093/gji/ggx452

Weibull, W. (1951). A statistical distribution function of wide applicability. *Journal of Applied Mechanics*, *18*, 293–297.

White, D.J., Take, W.A., and Bolton, M.D. (2003). Soil deformation measurement using particle image velocimetry (PIV) and photogrammetry. *Geothechnique*. DOI:10.1680/geot.2003.53.7.619

Wiebes, E. (2019). Kamerbrief Gaswinningsniveau Groningen in 2019-2020. Den Haag: Ministry of Economic affairs and climate of the Netherlands.

Wieneke, B. (2015). PIV uncertainty quantification from correlation statistics. *Measurement Science and Technology*. DOI:10.1088/0957-0233/26/7/074002

Wilson, M.D. (1992). Inherited Grain-Rimming Clays in Sandstones from Eoilian and Shelf Environments: Their Origin and Control on Reservoir Properties. *Society for Sedimentary Geology*.

Wong, T. -f., and Baud, P. (1999). Mechanical compaction of porous sandstone. *Oil and Gas Science*

and Technology, *54*(6), 715–727. DOI:10.2516/ogst:1999061

Wong, T. -f., and Baud, P. (2012). The brittle-ductile transition in porous rock: A review. *Journal of Structural Geology*, *44*, 25–53. DOI:10.1016/j.jsg.2012.07.010

Wong, T. -f., and Wu, L. -c. (1995). Tensile stress concentration and compressive failure in cemented granular material. *Geophysical Research Letters*, *22*(13), 1649–1652. Retrieved from http://onlinelibrary.wiley.com/doi/10.1029/95GL01596/full

Wong, T. -f., Szeto, H., and Zhang, J. (1992). Effect of loading path and porosity on the failure mode of porous rocks. *Applied Mechanics Reviews*, *45*(8), 281–293. DOI:10.1115/1.3119759

Wong, T. -f., David, C., and Zhu, W. (1997). The transition from brittle faulting to cataclastic flow in porous sandstones: Mechanical deformation. *Journal of Geophysical Research*, *102*, 3009–3025.

Wu, X.Y., Baud, P., and Wong, T. -f. (2000). Micromechanics of compressive failure and spatial evolution of anisotropic damage in Darley Dale sandstone. *International Journal of Rock Mechanics and Mining Sciences*, *37*(1–2), 143–160. DOI:10.1016/S1365-1609(99)00093-3

Xenaki, V.C., and Athanasopoulos, G.A. (2003). Liquefaction resistance of sand-silt mixtures: An experimental investigation of the effect of fines. *Soil Dynamics and Earthquake Engineering*, *23*(3), 183–194. DOI:10.1016/S0267-7261(02)00210-5

Yale, D.P., and Swami, V. (2017). Conversion of dynamic mechanical property calculations to static values for geomechanical modeling. *American Rock Mechanics Association*, *17-0644*.

Yang, H., Li, S., and Liu, X. (2016). Characteristics and resource prospects of tight oil in Ordos Basin, China. *Petroleum Research*. DOI:10.1016/S2096-2495(17)30028-5

Yang, X.-S. (2000). Pressure Solution in Sedimentary Basins: Effect of Temperature Gradient. *Earth and Planetary Science Letters*, *176*, 233–243. DOI:10.1016/S0012-821X(99)00321-0

Yin, H., and Dvorkin, J. (1994). Strength of cemented grains. *Geophysical Research Letters*, *21*(10), 903–906.

Zbinden, D., Rinaldi, A.P., Urpi, L., and Wiemer, S. (2017). On the physics-based processes behind production-induced seismicity in natural gas fields. *Journal of Geophysical Research: Solid Earth*. DOI:10.1002/2017JB014003

Zhang, C., Nguyen, G.D., and Kodikara, J. (2016). An application of breakage mechanics for predicting energy-size reduction relationships in comminution. *Powder Technology*. DOI:10.1016/j.powtec.2015.09.040

Zhang, J., Wong, T. -f., and Davis, D.M. (1990). Micromechanics of Pressure-Induced Grain Crushing in Porous Rocks, *95*, 341–352.

Zhang, Y., and Buscarnera, G. (2018). Breakage mechanics for granular materials in surface-reactive environments. *Journal of the Mechanics and Physics of Solids*. DOI:10.1016/j.jmps.2017.11.008

Zhang, Y.D., and Buscarnera, G. (2015). Prediction of breakage-induced couplings in unsaturated

granular soils. *Géotechnique*. DOI:10.1680/geot.14.p.086

Zhu, W., David, C., and Wong, T. -f. (1997). The transition from brittle faulting to cataclastic flow: Permeability evolution. *Journal of Geophysical Research*, *102*, 3027. DOI:10.1029/96JB03282

Ziegler, P.A. (1990). *Geological Atlas of Western and Central Europe* (2nd ed.). Bath: Geological Society Publishing House.

Zoback, M.D. (2010). *Reservoir Geomechanics* (12th paper). Cambridge University Press.

Lekensamenvatting

Olie- of gaswinning kan leiden tot bodemdaling en aardbevingen, zoals getoond in het grootste gasveld van Europa - het Groningen gasveld in Nederland (aardbevingmagnitude tot 3.6). In dit veld wordt bodemdaling (tot op heden maximaal 36 cm) veroorzaakt door inzakking (compactie/inklinking) van de op 3 kilometer diepte gelegen, gasvoerende zandsteen. Inzakking ontstaat door het verlagen van de gasdruk in de zandsteenporiën en daarmee de tegendruk op het gewicht van het overliggende gesteente op de zandsteenkorrels. Deze druk/spanningsveranderingen en de daarmee geassocieerde inzakking kunnen leiden tot verschuivingen van enkele centimeters langs oude aardbreuken, welke mogelijk in aardbevingen resulteren. Begrip van het inzakkingsgedrag van de gasvoerende zandsteen is dan ook essentieel voor ons begrip van zulke aardbevingen. Vaak wordt *aangenomen* dat inzakking tijdens gaswinning volledig omkeerbaar (elastisch) is, wat relatief gemakkelijk te beschrijven valt. Inzakking kan echter ook permanent zijn, wat mogelijk betekent dat inzakking tijdelijk doorgaat, zelfs na het stoppen van gaswinning. Permanente inzakking is veel minder goed begrepen.

Gegeven deze achtergrond heb ik laboratoriumexperimenten uitgevoerd op zandstenen uit het Groningen gasveld, waarin ik gasproductie simuleer op de druk- en temperatuur van de ondergrond op 3 km diepte. Uit de resultaten blijkt dat 30 tot 50% van de inzakking permanent is. Microscoopanalyses tonen dat deze permanente inzakking grotendeels veroorzaakt wordt door het samendrukken van micrometer-dikke kleirandjes tussen de zandsteenkorrels (zie kaftfoto). De resultaten laten verder zien dat: a) De spanningen in de zandsteen en op oude breuken beter beschreven zijn als er rekening gehouden wordt met permanente inzakking; b) Er 30 tot 50% minder energie potentieel beschikbaar is in de zandsteen voor aardbevingen dan verwacht zou worden als inzakking puur omkeerbaar zou zijn; en c) Tijdelijk doorgaande zandsteeninzakking na het stoppen van gaswinning vermoedelijk erg beperkt zal zijn.

Acknowledgements / Dankwoord

There you go, well over 270 pages of new science on a rock.

It is an amazing thing that so much can be said about clung-together sand and clay. Moreover, as you can tell from the impressive reference list in this thesis, I am clearly not the only one who has written about it! It is often said that for each new level of detail explored, there's always one that lies behind it. And that we may never fully understand the nature of things. Still, I feel that exactly in this unsolvable intricacy of its natural materials lies the true wonder of our planet. It takes a while, though (in my case four-and-a-half years), to appreciate just how intricate clung-together sand and clay can be, let alone the rest of the Earth (or *beyond!!*). In the mean time, I took great pleasure in immersing myself in this highly interesting landscape of sand grains and their micrometer-displacements, or in the words of the poet William Blake: "*To see a world in a grain of sand*".

Now I have that off my chest, there are a number of people who helped me on this journey and I am accordingly indebted to them all.

First and foremost, I owe a great gratitude to my professor and promotor, Chris Spiers. Chris, you picked me up at a welcome time, entrusted me with a job and gave me time to adjust to the new environment. For that alone I am truly very grateful. But I also learned from you on countless aspects, including material science, proper scientific methods and writing, presenting, clear definition of a problem and to devise ingenious/cunning ways to approach it. I take inspiration from the many different roles you fulfil so fluently (and often simultaneously), including that of a manager, a creative inventor, a perfectionist, a strict teacher and an interested friend. You further encourage originality in me and in others, which I think is one of the greater virtues in life. You were and remain a great mentor. Thanks!

I also want to give a great thanks to my co-promotor, Suzanne Hangx. You played a vital role in getting me up-to-speed in the first years of my HPT time. You exerted patience and your substantial knowledge on (sandstone) mechanics to give direction and scientific footing to my sometimes wild ideas. In later years you remained incredibly helpful in developing this work. In particular, I learned a lot from you on easily digestible presenting and writing (-imagine how lengthy this thesis would have been without you!).

Further thanks go to my other co-promotor, Colin Peach. You are the beating heart of

the lab. I could always approach you for questions on machinery, experiments, pumps, electronics, flow, thermodynamics, pressure vessels, seals, sensors and software and how they all interlink (sometimes seemingly cosmically). I also thoroughly enjoyed our four *vueltas* to Camarasa in Spain with all its secret pork and other delights, and to take in your profound geological and historical knowledge on the region.

I am also thankful to my closest collaborator (or partner in crime) in this project: Bart Verberne. While PhD's are usually solitary in nature, the overlapping aims of our projects resulted in us working closely together, sometimes even daily. This led to many fruitful scientific discussions, often littered with crude/banal jokes and lots of laughs. Our work together produced my favorite (split-cylinder) Chapter 4; the Helios ion-mill is still trembling after you left! Your significant knowledge on image acquisition and processing contributed greatly to this thesis, while your friendship and humor brought oxygen to the project (and occasionally to Tuesday meetings). Thanks for all of this, and I hope we stay in touch, in Japan and beyond.

The present research was funded by the Nederlandse Aardolie Maatschappij (NAM) and accordingly I am very grateful to them. In addition, the energetic, bi-yearly progress report meetings with employees and researchers from NAM, Shell Global Solutions, ExxonMobil and EBN never failed to provide a new boost to the research. Special thanks go to: Jan van Elk, Dirk Doornhof, Rob van Eijs, Sander Hol, Clemens Visser, Peter van den Bogert, Rick Wentinck, Fons Marcelis, Tony Mossop, Aletta Filippidou, Nora DeDontney and Marc Hettema. Rob and Dirk, an extra thanks to you for providing many useful comments and insights for this thesis.

To my paranymphs and friends Evangelos Korkolis and Luuk Hunfeld, you were usually the first to accommodate the unfiltered version of my joy and grunting that came with the work - thanks for bearing it all! Luuk, the first few weeks of our PhD's we were crunching, drilling, dissolving, breaking, sliding and scanning Groningen core material, (or perhaps more aptly put: "MacGyvering away") to produce the first data for NAM within a month's deadline. For sure, these frantic weeks are among the most memorable of my PhD. Evangelos, our explorations usually took place outside the lab (Primus, Kielegat, ..). There, we had many (in)fruitful discussions on always important matters, ranging from the attitudes of president Johnson and McNamara during the Vietnam war, to the right selection for Ajax. As generation buddies we 'grew up' together and shared many happy moments in and outside of the lab, of course together with Loes Buijze ("*Krrruahh"*), Mariska Schimmel and Martijn van den Ende.

Hans de Bresser ("*hou het efficient*!") and Andre Niemeijer, a special thanks to both of you. Your experience and insights benefited the research directly and I enjoyed our interactions to boot. Sabine den Hartog, you were my first mentor in the HPT (2011/2012) and I learned a lot from you, even though I did not always realize it at the time. Thanks a lot and I hope we keep running into each other in the future. Thanks to both of the Maartjes (Houben and Hamers), for helping out with microscopy work on several occasions. Dawin Baden and Ji Yun-Tao, what started out as a promise of a good joke ("A Chinese, a Guadeloupian and a Dutch guy go to Japan…"), was quickly turned into a successful and fun adventure. Thanks for all the laughs, the mango pudding *and* the coconut ice cream, and I wish both of you many days of Champions League! Dawin: thanks also for acting as Matlab Guru every now and then. Of course, I also want to thank my other colleagues (present and past) in the lab: Hadi (balls!!), Aditya, Jeroen, Peter, Caspar, Anastasia, Amin (the slimmest Elephant I know), Miao (brother-in-rock-drilling), Ross, Tim, Jianye, Eli (Jaartje nul-zes!), Anne P., Nawaz, Ayumi, Zahra and (the always cheerful) Wen. All of you liven(ed) up the HPT and brought a truly inspiring diversity into each day. New-to-the-lab: Chien-Cheng, Taka and Floris, I wish you the best of luck with your research!

The experiments and analyses reported in this thesis would have been impossible without the technical support I received from Gert Kastelein, Floris van Oort, Thony van der Gon Netscher, Eimert de Graaff, Gerard Kuijpers, Peter van Krieken, Leonard Bik and Otto Stiekema. I want to thank Gert and Floris in particular, who developed most of the tools/machinery developed specifically for this thesis, including the pistons for the Shuttle vessel (Chapter 2), the 4 kbar (!) Rene pressure vessel (Chapter 3) and the split-cylinder sample holder for the Helios microscope (Chapter 4). Items like these were always skillfully made and I enjoyed watching your craftsmanship.

All the above-mentioned colleagues are part of the HPT family, but no one contributed more to the family-feel of this group than the HPT-secretary Magda Mathot-Martens. Magda, the amount of support and care you've given to me and to others is truly incredible. You always keep a close eye on each member of the group, make sure that celebrations are celebrated and that everyone feels welcome. Thanks for everything!

Preserving a sound mental state of a PhD student (or at least maintaining a broadly constant average) is a daunting task. Thanks to all my friends outside the lab for routinely measuring my mental soundness (usually in the bar, in a zoo (?!) or in some far-away country), and for performing occasional repairs and damage control when needed: Michiel, Marcel, Kris, Richard, Paul, Joost, Luuk T., Eva, Diderik, Guy, Koen, Maureen, Frank,

Edwin and Roeland. I also want to thank the team at PVW Amsterdam for providing a welcoming writing retreat and for sharing the creative vibes, always present in their office.

Last, but certainly not least I am very thankful to my family. Jan, Wil, Jan(-*Julien*), Melissa, Evy, Xem, Jeroen en Jetske, bedankt dat jullie mij zo warm hebben opgenomen in de familie. Adam, bedankt voor het luisteren naar de pieken en dalen van het onderzoeksleven en voor het delen van je ervaring en droge humor als iemand-die-daar-ook-geweest-is. Anneloes, bedankt voor de vele geweldige momenten die we gedeeld hebben de afgelopen 31 jaar (sorry dat ik er niet eerder kon zijn!) – van de slappe lach hebben over het woord “stoel” (toen we nog wat jonger waren) tot het hiken langs de kust van Minehead (toen we alweer wat ouder waren) en nu het op de bank koffiedrinken met Myrna, Yorrik en Roos in het midden. Allemaal mooie herinneringen, je bent de beste grote zus die ik me kan wensen! Aan mijn vader Martien Pijnenburg: in mijn ogen blijf jij de echte academicus van de familie. Je stopte hart en ziel in je rollen als medisch ethicus en vader, met als resultaat dat jouw *identiteit* onlosmakelijk verweven is in je proefschrift en in je kinderen. In een volgend leven moeten we maar weer eens goed gedachten uitwisselen over wat het allemaal betekent: onderzoek, het ouderschap en als we er toch zitten - het leven. Aan mijn moeder, Susanne Pijnenburg, bedankt voor je luisterend oor en nuchtere wijsheid met betrekking tot dit onderzoek en tot vele onderwerpen daarbuiten. Je veelgebruikte leus ‘*vooruitzien is regeren*’ heb ik vaak toegepast, zeker binnen dit onderzoek (behalve misschien op het einde, toen de planning een eigen leven begon te leiden). Onze dochter Roos Susanne Pijnenburg zal trots zijn op het dragen van jouw naam.

Anne, onwijs bedankt voor alle steun en vreugde die je me hebt gegeven in de afgelopen jaren. Met name in het laatste jaar was jij een rots in de branding. Je vult me aan op vele vlakken, maar hebt me bovenal geleerd dat er vaak meer grijstinten bestaan dan ik soms denk. We delen een gevoel van verwondering over vele aspecten van het leven, groot en klein, en het openingscitaat van dit boekje refereert daar naar. Dit maakt elke dag met jou – en sinds kort ook met onze dochter Roos – een nieuw Avontuur. Ik kijk uit naar de rest van ons gedeelde leven!

List of publications

As of 18 September 2019

Manuscripts in preparation:

Pijnenburg, R.P.J. and Spiers, C.J. Microphysics of inelastic deformation in reservoir sandstones from the seismogenic center of the Groningen gas field

Verberne, B.A., Hangx, S.J.T., **Pijnenburg**, **R.P.J.,** Hamers, M.F., Drury, M.R., Spiers, C.J. Gas field drill core constrains mechanisms behind subsidence and induced seismicity

Ji, Y. Baden, D.H., Hunfeld, L.B. **Pijnenburg, R.P.J.**, Yamashita, F. Xu, S. Fukuyama, E. Niemeijer, A.R., Spiers, C.J. Friction of faults: Does size matter?

Manuscript submitted:

Pijnenburg, R. P. J., Verberne, B. A., Hangx S. J. T. and Spiers, C. J. Intergranular clay films control inelastic deformation in the Groningen gas reservoir: Evidence from split-cylinder deformation tests. *Submitted to Journal of Geophysical Research: Solid Earth*

Manuscripts published:

Pijnenburg, R.P.J., Verberne, B.A. Hangx, S.J.T. and Spiers C.J. (2019). Inelastic Deformation of the Slochteren Sandstone - Stress-Strain Relations and Implications for Induced Seismicity in the Groningen Gas Field. *Journal of Geophysical Research: Solid Earth*, 124 (5), (pp. 5254-5282)

Pijnenburg, R.P.J., Verberne, B.A. Hangx, S.J.T. and Spiers C.J. (2018). Deformation behavior of sandstones from the seismogenic Groningen gas field - Role of inelastic versus elastic mechanisms. *Journal of Geophysical Research: Solid Earth*, 123 (7), (pp. 5532-5558)

Busch, A., Kampman, N., Hangx, S.J.T., Snippe, J., Bickle, M., Bertier, P., Chapman, H., Spiers, C.J., **Pijnenburg, R.P.J.**, Samuelson, J., Evans, J.P., Maskell, A., Nicholl, J., Pipich, V., Di, Z., Rother, G. & Schaller, M. (2014). The Green River natural analogue as a field laboratory to study the long-term fate of CO2 in the subsurface - 12th International Conference on Greenhouse Gas Control Technologies, GHGT-12. *Energy Procedia*, 63, (pp. 2821-2830)

Curriculum Vitae

Date of Birth	5 August 1988
Place of Birth	Nijmegen, the Netherlands
E-mail	R.P.J.Pijnenburg@uu.nl

WORK EXPERIENCE

01/2015 – 10/2019 **PhD candidate**

Utrecht University, Experimental Rock Deformation

03/2014 – 12/2014 **Junior researcher**

Utrecht University, Experimental Rock Deformation

Researching long-term (centuries) chemo-mechanical effects of CO_2 storage in sandstone reservoirs and the integrity of the reservoir- and cap rock.

07/2012 – 01/2014 **Exploration geologist**

RSC Mining and Mineral Exploration, Perth, Australia

Project-based consultancy work for clients involved in the mining industry in Australia, Sweden, Mozambique and Kazakhstan. Responsibilities included core logging, giving core logging training, geological field mapping, geochemical assay and field logistics.

04/2012 – 07/2012 **Research trainee**

CSIRO Australian Resources Research Centre, Perth, Australia

I collected and analyzed mineralogical, geochemical and geophysical data from soils and integrated these to identify targets for mineral exploration.

EDUCATION

09/2010 – 09/2012 **MSc in Geology**

Utrecht University

09/2006 – 09/2009 **BSc in Earth Sciences**

Utrecht University

of which I spent the final semester at the

02/2009 – 07/2009 *National Taiwan University*